Modeling and Control of a Multibody Hinge-Barge Wave Energy Converter

Francesco Paparella

A thesis submitted to Maynooth University for the degree of Doctor of Philosophy

in the

Faculty of Science and Engineering

Electronic Engineering Department

September 2017

Head of Department: Dr. Ronan Farrell

Supervisor: Prof. John V. Ringwood

Contents

Abstract

Wave Energy Converters (WECs) are devices used to extract energy from the waves. The particular WEC considered in this thesis is a three-body hinge-barge WEC, which is an articulated floating structure composed of 3 rectangular bodies interconnected by hinges, and it operates longitudinally to the direction to the incoming wave. The relative motion between each pair of bodies drives a Power Take-Off (PTO) system, which extracts the energy from the waves. The objective of this thesis is to increase the energy that can be extracted by a three-body hinge-barge WEC using an optimal control strategy, which computes the optimal loads applied by the PTOs driven by the relative motion between the bodies. The optimal control is formulated in the time domain, and computes the PTO loads in a coordinated way, so that the total energy extracted by the device is maximized. The optimal control strategy is formulated for a three-body hinge-barge WEC that is equipped with either passive or active PTOs.

In this thesis, an optimal control strategy, for the maximization of the energy extracted by a three-body hinge-barge WEC, is derived with Pseudo-Spectral (PS) methods, which are a subset of the class of techniques used for the discretisation of integral and partial differential equations known as mean weighted residuals. In particular, PS methods based on Fourier basis functions, are used to derive an optimal control strategy, for a finite time horizon. Therefore, an optimal control strategy, with PS methods based on Fourier basis functions, cannot be applied for real-time control of the WEC, as Fourier basis functions can only represent the steady-state response of the WEC. However, PS methods based on Fourier basis functions provide a useful framework for the evaluation of the achievable power absorption performance of the WEC, with both active and passive PTOs. The Receding Horizon (RH) real-time optimal control of a three-body hinge-barge WEC is derived with PS methods based on Half-Range Chebyshev-Fourier (HRCF) basis functions. The RH optimal real-time controller, with PS methods based on HRCF basis functions, maximizes the energy extracted by the WEC at each time step over a moving control horizon. In contrast to Fourier basis functions, HRCF basis functions are well suited for the approximation of non-periodic signals, allowing the representation of both the transient and steady-state response of the WEC.

The optimal control strategy, with PS methods based on either Fourier or HRCF basis functions, is based on a dynamic model of the device, which is derived with two different modeling methodologies, that can be also applied to other types of multiple body WECs. The modeling methodologies are validated against wave-tank tests carried out on a 1/7th scale two-body hinge-barge device, and a 1/25th and 1/20th scale three-body hinge-barge device.

Declaration of authorship

I, Francesco Paparella, declare that this thesis titled "Modeling and Control of a Multibody Hinge-Barge Wave Energy Converter" and the work presented in it are my own. I confirm that:

- This work was done wholly or mainly while in candidature for a research degree at this University.
- Where any part of this thesis has previously been submitted for a degree or any other qualification at this University or any other institution, this has been clearly stated.
- Where I have consulted the published work of others, this is always clearly attributed.
- Where I have quoted from the work of others, the source is always given. With the exception of such quotations, this thesis is entirely my own work.
- I have acknowledged all main sources of help.
- Where the thesis is based on work done by myself jointly with others, I have made clear exactly what was done by others and what I have contributed myself.

Signature: _____ Date: _____

Acknowledgement

First of all, I would like to thank my supervisor Professor John Ringwood for the guidance and support that he gave me during my PhD studies. Special thanks to the past members of the Centre for Ocean Energy Research (COER), Giorgio, Sebastien, Romain and Ronan, for helping me with the theoretical aspects of my research. Also, many thanks to Tom from DkIT, Yerai from COER, and Satja from UL, for the help they gave me with the experimental activities of my research.

I would also like to thank Brian, Joe, Jim, David and Evan, from WECCA, for providing a small scale WEC and experimental equipment for my research. Many thanks to Harvey from OMEY Labs, for giving me the possibility to carry out the experimental tests at his facility.

I would like to thank all the people I met at the beginning of my stay in Ireland, for their friendship and trips around Ireland: Luca, Simone, Marco, Davide, Andrej, Paula, Victor, Josh, Tue, Owen and David. Also, I would like thank the people I met later on during my PhD, for their friendship and time together: Giuseppe, Markel, Marina, Nicolas, Alexis and Christian. Special thanks to my housemate and friend Gerard, for the time we spent together in Maynooth.

I would like to thank Ann and Joanne, from the administration office, and John Maloco and Denis, from the technical staff, for their assistance during my stay at COER.

Many thanks to my parents and my girlfriend Ineta, for the continuous support and advice that they gave me during all the period of my studies.

Acronyms

AR	Auto-Regressive
BDFs	Backward Difference Formula
DAEs	Differential and Algebraic Equations
DoF	Degrees of Freedom
EMEC	Europen Marine Energy Centre
EKF	Extended Kalman Filter
GoF	Goodness of Fit
HRCF	Half-Range Chebyshev-Fourier
INS	Inertial Navigation System
IMU	Inertial Measurement Unit
LS	Least Square
LRPRI	Long Range Predictive Identification
MPC	Model Predictive Control
MPGI	Moore-Penrose Generalized Inverse
MWP	McCabe Wave Pump
NSF	Null Space Formulation
ODEs	Ordinary Differential Equations
PS	Pseudo-Spectral
PTO	Power Take Off
RAO	Response Amplitude Operator
RMS	Root Mean Square
R-K	Runge-Kutta
RH	Receding Horizon
RHPSC	Receding Horizon Pseudo-Spectral Control
UKF	Udwadia and Kalaba Formulation
WEC	Wave Energy Converter

Nomenclature

Symbol	Description
a	Vertical distance between dashpot axis and the center line of the device
$\mathbf{B}^{b_k}$	Coriolis-Centripetal matrix of body k
$\mathbf{B}^{b_k}_{visc}$	Linearized viscous damping of body k
$\mathbf{B}$	Coriolis-Centripetal matrix of multibody system
$\mathbf{B}_{visc}$	Linearized viscous damping of multibody system
$\mathbf{B}_s$	Coriolis-Centripetal matrix for independent coordinates
$\mathbf{B}_{visc,s}$	Linearized viscous damping for independent coordinates
$\mathbf{B}_{rad,s}$	Radiation damping for independent coordinates
$\mathbf{B}_{eq,rad}$	Equivalent radiation damping
$\mathbf{B}_{eq,visc}$	Equivalent viscous damping
$\mathbf{C}$	Constraint equations
$\mathbf{C}_z$	Partial derivative of constraint equations
$\mathbf{C}_{\mathbf{q}_d}$	Partial derivatives of constraint equations respect to the dependent coordinates
$\mathbf{C}_{\mathbf{q}_s}$	Partial derivatives of constraint equations respect to the independent coordinates
c_{PTO}	coefficient passive PTO
$\mathbf{D}_\phi$	Derivation matrix PS Fourier methods
$\mathbf{D}$	Derivation matrix PS HRCF methods
d_k	Distance along the x-coordinate of body k from global frame
$\mathbf{F}_p$	PTO configuration matrix of multibody system
$\mathbf{F}_{p,s}$	PTO configuration matrix for independent coordinates
$\hat{\mathbf{F}}_{wave,s}$	Fourier transform excitation forces vector for independent coordinates
$\mathbf{F}_{wave,s}$	Scaled excitation forces vector for independent coordinates
$\hat{\mathbf{F}}_{eq,wave}$	Fourier transform equivalent excitation forces vector
$\mathbf{F}_{eq,wave}$	Scaled equivalent excitation forces vector
$\mathbf{f}^{b_k}_{wave}$	Excitation forces vector of body k in body frame
$\mathbf{f}^{b_k}_{ext}$	External forces vector of body k in body frame
$\mathbf{f}^{b_k}_{pto}$	PTO force vector of body k in body frame
$\mathbf{f}^{b_k}$	Moorings, hinge-friction, etc. force vector of body k in body frame
$\mathbf{f}_{wave}$	Excitation forces vector of multibody system

$\mathbf{f}_{eq,wave}$	Equivalent excitation forces vector
$\hat{\mathbf{f}}_{eq,wave}$	Estimated equivalent excitation forces vector
$\mathbf{f}$	Moorings, hinge-friction, etc. force vector of multibody system
$\mathbf{f}_{pto}$	PTO force vector of multibody system
$\mathbf{f}_{wave,s}$	Excitation forces vector for independent coordinates
$\mathbf{f}_{s}$	Moorings, hinge-friction, etc. force vector for independent coordinates
$\mathbf{f}_{pto,s}$	PTO force vector for independent coordinates
$\mathbf{G}^{b_k}$	Hydrostatic matrix of body k
$\mathbf{G}$	Hydrostatic matrix of multibody system
$\mathbf{G}_s$	Hydrostatic matrix for independent coordinates
$\mathbf{G}_{eq}$	Equivalent hydrostatic matrix
$\mathbf{G}_{rad}$	PS Fourier convolution integral matrix for velocities of multibody system
$\mathbf{G}_{rad,s}$	PS Fourier convolution integral matrix for independent velocities
$\mathbf{G}_{eq,rad}$	PS Fourier convolution integral matrix for equivalent velocities
H_s	Significant wave height
$\mathbf{H}$	Experimental transfer function between wave elevation and independent coordinates
$\hat{\mathbf{H}}$	Theoretical transfer function between wave elevation and independent coordinates
$\hat{\mathbf{H}}_{wave,s}$	Estimated transfer function between wave elevation and excitation forces
$\hat{\mathbf{H}}_{eq,wave}$	Estimated transfer function between wave elevation and equivalent excitation forces
$h_{g,k}$	Distance of center of mass of body k from point O_{bk} along the z-axis
$\mathbf{I}_{b_k}$	Inertia matrix of body k around origin body frame
$I_{yy,k}$	Moment of inertia of body k around the y-axis
$\mathbf{J}^{b_k}$	Transformation matrix between velocity vector in global and body frame of body k
$\mathbf{J}$	Transformation matrix between velocity vector in global and body frame of multibody system
$\mathbf{K}_{rad}^{b_k}$	Radiation impulse response function matrix of body k
$\mathbf{K}_{wave}^{b_k}$	Wave excitation force impulse response function matrix of body k
$\mathbf{K}_{rad}$	Radiation impulse response function matrix of multibody system
$\mathbf{K}_{wave}$	Wave excitation force impulse response function matrix of multibody system
$\mathbf{K}_{rad,s}$	Radiation impulse response function matrix for independent coordinates
$\mathbf{K}_{eq,rad}$	Radiation impulse response function matrix for equivalent reduced model
$\mathbf{k}_{rad,s}$	Scaled radiation impulse response function matrix for independent coordinates
$\mathbf{k}_{eq,rad}$	Scaled radiation impulse response function matrix for equivalent reduced model
$\mathbf{K}_{moor}$	Mooring matrix
$k_{moor,k}$	Mooring stiffness coefficient of body k
l	Length dashpot system
$l_{k,h}$	Distances of hinge from body k
$\mathbf{M}_{in}^{b_k}$	Rigid-body inertia matrix of body k
$\mathbf{M}_{\infty}^{b_k}$	Added mass at infinite frequency of body k
$\mathbf{M}_{in}$	Rigid-body inertia matrix of multibody system
$\mathbf{M}_{\infty}$	Added mass at infinite frequency of multibody system

$\mathbf{M}_s$	Rigid-body inertia matrix for independent coordinates
$\mathbf{M}_{eq,in}$	Equivalent rigid-body inertia matrix
$\mathbf{M}_{a,s}$	Added mass for independent coordinates
$\mathbf{M}_{eq,a}$	Equivalent added mass
$\mathbf{M}_{eq,\infty}$	Equivalent added mass at infinity
$\mathbf{M}_{\infty,s}$	Added mass at infinite frequency for independent coordinates
M	Order of expansion PS HRCF
m_k	Mass of body k
m	Number of Lagrange multipliers
N	Number of bodies of multibody system
N_x	Order of expansion PS Fourier Methods
N_f	Number of frequencies excitation force for feedforward estimator
n	Number of degrees of freedom of multibody system
n_c	Number of control forces
n_f	Number of frequencies excitation force for feedback estimator
$\mathbf{P}$	Transformation matrix between independent and dependent velocities
$\mathbf{P}_{rad,s}$	PS HRCF convolution integral matrix for independent velocities
$\mathbf{P}_{eq,rad}$	PS HRCF convolution integral matrix for equivalent velocities
$\mathbf{p}^i_{i,b_k}$	Position vector of point O_{b_k} with respect to the point i, in global frame
$\mathbf{p}^b_{i,b_k}$	Position vector of point O_{b_k} with respect to the point i, in body frame
$\mathbf{Q}$	Scaled position vector
$\mathbf{q}_k$	Position and orientation vector of body k in global frame
$\mathbf{q}$	Position vector of multibody system in global frame
$\mathbf{q}_s$	Position vector of independent coordinates
$\mathbf{q}_{eq}$	Equivalent position vector
$\mathbf{R}^i_b$	Rotation matrix from body frame to global frame
$\mathbf{r}_{g,k}$	Position vector of center of mass body k from origin of body frame
$\mathbf{S}$	Skew-symmetric matrix cross-product
$\mathbf{T}$	Transformation matrix between angular velocity vector and Euler angles derivatives
T	Fundamental period PS Fourier methods
T_0	Control time horizon
T_s	Sampling time
T_p	Peak period
t	Time
$\hat{\mathbf{U}}$	Fourier transform control force vector
$\mathbf{U}$	Scaled control force vector
$\mathbf{u}$	Control force vector
$\hat{\mathbf{u}}_p$	PS coefficients pth component of control force vector
$\hat{\mathbf{V}}$	Fourier transform velocity vector
$\mathbf{V}$	Scaled velocity vector

$\hat{\mathbf{V}}_{eq}$	Fourier transform equivalent velocity vector
$\mathbf{v}_k$	Linear and angular velocity vector of body k in body frame
$\mathbf{v}$	Linear and angular velocity vector of multibody system in body frame
$\mathbf{v}_d$	Dependent velocities
$\mathbf{v}_s$	Independent velocities
$\mathbf{v}_{eq}$	Equivalent velocities
$\hat{\mathbf{X}}_s$	Fourier transform degrees of freedom vector
$\hat{\mathbf{x}}_i^q$	PS coefficient ith component of position vector
$\hat{\mathbf{x}}_i^v$	PS coefficient ith component of velocity vector
$\hat{\mathbf{x}}_i^{ex}$	PS coefficient ith component of excitation force vector
$\hat{\mathbf{x}}_i^{rad}$	PS coefficient ith component of radiation force vector
$\mathbf{z}_k$	Position vector of body k in body frame
$\mathbf{z}$	Position vector of multibody system in body frame
z_k	Heave displacement of body k
$\hat{\eta}$	Fourier transform free surface elevation
η	Free surface elevation
$\boldsymbol{\Theta}_k$	Euler angles of body frame
θ	Pitch angle
$\boldsymbol{\lambda}$	Lagrange multipliers
$\boldsymbol{\Phi}$	PS basis function vector
ϕ	Roll angle
ψ	Yaw angle
$\boldsymbol{\omega}_{i,b}^b$	Angular velocity vector in body frame
ω	Radial frequency
ω_0	Fundamental frequency PS Fourier methods

Chapter 1

Introduction

1.1 Scope

The global energy consumption rose by about one-third from 2000 to 2014, and it is estimated that, in 2040, it will be 25% higher than in 2014 [1]. Given that the availability of traditional energy resources, such as fossil fuels, is finite, renewable energies will play a fundamental role in the satisfaction of the global energy demand [2]. In the past three decades, different technologies based on solar, wind and wave energy have been developed. The density of wave power, which is around 2-3 kW/m^2, is greater than the density of solar and wind power, which is 0.1-0.2 kW/m^2 and 0.4-0.6 kW/m^2, respectively [2]. Furthermore, the predictability of waves is generally higher than wind [2], [3].

In Figure 1.1, the distribution of the global wave energy resource is shown, with the largest values of average wave power in the mid-latitudes, between 30°and 60°[4]. As Figure 1.1 shows, the highest levels of wave energy are found off the western coast of the continents, which are exposed to the open ocean. The western coasts of Europe, North-America and Australia, are the locations with the largest wave potential.

Although wave energy is characterized by a large potential, many barriers hinder the development of Wave Energy Converters (WECs) for the extraction of the energy from the waves. For example, the structure of a WEC has to be robust enough to survive the harsh and hostile marine environment. Moreover, the hostility of the marine environment makes the maintenance of a WEC difficult, resulting in significant operational and maintenance costs. Also, the largest amount of wave power is usually located in remote areas away from the shore, increasing the overall installation costs due to moorings, transmission cables, etc.

Several WECs have been developed throughout history, which are based on different operating principles, for the extraction of the energy from the waves. Also, WECs can be classified according to the location where they are deployed. In fact, WECs can be deployed offshore, near-shore and on the shoreline. Around the world, different projects of WECs, at various stages of development, are currently being developed. Different studies show that the number of new concepts of WECs

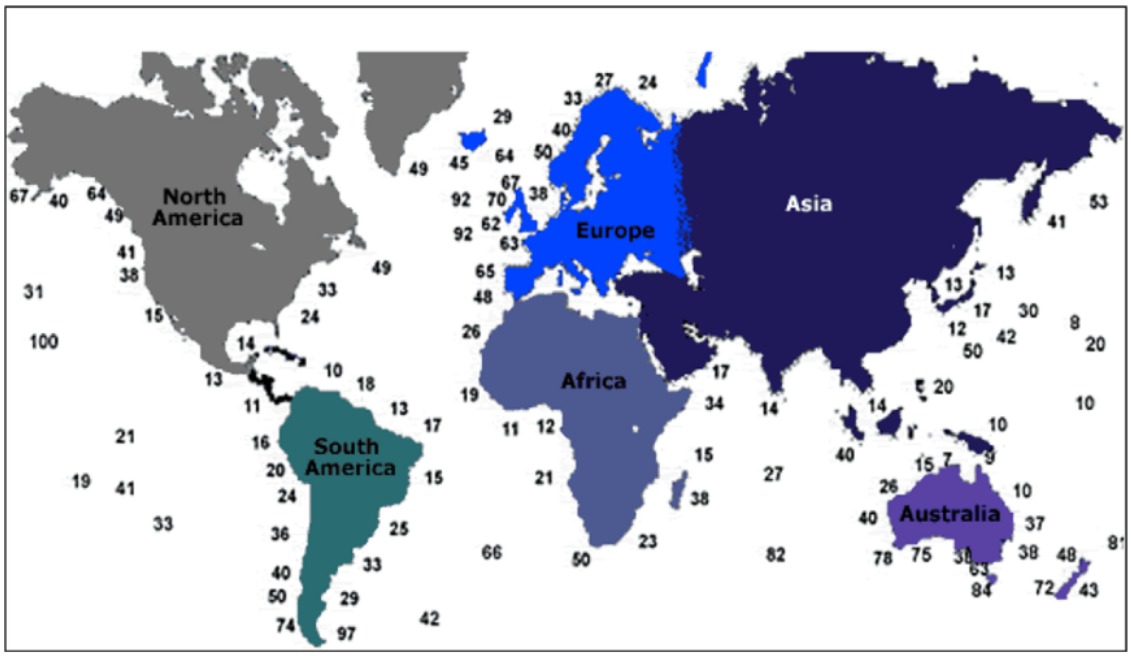

Figure 1.1: Global distribution of the average wave power in kW/m [4].

does not decrease, with the new WECs replacing the WECs that are not developed anymore [5]. Depending on the operating principle which is used to extract energy from the waves, WECs can be classified into 6 different categories: point absorbers, Oscillating Water Columns (OWCs), oscillating wave surge devices, overtopping devices, pressure differential devices and hinge-barge devices [2]. In Figure 1.2, an illustration of WECs based on different working principles is shown.

As shown in Figure 1.2, a point absorber converts the energy of the waves into electricity using its translational motion induced by the waves. Typically, a point absorber is floating on the water level, and is fixed to the sea-bed using a Power Take-Off (PTO) system, which converts the mechanical energy of the device into electricity. The diameter of a point absorber is significantly smaller than the wavelength of the incoming wave. An OWC is made of a concrete or steel chamber which is partly submerged in the water, and is open at the bottom [5]. The motion the water surface inside the chamber pushes air through a turbine, which is connected to an electrical generator. An oscillating wave surge device is made of a hinged flap at the sea bed, whose pitch motion, induced by the waves, drives a hydraulic PTO, which pumps high-pressure fluid to the shore via a sub-sea pipeline [5]. An overtopping device is made of a structure which is overtopped by the incoming wave, and the water is then stored into a reservoir. The water in the reservoir is then released back to the sea through a turbine, which is connected to an electrical generator [2]. A pressure differential device is an air-reservoir, consisting of a floater which is free to move vertically, and a stator which is anchored to the sea bed [6]. The position of the floater varies with the changing hydrodynamic pressure of the water, and the energy is extracted using the vertical motion. A hinge-barge device is composed of an assembly of floating bodies connected together by different type of joints. The relative motion between each pair of bodies drives a PTO, which

extracts the energy from the waves.

A single-body WEC, such as the point absorber, has only one operational mode, and is characterized by a narrow frequency band where the energy is extracted from the waves. Instead, a multibody WEC, such as the hinge-barge device, can extract energy from multiple modes, allowing the extraction of the energy from the waves over a broader frequency band than the frequency band of a single body WEC [7]. Hinge-barge WECs are discussed in more detail in Chapter 2.

The focus of this thesis is to increase the energy that can be extracted by a three-body hinge-barge WEC using an optimal control strategy, which computes the optimal loads applied by the PTOs driven by the relative motion between the bodies. In particular, the optimal control strategy is based on a dynamic model of the device, which is derived with two different modeling methodologies, that can be also applied to other types of multiple body WECs. The modeling methodologies are validated against wave-tank tests carried out on a 1/7th scale two-body hinge-barge device, and a 1/25th and 1/20th scale three-body hinge-barge device. More, about the motivation for the research carried out in this thesis, is discussed in Section 1.2.

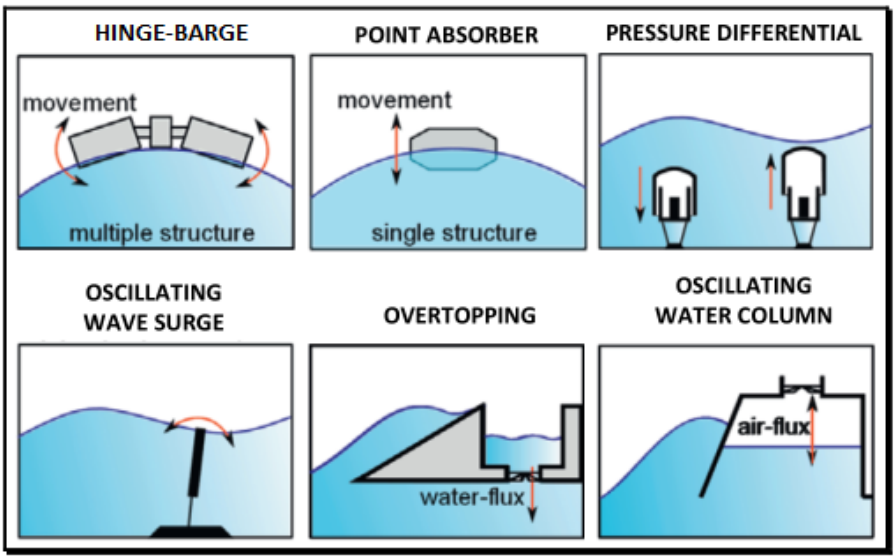

Figure 1.2: Classification of WECs based on the working principle for the extraction of the energy from the waves [2],[8].

1.2 Motivation

The economical viability of WECs can be improved using an optimal control strategy, which broadens the frequency band where the extraction of the energy from the waves takes place [9]. In [10], an optimal control strategy for the maximization of the energy extracted by a single-body and multi-body WECs, termed as complex-conjugate control, is derived in the frequency domain. Complex-conjugate control maximizes the energy extracted by a WEC under the assumption that the dynamics of the WEC is described by a linear dynamic model, the incoming wave is composed

of a single frequency component, and an active PTO is used for the energy extraction. An active PTO can deliver power to the WEC, as well as absorb power from the WEC. In contrast to an active PTO, a passive PTO can only absorb energy from the WEC.

However, real waves are not regular, but rather irregular, and are composed of multiple frequencies. Therefore, the application of complex-conjugate control for the maximization of the energy extracted by a WEC, under irregular waves, is difficult to implement. In fact, the derivation of the complex-conjugate control, in the time domain, involves a non-casual relationship between the optimal force applied by the PTO and the velocity of the WEC [10]. Alternatively, the condition for the maximization of the energy extracted by the WEC, with complex-conjugate control, involves a non-casual relationship between the velocity of the WEC and the excitation force acting on the WEC, due to the action of the waves [11]. Therefore, complex-conjugate control, in the time domain, requires knowledge of either the future velocity of the WEC, or the future excitation force [12].

Also, the optimal force applied by the PTO, computed by complex-conjugate control, induces a motion of the WEC which can be unrealistically large, resulting into a violation of the physical limits on the position and velocity of the WEC. Also, the costs involved with the use of a bi-directional PTO can exceed the increment in the value of absorbed power that can be achieved, with respect to a simpler passive PTO [13].

In this work, an optimal control strategy for the maximization of the energy extracted by a three-body hinge-barge WEC, is derived in the time domain, for both regular and irregular waves. The optimal control strategy is based on a dynamic model of the WEC. Therefore, a dynamic model, that accurately represents the dynamic response of the WEC to the action of the waves, plays a fundamental role into the maximization of the energy extracted by the WEC. In this thesis, a dynamic model of a multibody hinge-barge WEC is derived with two different formulations, that can be also applied to other types of multibody WEC. The two formulations are validated against tank tests carried out on small scale models of a two-body and three-body hinge-barge WECs.

For this study, while the need for knowledge of the current excitation forces acting on a three-body hinge-barge device, is satisfied with the development of two different types of estimators, future knowledge of the excitation forces, is obtained using a prediction algorithm, based on past values of the excitation forces.

In this thesis, an optimal control strategy is formulated for a three-body hinge-barge WEC that is equipped with either passive or active PTOs. Furthermore, the optimal control strategy is formulated in such a way that the physical limits on the positions, velocities and PTO forces of the hinge-barge WEC, are taken into account in the maximization of the energy extracted by the WEC.

1.3 Objectives

The main objectives of this thesis are:

- Formulation of a dynamic model for a multibody hinge-barge WEC, based on two different modeling methodologies.
- Validation of the modeling methodologies applied to small scale two-body and three-body hinge-barge WECs, against wave-tank tests.
- Derivation of a reduced equivalent dynamic model for a three-body hinge-barge WEC, for the formulation of a computationally attractive optimal control strategy.
- Design of an optimal control strategy, based on a reduced equivalent model of a three-body hinge-barge device, for both regular and irregular waves, with active and passive PTOs.
- Comparison of the power absorption performance of a three-body hinge-barge device, obtained with the optimal control strategy, with the power absorption performance obtained with complex-conjugate control and a standard control strategy based on optimal linear damping coefficients of passive PTOs.
- Development of two algorithms for the estimation of the excitation forces acting on a three-body hinge-barge device.
- Design of an algorithm for the prediction of the excitation forces acting on a three-body hinge-barge device.
- Deployment of a system set-up for wave-tank testing of a 1/20th scale three-body hinge-barge device.
- Design and calibration of a motion capture system for wave-tank testing of small scale WECs.
- Preliminary tank tests for the control of a 1/20th scale three-body hinge-barge device.

1.4 Main contributions

The main novel contributions of this thesis are summarised as follows:

- In Chapter 3, two different modeling methodologies are adopted to derive a dynamic model of a multi-body hinge-barge WEC: the Differential and Algebraic Equations (DAEs) formulation and the Ordinary Differential Equations (ODEs) formulation. The DAE formulation describes the dynamics of a multibody hinge-barge WEC, in terms of the motion coordinates of the all the bodies, and reaction forces introduced by the joints. The ODE formulation describes the dynamics of a multibody hinge-barge WEC, in terms of a set of independent coordinates which are fewer than the motion coordinates of all the bodies. Therefore, the ODE formulation is computationally more efficient than the DAE formulation, but it does not provide any information regarding the reaction forces. The information regarding the

reaction forces, provided by the DAE formulation, can be used for the mechanical design of the joints between the bodies.

- In Chapter 3, it is shown that a dynamic model of a 1/7th scale two-body hinge-barge WEC and of a 1/25th scale three-body hinge-barge WEC, obtained with the DAE and ODE formulations, can be efficiently solved with Pseudo-Spectral (PS) methods, based on Fourier basis functions, which are a subset of the class of techniques used for the discretisation of integral and partial differential equations known as mean weighted residuals. In particular, with respect to reference methods based on the integration of the equations of motion, e.g. the Runge-Kutta (R-K) method, PS methods are computationally more efficient for short time steps. Furthermore, for large time steps, PS methods are computationally more stable than the R-K method.

- An equivalent reduced dynamic model for a three-body hinge-barge WEC, which is described only in terms of the relative rotations between the barges, is derived in Chapter 4. The equivalent reduced dynamic model is computationally more efficient than both the DAE and ODE formulations, as it involves a smaller number of variables than the variables involved by the dynamic models obtained with both the DAE and ODE formulations. Therefore, the equivalent reduced dynamic model is particularly suitable for the formulation of an optimal control strategy.

- In Chapter 4, results show that an optimal control strategy derived with PS methods, based on Fourier basis functions, applied to a 1/25th scale three-body hinge-barge device, outperforms a standard control strategy based on optimal linear damping coefficients of passive PTOs. In particular, for a three-body hinge-barge device equipped with active PTOs, an optimal control strategy derived with PS methods, based on Fourier-basis functions, shows a power absorption performance which is the same as the power absorption performance of complex-conjugate control. For a three-body hinge-barge device equipped with passive PTOs, an optimal control strategy derived with PS methods, based on Fourier-basis functions, shows a power absorption performance which is comparable to the power absorption performance obtained with active PTOs.

- An optimal control strategy derived with PS methods, based on Fourier-basis functions, cannot be applied for real-time control of a three-body hinge-barge WEC, as Fourier basis functions can only represent the steady-state response of the WEC. In Chapter 5, a receding horizon real-time optimal control strategy, for a three-body hinge-barge WEC, is obtained with PS methods based on Half-Range Chebyshev Fourier (HRCF) basis functions. In contrast to Fourier basis functions, HRCF basis functions are well suited for the approximation of non-periodic signals, allowing the representation of both the transient and steady-state response of the WEC. Results show that there are no computational disadvantages in using HRCF basis functions, as opposed to Fourier basis functions, for the formulation of the optimal control problem.

- An optimal control strategy derived with PS methods based on either Fourier or HRCF basis functions, relies heavily on knowledge of the current and future excitation forces acting on the WEC. In Chapter 6, the problem of estimation of the current excitation forces acting on the WEC is addressed with two different estimator types: feedback and feedforward. The feedback estimator is based on a dynamic model of the WEC in the time domain, and the measurements of the position and velocity of the device. The feedforward estimator is based on a dynamic model of the WEC in the frequency domain, and is based on the measurement of the position coordinates of the device and the surface elevation up-wave of the device. Results show that, the feedforward estimator performs slightly better than the feedback estimator, with an accuracy of the estimated excitation forces that is 20% higher than the accuracy of the estimated excitation forces given by the feedback estimator. In Chapter 6, the problem of prediction of the future excitation forces acting on the WEC is addressed with a simple Auto-Regressive (AR) model, which is based only on the past history of the estimated excitation forces.

- In order to experimentally validate a control strategy based on optimal linear damping coefficients of passive PTOs, a system set-up for wave-tank testing of a 1/20th scale three-body hinge barge WEC, is presented Chapter 7. The system set-up features a motion capture system, which is developed and calibrated in Chapter 8, for the measurement of the motion of the central barge, and rotational encoders for the measurement of the relative rotation of the lateral barges, with respect to the central barge. The WEC is equipped with two hydraulic dampers, whose damping forces can be changed by varying the opening of a flow control valve.

- In Chapter 8, a low-cost motion capture system, based on an optimal combination of an Inertial Measurement Unit (IMU) with ultrasound sensors, is proposed for wave-tank testing of small scale WECs. The low-cost motion capture system, developed in Chapter 8, provides a measurement of the motion of small scale WEC at a less expensive cost than a traditional optical motion capture systems. The low-cost motion capture system is validated against experimental tests carried out with a servo controlled six-axis robot arm.

- In Chapter 9, wave-tank tests are performed on a 1/20th scale three-body hinge-barge device. A linear dynamic model of the device is validated against tank tests, and is used to formulate a control strategy based based on optimal linear damping coefficients of the hydraulic dampers.

1.4.1 List of publications and awards

The contributions of this thesis resulted in a number of publications, outlined as follows:

- Paparella, F. and Ringwood, J.V., “Receding horizon pseudospectral control for energy maximization of a three-body hinge-barge wave energy device”, accepted for presentation at EWTEC 2017, Cork, 2017.

- Paparella, F., Sivcev, S., Toal. D. and Ringwood, J.V., "A low-cost motion capture system for small-scale wave energy device tank testing", submitted to IEEE Transactions on Instrumentation and Measurement.
- Garcia-Abril, M., Paparella, F. and Ringwood, J.V., "Excitation force estimation and forecasting for wave energy applications", in Proc. of 20th IFAC World Congress, Toulouse, France, 2017.
- Peña-Sanchez, Y., Garcia-Abril, M., Paparella, F. and Ringwood, J.V., "Estimation and forecasting of excitation force for arrays of wave energy devices", accepted for presentation at EWTEC 2017, Cork, 2017.
- Paparella, F. and Ringwood, J.V., "Optimal control of a three-body hinge-barge wave energy device using pseudospectral methods", IEEE Trans. On Sustainable Energy, Vol. 8, No. 1, pp 200-208, 2017.
- Paparella, F. and Ringwood, J.V.,"Enhancement of the wave energy characteristics of a hinge-barge using pseudo-spectral control", in Proc. UKACC Control 2016, Belfast, 2016.
- Paparella, F., Bacelli, G., Paulmeno, A., Mouring, S. and Ringwood, J.V., "Multibody modelling of wave energy converters using pseudo-spectral methods with application to a three-body hinge-barge device", IEEE Trans. On Sustainable Energy, Vol. 7, No. 3, pp 966-974, 2016.
- Paparella, F., Bacelli, G., Ó'Catháin, M. and Ringwood, J.V.. "On the solution of multibody wave energy converter motions using pseudo-spectral methods". in Proc. EWTEC, Nantes, France, Sept. 2015, pp 8B1-5-1 8B1-5-9, 2015.
- Paparella, F., Monk, K., Winands, V., Lopes, M., Conley, D., Ringwood, J.V.. " Up- Wave And Autoregressive Methods For Short-Term Wave Forecasting For An Oscillating Water Column", IEEE Trans. On Sustainable Energy, Vol 6, No 1, pp 1-8, 2014.
- Paparella, F., Monk, K., Winands, V., Lopes, M., Conley, D., Ringwood, J.V.. "Benefits Of Up-Wave Measurements In Linear Short-Term Wave Forecasting For Wave Energy Applications". in Proc. IEEE Conference On Control Applications (CCA), Antibes, Oct. 2014, pp 2048-2053, 2014.

A best student paper award has been received for the paper "Enhancement of the wave energy characteristics of a hinge-barge using pseudo-spectral control", in Proc. UKACC Control 2016, Belfast, 2016.

1.5 Organization of the thesis

The thesis is composed of 9 additional chapters following this chapter, the subjects of which are outlined in the remainder of this section. Each chapter is provided with a dedicated literature

review, as the nature of the subject material of each chapter is substantially different.

In Chapter 2, the working principle of a hinge-barge WEC is described in detail, together with a literature review of the different commercial versions of a hinge-barge WEC. Furthermore, a literature review on the dynamic modeling techniques and the optimal control strategies, for a multibody hinge-barge WEC, is presented.

In Chapter 3, a literature review of the main modeling techniques, used for the description of the dynamics of a generic multibody system, is presented. In particular, among the different modeling techniques presented in the literature review, the DAE and ODE formulations are selected for the dynamic modeling of a multibody hinge-barge WEC. Both the DAE and ODE formulations, applied to a 1/7th scale two-body and 1/25th scale three-body hinge-barge WECs, are validated against wave-tank tests. Both the dynamic models obtained with the DAE and ODE formulations are linearized around the equilibrium position of the WECs, and the resulting linearized dynamic models are solved with PS methods, based on Fourier basis functions. Furthermore, a comparison between the DAE and ODE formulations, and a method based on the integration of the equations of motion, using an explicit 4th order R-K method with a fixed time step, is made.

In Chapter 4, the theory behind the complex-conjugate control for the maximization of the energy extracted from a WEC is presented, followed by an extensive review of the control methods proposed in the literature. In particular, among the different control strategies presented in the literature review, an optimal control strategy, with PS methods based on Fourier basis functions, is applied to a three-body hinge-barge wave energy device. An equivalent reduced dynamic model of the WEC, which is described only in terms of the relative pitch rotations between the barges, is derived for the control formulation. The optimal control strategy takes into account the hydrodynamic and kinematic interactions between the bodies, and the PTO loads at the joints are controlled in a coordinated way, so that the total energy extracted by the device is maximized. The optimal control strategy is developed for a three-body hinge-barge equipped with either active or passive PTOs, under both regular and irregular waves. The power absorbed by a 1/25th scale three-body hinge-barge device, with PS optimal control based on the ODE, DAE and reduced equivalent model formulations, is compared to the power absorbed with complex-conjugate control and a standard control strategy based on optimal linear damping coefficients of passive PTOs.

In Chapter 5, a receding horizon real-time optimal control of a three-body hinge-barge device, with PS methods based on HRCF basis functions, is presented. While Fourier basis functions can only represent the steady-state response of the WEC, HRCF basis functions are well suited for the approximation of non-periodic signals, allowing the representation of both the transient and steady-state response of the device. HRCF functions represent a Fourier extension for nonperiodic signals and, therefore, are especially suited for the wave energy field, since wave elevation and fluid structure interaction forces are all well described using Fourier analysis. The power absorbed by a 1/25th scale three-body hinge-barge device, with an optimal control strategy with PS methods based on HRCF basis functions, is compared to the power absorbed with an optimal control strategy with PS methods based on Fourier basis functions.

In Chapter 6, a literature review, on the techniques adopted for the estimation the excitation force acting on a single-body WEC, is presented. Two different estimator types, for the estimation of the excitation forces of a three-body hinge-barge device, are developed: feedback and feedforward. The feedback estimator is formulated in the time-domain, and is based on a Kalman filter. The Kalman filter is based on a dynamic model of the device and the measurements of the position and velocity of the device, with the excitation forces considered to be unknown inputs. The feedforward estimator is formulated in the frequency domain, and is based on the measurement of the position of the device and of the surface elevation up-wave of the device. The feedforward estimator is based on the identification of the transfer function between the wave elevation and the excitation forces. In Chapter 6, for the prediction of the excitation forces, an Auto-Regressive (AR) model is fitted to the estimated excitation forces given by the feedback and feedforward estimator, and used to predict their future values.

In Chapter 7, a system set-up for wave-tank testing of a 1/20th scale three-body hinge barge device is presented. The system set-up is composed of 3 functional parts: control, actuators and sensors. The actuators are comprised of two hydraulic dampers, which are used to dissipate the mechanical energy of the device. The hydraulic dampers act as passive PTOs, which convert the energy of the waves into mechanical energy. The damping forces of the dampers can be changed by varying the opening of a flow control valve. The sensor suite comprises a motion capture system, which is developed and calibrated in Chapter 8, for the measurement of the motion of the central barge, and rotational encoders for the measurement of the relative rotation of the lateral barges, with respect to the central barge. The control part collects the data from the sensors, and changes the opening of the flow control valves in order to maximize the energy dissipated by the hydraulic dampers.

In Chapter 8, a literature review on the motion capture systems that are usually adopted for wave-tank testing of a small scale WEC, is presented. The principal drawback of the motion capture systems, usually adopted for the wave-tank testing of a WEC, is their cost, which can be high and, therefore, the overall cost for wave tank testing is increased. In Chapter 8, a low-cost motion capture system, based on a optimal combination of an Inertial Measurement Unit (IMU) with ultrasound sensors, is proposed for the wave-tank testing of a WEC. The IMU is mounted on the WEC and measures the accelerations and angular velocities of the WEC. The ultrasound sensors are composed of a set of receivers placed around the device, and a transmitter which is mounted on the same point of the WEC where the IMU is placed. The ultrasound sensors measure the absolute position of the WEC with respect to a fixed reference frame. A loosely coupled ultrasound sensor aided IMU with an Extended Kalman Filter (EKF) is proposed for the integration of the data from the IMU and ultrasound sensors.

In Chapter 9, wave-tank tests of a 1/20th scale three-body hinge-barge device, are presented. The wave-tank tests are performed with the system set-up presented in Chapter 7, and the motion capture system presented in Chapter 8. The wave-tank tests are carried out for both regular and irregular waves. A linear dynamic model of the WEC is tuned and validated with wave-tank tests, for the formulation of a control strategy based based on optimal linear damping coefficients of the

hydraulic dampers.

Finally, conclusions and possible future directions of this research work are documented in Chapter 10.

Chapter 2

Overview of multibody hinge-barge wave energy converters

2.1 Introduction

Multibody hinge-barge WECs are composed of an assembly of bodies connected together by different type of joints. Typically, a multibody hinge-barge is designed to operate along the direction of the incoming wave. In Figure 2.1, an n-body hinge-barge WEC operating along the direction of the incoming wave is depicted. As shown in Figure 2.1, the device is composed of n bodies connected together by hinges which permit relative pitch motion. As shown in Figure 2.1, the relative pitch motion between each pair of bodies is used to drive a PTO which extracts the energy from the waves.

For waves of length that are long compared to the overall length of the device, the device essentially behaves as a rigid body, with no relative motion between the bodies. Therefore, for long waves, no energy is extracted from the waves. Instead, for waves of length comparable to the overall length of the device, the relative motion between the bodies increases. In particular, the power absorbed by the PTOs is maximum when the motion of each pair of bodies is in anti-phase. Typically, for a hinge-barge WEC, the maximum power absorption is realized when the length of each body is half wavelength. By way of example, in Figures 2.2a and 2.2b, the operating condition where the absorbed power is maximum is shown for a hinge-barge composed of 3 and 4 bodies, respectively. Note that, as shown in Figure 2.2b, the 4 body hinge-barge device has a total length equal to 2 wavelengths.

Single-body WECs that have only one operational mode are characterized by a narrow frequency band where the energy is extracted from the waves, although the frequency band can be broaden by using an optimal control strategy [9]. Instead, multibody hinge-barge WECs can extract energy from multiple modes, allowing the energy to be extracted from the waves over a broader frequency band than the frequency band of a single body WEC [7]. Furthermore, the energy extraction of a single-body WEC relies on the connection of the WEC to a fixed reference on the sea-bed, with associated extreme loads on the connecting structures and sea-bed foundation.

In contrast, the energy extraction of a multibody WEC takes place above the floats, making the deployment and maintenance of the equipment for the energy extraction easier for a multibody WEC than for a singe-body WEC.

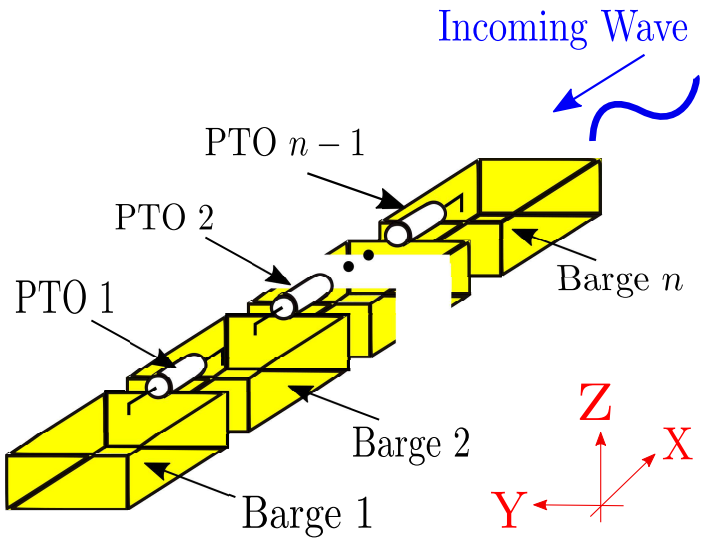

Figure 2.1: Schematic of a n-body hinge-barge wave energy converter.

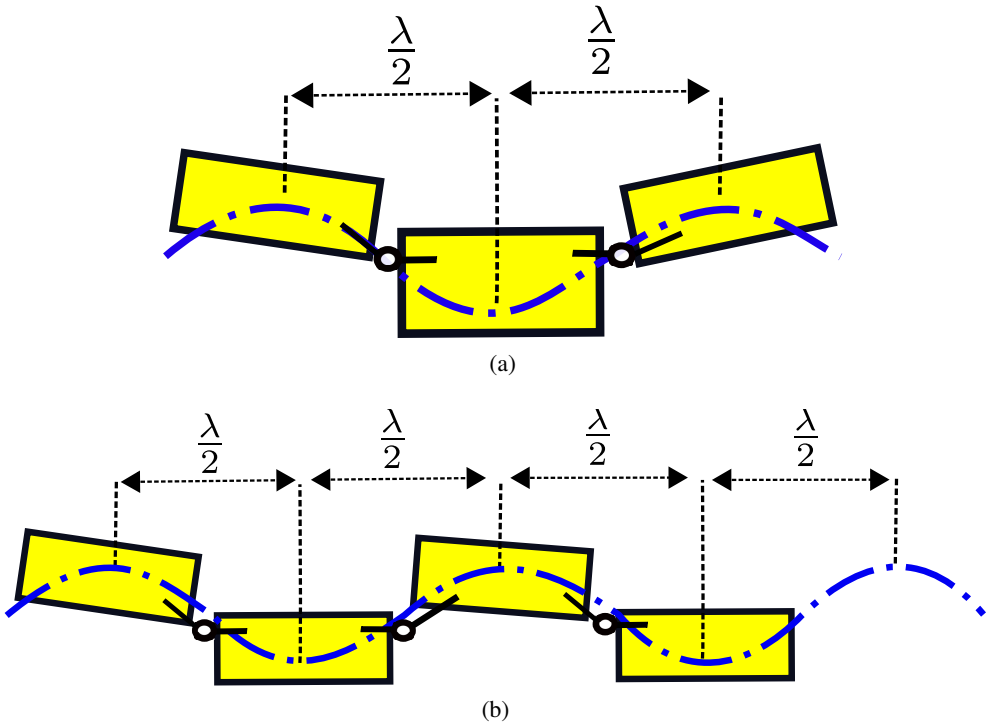

Figure 2.2: Optimal operating condition for maximum power absorption for a hinge-barge composed of 3 (a) and 4 (b) bodies.

The motion of each body of a multibody hinge-barge, in the 3D space, can be described by 3 coordinates for position and 3 coordinates for orientation. As shown in Figure 2.1, for position, the coordinate along the X-axis is referred to as surge, the coordinate along the Y-axis is referred to as sway and the coordinate along the Z-axis is referred to as heave. As shown in Figure 2.1, for orientation, the rotation around the X-axis is referred to as roll, the rotation around the Y-axis is referred to as pitch and the rotation around the Z-axis is referred to as yaw.

For the conversion of the energy of the waves into electrical energy, two type of PTOs can be used: hydraulic systems and direct electrical generators [14], [15]. Hydraulic PTOs are composed of hydraulic cylinders which are connected between the bodies, pressure accumulators and an hydraulic motor. In Figure 2.3, an example of constant pressure PTO system is shown. The hydraulic cylinders pump an hydraulic fluid which flows through an hydraulic motor. The hydraulic motor is coupled with an electrical rotating generator which converts the hydraulic energy into electrical energy that can be transmitted to the electrical grid. Alternatively to the hydraulic PTO, an electrical linear generator connected between the bodies can be used. The linear generator directly converts the relative pitch motion between bodies into electrical energy, with no need to convert the energy from the waves into hydraulic energy.

The remainder of this chapter is organized as follows: in Section 2.2, different commercial hinge-barge devices are presented while, in Section 2.3, a literature review on the dynamic modeling of a hinge-barge device is presented. In Section 2.4, a literature review on the control of a hinge-barge WEC is presented while, in Secton 2.5, overall conclusions are drawn.

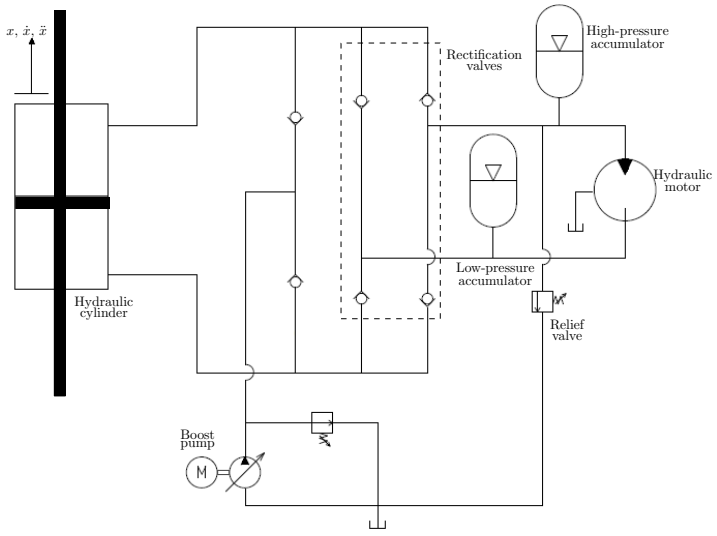

Figure 2.3: A constant pressure PTO system comprising cylinder, valves, high and low pressure accumulators, motor and generator [16].

2.2 Commercial hinge-barge WECs

During the years, different commercial versions of a hinge-barge WEC based on the operating principle of the device shown in Figure 2.1 have been developed:

- The McCabe Wave Pump
- The Pelamis
- The Sea Power WEC
- The Mocean WEC
- The M4 WEC

In the following of this section, the devices listed above are described in more detail, and a comparison between the devices is also made.

2.2.1 The McCabe Wave Pump

The McCabe Wave Pump (MWP) is shown in Figure 2.4, and is composed of 3 rectangular steel pontoons hinged together, with the motion of the central pontoon damped by a submerged damper plate [5]. The forward and aft pontoon relatively pitch with respect to the central pontoon as the wave travels along the device. Two hydraulic rams convert the relative pitch motion between the pontoons into useful energy. The damper plate reduces the heave motion of the central pontoon and, therefore, the relative motion between the forward and aft pontoon, with respect to the central pontoon, is increased. Therefore, the use of the damper plate widens the device bandwidth.

The full scale MWP is 40 m long and 4 m wide, and it was deployed off the west coast of Ireland in Shannon Estuary in 1996 [17]. The MWP was proposed to provide electricity or potable water. For the production of potable water, the hydraulic rams placed above the hinges pump seawater water at high pressure through a reverse-osmosis desalination plant [17].

2.2.2 The Pelamis

The Pelamis is a snake-like WEC developed in the United Kingdom, and is shown in Figure 2.5. The Pelamis device is composed of multiple cylindrical sections linked together by multi Degrees of Freedom (DoF) joints [7], [5]. Each section is typically half a wavelength long so the relative pitching motion between sections is maximized. The device is floating with a mooring and is usually about two wavelengths long. The relative motion between the cylindrical sections drives hydraulic rams which pump pressurized oil through hydraulic motors coupled with electrical generators. Unlike the MWP, the joints allow a relative pitch and yaw motion between the sections of the device, capturing energy from relative pitch and yaw motion.

Two different versions of the Pelamis WEC have been developed: P1 and P2. The P1 device is composed of 4 cylindrical sections and was deployed off the coast of Portugal in 2008. The

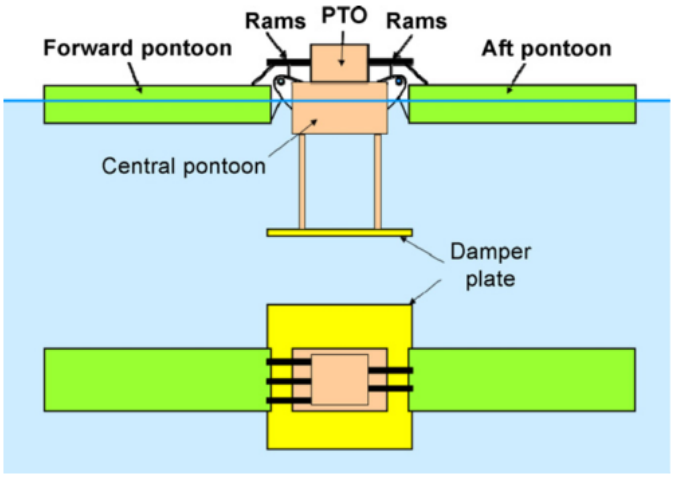

Figure 2.4: Side and top view of the McCabe Wave Pump [5].

sections of the P1 device have a diameter of 3.5 m and and the overall machine length is 120 m. The P2 has five sections linked by four joints. The sections have a diameter of 4m and a length of 36 m. The overall machine length is 180m, and is rated at 750 kW, depending on the incident wave conditions [7]. The P2 device was tested at the Europen Marine Energy Centre (EMEC) in 2010, at Orkney, Scotland.

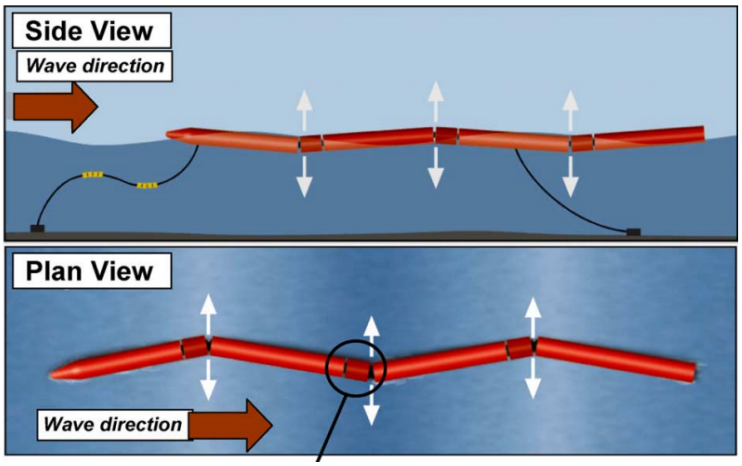

Figure 2.5: Side and Top view of the Pelamis device [18]

2.2.3 The Sea Power WEC

The Sea Power WEC is being developed in Ireland, and is shown in Figure 2.6. The device is composed of 2 bodies hinged together [19], with a long body fixed on two floats and a shorter body fixed on one float. The PTO is located over the hinge, and it is driven by the relative pitch motion between the two bodies.

Two different types of PTO have been developed: a hydraulic seawater PTO system and a mechanical direct drive PTO system. The hydraulic seawater PTO system is used to convert seawater into fresh water, and it composed of a double acting, reciprocating pump that delivers seawater at high-pressure to a reverse-osmosis desalination plant. The mechanical direct drive PTO system transforms the reciprocating linear motion of the piston, driven by the relative pitch motion between the bodies, into a rotating motion of the generator. Two one-way freewheeling bearings ensure that the generator rotates in one direction only [20]. A $1/4th$ scale device was deployed in 2016, in Galway bay, Ireland.

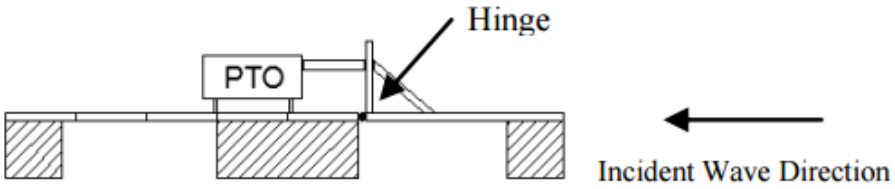

Figure 2.6: Side view of the Sea Power device [19].

2.2.4 The Mocean WEC

The Mocean WEC is developed in the United Kingdom, and is a hinged-raft as shown in Figure 2.7. The device is composed of 2 bodies, and the relative pitch motion between the bodies is used to drive a PTO system. The feature that most distinguishes the Mocean device from other hinge-barge devices is the geometry of the bodies which is designed in order to broaden the range of frequencies where the energy is extracted by the wave. The design of the geometry of the bodies is based on varying the ratio between the water-plane area and the submerged volume. While the water-plane area defines the hydrostatic restoring force, the volume affects the mass and added mass. Therefore, the frequency response of the device can be tuned in order to improve the power absorption in waves with wavelengths that are significantly longer than the overall length of the machine [21].

2.2.5 The M4 WEC

The M4 WEC is developed in the United Kingdom, and is composed of 3 cylindrical floats connected together as shown in Figure 2.8. The bow, mid and stern floats are small, medium and large, respectively. The increase of the size of the float along the direction of the incoming wave is used to roughly align the device to the incident waves [22]. The spacing between the floats is half a wavelength apart at the optimal operating condition, so that the motions of adjacent floats are in anti-phase [23]. Therefore, at the optimal operating condition, the relative motions between the floats is maximum, with an increase of the energy extracted from the waves by the device. While

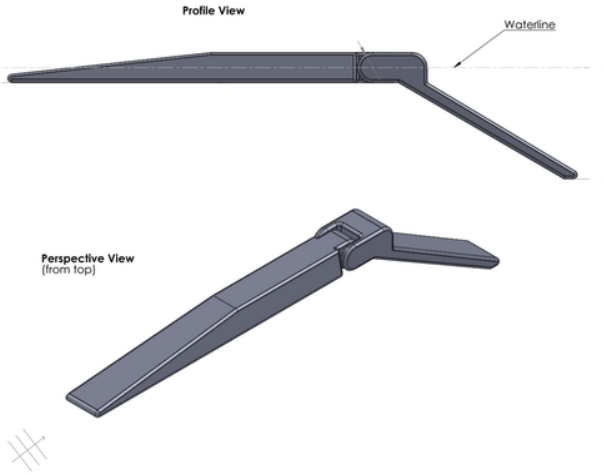

Figure 2.7: Side and perspective view of the Mocean device [21].

the bow and mid float are rigidly connected, the stern float is hinged to the mid float, with the relative motion between the stern and mid float used to drive a PTO. The draft of the stern float is designed in order to have a heave resonance of the stern float at a prominent wave frequency, and the draft of the mid float is smaller than the draft of the stern float so that its resonance is higher than the resonance of the stern. Therefore, the energy of the waves can be extracted over a wider range of frequencies than the range of a single heaving float. The bow float is designed so that the diffraction of the waves generated by the mid and stern float is minimal, and the relative motion between the mid and stern float is not reduced.

Experimental results on a 1/8th scale device show capture widths greater than 25% of a wavelength in regular waves, and greater than 20% of a wavelength in irregular waves across a broad range of wave periods [23].

As shown in Figure 2.6 and 2.8, although the Sea Power and M4 WEC have the same number of floats, the geometry of the floats is different. Furthermore, while for the Sea Power WEC the hinge is placed between the mid body and bow float, for the M4 WEC, the hinge is placed above the mid float. Also, while the Sea Power WEC uses the relative motion between the bow and mid float to drive the PTO, for the M4 WEC, the relative motion between the mid and stern float is used to drive the PTO.

2.2.6 Comparison of devices

In this section, the hinge-barge WECs described previously are compared in terms of number of bodies, motion and orientation coordinates of each body, number of DoF, number of modes used for the energy extraction from the waves and type of the bodies. The modes used for the energy extraction are the modes of the device that drive the PTOs, and are generally less than the number of DoF of the device. In Table 2.1, the comparison between different type of hinge-barge WECs

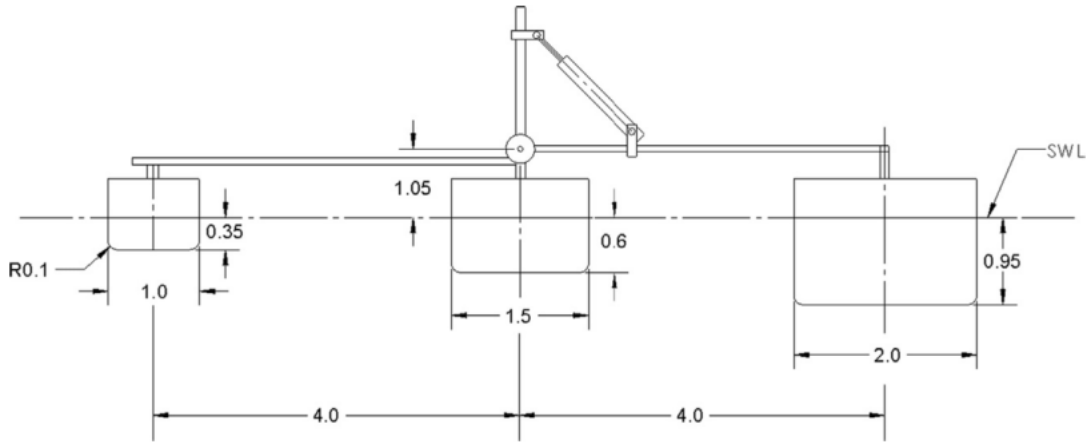

Figure 2.8: Side of the M4 device [22].

is shown.

While the Pelamis WEC has the biggest number of bodies, which can be 4 or 5 depending of the version of the Pelamis WEC considered, the Mocean WEC has the smallest number of bodies, which is 2. However, as shown in Figures 2.6 and 2.8, the Sea Power WEC and M4 WEC have 2 bodies rigidly connected together and, therefore, both WECs effectively behave as 2-body hinge-barge WECs, as the Mocean WEC.

While each body of all hinge-barge WECs are designed to move in surge, heave and pitch, only the bodies of the Pelamis WEC can move in sway and yaw, given the particular type of joints that connect the bodies. Note that, the bodies of the hinge-barge WECs presented in Table 2.1 are not designed to move in roll.

As shown in Table 2.1, the Sea Power WEC, Mocean WEC and M4 WEC have a number of DoF equal to 4. The Sea Power WEC and M4 WEC are designed to operate in the plane defined by the X-Z axis shown in Figure 2.1 and, therefore, if the two bodies rigidly connected together are considered as a single body with 3 DoF corresponding to the heave, surge and pitch motion, the remaining DoF is the relative pitch rotation between the bodies rigidly connected together and the remaining body. The Mocean WEC is also designed to operate in the plane defined by the X-Z axis shown in Figure 2.1, with one of the bodies assigned with 3 DoF corresponding to the heave, surge and pitch motion, and the remaining DoF is the relative pitch rotation of the second body with respect to the first body.

The McCabe Wave Pump has a number of DoF equal to 5. As the Sea Power WEC, M4 WEC and Mocean WEC, the McCabe WEC is designed to operate in the plane defined by the X-Z axis, with the central body assigned with 3 DoF corresponding to the heave, surge and pitch motion, and the 2 remaining DoF are the relative pitch rotations of the lateral bodies with respect to the central body.

In contrast to the Sea Power WEC, M4 WEC, Mocean WEC and the McCabe WEC, the Pelamis WEC is designed to operate in the 3D space defined by the X-Y-Z axis shown in Figure 2.1 and, therefore, if one of bodies is assigned with 5 DoF corresponding to the heave, surge, sway,

pitch and yaw, the remaining 6 DoF are the relative pitch and yaw rotations between each pair of bodies.

In terms of modes for the energy extraction from the waves, as shown in Table 2.1, the Sea Power WEC, the Mocean WEC and the M4 WEC have only 1 mode for the energy extraction, which is the relative pitch rotation between the bodies. The McCabe Wave Pump has 2 modes for the energy extraction, which are the relative pitch rotations between the lateral bodies and the central body. The Pelamis WEC has 6 modes of the energy extraction, which are the relative pitch and yaw rotations between each pair of bodies.

In terms of type of bodies, while both the McCabe Wave Pump and the Sea Power WEC have rectangular floats, the Pelamis has cylindrical sections. While the McCabe Wave Pump, Sea Power WEC, Pelamis and M4 WEC are characterized by a fairly simple shape of the floats, the Mocean WEC is composed of 2 rafts whose shape is optimized in order to broaden the range of frequencies where the energy is extracted from the waves.

	McCabe Wave Pump	Pelamis	Sea Power WEC	Mocean WEC	M4 WEC
Numb of bodies	3	4-5	3	2	3
Surge	✓	✓	✓	✓	✓
Sway	✗	✓	✗	✗	✗
Heave	✓	✓	✓	✓	✓
Roll	✗	✗	✗	✗	✗
Pitch	✓	✓	✓	✓	✓
Yaw	✗	✓	✗	✗	✗
Numb DoF	5	11	4	4	4
Numb Energy extraction modes	2	6	1	1	1
Type of bodies	Rectangular Pontoons	Cylindrical Sections	Rectangular floats	Sloped rafts	Cylindrical buoys

Table 2.1: Hinge-barge WECs compared in terms of number of bodies, motion and orientation coordinates of each body, number of DoF, number of modes used for energy extraction and type of bodies.

2.3 Literature review on dynamic modeling of hinge-barge WECs

The dynamic modeling of a multibody hinge-barge WEC represents a more challenging task than the dynamic modeling of single-body device. While the dynamic modeling of a single-body device does not involve constraints, the dynamic modeling of a multibody hinge-barge device requires the description of the kinematic constraints introduced by the joints between the bodies.

If no constraints are applied to the bodies of a multibody system, the motion of the bodies is independent from each other. When kinematic constraints are introduced between bodies, the motion of the bodies is not independent. Therefore, a set of minimal DoF can be used to describe the motion of all the bodies.

Apart from the kinematic coupling introduced by the joints, the bodies of a multibody hinge-barge device are also hydrodynamically coupled. In fact, the motion of each body in the water generates radiated waves which induce hydrodynamic forces on the other bodies [10]. Over the years, different mathematical models have been developed to describe the dynamics of a multibody hinge-barge device.

In [24], a linear dynamic model for a hinge-barge device composed of 5 bodies is presented, where the motion of the bodies is constrained to heave and pitch only. The hydrodynamic forces acting on the bodies are derived from linear potential theory [10], and are computed with the Wamit software [25]. The kinematic constraints are linearized around the equilibrium position of the device, based on the assumption of small pitch angles between the bodies.

In [26], a modeling methodology for multibody WECs with application to a 3-body hinge-barge device is presented. The dynamic model of the device is based on a fully non-linear representation of the kinematic constraints. Unlike the model presented in [24], the motion of the bodies is not constrained in surge. A comparison between the nonlinear model and a model linearized around the equilibrium position is made. The comparison shows that, for small pitch angles between the bodies, the non-linear model and linear model approximately compute the same motion of the bodies.

In [17], a dynamic model for a generic hinge-barge device made of n-bodies is presented, with the motion of the bodies not constrained in surge. Large pitch angles between the bodies are considered and, therefore, no small angle approximation is used in the development of the kinematic constraints. The hydrodynamic forces are computed based on linear potential theory, and a numerical approximation of the hydrodynamic forces is obtained with a panel method [27]. Furthermore, experimental tank tests are carried out on a $1/27^{th}$ scale MWP device for both monochromatic and polychromatic waves. The results show a good agreement between the motion computed with the dynamic model and the tank tests.

In [28] and [29], a modeling methodology for multibody marine systems with application to a 2-body hinge-barge device is presented. The analysis of the motion considers the surge, heave and pitch of the bodies. A nonlinear representation of the kinematic constraints is considered, and all the hydrodynamic forces acting on the device are computed with the Wamit software [25]. The developed model is validated against tank experiments on a $1/7^{th}$ scale of the section of the MWP

device corresponding to an assembly of the forward and central barge. The tank tests are carried out for monochromatic waves only, and the results show a good agreement between the motion computed by the dynamic model and the tank tests.

In [30], the numerical tool WaveDyn for the dynamic simulation of multibody WECs is validated against experimental tank tests carried out on a $1/21^{th}$ scale Pelamis model. The tank tests are carried out for both monochromatic and polychromatic waves. The hydrodynamic forces are implemented using a predominantly linear formulation, which imports data from the Wamit software [25]. No further details on the algorithm used for the simulation of the device motion are provided. The motion computed by the dynamic model shows a good agreement with the tank tests for both monochromatic and polychromatic waves.

In [31], a methodology to model and simulate multibody WECs is presented, where a set of Denavit-Hartenberg parameters is used to describe the interconnection of the bodies. Then, a recursive technique is used to solve the dynamics of the device. The hydrodynamic forces are computed with a linear potential flow solver.

In [23], a linear dynamic model for the description of the dynamics of the M4 WEC is developed, where the bodies are considered to move in heave, surge and pitch. The hydrodynamic forces acting on the bodies are derived from linear potential theory, and are computed with the Wamit software [25]. The equations of motion of the dynamic model are solve with second-order time-stepping algorithm. Tank tests are carried out on a 1/8th scale device to compare the power absorbed during the tank tests to the absorbed power computed by the dynamic model. In [22], a different linear modeling methodology than the methodology developed in [23] is used to describe the dynamic of the M4 WEC; an axisymmetric diffraction analysis [32] is used for each body, with no hydrodynamic interaction between the bodies. However, the dynamics of the bodies is more detailed. In fact, in [32], while the bodies are considered to be rigid, the connecting elements between the bodies assumed to be flexible.

2.4 Literature review on control of hinge-barge WECs

The maximization of the energy extracted by a multibody hinge-barge WEC requires a controller which computes the optimal trajectories for the PTO forces and velocities of the bodies, and takes into account all the kinematic and hydrodynamic interaction between the bodies and the effects of the PTO forces on the device response. Therefore, the complexity of the controller increases with the number of PTOs and bodies involved.

In [10], a theory for the calculation of the maximum power absorption of a generic multibody WEC is presented. The theory is formulated in the frequency domain, and it computes the optimal trajectory of the velocities of the bodies and PTO forces under the assumption of reactive control, with no constraints on the amplitude of velocities and PTO forces. Reactive control requires a PTO that can deliver power from the grid to the device, as well as absorbing power from the device.

In [33], a hinged 5-body WEC consisting of a circular center floater hinged to 4 smaller spherical buoys is considered. The relative rotation between the central body and each buoy is used

to drive a PTO, and the absorbed energy is maximized for both regular and irregular waves. For regular waves, a numerical procedure is carried out to compute the optimal velocities and control forces at each frequency of the incident wave, for both passive and reactive control. For reactive control, the numerical procedure involves a convex optimization problem which consists of maximizing the absorbed power under constraints on the amplitudes of the velocities. However, for passive control, the absorbed power is constrained to be non-negative and, therefore, a non-convex optimization problem is involved. Thus, for passive control, the numerical procedure can find a minimum which is not globally optimal, but rather only locally optimal. An alternative approach to constrain the power to be non-negative is to optimize the damping coefficients of passive PTOs at each frequency of the incoming wave. However, the convexity of the optimization of the damping coefficients of passive PTOs is difficult to asses. For irregular waves, only the optimization of frequency-independent damping coefficients of passive PTOs is considered for waves represented by different realizations of a Jonswap spectrum [34].

In [7], the optimal control of the Pelamis WEC is presented. The control of the power absorbed at each joint axis is realized, considering the inputs from all axes. Therefore, the real-time control of all forces is realized with respect to the entire machine response. However, very few details on the control strategies for the Pelamis WEC are provided in [7]. In [18], the optimal control of a hydraulic PTO for the Pelamis WEC is considered. The hydraulic PTO for each joint axis is composed of hydraulic cylinders, a high and low pressure accumulators, a hydraulic motor coupled to an electric generator and flow valves. The high-pressure accumulator is used to smooth the supply of electrical energy to the grid. The impeding joint moment provided by the cylinders must be varied throughout each wave cycle such that energy extracted from the waves is maximized. In particular, a reactive control is used to enable impedance matching to maximize power capture. Real-time control of the joint moment is achieved with the use of sets of electronically controlled valves, which control the flow of fluid between the hydraulic cylinders and the accumulator. Both experiments on a 1/7th and full scale device, and numerical simulations, have been carried out in order to validate the optimal control strategy of the hydraulic PTO.

2.5 Conclusions

As shown in Section 2.3, the problem of the dynamic modeling of a multibody hinge-barge device has been given consideration by several authors. However, as shown in Section 2.4, documentation on the optimal control of a multibody hinge-barge device is missing in the available literature. As shown in Section 2.4, only the optimal control of generic multibody WECs in the frequency domain is considered, with no real-time implementation of the controller available.

In Chapter 3, a general framework for the derivation of a dynamic model of a multibody hinge-barge WEC is presented, which is used for the formulation of an optimal control strategy for a three-body hinge-barge device in Chapter 4.

Chapter 3

Dynamic modelling of multibody hinge-barge wave energy converters

In this chapter, a general framework for the derivation of a dynamic model of a multibody hinge-barge WEC is presented, which is used for the formulation of an optimal control strategy for a three-body hinge-barge WEC presented in Chapter 4. In the following of this chapter, a literature review on the dynamic modelling of multibody systems is presented.

3.1 Literature review on dynamic modelling of multibody systems

Multibody wave energy converters are composed of an assembly of bodies connected together by different type of joints. The motion of each body is restrained by the kinematic constraints introduced by the joints. Two different formulations can be used to describe the dynamics of a multi-body system: the Differential and Algebraic Equations (DAEs) and the Ordinary Differential Equations (ODEs) formulation. In the DAE formulation, a set of redundant n generalized coordinates is used to describe the dynamics of the system, and the equations of motion result in $2n$ differential and m constraint equations. In addition, m unknowns called Lagrange multipliers are added into the differential equations to take into account the reaction forces introduced by the kinematic constraints. The Lagrange multipliers are algebraic variables, so that their time derivative does not feature in the equations. The resulting system is a set of DAEs for the generalized coordinates and Lagrange multipliers.

In the ODE formulation, the generalized coordinates are expressed with respect to a set of $(n-m)$ independent coordinates, also called DoF, by means of the constraint equations. Therefore, the DAE system can be transformed into a reduced number of $2(n-m)$ ordinary differential equations (ODEs) for the independent coordinates with elimination of the Lagrange multipliers.

Regarding solution techniques for DAE systems, index reduction techniques combined with backwardward difference methods (BDFs) have been proposed in [35]. The index of a DAE system composed of the Euler-Lagrange equations is reduced from three to two, and then a variable-order, variable-step BDF method is applied to the resulting system of equations.

Alternatively, the DAE system can be reduced to an ODE system by means of an appropriate transformation of coordinates. In Maggi's formulation [36], the generalized velocities are expressed in terms of the kinematic characteristics, which are the velocities of the DoF. Then, the Euler-Lagrange equations are derived for the kinematic characteristics with elimination of the Lagrange multipliers by means of the null-space of the constraint matrix [37],[38]. In the Index-1 formulation [39], the Euler-Lagrange equations for the generalized coordinates, together with the constraints at the acceleration level, form an Index-1 system of DAEs which can be solved for the generalized coordinates and Lagrange multipliers. Then, the accelerations are integrated in order to obtain the positions and velocities of the generalized coordinates. In the Udwadia and Kalaba Formulation (UKF) [40], a more compact form of the Index-1 formulation was derived by means of the Moore-Penrose Generalized Inverse (MPGI). In the Null Space Formulation (NSF) [39], [41], [42], the Lagrange multipliers that appear in the Index-1 formulation are eliminated from the Euler-Lagrange equations by means of the null space introduced in Maggi's formulation. Therefore, a system of second order ODEs for the generalized coordinates is obtained.

The number of variables needed to describe the dynamics of a constrained system in the DAE formulation is $2n+m$ (n generalized positions, n generalized velocities and m Lagrange's multipliers), while for the ODE formulation, the number of variables is reduced to $2n$ for the Index-1 formulation, NSF and UKF, and $2(n-m)$ for Maggi's formulation. However, a reduction in the number of variables requires an extra computational effort; in Maggi's and the NSF formulation, the computation of the null space of the constraint matrix is required, while in the UKF formulation, MPGIs are calculated. Nevertheless, the matrices in the DAE formulation are characterized by a high sparsity, so that efficient solution techniques can be used [43], [44].

In this chapter, Pseudo-Spectral (PS) methods are applied to both the DAE and ODE formulations, in order to obtain the solution for the dynamics of a multi-body system. PS methods are a subset of the class of techniques used for the discretisation of integral and partial differential equations known as mean weighted residuals [45], [46]. Apart from providing a solution for the dynamics of a multi-body system, PS methods can also be used to efficiently solve an optimal control problem for the device [47].

The remainder of this chapter is organized as follows: in Section 3.2, the DAE and ODE formulations are applied to a multi-body system, while, in Section 3.3, PS methods are used to obtain a solution for the dynamics of a multi-body system. In Section 3.4, a two-body hinge-barge device is considered as a case study, and the DAE and ODE formulations are applied in order to derive the equations of motion. The DAE and ODE formulations applied to the two-body hinge-barge device are compared against tank tests carried out for regular waves to verify their validity. Furthermore, the comparison between the computational time required by the PS methods and by the Runge-Kutta (R-K) method to solve the dynamics of a two-body hinge-barge device is considered. In Section 3.5, a three-body hinge-barge device is considered as a case study, and the DAE and ODE formulations are applied in order to derive the equations of motion. The DAE and ODE formulations applied to the three-body hinge-barge device are compared against tank tests carried out for both regular and irregular waves to verify their validity. Furthermore, the

comparison between the computational time required by the PS methods and by the R-K method to solve the dynamics of a three-body hinge-barge device is considered. Finally, overall conclusions are drawn in Section 3.6.

3.2 Equations of motion of a multi-body system

3.2.1 Reference frames

For the description of the motion of a body in space, six coordinates are required: three coordinates for position and three coordinates for rotation. For the analysis of multibody systems, two types of coordinate frames are defined: the *global* or *inertial* frame and the *body* frame. The global frame is fixed to a point in space, and therefore its position and orientation are constant in time. The body frame is attached to a point of the body, and its position and orientation change with time. A body frame is assigned to each body composing a multi-body system. In Figure 3.1, a free floating unconstrained body k is represented together with a global frame $X_iY_iZ_i$ and a body frame $X_bY_bZ_b$. The vector $\mathbf{p}_{i,b_k} \in \mathbb{R}^{3\times 1}$ represents the position of the origin of the body frame O_{b_k} with respect to the point i. The components of the vector $\mathbf{p}_{i,b_k}$ can be transformed from the body frame to the global frame by using the following transformation:

$$\mathbf{p}^i_{i,b_k} = \mathbf{R}^i_b(\boldsymbol{\Theta}_k)\mathbf{p}^b_{i,b_k} \tag{3.1}$$

where the vectors $\mathbf{p}^b_{i,b_k}$ and $\mathbf{p}^i_{i,b_k}$ represent the position vector of O_{b_k} with respect to the point i, expressed in the body frame and global frame, respectively. The matrix $\mathbf{R}^i_b(\boldsymbol{\Theta}_k) \in \mathbb{R}^{3\times 3}$, used for the transformation of coordinates, is a function of the vector of Euler angles $\boldsymbol{\Theta}_k = [\phi\ \theta\ \psi]^T$, where ϕ is the roll angle, θ the pitch angle and ψ the yaw angle of the body [48]. The velocities of the Euler angles can be obtained from the angular velocity vector $\boldsymbol{\omega}^b_{i,b}$ expressed in the body frame coordinates as follows:

$$\dot{\boldsymbol{\Theta}}_k = \mathbf{T}(\boldsymbol{\Theta}_k)\boldsymbol{\omega}^b_{i,b_k} \tag{3.2}$$

where the matrix $\mathbf{T}(\boldsymbol{\Theta}_k)$ is a function of Euler angles, and can be obtained by linear superposition of the rotations of the body frame around its axis [48].

3.2.2 Dynamics of an unconstrained body

The Newton-Euler equations of motion for a free floating unconstrained body are represented as a system of first-order integro-differential equations as follows [48]:

$$\dot{\mathbf{q}}_k = \mathbf{J}^{b_k}(\boldsymbol{\Theta})\mathbf{v}_k \tag{3.3}$$

$$\mathbf{M}^{b_k}\dot{\mathbf{v}}_k + (\mathbf{B}^{b_k} + \mathbf{B}^{b_k}_{visc})\mathbf{v}_k = -\mathbf{G}^{b_k}\boldsymbol{q}_k - \mathbf{M}^{b_k}_{\infty}\dot{\mathbf{v}}_k - \int_{-\infty}^{t}\mathbf{K}^{b_k}_{rad}(t-\tau)\mathbf{v}_k, d\tau + \mathbf{f}^{b_k}_{wave} + \mathbf{f}^{b_k}_{ext} \tag{3.4}$$

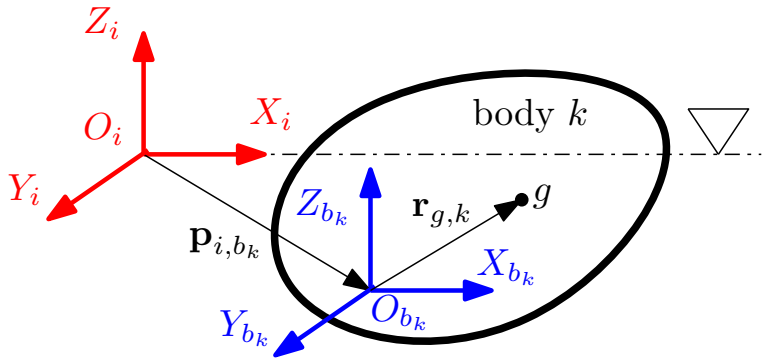

Figure 3.1: A free floating unconstrained body k, where $X_iY_iZ_i$ and $X_bY_bZ_b$ represent the global and body reference frames, respectively.

where:

$$\mathbf{q}_k = [\mathbf{p}^{i^T}_{i,b_k} \; \boldsymbol{\Theta}^T_k]^T \tag{3.5}$$

$$\mathbf{v}_k = [\mathbf{v}^{b^T}_{i,b_k} \; \boldsymbol{\omega}^{b^T}_{i,b_k}]^T \tag{3.6}$$

$$\mathbf{J}^{b_k}(\boldsymbol{\Theta}) = \begin{bmatrix} \mathbf{R}^i_b(\boldsymbol{\Theta}_k) & \mathbf{0}_{3\times3} \\ \mathbf{0}_{3\times3} & \mathbf{T}(\boldsymbol{\Theta}_k) \end{bmatrix} \tag{3.7}$$

$$\mathbf{M}^{b_k} = \begin{bmatrix} m_k\mathbf{I}_{3\times3} & -m_k\mathbf{S}(\mathbf{r}_{g,k}) \\ m_k\mathbf{S}(\mathbf{r}_{g,k}) & \mathbf{I}_{b_k} \end{bmatrix} \tag{3.8}$$

$$\mathbf{B}^{b_k} = \begin{bmatrix} m_k\mathbf{S}(\boldsymbol{\omega}^b_{i,b_k}) & -m_k\mathbf{S}(\boldsymbol{\omega}^b_{i,b_k})\mathbf{S}(\mathbf{r}_{g,k}) \\ m_k\mathbf{S}(\mathbf{r}_{g,k})\mathbf{S}(\boldsymbol{\omega}^b_{i,b_k}) & -\mathbf{S}(\mathbf{I}_{b_k}\boldsymbol{\omega}^b_{i,b_k}) \end{bmatrix} \tag{3.9}$$

$$\mathbf{f}^{b_k}_{wave} = \int_{-\infty}^{\infty} \mathbf{K}^{b_k}_{wave}(t-\tau)\eta(\tau), d\tau \tag{3.10}$$

$$\mathbf{f}^{b_k}_{ext} = \mathbf{f}^{b_k}_{pto} + \mathbf{f}^{b_k} \tag{3.11}$$

with m_k the mass of the body, $\mathbf{r}_{g,k}$ the distance vector of the center of mass from the origin of the body frame, $\mathbf{I}_{b_k}$ the inertia matrix of the body around the origin of the body frame, $\mathbf{M}^{b_k}_{in}$ the rigid-body inertia matrix of the body, $\mathbf{B}^{b_k}$ the Coriolis-Centripetal matrix, $\mathbf{B}^{b_k}_{visc}$ the linearized viscous damping, $\mathbf{G}^{b_k}$ the hydrostatic matrix, $\mathbf{f}^{b_k}_{wave}$ the vector of the excitation forces due the action of the waves on the body, $\mathbf{f}^{b_k}_{pto}$ the force vector due to the PTO system, $\mathbf{f}^{b_k}$ the vector of forces due to moorings, hinge-friction, etc. , $\mathbf{K}^{b_k}_{rad}$ contains impulse response functions of the radiation forces, $\mathbf{K}^{b_k}_{wave}$ contains the impulse response functions of the wave excitation forces, $\mathbf{M}^{b_k}_{\infty}$ the added mass at infinite frequency, η the free surface elevation and $\mathbf{S}$ a skew-symmetric matrix for the cross-product $\mathbf{a}\times\mathbf{b} := \mathbf{S}(\mathbf{a})\mathbf{b}$.

The terms on the left-hand side of equation (3.4) represent the rigid-body dynamics of the unconstrained body, expressed about the origin of the body frame $X_bY_bZ_b$. The hydrodynamic parameters $\mathbf{G}^{b_k}$, $\mathbf{M}^{b_k}_{\infty}$, $\mathbf{K}^{b_k}_{rad}$ and $\mathbf{K}^{b_k}_{wave}$ are computed by means of the boundary element software WAMIT [25], which computes all the quantities in the hydrodynamic h-frame. The transformation

matrix $\mathbf{R}_b^h$ is used to convert the hydrodynamic parameters from the h-frame to the body frame [49]. Under the assumption of small oscillations of the body frame with respect to the h-frame, the matrix $\mathbf{R}_b^h$ reduces to the identity matrix $\mathbf{I}_{3\times3}$.

3.2.3 DAE formulation for N interconnected bodies

In case of N interconnected bodies, m algebraic equations are required in order to describe the constraints introduced by the joints. The constraint equations can be represented as follows:

$$\mathbf{C}(\mathbf{z},t) = 0 \tag{3.12}$$

where $\mathbf{z} = [\mathbf{z}_1^T \; .. \; \mathbf{z}_N^T]^T \in \mathbb{R}^{(6\times N)\times 1}$ and $\mathbf{z}_k = [\mathbf{p}^{b^T}_{i,b_k} \; \mathbf{\Theta}_k^T]^T$, with $k = 1,..N$. The constraint equations (3.12) are considered to be *holonomic*, since the generalized velocities do not appear in the equations. An additional term, representing the constraint forces, is added into the Newton-Euler equations of motion. The constraint forces are represented by a set of m Lagrange multipliers $\boldsymbol{\lambda}$, which are algebraic variables, since their time derivatives do not appear in the equations of motion. Thus, the equations of motion for a system composed of N interconnected bodies can be represented by a set of DAEs, given as follows [50]:

$$\dot{\mathbf{q}} = \mathbf{J}(\mathbf{\Theta})\mathbf{v} \tag{3.13}$$

$$\mathbf{M}\dot{\mathbf{v}} + (\mathbf{B}+\mathbf{B}_{visc})\mathbf{v} + \mathbf{C}_z^T\boldsymbol{\lambda} = -\mathbf{G}\mathbf{q} - \mathbf{M}_\infty\dot{\mathbf{v}} - \int_{-\infty}^{t}\mathbf{K}_{rad}(t-\tau)\mathbf{v}, d\tau + \mathbf{f}_{wave} + \mathbf{f} + \mathbf{f}_{pto} \tag{3.14}$$

$$\mathbf{C}(\mathbf{z},t) = 0 \tag{3.15}$$

where:

$$\mathbf{q} = [\mathbf{q}_1^T \; \mathbf{q}_2^T \; .. \; \mathbf{q}_N^T]^T \tag{3.16}$$

$$\mathbf{v} = [\mathbf{v}_1^T \; \mathbf{v}_2^T \; .. \; \mathbf{v}_N^T]^T \tag{3.17}$$

$$\mathbf{J}(\mathbf{\Theta}) = \text{diag}(\mathbf{J}^{b_1}(\mathbf{\Theta}), .., \mathbf{J}^{b_N}(\mathbf{\Theta}) \tag{3.18}$$

$$\mathbf{M} = \text{diag}(\mathbf{M}^{b_1}, .., \mathbf{M}^{b_N}) \tag{3.19}$$

$$\mathbf{B} = \text{diag}(\mathbf{B}^{b_1}, .., \mathbf{B}^{b_N}) \tag{3.20}$$

$$\mathbf{B}_{visc} = \text{diag}(\mathbf{B}_{visc}^{b_1}, .., \mathbf{B}_{visc}^{b_N}) \tag{3.21}$$

$$\mathbf{G} = \text{diag}(\mathbf{G}^{b_1}, .., \mathbf{G}^{b_1}) \tag{3.22}$$

$$\mathbf{M}_\infty = \text{diag}(\mathbf{M}_\infty^{b_1}, .., \mathbf{M}_\infty^{b_N}) \tag{3.23}$$

$$\mathbf{f}_{wave} = [\mathbf{f}_{wave}^{b_1{}^T} .. \; \mathbf{f}_{wave}^{b_N{}^T}]^T \tag{3.24}$$

$$\mathbf{f} = [\mathbf{f}^{b_1{}^T} .. \; \mathbf{f}^{b_N{}^T}]^T \tag{3.25}$$

$$\mathbf{f}_{pto} = [\mathbf{f}_{pto}^{b_1{}^T} .. \; \mathbf{f}_{pto}^{b_N{}^T}]^T \tag{3.26}$$

$$\tag{3.27}$$

where the matrix $\mathbf{C}_z$ represents the partial derivative of the constraint equations with respect to the vector of generalized positions $\mathbf{z}$. In the DAE formulation, the total number of variables required to describe the motion of N interconnected bodies is $2\times(6\times N)+m$, i.e. $6\times N$ positions, $6\times N$ velocities and m Lagranges multipliers.

3.2.4 ODE formulation for N interconnected bodies

As an alternative to the DAE formulation, using the constraints in equation (3.12), the dynamics of N interconnected bodies can be described by means of a set of $n=(6\times N-m)$ independent coordinates, or DoF. The vector of generalized velocities $\mathbf{v}$ can be partitioned into dependent velocities $\mathbf{v}_d$, and independent velocities $\mathbf{v}_s$, as follows:

$$\mathbf{v}=\begin{bmatrix}\mathbf{v}_d\\ \mathbf{v}_s\end{bmatrix} \tag{3.28}$$

$\mathbf{v}_d$ and $\mathbf{v}_s$ are related as follows [50]:

$$\mathbf{v}_d=\mathbf{C}_s\mathbf{v}_s=-\mathbf{C}_{\mathbf{q}_d}^{-1}\mathbf{C}_{\mathbf{q}_s}\mathbf{v}_s \tag{3.29}$$

where $\mathbf{C}_{\mathbf{q}_d}$ and $\mathbf{C}_{\mathbf{q}_s}$ represent the partial derivatives of the constraint equations associated with the dependent and independent coordinates, respectively. Therefore, the vector of generalized velocities $\mathbf{v}$ can be written in terms of the independent velocities $\mathbf{v}_s$, as follows:

$$\mathbf{v}=\mathbf{P}\mathbf{v}_s=\begin{bmatrix}\mathbf{C}_s\\ \mathbf{I}_n\end{bmatrix}\mathbf{v}_s \tag{3.30}$$

where $\mathbf{I}_n$ is the identity matrix of dimension n. The time derivative of the generalized velocities can be expressed as:

$$\dot{\mathbf{v}}=\mathbf{P}\dot{\mathbf{v}}_s+\dot{\mathbf{P}}\mathbf{v}_s \tag{3.31}$$

Substituting (3.30) and (3.31) into (3.14), and multiplying both sides of the resulting equation by $\mathbf{P}^T$, the following system of first order integro-differential equations is obtained:

$$\dot{\mathbf{q}}_s=\mathbf{v}_s \tag{3.32}$$

$$\mathbf{M}_s\dot{\mathbf{v}}_s+(\mathbf{B}_s+\mathbf{B}_{visc,s})\mathbf{v}_s=-\mathbf{G}_s\mathbf{q}_s-\mathbf{M}_{\infty,s}\dot{\mathbf{v}}_s-\int_{-\infty}^{t}\mathbf{K}_{rad,s}(t-\tau)\mathbf{v}_s,d\tau+\mathbf{f}_{wave,s}+\mathbf{f}_s+\mathbf{f}_{pto,s} \tag{3.33}$$

where:

$$\mathbf{M}_s = \mathbf{P}^T \mathbf{M} \mathbf{P} \tag{3.34}$$

$$\mathbf{B}_s = \mathbf{P}^T \mathbf{B} \mathbf{P} + \mathbf{P}^T \mathbf{M} \dot{\mathbf{P}} + \mathbf{P}^T \mathbf{M}_\infty \dot{\mathbf{P}} \tag{3.35}$$

$$\mathbf{B}_{visc,s} = \mathbf{P}^T \mathbf{B}_{visc} \mathbf{P} \tag{3.36}$$

$$\mathbf{G}_s = \mathbf{P}^T \mathbf{G} \mathbf{P} \tag{3.37}$$

$$\mathbf{M}_{\infty,s} = \mathbf{P}^T \mathbf{M}_\infty \mathbf{P} \tag{3.38}$$

$$\mathbf{K}_{rad,s} = \mathbf{P}^T \mathbf{K}_{rad} \mathbf{P} \tag{3.39}$$

$$\mathbf{f}_{wave,s} = \mathbf{P}^T \mathbf{f}_{wave} \tag{3.40}$$

$$\mathbf{f}_s = \mathbf{P}^T \mathbf{f} \tag{3.41}$$

$$\mathbf{f}_{pto,s} = \mathbf{P}^T \mathbf{f}_{pto} \tag{3.42}$$

Thus, the equations of motion of a system composed of N interconnected bodies can be represented by a set of ODEs for the independent coordinates. In the ODE formulation, the total number of variables required for describing the motion is $2n$ (n positions and n velocities).

3.3 Pseudo-spectral approximation methods

In this section, PS methods are used to compute an approximate solution to the integro-differential equations obtained for the DAE and ODE formulations. The positions and velocities that appear in the equations of motion obtained for the DAE and ODE formulations can be approximated with a linear combination of basis functions. Assuming that the waves can be described as a summation of sinusoidal components, non-zero mean trigonometric polynomials (truncated Fourier series) represent a sensible choice for the approximation of positions and velocities. Therefore, the ith components of the position and velocity vector are given as follows:

$$q_i(t) \approx q_i^{N_x}(t) = \sum_{k=0}^{N_x} x_{i,k}^{q,c} cos(k\omega_0 t) + x_{i,k}^{q,s} sin(k\omega_0 t) = \mathbf{\Phi}(t) \hat{\mathbf{x}}_i^q \tag{3.43}$$

$$v_i(t) \approx v_i^{N_x}(t) = \sum_{k=0}^{N_x} x_{i,k}^{v,c} cos(k\omega_0 t) + x_{i,k}^{v,s} sin(k\omega_0 t) = \mathbf{\Phi}(t) \hat{\mathbf{x}}_i^v \tag{3.44}$$

where $i = 1,..,6N$ and $i = 1,..,n$ for the DAE and ODE formulations, respectively. The parameter N_x is the order of expansion for the position and velocity of the states. The vector of the coefficients $\hat{\mathbf{x}}_i^q$ and $\hat{\mathbf{x}}_i^v$ of the approximated ith components of the position and velocity vector are given as follows:

$$\hat{\mathbf{x}}_i^q = \begin{bmatrix} x_{i,1}^{q,c} & x_{i,1}^{q,s} & .. & x_{i,N_x}^{q,c} & x_{i,N_x}^{q,s} \end{bmatrix}^T \tag{3.45}$$

$$\hat{\mathbf{x}}_i^v = \begin{bmatrix} x_{i,1}^{v,c} & x_{i,1}^{v,s} & .. & x_{i,N_x}^{v,c} & x_{i,N_x}^{v,s} \end{bmatrix}^T \tag{3.46}$$

and the vector of the basis function $\mathbf{\Phi}(t)$ is given as follows:

$$\mathbf{\Phi}(t) = [cos(\omega_0 t)\ sin(\omega_0 t)\ ..\ cos(N_x\omega_0 t)\ sin(N_x\omega_0 t)]^T \tag{3.47}$$

where $\omega_0 = 2\pi/T$ is the fundamental frequency. The derivatives of the ith components of the position and velocity vector are, respectively,

$$\dot{q}_i^{N_x}(t) = \dot{\mathbf{\Phi}}(t)^T \hat{\mathbf{x}}_i^q = \mathbf{\Phi}(t)^T \mathbf{D}_\phi \hat{\mathbf{x}}_i^q \tag{3.48}$$

$$\dot{v}_i^{N_x}(t) = \dot{\mathbf{\Phi}}(t)^T \hat{\mathbf{x}}_i^v = \mathbf{\Phi}(t)^T \mathbf{D}_\phi \hat{\mathbf{x}}_i^v \tag{3.49}$$

where $\mathbf{D}_\phi \in \mathbb{R}^{2N_x \times 2N_x}$ is a block diagonal matrix, with the k-th block is given as follows:

$$\mathbf{D}_{\phi,k} = \begin{bmatrix} 0 & k\omega_0 \\ -k\omega_0 & 0 \end{bmatrix} \tag{3.50}$$

The convolution integral in equation (3.14) and (3.33) can be expressed as a function of the PS coefficients $\hat{\mathbf{x}}_i^v$. The derivation of the convolution integral expressed with the coefficients $\hat{\mathbf{x}}_i^v$ can be carried out at one frequency at the time, because of the linearity of the convolution integral [47]. Thus, if the following vector of the basis functions $\mathbf{\Phi}^k$ and coefficients $\hat{\mathbf{x}}_i^{v,k}$ are considered:

$$\mathbf{\Phi}^k(t) = [cos(k\omega_0 t)\ sin(k\omega_0 t)]^T \tag{3.51}$$

$$\hat{\mathbf{x}}_i^{v,k} = \begin{bmatrix} \hat{\mathbf{x}}_{i,c}^{v,k} & \hat{\mathbf{x}}_{i,s}^{v,k} \end{bmatrix}^T \tag{3.52}$$

then, the convolution integral of the element $K_{rad_{i,ii}}$ of the impulse response matrix $\mathbf{K}_{rad}$, with $i = 1,..6N$ and $ii = 1,..6N$, in equation (3.14) becomes:

$$\int_{-\infty}^{t} K_{rad_{i,ii}}(t-\tau)v_i,d\tau = \int_{0}^{\infty} K_{rad_{i,ii}}(t-\tau)v_i d\tau \tag{3.53}$$

$$= \int_{0}^{\infty} K_{rad_{i,ii}} \mathbf{\Phi}^k(t-\tau)^T \hat{\mathbf{x}}_i^{v,k} d\tau \tag{3.54}$$

$$= \int_{0}^{\infty} K_{rad_{i,ii}}(\ cos\,(k\omega_0 t)\,\hat{\mathbf{x}}_{i,c}^{v,k} + sin\,(k\omega_0 t)\,\hat{\mathbf{x}}_{i,s}^{v,k})\ d\tau \tag{3.55}$$

$$= \hat{\mathbf{x}}_{i,s}^{v,k} sin\,(k\omega_0 t) \int_{0}^{\infty} K_{rad_{i,ii}} cos\,(k\omega_0 t)\,d\tau - \hat{\mathbf{x}}_{i,s}^{v,k} cos\,(k\omega_0 t) \int_{0}^{\infty} K_{rad_{i,ii}} sin\,(k\omega_0 t)\,d\tau \tag{3.56}$$

$$+ \hat{\mathbf{x}}_{i,c}^{v,k} cos\,(k\omega_0 t) \int_{0}^{\infty} K_{rad_{i,ii}} cos\,(k\omega_0 t)\,d\tau + \hat{\mathbf{x}}_{i,c}^{v,k} sin\,(k\omega_0 t) \int_{0}^{\infty} K_{rad_{i,ii}} sin\,(k\omega_0 t)\,d\tau \tag{3.57}$$

Given the Ogilve's relations [51]:

$$\int_{0}^{\infty} K_{rad_{i,ii}} sin(\omega t) dt = -\omega(\ M_{a_{i,ii}}(\omega) - M_{\infty_{i,ii}}) \tag{3.58}$$

$$\int_{0}^{\infty} K_{rad_{i,ii}} cos(\omega t) dt = R_{rad_{i,ii}}(\omega) \tag{3.59}$$

then, the convolution integral finally becomes:

$$\int_{-\infty}^{t} K_{rad_{i,ii}}(t-\tau)v_i,d\tau = \hat{\mathbf{x}}_{i,s}^{v,k} sin\,(k\omega_0 t)\,R_{rad_{i,ii}}(k\omega_0) - \hat{\mathbf{x}}_{i,s}^{v,k} cos\,(k\omega_0 t)\,(\ -k\omega_0(\ M_{a_{i,ii}}(k\omega_0) - M_{\infty_{i,ii}})\ ) \tag{3.60}$$

$$+ \hat{\mathbf{x}}_{i,c}^{v,k} cos\,(k\omega_0 t)\,R_{rad_{i,ii}}(k\omega_0) + \hat{\mathbf{x}}_{i,c}^{v,k} sin\,(k\omega_0 t)\,(\ -k\omega_0(\ M_{a_{i,ii}}(k\omega_0) - M_{\infty_{i,ii}})\ ) \tag{3.61}$$

$$= \mathbf{\Phi}^k(t) \begin{bmatrix} R_{rad_{i,ii}}(k\omega_0) & k\omega_0 M_{a_{i,ii}}(k\omega_0) \\ -k\omega_0 M_{a_{i,ii}}(k\omega_0) & R_{rad_{i,ii}}(k\omega_0) \end{bmatrix} \hat{\mathbf{x}}_i^{v,k} - M_{\infty_{i,ii}} \mathbf{\Phi}^k(t) \mathbf{D}_{\phi,k} \hat{\mathbf{x}}_i^{v,k} \tag{3.62}$$

$$= \mathbf{\Phi}^k(t) \mathbf{G}_{rad_{i,ii}}^k \hat{\mathbf{x}}_i^{v,k} - M_{\infty_{i,ii}} \mathbf{\Phi}^k(t) \mathbf{D}_{\phi,k} \hat{\mathbf{x}}_i^{v,k} \tag{3.63}$$

Therefore, the matrix $\mathbf{G}_{rad_{i,i}}$ for the convolution integral of the impulse response $K_{rad_{i,ii}}$ can be obtained by combination of the block matrixes $\mathbf{G}_{rad_{i,ii}}^k$ as follows:

$$\mathbf{G}_{rad_{i,ii}} = \begin{bmatrix} \mathbf{G}_{rad,i,ii}^1 & \mathbf{0}_{2,2} & \mathbf{0}_{2,2} \\ \mathbf{0}_{2,2} & \mathbf{G}_{rad,i,ii}^2 & \mathbf{0}_{2,2} \\ & \cdots & \\ \mathbf{0}_{2,2} & \mathbf{0}_{2,2} & \mathbf{G}_{rad,i,ii}^{N_x} \end{bmatrix} \tag{3.64}$$

A similar development can be carried out for the convolution integral of each element $K_{rad,s_{i,ii}}$

of the impulse response matrix $\mathbf{K}_{rad,s}$, with $i = 1,..n$ and $ii = 1,..n$, in equation (3.33).

Regarding the DAE formulation, substituting the approximated states (3.43), (3.44) and their time derivatives (3.48), (3.49) into the equations of motion (3.13)-(3.15) yields the following equations of motion in residual form:

$$r_i^q(t) = \mathbf{\Phi}(t)\mathbf{D}_\phi\hat{\mathbf{x}}_i^q - \sum_{p=1}^{6N} J_{i,p}\mathbf{\Phi}(t)\hat{\mathbf{x}}_p^v \tag{3.65}$$

$$\begin{aligned} r_i^v(t) = &\sum_{p=1}^{6N} M_{i,p}\mathbf{\Phi}(t)\mathbf{D}_\phi\hat{\mathbf{x}}_p^v + \sum_{p=1}^{6N} B_{i,p}\mathbf{\Phi}(t)\hat{\mathbf{x}}_p^v + \sum_{p=1}^{6N} G_{i,p}\mathbf{\Phi}(t)\hat{\mathbf{x}}_p^q + \sum_{p=1}^{6N} \mathbf{\Phi}(t)\mathbf{G}_{rad_{i,p}}\hat{\mathbf{x}}_p^v + .. \\ &\sum_{p=1}^{m} C_{q_{i,p}}^T\mathbf{\Phi}(t)\hat{\mathbf{x}}_p^\lambda(t) - f_{wave,i}(t) - f_i(t) - \sum_{p=1}^{n_c} F_{p_{i,p}}u_p(t) \end{aligned} \tag{3.66}$$

$$r_j^C(t) = C_j(\mathbf{q},t) \tag{3.67}$$

where $i = 1,..,6N$, $j = 1,..,m$, and $J_{i,p}$, $M_{i,p}$, $B_{i,p}$, $G_{i,p}$, $K_{rad_{i,p}}$, $C_{q_{i,pp}}^T$ and $F_{p_{i,p}}$ are the elements of the matrix $\mathbf{J}(\mathbf{\Theta})$, $\mathbf{M}$, $\mathbf{B}$, $\mathbf{G}$, $\mathbf{K}_{rad}$, $\mathbf{C}_q^T$ and $\mathbf{F}_p$, respectively. Regarding the ODE formulation, substituting the approximated states (3.43), (3.44) and their time derivatives (3.48), (3.49) into the equations of motion (3.32)-(3.33), yields the following equations of motion in residual form:

$$r_i^q(t) = \mathbf{\Phi}(t)\mathbf{D}_\phi\hat{\mathbf{x}}_i^q - \mathbf{\Phi}(t)\hat{\mathbf{x}}_i^v \tag{3.68}$$

$$\begin{aligned} r_i^v(t) = &\sum_{p=1}^{n} M_{s_{i,p}}\mathbf{\Phi}(t)\mathbf{D}_\phi\hat{\mathbf{x}}_p^v(t) + \sum_{p=1}^{n} B_{s_{i,p}}\mathbf{\Phi}(t)\hat{\mathbf{x}}_p^v + \sum_{p=1}^{n} G_{s_{i,p}}\mathbf{\Phi}(t)\hat{\mathbf{x}}_p^q + \sum_{p=1}^{n} \mathbf{\Phi}(t)\mathbf{G}_{rad,s_{i,p}}\hat{\mathbf{x}}_p^v \\ &- f_{wave,s_i}(t) - f_{s_i}(t) - \sum_{p=1}^{n_c} F_{p,s_{i,p}}u_p(t) \end{aligned} \tag{3.69}$$

where $i = 1,..,n$, and $M_{s_{i,p}}$, $B_{s_{i,p}}$, $G_{s_{i,p}}$, $K_{rad,s_{i,p}}$ and $F_{p,s_{i,p}}$ are the elements of the matrix $\mathbf{M}_s$, $\mathbf{B}_s$, $\mathbf{G}_s$, $\mathbf{K}_{rad,s}$ and $\mathbf{F}_{p,s}$, respectively. PS methods are used to compute the coefficients $\hat{\mathbf{x}}_i^q$ and $\hat{\mathbf{x}}_i^v$ that minimize the residuals (3.65)-(3.67) and (3.68)-(3.69) for the DAE and ODE formulations, respectively [52]. The PS methods force the residuals of the equations of motion to be zero at a certain number of points in time t_k, called *nodes*. If the number of nodes is N_c, then a linear system of $(2\times 6N+m)\times N_c$ and $2\times n\times N_c$ equations is solved for the DAE and ODE formulations, respectively. The number of nodes depends on multiple factors, including the order of the expansion N_x [53].

3.4 Case study: two-body hinge-barge device

In the following section, a two-body hinge barge device is considered as a case study. As shown in Figure 3.2, the device is made of two bodies interconnected by a hinge. An example of such systems is the SeaPower Platform [20]. The damping plate connected to body 1 aims to reduce the

vertical motion of body 1, and increase the pitch motion of body 2. The analysis of the motion of the device is restricted to the two dimensional plane $X-Z$. In Figure 3.8, the device is represented together with the global frame X_iZ_i, while the body frames $X_{b1}Z_{b1}$ and $X_{b2}Z_{b2}$ are assigned to body 1 and body 2, respectively. The total number of degrees of freedom of the system is three: the heave displacement z_1 of body 1, the pitch angle θ_1 of body 1, and the pitch angle θ_2 of body 2.

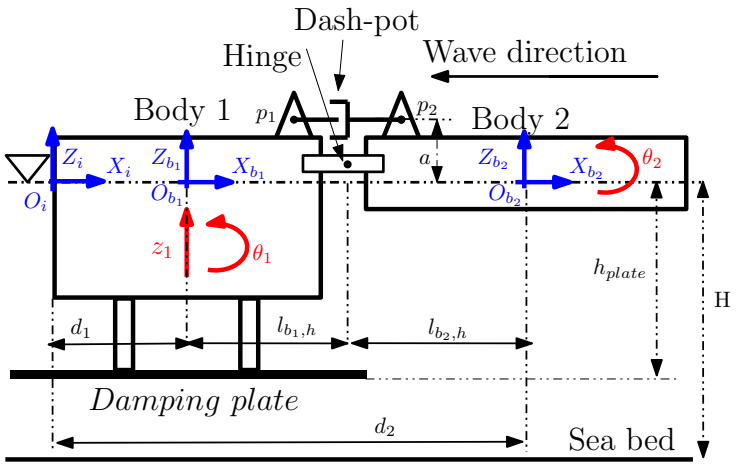

Figure 3.2: Two-body hinge barge device, where X_iZ_i, $X_{b1}Z_{b1}$ and $X_{b2}Z_{b2}$ represent the global frame, frame of body 1 and body 2, respectively.

3.4.1 DAE formulation for a two-body hinge-barge device

In the following subsection, the DAE formulation is applied in order to obtain the equations of motion of a two-body hinge-barge device. The vector of generalized positions considered for the two-body hinge-barge device is given as follows:

$$\mathbf{z} = [\mathbf{z}_1\ \mathbf{z}_2]^T = [z^b_{i,b_1}\ \theta_1\ z^b_{i,b_2}\ \theta_2]^T \tag{3.70}$$

where z^b_{i,b_k} and θ_k are the heaving displacements and pitch angle of body k, respectively, with $k = 1,2$. The block matrices $\mathbf{J}_k(\boldsymbol{\Theta})$ of the transformation matrix $\mathbf{J}(\boldsymbol{\Theta})$ in equation (3.18) are given as:

$$\mathbf{J}^{b_k} = \begin{bmatrix} c(\theta_k) & 0 \\ 0 & 1 \end{bmatrix} \tag{3.71}$$

The block matrices $\mathbf{M}_k$ of the rigid-body inertia matrix $\mathbf{M}_{in}$ in equation (3.19) are given as:

$$\mathbf{M}^{b_k} = \begin{bmatrix} m_k & 0 \\ 0 & I_{yy,k} + m_k h^2_{g,k} \end{bmatrix} \tag{3.72}$$

where $k = 1,2$, m_k is the mass of body k, $I_{yy,k}$ is the moment of inertia of body k around the y-axis and $h_{g,k}$ is the distance of the center of mass of body k from point O_{bk} along the z-axis.

The hydrodynamic loads $\mathbf{G}$, $\mathbf{M}_\infty$, $\mathbf{K}_{rad}$ and $\mathbf{f}_{wave}$ in equations (3.22), (3.23), (3.14) and (3.24) respectively, are obtained by means of the boundary element software WAMIT [25]. As shown in Figure 3.2, the PTO system can be modeled as a linear dash-pot system connected to points p_1 and p_2. The component of the PTO force along the line connecting points p_1 and p_2 is as follows:

$$F_s = c_{PTO}\dot{l} \tag{3.73}$$

where c_{PTO} and l are respectively the damping coefficient and displacement between the points p_1 and p_2 of the dash-pot system. For small displacements of body 1 and 2, the rate of change of the length l can be approximated as follows:

$$\dot{l} \approx a(\dot{\theta}_2 - \dot{\theta}_1) \tag{3.74}$$

where a is the vertical distance of points p_1 and p_2 from the center line of the device. Therefore, the vector of the loads due to the PTO systems in equation (3.14) acting on the device in equation is given as follows:

$$\mathbf{f}_{PTO} = \begin{bmatrix} 0 \\ -F_{s1}a \\ 0 \\ F_{s1}a \end{bmatrix} \tag{3.75}$$

The moorings are assumed to be connected only to body 1, and therefore, the vector $\mathbf{f}$ in equation (3.26) is given as follows [28]:

$$\mathbf{f} = -\mathbf{K}_{moor}\mathbf{q} \tag{3.76}$$

where:

$$\mathbf{K}_{moor} = \begin{bmatrix} k_{moor,1} & 0 & 0 & 0 \\ 0 & k_{moor,2} & 0 & 0 \\ 0 & 0 & 0 & 0 \\ 0 & 0 & 0 & 0 \end{bmatrix} \tag{3.77}$$

where $k_{moor,k}$, with $k = 1,2$, are the stiffness coefficients of the moorings.

In the following, the constraint equations for the two-body hinge-barge device are derived. The hinge between the two barges introduces the following constraint equations:

$$\mathbf{R}_b^i(\theta_1)\left(\begin{bmatrix} d_1 \\ z_{i,b_1}^b \end{bmatrix} + \begin{bmatrix} l_{1,h} \\ 0 \end{bmatrix}\right) - \mathbf{R}_b^i(\theta_2)\left(\begin{bmatrix} d_2 \\ z_{i,b2}^b \end{bmatrix} + \begin{bmatrix} -l_{2,h} \\ 0 \end{bmatrix}\right) = 0 \tag{3.78}$$

where $l_{1,h}$ and $l_{2,h}$ are the distances of the hinge from O_{b_1} and O_{b_2}, respectively, while d_1 and d_2 are the distances of O_{b_1} and O_{b_2} from the global frame X_iZ_i, respectively. The rotation matrices $\mathbf{R}_b^i$ are given as follows:

$$\mathbf{R}_b^i(\theta_k) = \begin{bmatrix} c(\theta_k) & -s(\theta_k) \\ s(\theta_k) & c(\theta_k) \end{bmatrix} \tag{3.79}$$

where $k = 1,2$. The constraints in equation (3.78) force the global position of the hinge defined by the coordinates of body 1 to be equal to the global position of the hinge defined by the coordinates of body 2. The matrix of the partial derivatives of constraint equations (3.78) computed with respect to the generalized positions and linearized around the equilibrium position, is given as follows:

$$\mathbf{C}_z = \begin{bmatrix} 1 & l_{1,h} & -1 & l_{2,h} \end{bmatrix} \tag{3.80}$$

3.4.2 ODE formulation for a two-body hinge-barge device

In the following subsection, the ODE formulation is applied in order to obtain the equations of motion of a two-body hinge-barge device. The vector of independent velocities of the device is given as follows:

$$\mathbf{v}_s = [\dot{z}_{i,b_1}^b \ \dot{\theta}_1 \ \dot{\theta}_2]^T \tag{3.81}$$

Given the matrix $\mathbf{C}_z$ in equation (3.80), the transformation matrix $\mathbf{P}$ in equation (3.30), used to express the relation between the vector of generalized velocities and independent velocities, is given as follows:

$$\mathbf{P} = \begin{bmatrix} 1 & 0 & 0 \\ 0 & 1 & 0 \\ 1 & l_{1,h} & l_{2,h} \\ 0 & 0 & 1 \end{bmatrix} \tag{3.82}$$

By means of the matrix $\mathbf{P}$, the quantities defined in equations (3.34)-(3.42) can be calculated in order to obtain the equations of motion of the device expressed with respect to the DoF.

3.4.3 Model validation

In this section, a particular two-body hinge-barge device was tested by Mícheál Ó'Catháin in a wave-tank in order to validate the DAE and ODE formulations against experimental data. The device is a $1/7th$ scale model of the section of the MWP device corresponding to an assembly of the forward and central barge. The dimensions of barge 1 are: length= 1.1 m, width=0.67 m and height=0.57 m. The dimensions of barge 2 are: length= 2.5 m, width=0.64 m and height=0.12m.

Full details on the wave-tank experiments are reported in [29]. A series of regular wave tests was performed for a range of frequencies of the incident wave ω from 2.61 rad/sec to 7.85 rad/secs, with the direction of the waves along the longitudinal direction of the device. The amplitude of the incident wave was set to 0.06 m for each test. The advantage of testing the device with monochromatic waves is that the response of the device can be obtained at each frequency. The heave motion of body 2 was recorded and compared against the response obtained from the DAE and ODE formulations derived in sections 3.4.1 and 3.4.2, respectively. PS methods were applied to compute an approximated solution for the equations of motion obtained for the DAE and ODE formulations. The order of expansion N_x for the position and velocity of the states is set equal to 1, since the excitation force is monochromatic. Also, the fundamental frequency ω_0 is set equal to the frequency of the incident wave. Simulations of the device were carried out in MATLAB running on a PC with a 3.40 GHz quad core processor and 8 GB RAM.

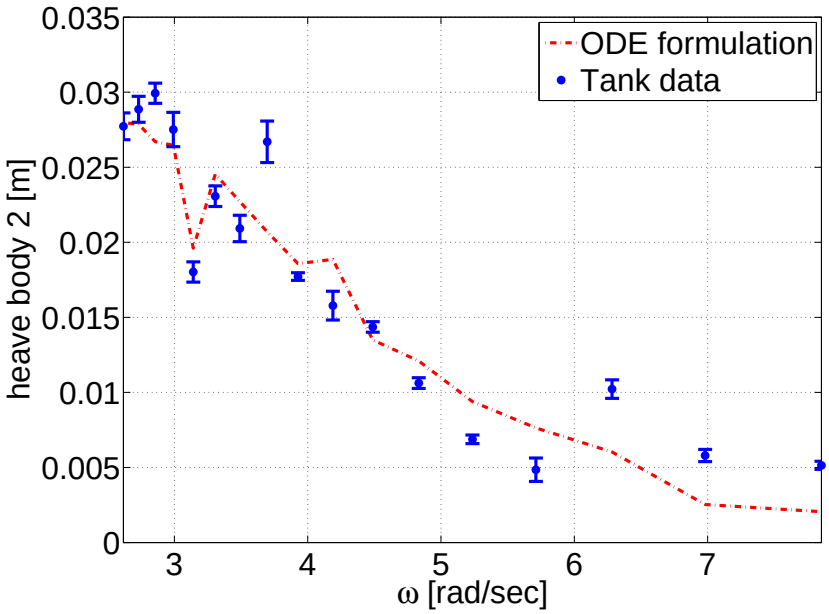

Figure 3.3: Frequency response of the heave of body 2 obtained from tank experiments with error bars for the uncertainty and ODE formulation for an incident wave of amplitude equal to 60 mm

In Figure 3.3, the frequency response of the heave of body 2, obtained from the tank experiments, is compared against the response obtained from the ODE formulation. The uncertainty on the measurement of the frequency response of the heave of body 2, obtained from the tank experiments, is represented by using error bars with interval $\pm\sigma$, where σ is the standard deviation. For each frequency of the regular wave, the standard deviation is computed as follows:

$$\sigma = \sqrt{\frac{\sum_{k}^{n_{data}} (Z^{b}_{i,b_2}(k) - \overline{Z}^{b}_{i,b_2})^2}{n_{data}}} \tag{3.83}$$

where n_{data} is the number of peaks of the heave of body 2, $Z^{b}_{i,b_1}(k)$ is the amplitude of the peak

k-th and $\overline{Z}^{b}_{i,b_1}$ is the average peak amplitude.

Note that, the responses of the heave of body 2, obtained with the ODE and DAE formulations based on a linear dynamic model, are identical. Therefore, for a linear dynamic model of the device, the DAE and ODE formulations are equivalent representations of the dynamics of the device. In general, for a nonlinear model of the device, the DAE and ODE formulations can provide a different response of the device.

As Figure 3.3 shows, with respect to the tank experiments, the ODE and DAE formulations give an accurate frequency response of the heave of body 2 for a range of frequencies from 2.61 rad/sec to 5.8 rad/sec. However, for frequencies greater than 5.8 rad/s, the ODE and DAE formulations give a less accurate response. The total root mean square error across the range of tested frequencies is equal to 0.0035 m for the ODE and DAE formulation. By way of example, the time response for the heave of body 2, given by the ODE and DAE formulations compared to the tank experiment, is shown for a regular wave of frequency $\omega = 3.14$ rad/secs in Figure 3.4a, frequency $\omega = 4.18$ rad/secs in Figure 3.4b, frequency $\omega = 5.23$ rad/secs in Figure 3.4c and frequency $\omega = 6.28$ rad/secs in Figure 3.4d.

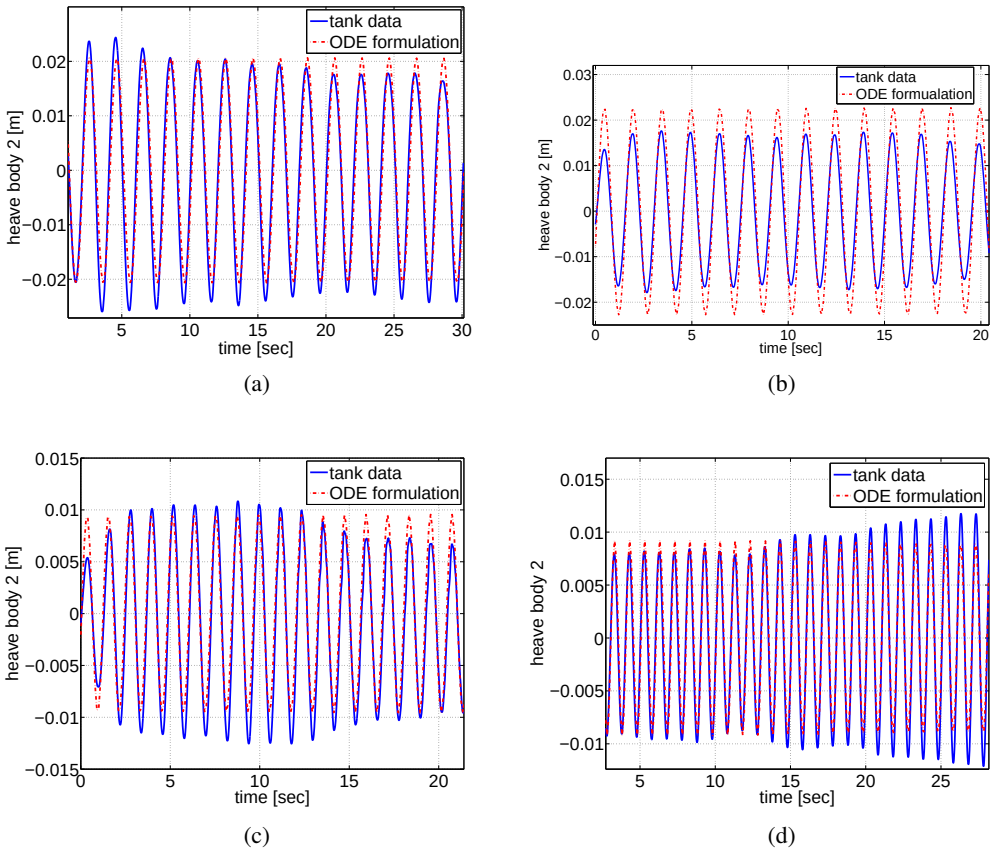

Figure 3.4: Comparison between the heave of body 2 given by tank tests and ODE formulation for regular waves of frequency $\omega = 3.14$ (a), $\omega = 4.18$ (b), $\omega = 5.23$ (c) and $\omega = 6.28$ (d)

3.4.4 Computational considerations

With regard to the computational time, a comparison between the DAE and ODE formulations, and a method based on the numerical integration of the equations of motion, e.g. an explicit R-K method of the 4th order with a fixed time step, is made. The comparison is carried out for an incident wave made using a Jonswap spectrum, which is given as follows [34]:

$$S(\omega) = \frac{\alpha g^2}{\omega^M} e^{-\frac{M}{N}\left(\frac{\omega_p}{\omega}\right)^N} \gamma^a \tag{3.84}$$

where $M = 5$, $N = 4$ and:

$$\sigma = \begin{cases} 0.07 & if\ \omega < \omega_p \\ 0.09 & if\ \omega \geq \omega_p \end{cases} \tag{3.85}$$

$$\alpha = 5.061 \frac{H_s^2}{T_p^4} (\ 1 - 0.287\, ln(\gamma)) \tag{3.86}$$

$$a = e^{\frac{-(\omega/\omega_p - 1)^2}{2\sigma^2}} \tag{3.87}$$

For 1/7th scale model of the section of the MWP device, a Jonswap spectrum for the incoming wave with peak period $T_p = 3$ seconds and significant wave height $H_s = 15$ cm is considered, and is shown in Figure 3.5.

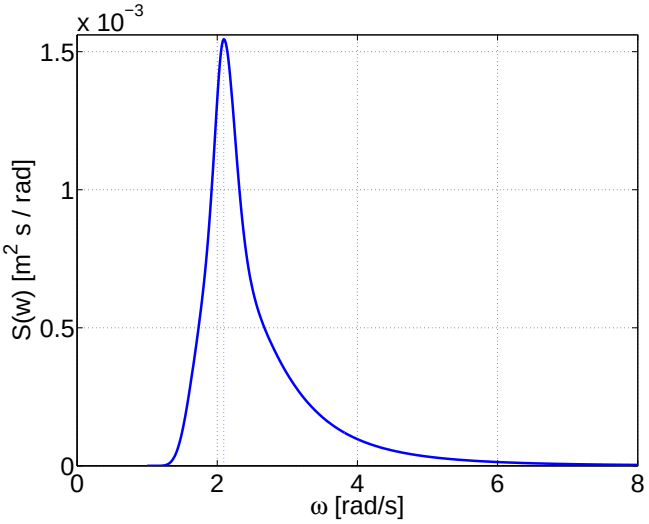

Figure 3.5: Jonswap spectrum with peak period T_p = 3 s and significant wave height H_s = 15 cm.

While the R-K method is used to solve both the transient and steady-state response of the device, the DAE and ODE formulations are used to obtain the steady-state response of the device only. It is important to highlight that, at steady-state, the response obtained with the R-K method, and DAE and ODE formulations, are identical. Note that, for the R-K method, the convolution

integral for the radiation forces is approximated by means of a state-space model [54], while, for the PS methods, the representation of the convolution integral is exact within the limits of the approximation of the variables of interest introduced by the Truncated Fourier series [47]. Furthermore, for the PS methods, the number of frequencies considered in the Truncated Fourier series covers the full range of frequencies of the spectrum of the incident wave, so that the response of the device is correctly represented. The R-K method implemented with an exact numerical representation of the convolution integral does not converge, due to the complex hydrodynamic interactions between the bodies of the device.

For a simulation time of 30 seconds, in Figure 3.6, the computational time required by the DAE and ODE formulations is compared to the computational time required by the R-K method for different sizes of the time step. As Figure 3.6 shows, the DAE and ODE formulations are more efficient than the R-K method for all time steps. Furthermore, the computational time required by the ODE formulation is smaller than the computational time required by the DAE formulation. Note that, for the DAE and ODE formulations, the computational time does not change for different sizes of the time step since the DAE and ODE formulations are solved with a fixed number of collocation points, and then, the solution is interpolated along the simulation time for different time steps. Therefore, the computational time required by the DAE and ODE formulation is independent of the size of the time step.

While the size of the time step in the R-K method must be bounded in order to guarantee stability ($\Delta T < 0.1$s), PS methods are naturally stable, since motion variables are composed of the sum of bounded functions. The specific choice of ΔT depends on the bandwidth of the WEC, BW_{WEC} Hz, with $\Delta T = 1/(10BW_{WEC})$ offered as a guideline. For short time steps, the DAE and ODE formulations are computationally faster than the Runge-Kutta method, allowing the simulation of stiff problems, where a small time step is required in order to describe the rapid transients of the solution. Stiffness can be introduced into the dynamic model of a wave energy converter when, for example, the water hammer effects in the PTO system are considered. It is interesting to note that the ODE formulation is computationally faster than the DAE formulation for all the time steps. The fact that the ODE formulation requires a shorter computational time than the DAE formulation could be significant in the real-time model-based control of the device.

For a time step of 0.06 seconds, in Figure 3.7, the computational time required by the DAE and ODE formulations is compared to the computational time required by the Runge-Kutta method for different simulation times. As Figure 3.7 shows, the Runge-Kutta method is less efficient than the DAE and ODE formulations for short simulation times.

3.5 Case study: three-body hinge-barge device

A three-body hinge-barge device such as the MWP [5] is considered as a case study. As shown in Figure 3.8, the device is composed of 3 rectangular bodies interconnected by hinges. Generally, the relative pitch motion between bodies is used to drive a Power TakeOff (PTO) system in order

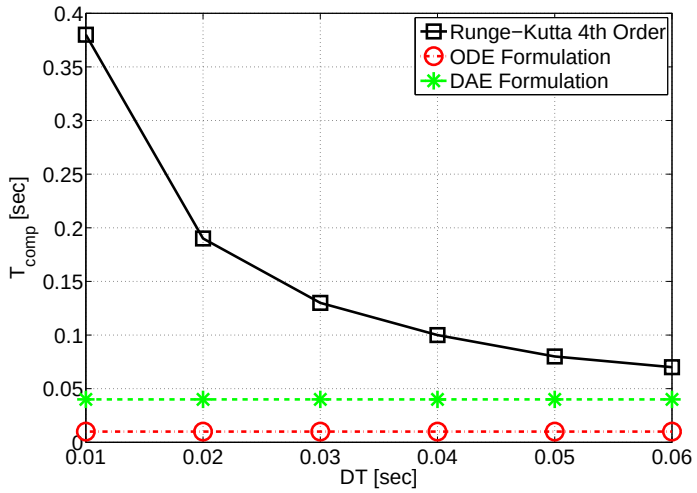

Figure 3.6: Computational time required by the Runge-Kutta method, DAE and ODE formulations computed for different time steps and simulation time equal to 30 seconds

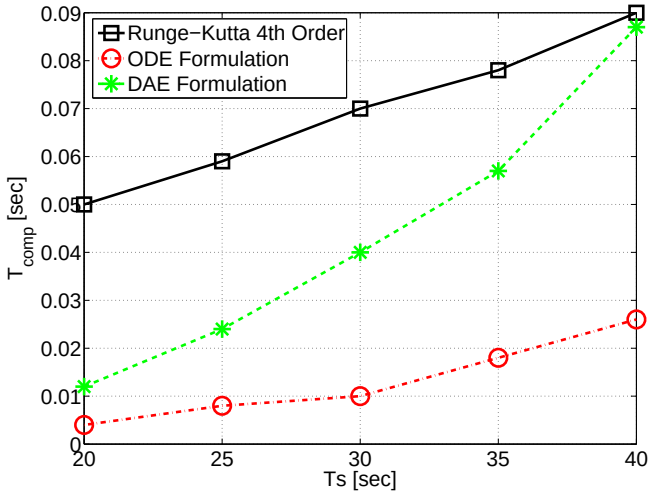

Figure 3.7: Computational time required by the Runge-Kutta method, DAE and ODE formulations computed for different simulation times and time step equal to 0.06 seconds

to convert the energy from the waves into mechanical energy. The damping plate connected to body 2 aims to reduce the vertical motion of body 2, increasing the pitch motions of body 1 and 3. The analysis of the motion of the devices is restricted to the two dimensional plane $X-Z$. In Figure 3.8, the device is represented together with the global frame X_iZ_i, while a body frame is assigned to each body composing the device. The total number of degrees of freedom of the system in Figure 3.8 is four: the heave displacement z_2 of body 2, and the pitch angles θ_1, θ_2 and θ_3 of bodies 1, 2 and 3, respectively.

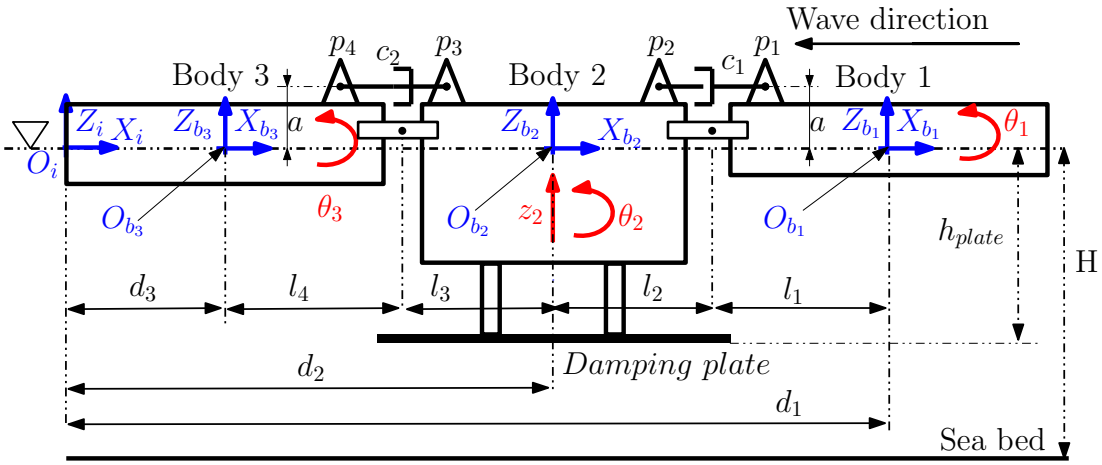

Figure 3.8: Three-body hinge-barge device, where X_iZ_i represents the global frame, and a local frame is assigned to each body composing the device.

3.5.1 DAE formulation for a three-body hinge-barge device

In the following subsection, the DAE formulation is applied in order to obtain the equations of motion for a three-body hinge-barge device. The vector of generalized positions, considered for the three-body hinge-barge device, is:

$$\mathbf{z} = [\mathbf{z}_1\ \mathbf{z}_2\ \mathbf{z}_3]^T = [z^b_{i,b_1}\ \theta_1\ z^b_{i,b_2}\ \theta_2\ z^b_{i,b_3}\ \theta_3]^T \tag{3.88}$$

where z^b_{i,b_k} and θ_k are the heave displacement and pitch angle of body k, respectively, with $k = 1,2,3$. The block matrix $\mathbf{J}_k(\boldsymbol{\Theta})$ of the transformation matrix $\mathbf{J}(\boldsymbol{\Theta})$ in equation (3.18) is given as:

$$\mathbf{J}^{b_k} = \begin{bmatrix} c(\theta_k) & 0 \\ 0 & 1 \end{bmatrix} \tag{3.89}$$

where $k = 1,2,3$. The block matrix $\mathbf{M}_k$ of the rigid-body inertia matrix $\mathbf{M}_{in}$ in equation (3.19) is given as:

$$\mathbf{M}^{b_k} = \begin{bmatrix} m_k & 0 \\ 0 & I_{yy,k} + m_k h^2_{g,k} \end{bmatrix} \tag{3.90}$$

where $k = 1,2,3$, m_k is the mass of body k, $I_{yy,k}$ is the moment of inertia of body k around the y-axis and $h_{g,k}$ is the distance of the center of mass of body k from point O_{bk} along the z-axis. The hydrodynamic loads $\mathbf{G}$, $\mathbf{M}_\infty$, $\mathbf{K}_{rad}$ and $\mathbf{f}_{wave}$, in equations (3.22), (3.23), (3.14) and (3.24) respectively, are obtained by means of the boundary element software WAMIT [25]. The vector of PTO forces $\mathbf{f}_{pto}$ in equation (3.14) is given by the forces due to the PTO systems connecting body 2 to bodies 1 and 3. As shown in Figure 3.8, each PTO system can be modeled as a linear dash-pot system. Considering the PTO system connecting points p_1 and p_2, the axial force is

given as follows:

$$F_{s1} = c_1 \dot{l}_1 \tag{3.91}$$

where c_1 and l_1 are the damping coefficient and displacement of the dash-pot system, respectively. For small displacements of body 1 and 2, $\dot{l}_1$ can be approximated as follows:

$$\dot{l}_1 \approx a(\dot{\theta}_1 - \dot{\theta}_2) \tag{3.92}$$

where a represent the vertical distance between the line of action of the PTO force and the center-line of the device. Similarly, for the PTO connecting points p_3 and p_4, the axial force is given as follows:

$$F_{s2} = c_2 \dot{l}_2 \tag{3.93}$$

with $\dot{l}_2$ calculated as follows:

$$\dot{l}_2 \approx a(\dot{\theta}_3 - \dot{\theta}_2) \tag{3.94}$$

Therefore, the vector of loads in equation (3.14), due to the PTO systems acting on the device, is given as follows:

$$\mathbf{f}_{PTO} = -\begin{bmatrix} 0 \\ F_{s1}a \\ 0 \\ -F_{s1}a - F_{s2}a \\ 0 \\ F_{s2}a \end{bmatrix} \tag{3.95}$$

Now, the constraint equations for the three-body hinge-barge device are derived. The hinge between body 2 and 3 introduces the following constraint equations:

$$\mathbf{R}_b^i(\theta_2)\left(\begin{bmatrix} d_2 \\ z_{i,b_2}^b \end{bmatrix} + \begin{bmatrix} -l_{3,h} \\ 0 \end{bmatrix}\right) - \mathbf{R}_b^i(\theta_3)\left(\begin{bmatrix} d_3 \\ z_{i,b3}^b \end{bmatrix} + \begin{bmatrix} l_{4,h} \\ 0 \end{bmatrix}\right) = 0 \tag{3.96}$$

where $l_{3,h}$ and $l_{4,h}$ are the distances of the hinge from O_{b_2} and O_{b_3}, respectively, while d_2 and d_3 are the distances of O_{b_2} and O_{b_3} from the global frame X_iZ_i, respectively. The hinge between body 1 and 2 introduces the following constraint equations:

$$\mathbf{R}_b^i(\theta_1)\left(\begin{bmatrix} d_1 \\ z_{i,b_1}^b \end{bmatrix} + \begin{bmatrix} -l_{1,h} \\ 0 \end{bmatrix}\right) - \mathbf{R}_b^i(\theta_2)\left(\begin{bmatrix} d_2 \\ z_{i,b2}^b \end{bmatrix} + \begin{bmatrix} l_{2,h} \\ 0 \end{bmatrix}\right) = 0 \tag{3.97}$$

where $l_{1,h}$ and $l_{2,h}$ are the distances of the hinge from O_{b_1} and O_{b_2}, respectively, while d_1 is the distance of O_{b_1} from the global frame $X_g Z_g$. The rotation matrices $\mathbf{R}_b^i$ are given as follows:

$$\mathbf{R}_b^i(\theta_k) = \begin{bmatrix} c(\theta_k) & -s(\theta_k) \\ s(\theta_k) & c(\theta_k) \end{bmatrix} \tag{3.98}$$

where $c(\theta_k) = cos(\theta_k)$ and $s(\theta_k) = sin(\theta_k)$, with $k = 1,2,3$. The constraints in equation (3.96) force the global position of the hinge defined by the coordinates of body 2 to be equal to the global position of the hinge defined by the coordinates of body 3. Similar considerations can be made for the constraints in equation (3.97). The matrix of the partial derivatives of constraint equations (3.96) and (3.97), computed with respect to the generalized positions and linearized around the equilibrium position, is given as follows:

$$\mathbf{C}_z = \begin{bmatrix} 0 & 0 & 1 & -l_{3,h} & -1 & -l_{4,h} \\ 1 & -l_{1,h} & -1 & -l_{2,h} & 0 & 0 \end{bmatrix} \tag{3.99}$$

3.5.2 ODE formulation for a three-body hinge-barge device

The ODE formulation is now applied to obtain the equations of motion of a three-body hinge-barge device. The vector of independent velocities of the device is:

$$\mathbf{v}_s = [\dot{\theta}_1 \ \dot{z}^b_{i,b_2} \ \ \dot{\theta}_2 \ \dot{\theta}_3]^T \tag{3.100}$$

Given the matrix $\mathbf{C}_z$ from equation (3.99), the transformation matrix $\mathbf{P}$ in equation (3.30) is used to express the relation between the vector of generalized velocities and independent velocities as follows:

$$\mathbf{P} = \begin{bmatrix} l_{1,h} & 1 & l_{2,h} & 0 \\ 1 & 0 & 0 & 0 \\ 0 & 1 & 0 & 0 \\ 0 & 0 & 1 & 0 \\ 0 & 1 & -l_{3,h} & -l_{4,h} \\ 0 & 0 & 0 & 1 \end{bmatrix} \tag{3.101}$$

Using $\mathbf{P}$, the quantities defined in equations (3.34)-(3.42) can be calculated in order to obtain the equations of motion of the device expressed with respect to the degrees of freedom.

3.5.3 Model validation

A specific $1/25th$ scale three-body hinge-barge device was tested in a wave tank using facilities of the U.S. Naval Academy, Annapolis [55]. The tank tests were made in a 36.6 m long, 1.5 m deep and 2.44 m wide wave tank at the US Naval Academy. The dimensions of the fore barge are: length= 0.68 m, width=0.4 m and height=0.1 m. The dimensions of the central barge are:

length= 0.28 m, width=0.4 m and height=0.15m. The dimensions of the aft barge are: length= 1 m, width=0.4 m and height=0.1 m.

3.5.3.1 Tank tests

The following measurements were recorded during the tests:

- Heave displacement of body 2
- Pitch angles of bodies 1, 2 and 3
- Incident wave at 6.1 *m* upwave of the device
- Axial forces along the dashpots

A series of tanks tests, with regular and irregular waves, was performed, with the direction of the waves along the longitudinal direction of the device. For regular waves, a series of tests with a range of frequencies ω from 3.14 rad/sec to 7.54 rad/secs and amplitude of 0.03 m was performed. In Figure 3.10, the Response Amplitude Operators (RAOs) between the incident wave and the DoF of the device are shown for regular waves. For irregular waves, two different tank tests were performed:

- Irregular wave test 1: incident wave made using a BRETSCHNEIDER spectrum with a significant wave height $H_s = 15$ cm and peak period $T_p = 1.276$ seconds.
- Irregular wave test 2: incident wave made using a JONSWAP spectrum with a significant wave height $H_s = 15$ cm and peak period $T_p = 1.276$ seconds.

The Bretschneider spectrum is given as follows [34]:

$$S(\omega) = \frac{\alpha g^2}{\omega^M} e^{-\frac{M}{N}\left(\frac{\omega_p}{\omega}\right)^N} \tag{3.102}$$

where $M = 5$, $N = 4$ and:

$$\alpha = 5.061 \frac{H_s^2}{T_p^4} \tag{3.103}$$

In Figure 3.9, the JONSWAP and the BRETSCHNEIDER spectrums, obtained from the tank experiments, are compared. As Figure 3.9 shows, the BRETSCHNEIDER spectrum is characterized by a broader spectral distribution than the JONSWAP spectrum.

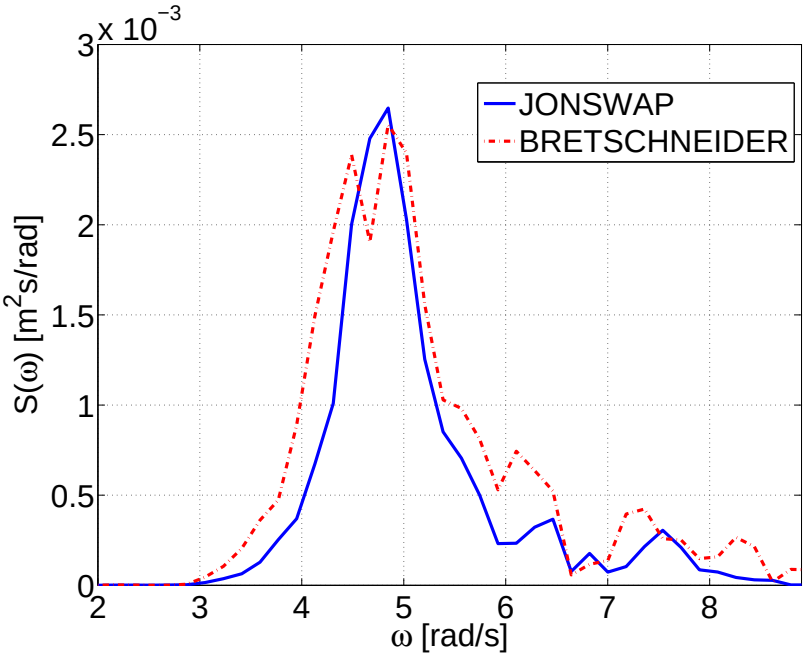

Figure 3.9: Comparison between the JONSWAP and the BRETSCHNEIDER spectrums with a significant wave height $H_s = 15$ cm and peak period $T_p = 1.276$ seconds obtained from the tank experiments.

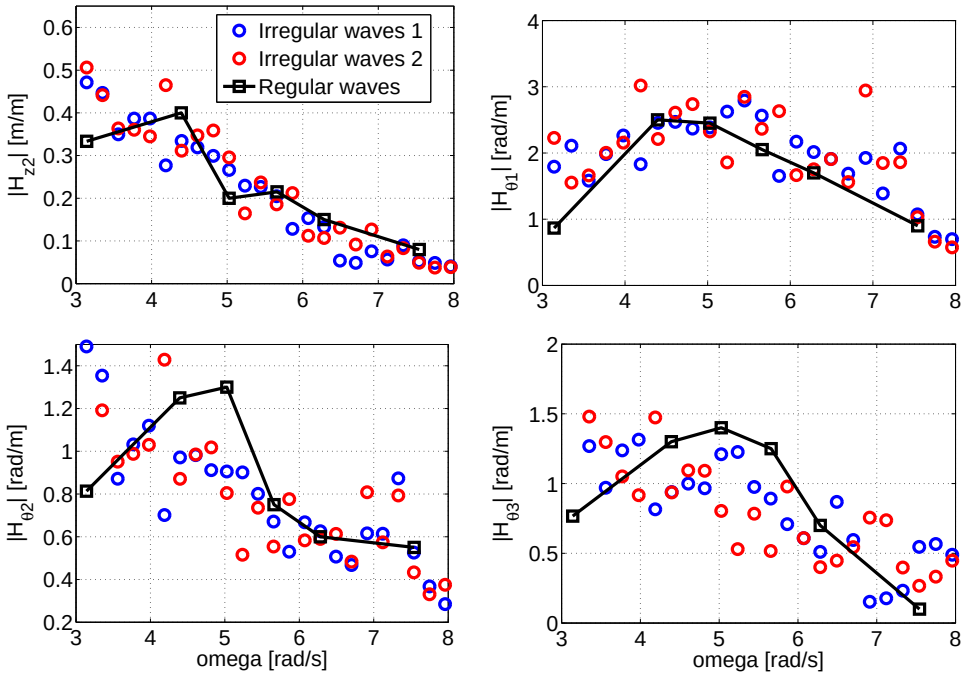

Figure 3.10: RAOs for the degrees of freedom of a three-body hinge-barge device measured with regular and irregular wave tank tests

3.5.3.2 Model Tuning

Given the frequency domain model of the device with the hydrodynamic parameters computed from the Wamit software, the viscous damping matrix $\mathbf{B}_{visc,s}$ in equation (3.33) can be identified using irregular wave test 1. The transfer function in the frequency domain, between the DoF of the device and the incident wave, is:

$$\mathbf{H}(\omega) = \frac{\hat{\mathbf{X}}_s(\omega)}{\hat{\eta}(\omega)} \tag{3.104}$$

where $\hat{\mathbf{X}}_s(\omega)$ is a complex vector representing the displacements of the DoF of the device. The transfer function $\mathbf{H}(\omega)$ can be determined experimentally from the tank data with irregular waves [56]. While the module of the transfer function $\mathbf{H}(\omega)$ is obtained by using the spectral densities of the positions of the Dof of the device and wave elevation, the phase of the transfer function $\mathbf{H}(\omega)$ is obtained by using the cross power spectral density between positions of the Dof of the device and wave elevation. The spectral densities and cross power spectral density are evaluated by using Welch's method, where the input signals are split into overlapping segments of length L, with a 50% overlap. The overlapping segments are windowed by a Hanning window, in order to avoid the frequency leakage to the non-periodicity of the segments. Thus, the transfer function $\mathbf{H}(\omega)$ is computed as follows:

$$\mathbf{H}(\omega) = \sqrt{\frac{S_{x_s x_s}}{S_{\eta\eta}}} e^{j\angle S_{x_s\eta}} \tag{3.105}$$

where $S_{x_s x_s}$, $S_{\eta\eta}$ and $S_{x_s\eta}$ are the power spectral density of the DoF of the device, power spectral density of the wave elevation and the cross power spectral density between the DoF of the device and the wave elevation, respectively. As shown in Figure 3.10, the RAOs for the heave of the central barge and pitch angle of the fore barge for regular waves show a good agreement with the transfer functions for the heave of the central barge and pitch angle of the fore barge computed with irregular waves. Furthermore, as shown in Figure 3.10, the transfer function for the pitch angles of the central and aft barge with irregular waves shows a good agreement with RAOs for the pitch angles of the central and aft barge with regular waves in terms of resonant frequency. However, the amplitude of the transfer function for the pitch angles of the central and aft barge with irregular waves are smaller than the RAOs for the pitch angles of the central and aft barge with regular waves.

The theoretical transfer function between the DoF of the device and the incident wave is:

$$\hat{\mathbf{H}}(\omega) = \frac{\mathbf{H}_{wave,s}(\omega)}{-\omega^2(\mathbf{M}_s + \mathbf{M}_{a,s}(\omega)) + j\omega(\mathbf{B}_{visc,s} + \mathbf{B}_{rad,s}(\omega)) + \mathbf{G}_s} \tag{3.106}$$

where $\mathbf{M}_s$ is the inertia matrix, $\mathbf{B}_{visc,s}$ is the viscous damping matrix, $\mathbf{G}_s$ is the hydrostatic stiffness, $\mathbf{M}_{a,s}$ is the added mass, $\mathbf{B}_{rad,s}$ is the radiation damping and $\mathbf{H}_{wave,s}$ is the transfer function betweeen the excitation forces vector and the incident wave. The problem of identification of the viscous damping matrix $\mathbf{B}_{visc,s}$ in equation (3.106) is formulated as an optimization problem as

follows:

$$\min_{\mathbf{B}_{visc,s}} \quad J_{LS} \tag{3.107}$$

where the cost function J_{LS} to be minimized is the total sum of squared errors between the transfer functions $\mathbf{H}(\omega)$ and $\hat{\mathbf{H}}(\omega)$, across the range of frequencies of the spectrum of the incident wave,

$$J_{LS} = \sum_{i=1}^{n_f} \sum_{j=1}^{n} |H_j(\omega_i) - \hat{H}_j(\omega_i)|^2 \tag{3.108}$$

where n_f is the number of frequencies of the spectrum of the incident wave, n is the number of degrees of freedom, H_j and $\hat{H}_j$ are the experimental and theoretical transfer function between the j-th Dof and the incident wave, respectively. The elements of the viscous damping matrix $\mathbf{B}_{visc,s}$ are used as decision variables for the computation of the minimum of the cost function defined in equation (3.108).

To validate the identified model, the tests with regular waves can be used. PS methods were applied to compute an approximated solution for the equations of motion obtained for the DAE and ODE formulations. The order of expansion N_x for the position and velocity of the states is set equal to 1, according with the monochromatic wave conditions. The fundamental frequency ω_0 is set equal to the frequency of the incident wave. Simulations of the device were carried out in MATLAB running on a PC with a 3.40 GHz quad core processor and 8 GB RAM.

In Figure 3.11, the frequency response of the DoF of the device, obtained from the tank experiments, is compared to the response obtained from the tuned dynamic model. The uncertainty on the measurement of the frequency response of the DoF of the device, obtained from the tank experiments, is represented by using error bars with interval $\pm\sigma_{X_{s,i}}$, where $\sigma_{X_{s,i}}$ is the standard deviation of the i-th DoF. For each frequency of the regular wave, the standard deviation $\sigma_{X_{s,i}}$ is computed as follows:

$$\sigma_{X_{s,i}} = \sqrt{\frac{\sum_k^{n_{data}} (X_{s,i}(k) - \overline{X}_{s,i})^2}{n_{data}}} \tag{3.109}$$

where n_{data} is the number of peaks of the i-th DoF, $X_{s,i}(k)$ is the amplitude of the peak k-th and $\overline{X}_{s,i}$ is the average peak amplitude.

The resonant frequencies of the device can be computed as the eigenvalues of the state matrix $\mathbf{A}_{st}$ of the state-space representation of the system, which is given as follows:

$$\mathbf{A}_{st} = \begin{bmatrix} \mathbf{0}_{n,n} & \mathbf{I}_{n,n} \\ -(\mathbf{M}_s + \mathbf{M}_{a,s}(\omega))^{-1}\mathbf{G}_s & -(\mathbf{M}_s + \mathbf{M}_{a,s}(\omega))^{-1}(\mathbf{B}_{visc,s} + \mathbf{B}_{rad,s}(\omega)) \end{bmatrix} \tag{3.110}$$

The matrix $\mathbf{A}_{st}$ has three pairs of complex conjugate eigenvalues which have natural frequencies of 5.05 rad/s, 6.15 rad/s and 7.83 rad/s.

By way of example, the time response for the heave of body 2, given by the ODE formulation compared to the tank experiment, is shown for regular waves of frequency $\omega = 3.14$ rad/secs in Figure 3.12a, frequency $\omega = 5.02$ rad/secs in Figure 3.12b, frequency $\omega = 5.65$ rad/secs in Figure 3.12c, and frequency $\omega = 6.28$ rad/secs in Figure 3.12d. The time response for the pitch angles of body 1, 2 and 3 given by the ODE formulation compared to the tank experiment is shown for regular waves of frequency $\omega = 3.14$ rad/secs in Figure 3.13a, frequency $\omega = 5.65$ rad/secs in Figure 3.13b and frequency $\omega = 6.28$ rad/secs in Figure 3.13c.

As for the 2-body hinge-barge device presented in Section 3.4, the responses of the heave of body 2 and of the pitch angles of the three bodies, obtained with the ODE and DAE formulations based on a linear dynamic model, are identical. Therefore, for a linear dynamic model of the device, the DAE and ODE formulation are equivalent representations of the dynamics of the device.

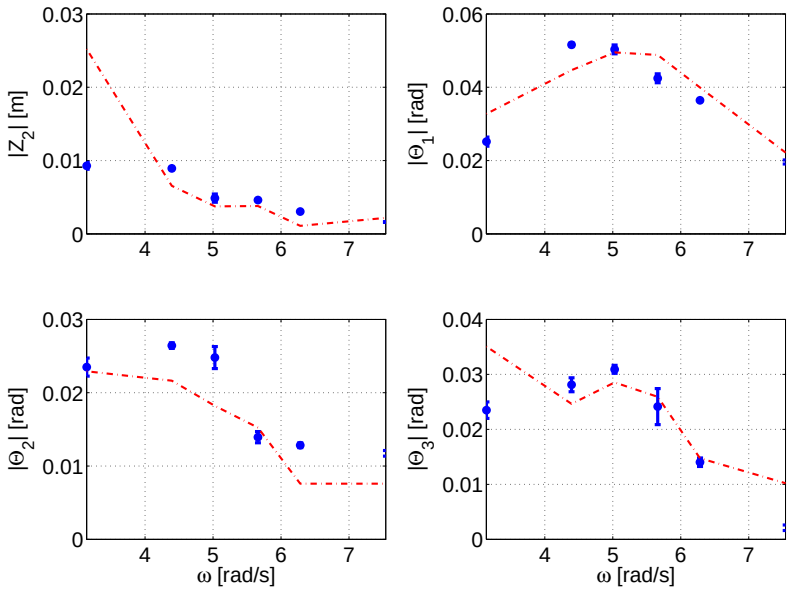

Figure 3.11: Frequency response of the DoF of a three-body hinge-barge device, obtained with the tank experiments with error bars for the uncertainty and tuned dynamic model for regular waves.

In order to validate the identified model with irregular waves, irregular wave test 2 can be used. Given the linear model of the device derived in Sections 3.5.1 and 3.5.2, the range of frequencies for the position and velocity spectra is the same as the range of frequencies of the spectrum of the incident wave. Therefore, for a fundamental frequency $\omega_0 = 0.12$ rad/s and a maximum frequency of the spectrum of the incoming wave of $\omega_{max} = 8$ rad/s, the order of expansion for the position and velocity of the states is computed as $N_x = \omega_{max}/\omega_0 = 70$. In Figure 3.14, the frequency response of the heave of body 2, obtained from irregular wave test 2, is compared against the response obtained from the ODE formulation. The uncertainty on the measurement of the frequency response of the

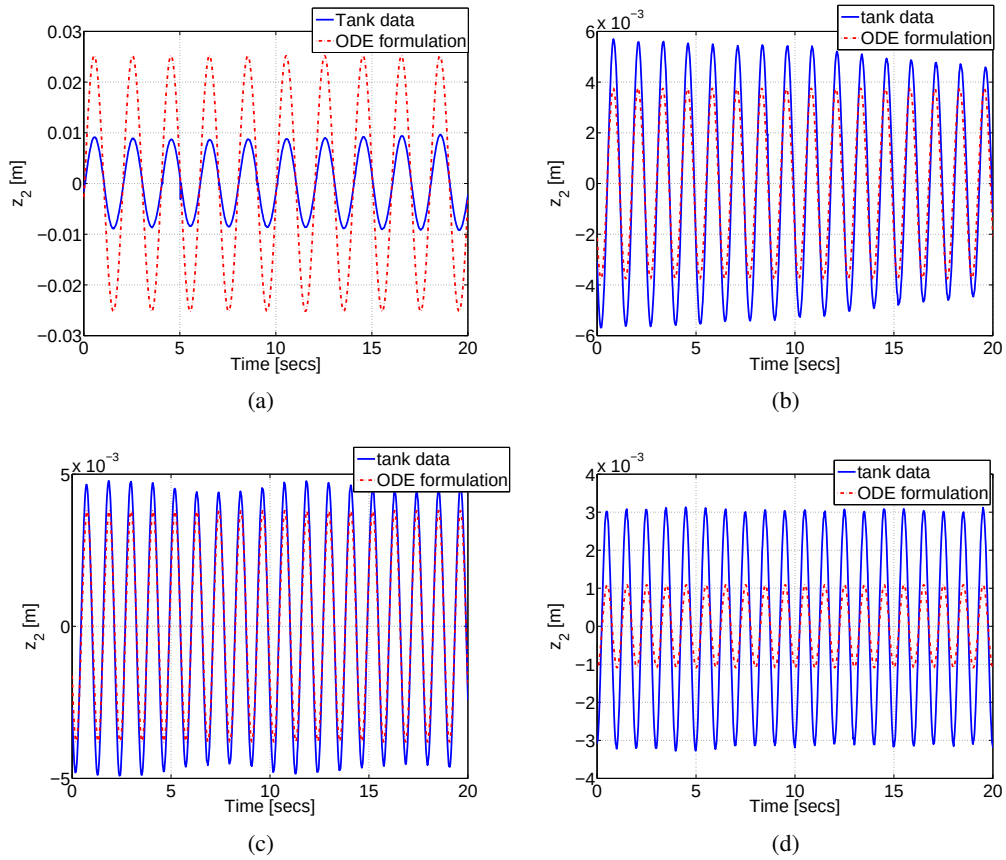

Figure 3.12: Comparison between the heave of body 2 given by tank tests and ODE formulation for regular waves of frequency $\omega = 3.14$ (a), $\omega = 5.02$ (b), $\omega = 5.65$ (c) and $\omega = 6.28$ (d)

heave of body 2, with the irregular wave test 2, is chosen equal to the maximum uncertainty of the tests with regular waves of comparable scale. In Figure 3.15, the frequency responses of the pitch angles of bodies 1, 2 and 3, obtained from irregular wave test 2, are compared against the responses obtained from the ODE formulation. As for the tests of the heave of body 2, the uncertainty on the measurement of the frequency response of the pitch angles, with the irregular wave test 2, is chosen equal to the maximum uncertainty of the tests with regular waves of comparable scale. In Figure 3.16, the time domain response of the heave of body 2, obtained from irregular wave test 2, is compared against the response obtained from the ODE formulation. In Figure 3.17, the time domain responses of the pitch angles of bodies 1, 2 and 3, obtained from irregular wave test 2, are compared against the responses obtained from the ODE formulation.

3.5.4 Computational considerations

A comparison between the DAE and ODE formulations, and a method based on the integration of the equations of motion, using an explicit 4th order R-K method with a fixed time step, is made. The comparison is carried out for an incident wave made using a Jonswap spectrum with a significant wave height $H_s = 15$ cm and peak period $T_p = 1.27$ seconds.

While the R-K method is used to solve both the transient and steady-state response of the device, the DAE and ODE formulations are used to obtain the steady-state response of the device only. It is important to highlight that, at steady-state, the response obtained from the R-K method, and DAE and ODE formulations, is identical. As for the 2-body hinge-barge presented in Section 3.4.4, for the R-K method, the convolution integral for the radiation forces is approximated by means of a state-space model [54], while for the PS methods, the representation of the convolution integral is exact within the limits of the approximation of the variables of interest introduced by the Truncated Fourier series [47]. As for the 2-body hinge-barge device presented in Section 3.4.4, the R-K method implemented with an exact numerical representation of the convolution integral does not converge, due to the complex hydrodynamic interactions between the bodies of the device.

For a nominal simulation time of 20s, the computation time T_{comp} required by the DAE and ODE formulations is compared to that for R-K, for different time step sizes, in Figure 3.18. Figure 3.18 confirms that the ODE formulation is more efficient than R-K for short time steps and, for the DAE and ODE formulations, T_{comp} does not change significantly with time step, due to the use of a fixed number of collocation points. Note that the DAE formulation is computationally slower than both the ODE formulation and R-K method, for all the time steps. However, it should be borne in mind that T_{comp} depends on the order of the finite order radiation damping approximation used in R-K, with a relatively small order of 3 used for this baseline comparison.

For a specific time step of 0.04s, T_{comp} for the DAE, ODE and R-K formulations for different simulation times T_s is compared in Figure 3.19, showing that the DAE formulation is computationally less efficient than both the ODE and R-K methods, for all T_s. The Runge-Kutta method is computationally faster than the ODE formulation for long T_s, though a higher-order convolution approximation will increase the slope of the R-K trace in Figure 3.19. In terms of likely simulation requirements, system simulation is likely to require a $T_s > 100s$, while predictive control algorithms will likely employ a prediction horizon of $T_s < 20$s [57].

3.6 Conclusions

This chapter demonstrates that PS methods are a compact and numerically efficient formulation for solving the dynamics of multi-body wave energy devices. Two different case studies were considered: a two-body and a three-body hinge barge devices. For the two-body hinge-barge device, experimental tests with monochromatic waves were carried out in order to validate the use of PS methods for solving the dynamics of the device. Both DAE and ODE PS formulations were

applied in order to describe the dynamics of the device, showing good agreement with experimental tests in terms of device motion. However, experimental tests with polychromatic waves are necessary in order to validate PS methods under a wider range of conditions. For the three-body hinge-barge device, experimental tests with both monochromatic and polychromatic waves were carried out to validate the use of the PS models. Both DAE and ODE PS formulations showed good agreement with experimental tests in terms of device motion.

For a two-body hinge-barge device, the PS ODE formulation is superior to the PS DAE formulation in terms of computational time required to obtain the motion of the device. With respect to reference methods based on the integration of the equations of motion, e.g. the Runge-Kutta method, both PS ODE and DAE formulations are computationally more efficient for time steps that range from 0.01 seconds to 0.06 seconds. Furthermore, for time steps larger than 0.06 seconds, PS methods are computationally more stable than the Runge-Kutta method. In terms of solution accuracy, PS methods can be less accurate than the Runge-Kutta method, since they compute an approximation of the solution based on a finite number of expansion coefficients. However, within the bounds of this approximation, the convolution integral corresponding to the WEC radiation damping term is solved exactly. This is in contrast to the R-K method, where the convolution integral is approximated as the output of a finite order linear system.

For a three-body hinge-barge device, the PS ODE formulation requires shorter computational times than the PS DAE formulation. With respect to the reference R-K method, the PS ODE formulation is computationally faster for small time steps. However, the PS DAE formulation is computationally slower than the R-K method for all time steps.

For the optimal control of multi-body wave energy converters, PS methods are generally more efficient than traditional methods such as Model Predictive Control (MPC), which relies on the simulation capabilities of the integration method in order to compute the optimal solution of the control input [58]. In Chapter 4, PS methods based on Fourier basis functions are applied to formulate the optimal control problem of a three-body hinge-barge device. A useful feature of PS is that only a small extra computational effort is required to compute the expansion coefficients for the optimal control force, in addition to the expansion coefficients for the state variables.

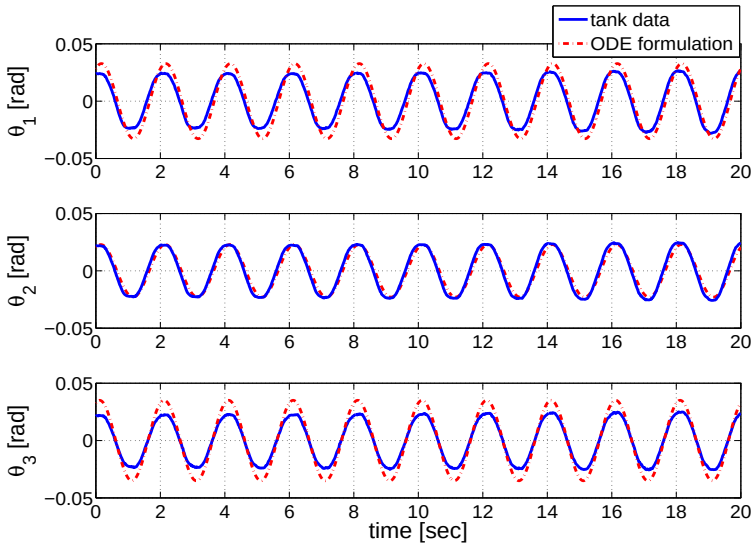

(a)

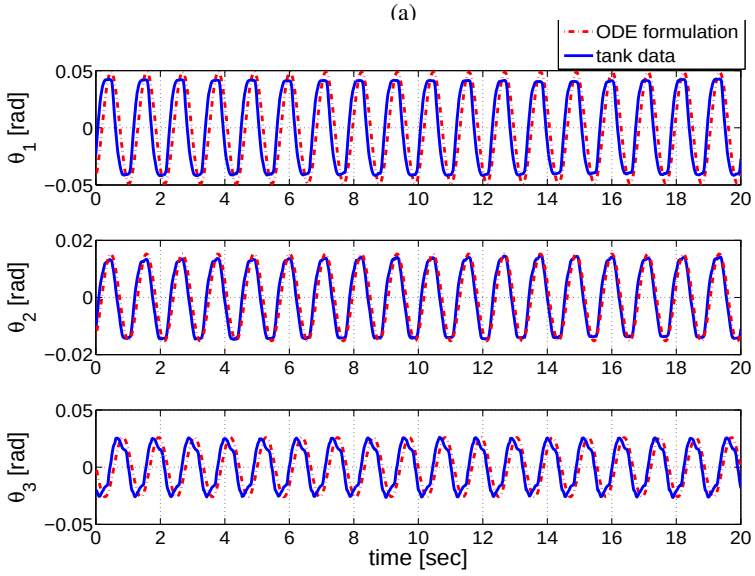

(b)

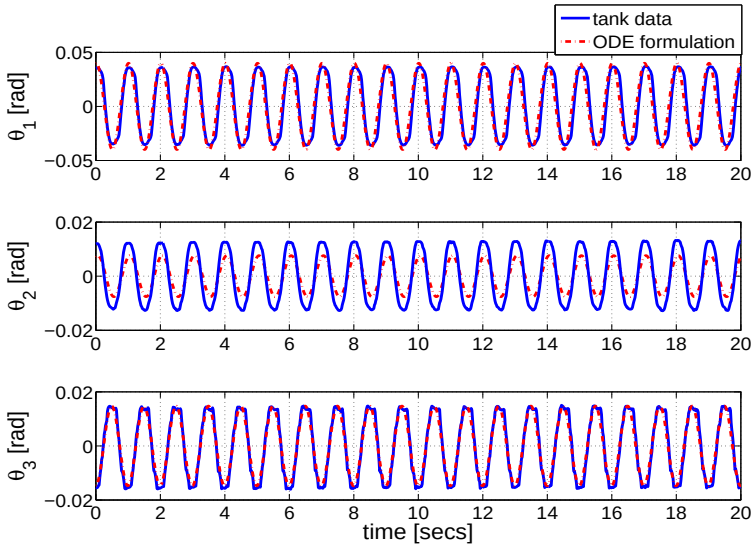

(c)

Figure 3.13: Comparison between the pitch angles of body 1, 2 and 3 given by tank tests and ODE formulation for regular waves of frequency $\omega = 3.14$ (a), $\omega = 5.65$ (b) and $\omega = 6.28$ (c)

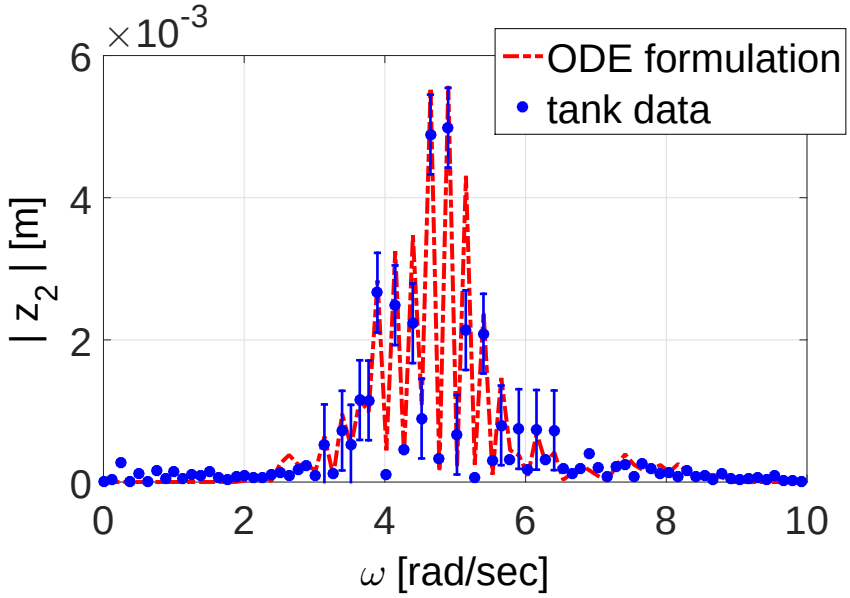

Figure 3.14: Frequency response of the heave of body 2 obtained from tank experiments with error bars for the uncertainty and ODE formulation for an irregular wave made using using Jonswap spectrum with a significant wave height $H_s = 15$ cm and peak period $T_p = 1.276$ sec.

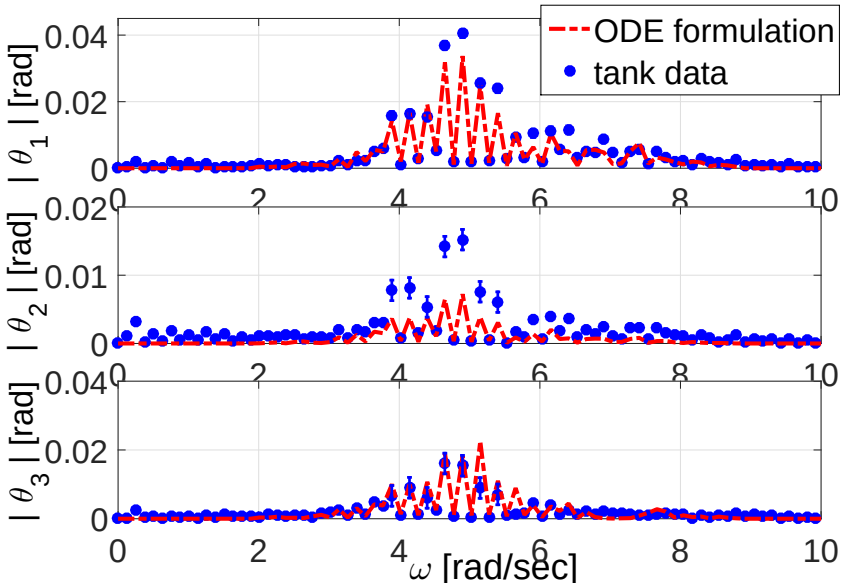

Figure 3.15: Frequency response of the pitch angles of body 1, 2 and 3 obtained from tank experiments with error bars for the uncertainty and ODE formulation for an irregular wave made using using Jonswap spectrum with a significant wave height $H_s = 15$ cm and peak period $T_p = 1.276$ sec.

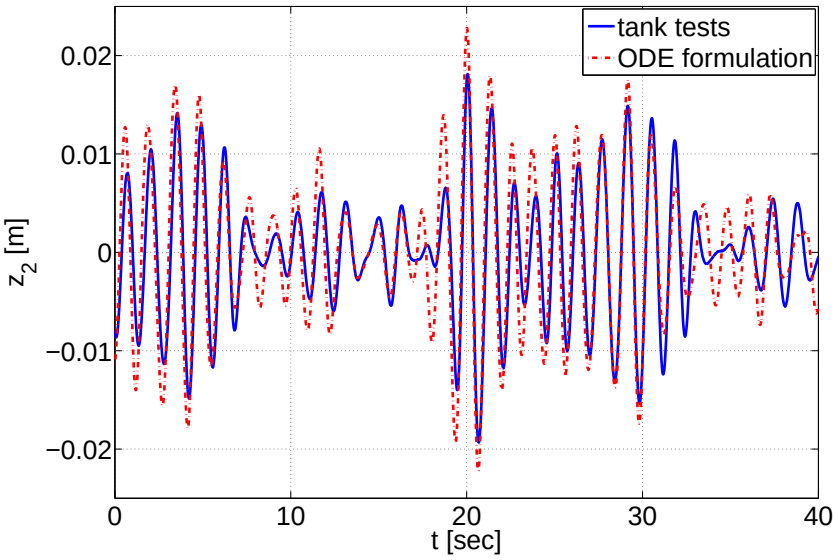

Figure 3.16: Time domain response of the heave of body 2 obtained from tank experiments and ODE formulation for an irregular wave made using using Jonswap spectrum with a significant wave height $H_s = 15$ cm and peak period $T_p = 1.276$ sec.

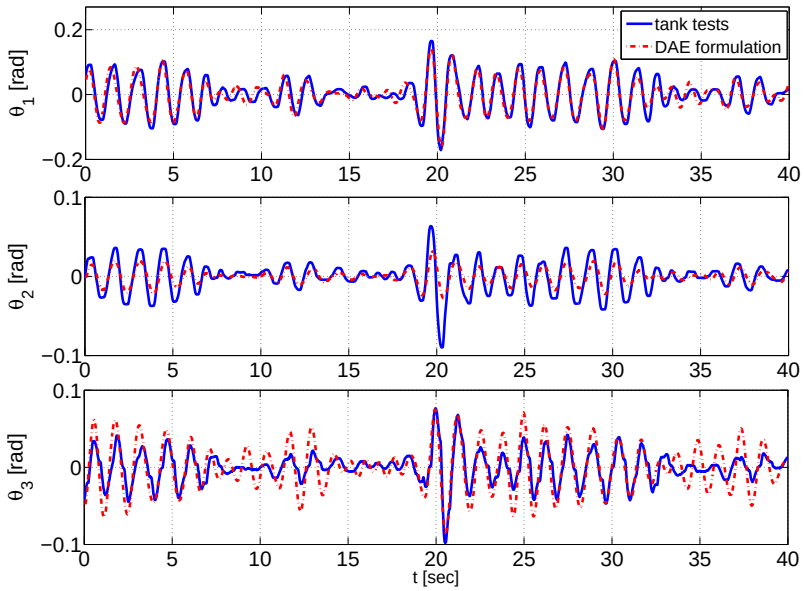

Figure 3.17: Time domain response of the pitch angles of body 1, 2 and 3 obtained from tank experiments and ODE formulation for an irregular wave made using using Jonswap spectrum with a significant wave height $H_s = 15$ cm and peak period $T_p = 1.276$ sec.

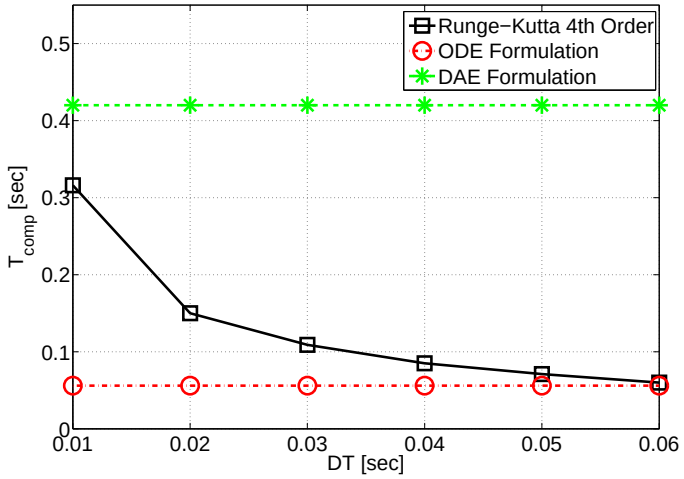

Figure 3.18: Computational time required by the Runge-Kutta method, DAE and ODE formulations computed for different time steps and simulation time equal to 20 seconds

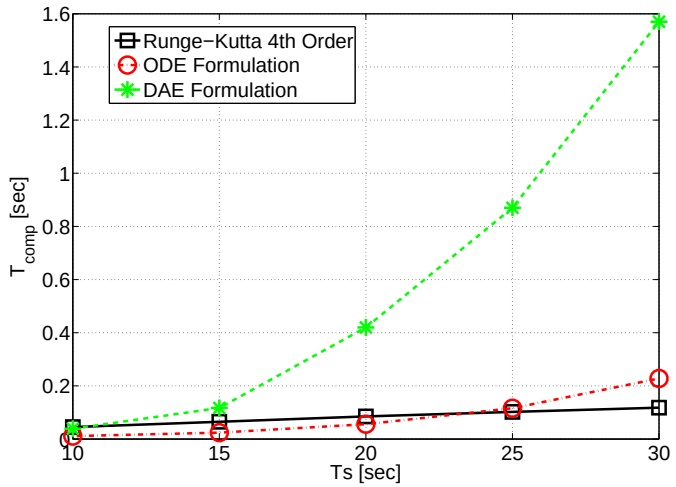

Figure 3.19: Computational time required by the Runge-Kutta method, DAE and ODE formulations computed for different simulation times and time step equal to 0.04 seconds

Chapter 4

Pseudo-spectral optimal control of a three-body hinge-barge device

In Section 3.5, a dynamic model for a three-body hinge-barge device is derived, which can be used to formulate the optimal control problem of the device. The optimal control problem consists in maximizing the energy extracted by the device for different wave conditions, considering the limitations on the achievable positions, velocities and PTO forces. In Section 2.4, an overview of optimal control strategies, for multibody hinge-barge WECs, is presented. The optimal control strategies developed for multibody hinge-barge WECs represent a subset of the broader set of control strategies applied to the wave energy conversion. In the remainder of this chapter, an overview of the control strategies adopted for wave energy applications is presented.

4.1 Literature review on optimal control of wave energy converters

One of the first control strategies developed for WECs is reactive control, or complex-conjugate (CC) control [10]. CC control is formulated in the frequency domain, and maximizes the energy extracted by a WEC under the assumptions of regular waves, linear dynamic model of the WEC and active PTO that can deliver power to the WEC, as well as absorbing power. A scheme for CC control applied to a single-DoF WEC is shown in Figure 4.1a. As shown in Figure 4.1a, CC control computes the following optimal control force $U_{opt}(\omega)$:

$$U_{opt}(\omega) = Z_{opt}(\omega)V(\omega) = Z^*(\omega)V(\omega) \tag{4.1}$$

where $Z^*(\omega)$ is the complex-conjugate of the WEC mechanical impedance $Z(\omega)$ and $V(\omega)$ is the Fourier transform of the velocity. As shown in equation 4.1, CC control defines the optimal profile of PTO force at the frequency of the incoming regular wave. However, real waves are not regular, but rather irregular, and are composed of multiple frequencies. Therefore, CC is difficult to implement under irregular waves. CC control is a non-causal control strategy, as the inverse Fourier transform of $Z^*(\omega)$ is non-causal and, therefore, the optimal control force $u_{opt}(t)$, in the

time domain, depends on future values of the velocity $v(t)$. Furthermore, with CC control, the motion of the WEC and PTO force undergoes large oscillations, as constraints on the motion and PTO forces cannot be incorporated into CC control. Another difficulty with CC is the use of active PTO, which are difficult to realize in practice [59].

Another optimal control strategy based on the same theory of CC control is the Phase and Amplitude (PA) control [10]. A scheme for PA control applied to a single-DoF WEC is shown in Figure 4.1b. As shown in Figure 4.1b, CC control computes the reference velocity $V_{opt}(\omega)$ as follows:

$$V_{opt}(\omega) = \frac{F_{ex}(\omega)}{2R(\omega)} \tag{4.2}$$

where $F_{ex}(\omega)$ is the Fourier transform of the excitation force and $R(\omega)$ is the sum of the radiation and viscous damping of the WEC. The condition on the optimal reference velocity $V_{PTO}(\omega)$ in equation (4.2) maximizes the energy extracted by the WEC, as in the case of CC control. The reference velocity $V_{opt}(\omega)$ is tracked by an inner control loop that computes the PTO force applied to the WEC. Therefore, with PA control, the velocity of the WEC is in phase with the excitation force, with amplitude $|V_{opt}(\omega)| = |F_{ex}(\omega)|/2R(\omega)$. Note that, the optimal velocity $V_{PTO}(\omega)$ computed in equation (4.2) is frequency dependent. Therefore, PA control is difficult to implement under irregular waves. Also, as for CC control, PA control is a non-causal control strategy, as the inverse Fourier transform of $1/2R(\omega)$ is non-causal and, therefore, the optimal velocity $v_{opt}(t)$ in the time domain depends on future values of the excitation force $f_{ex}(t)$. As for CC control, with PA control, the motion of the WEC and PTO force undergoes large oscillations. One of the first applications of reactive control applied to the Salter Duck is described in [60]. CC control is also applied to the Salter duck in [61]. In [62], an implementation of CC control applied to a semi-submerged sphere oscillating in heave is presented.

CC and PA control require the prediction of the future velocity of the WEC and excitation force, respectively, due to their non-causality nature. The WEC velocity or excitation force can be predicted using a wave probe at some distance ahead of the device, or using a mathematical model that extrapolates the future values of WEC velocity and excitation force based on their past history. In Chapter 6, a mathematical model is used to predict the excitation force acting on three-body hinge-barge device into the future based on its past history. Alternatively, the need of the prediction of the WEC velocity or excitation force can be eliminated with the use of a sub-optimal causal control. The main idea behind a sub-optimal causal control technique, is to approximate the ideal non-realizable transfer function associated with CC and PA control with a causal transfer function in the frequency range containing most of the wave energy. In [63], two causal approximations of the ideal non-causal controller are considered for a piston wave absorber. The performances of the two causal approximations are compared to the performances of a low-frequency asymptotic Sommerfeld relation. In [64], an approximation of the model of a single-body heaving WEC with a second order oscillator is considered, and the non-causal transfer function between the optimal velocity and the excitation force is approximated by a constant. In [65], [66] an optimal causal

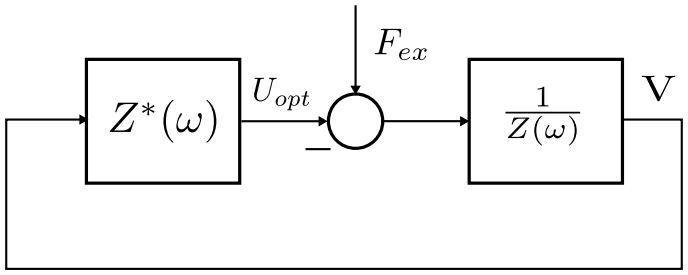

(a)

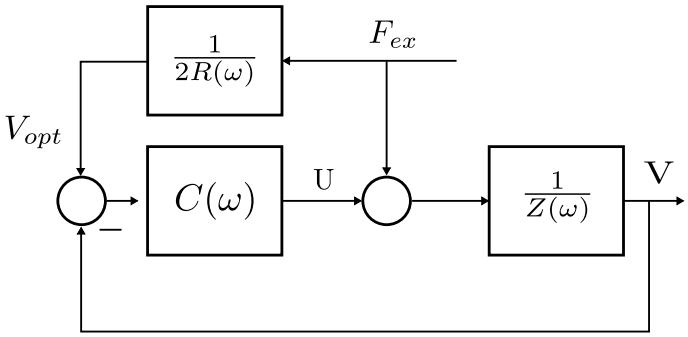

(b)

Figure 4.1: Scheme for Complex-Cojugate (CC) control (a) and Phase and Amplitude (PA) control.

control is applied to a WEC attached to 3 generators by tethers, with the device that can extract energy from the surge, heave, and rotation motions simultaneously. The optimal causal control relies on measurements of the generator velocities and spectral characteristics of the sea, and is found as a nonstandard Linear Quadratic Gaussian (LQG) controller. An optimal causal control that does not require predictions of the future velocities of the WEC is proposed in [67].

The requirement of PA control to use a PTO that can deliver power to the WEC can be obviated by using a discrete suboptimal controller termed latching [68], [69], [70] which aims to satisfy the condition on the optimal velocity given by equation (4.2). The latching control keeps the WEC velocity in phase with the excitation force by locking the device in a fixed position when the velocity reaches a zero value for a certain time interval. The latching of the WEC can be realized with a mechanical brake or the closure of a valve, in case of a hydraulic PTO. Although latching control does not involve an active PTO, the choice of the time during which the WEC is locked is the solution of an optimization problem which can be difficult to solve. Furthermore, for latching control, the prediction of the future excitation force is required. A counterpart to latching control is declutching control, which is presented in [71]. As opposed to latching control, declutching control consists of unloading the WEC during some parts of the power cycle and, therefore, the PTO force is set equal to zero [72]. A combination of latching and declutching control is presented in [73], where a considerable increase in the energy extracted by a WEC can be achieved with respect to the use of latching and declutching control independently. In general, for monochromatic sea and under the assumption of linearity of the model of the device, latching

and declutching control are optimal for a resonant frequency of the device greater and smaller than the wave period, respectively.

CC and PA control maximize the energy extracted by a WEC, without considering constraints on the maximum motion amplitudes achievable by the device. It is important that the motion of the device is restrained due to limits such as the maximum stroke of the PTO or mooring lines. In [74], a theoretical study on the maximum power absorption of a WEC under constraints on the velocity, and therefore on the position, is carried out in the frequency domain. In [75], a linear frequency domain model has been developed for a heaving point absorber, relatively moving with respect to a floating reference. Three different restrictions are considered in the maximization of the extracted power from the WEC: restriction on the probability of occurrence of slamming of the point absorber, restriction on the amplitude of the point absorber motion and restriction on the force applied by the PTO.

From the control strategies presented before, it is clear that a successful control strategy for a WEC has to maximize the extracted energy and handle constraints on the motions and the PTO force, based on the prediction of the excitation force. MPC represents a natural choice for the control of a WEC, since is formulated as an optimization problem based on a cost function which can be the energy extracted by a WEC, a mathematical model that can be used to predict the future response of the WEC, given initial conditions of the state variables and future excitation force, and constraints on the variables of interest. In [6], MPC is applied to the Archimedes Wave Swing, where the cost function to be maximized is the power absorbed by the PTO. A linear dynamic model is considered for the device, and constraints on position and velocity are considered. The excitation force is estimated from the motion of the device, and predicted by means of an auto-regressive (AR) model based on past values of the excitation force. In [76], the constrained optimal control of a heaving sphere is realized with a MPC, where constraints on the motion and on the PTO force are considered. A linear dynamic model is considered for the device, and the cost function to be maximized is made of the difference between the excitation power and lost power due to the radiation and viscous force, as opposed to the power absorbed by the PTO. The performances of the MPC applied to a heaving sphere are found to be close to the maximum power absorption under CC control. The wave excitation force is predicted by use of an augmented Kalman filter based on a damped harmonic oscillator model of the wave process. In [77], MPC is applied to a heaving point absorber, with constraints on position and velocity. A linear dynamic model is considered for the device, and no constraints on the PTO force are considered, in order avoid feasibility issues. The cost function to be maximized is the power absorbed by the PTO. In [78], a nonlinear MPC is applied to a model-scale point absorber, where a passive PTO with variable damping is considered. The nonlinearity of the control problem is due to the nature of the mathematical model used to describe the PTO, where the control force is given by the multiplication of the WEC velocity and variable damping. Constraints on the position and maximum value of the variable damping are considered. In [79], a nonlinear MPC is applied to two-body point-absorber, where a linear model for the hydrodynamic forces and a nonlinear model for the mooring forces are considered.

A valid alternative to MPC for the energy maximization of a WEC, with constraints on the motion of the device and PTO force, is the optimal control with PS methods, which are a subset of the class of techniques used for the discretisation of integral and partial differential equations known as mean weighted residuals [45], [46]. In [47], PS methods with Fourier basis function are applied for the optimal control of WECs, where only the steady-state solution to the optimal control problem is considered. In [80], a Receding Horizon Pseudo-Spectral Control (RHPSC), that also considers transient effects, is employed. In Chapter 5, the RHPSC is adopted for the real-time control of a three-body hinge-barge device. In [81], a nonlinear MPC using PS methods with Lagrangian polynomials applied to heaving point-absorber is considered. The major nonlinearity of the model of the device is due to the nonlinear buoyancy force. The differential flatness of the WEC model is exploited in order to reduce the computational burden required to the controller, where only one variable is parametrized with the chosen basis functions. In [58], a critical comparison between MPC and RHPSC control for wave energy devices is made. Results show that the relative computational burden for MPC is significantly greater than for RHPSC. Furthermore, MPC appears to be sensitive to the finite-order parametrization of the radiation force, with an high order of the approximation needed to correctly represent the radiation forces. In contrast to MPC, as shown in Section 3.3, PS control with Fourier basis functions provides an exact representation of the radiation forces, within the boundaries of the approximation of the variables of interest. Similarly to PS control with Fourier basis functions, in Section 5.3, it is demonstrated that RHPSC provides an exact representation of the radiation forces too. Also, in Chapter 3, it is proven that PS methods are a compact and numerically efficient formulation for solving the dynamics of a system.

The objective of this chapter is to asses the value of optimal control with PS methods based on Fourier basis functions applied to a three-body hinge-barge wave energy device. The optimal control is based on the model of the device, and it takes into account the hydrodynamic and kinematic interactions between the bodies. The PTO loads at the joints are controlled in a coordinated way, so that the total energy extracted by the device is maximized. Both passive and active controllers, which compute the optimal profile of velocities and control forces of the PTOs, are considered for both regular and irregular waves. PS methods are used to transform the optimal control problem of the hinge-barge device into a finite dimensional optimization problem which can be nonconvex for both passive and active control. In this chapter, only the steady-state solution to the optimal control problem is considered, and the transient response of the device is neglected. Therefore, the optimal control with PS methods based on Fourier basis functions cannot be applied for real-time control of the WEC, but provides an useful framework for the evaluation of the achievable power absorption under both active and passive control. In Chapter 5, RHPSC for real-time control of a three-body hinge-barge device is presented.

The remainder of this chapter is organized as follows: in Section 4.2, a reduced equivalent dynamic model of a three-body hinge-barge device for the control formulation is presented, while, in Section 4.3, PS control with Fourier basis functions is applied to a three-body hinge-barge device. In Section 4.4, the maximum theoretical power absorption of the device under reactive

control is presented, while, in Section 4.5, PS methods with Fourier basis functions are compared to a standard optimal controller for both monochromatic and polychromatic waves. In Section 4.6, considerations on the computational time required by PS methods with Fourier basis function to compute the active and passive control of the device are presented. Finally, overall conclusions are drawn in Section 4.7.

4.2 Reduced equivalent dynamic model of a three-body hinge-barge device for control formulation

In Section 3.5.2, a full dynamic model of a three-body hinge-barge device, described in terms of the motion of the DoF of the device, is presented. An equivalent reduced dynamic model, which is described only in terms of the relative pitch rotations between the barges, can be obtained [82], [83]. The equivalent reduced model is described in terms of the relative pitch rotations which are the modes that are used to extract energy from the device. Therefore, the equivalent reduced dynamic model is particularly suitable for formulating the optimal control problem, since it involves a smaller number of variables than the full dynamic model. However, with the equivalent reduced dynamic model, no information on the heave and pitch rotation of the central barge is provided. Thus, with the reduced equivalent model, no constraints on the heave and absolute pitch rotation of the central barge can be enforced, as the reduced equivalent model is described in terms of the relative pitch rotations only. Therefore, the equivalent reduced dynamic model represents a less comprehensive description of the motion of the device than the full dynamic model, but considerably reduces the computational effort required for the calculation of the controller.

The fully dynamic model, presented in Section 3.5.2, can be rewritten in terms of the vector of independent velocities as follows:

$$\mathbf{v}_s = [\dot{z}^b_{i,b_2}\ \dot{\theta}_2\ \dot{\theta}_{rel,1}\ \dot{\theta}_{rel,2}]^T \tag{4.3}$$

where z_2 is the heave displacement of body 2, θ_2 is the pitch angle of body 2, $\theta_{rel,1}$ and $\theta_{rel,2}$ are the relative pitch angles of bodies 1 and 3 with respect to body 2, respectively. As shown in Figure 3.8, the control forces are represented by PTO torques acting on the relative pitch motion between body 2 and bodies 1 and 3. The number of control forces is $n_c = 2$. The full dynamic model of the device in the frequency domain derived in Section 3.5.3.2 can be rewritten as follows:

$$\begin{aligned}(-\omega^2(\mathbf{M}_s + \mathbf{M}_{a,s}(\omega)) + j\omega(\mathbf{B}_{rad,s}(\omega) + \mathbf{B}_{visc,s}) + ..\\ \mathbf{G}_s)\hat{\mathbf{X}}_s(\omega) = \hat{\mathbf{F}}_{wave,s}(\omega) + \mathbf{F}_{p,s}\hat{\mathbf{U}}\end{aligned} \tag{4.4}$$

where $\hat{\mathbf{U}} \in \mathbb{R}^{n_c \times 1}$ is the Fourier transform of the control force vector, $\mathbf{F}_{p,s} \in \mathbb{R}^{n \times n_c}$ is the configuration matrix of the PTO and $\mathbf{F}_{wave,s}$ is the Fourier transform of the excitation force vector. The full dynamic model of the device in equation (4.4) can be rewritten, in the frequency domain, as follows:

$$(\mathbf{B} + j\omega\mathbf{C})\hat{\mathbf{V}} = \hat{\mathbf{F}}_{wave,s} + \mathbf{F}_{p,s}\hat{\mathbf{U}} \tag{4.5}$$

where:

$$\hat{\mathbf{V}} = \left[\dot{Z}^b_{i,b_2}\ \dot{\Theta}_2\ \dot{\Theta}_{rel,1}\ \dot{\Theta}_{rel,2}\right]^T \tag{4.6}$$

$$\mathbf{B} = \begin{bmatrix} \mathbf{B}_{11} & \mathbf{B}_{12} \\ \mathbf{B}_{21} & \mathbf{B}_{22} \end{bmatrix} \tag{4.7}$$

$$\mathbf{C} = \begin{bmatrix} \mathbf{C}_{11} & \mathbf{C}_{12} \\ \mathbf{C}_{21} & \mathbf{C}_{22} \end{bmatrix} \tag{4.8}$$

$$\hat{\mathbf{F}}_{wave,s} = \left[\hat{\mathbf{F}}_{wave,1}\ \hat{\mathbf{F}}_{wave,2}\right]^T \tag{4.9}$$

$$\mathbf{F}_{p,s} = \left[\mathbf{0}_2\ \mathbf{I}_2\right]^T \tag{4.10}$$

Note that, the dependency of the variables and matrices in equations (4.5)-(4.9) on ω is dropped in order to simplify the notation. Then, equation (4.5) can be written as a system of two matrix equations:

$$\begin{bmatrix} \dot{Z}^b_{i,b_2} \\ \dot{\Theta}_2 \end{bmatrix} = \mathbf{Z}_f^{-1}\left(\hat{\mathbf{F}}_{wave,1} - \mathbf{T}\begin{bmatrix} \dot{\Theta}_{rel,1} \\ \dot{\Theta}_{rel,2} \end{bmatrix}\right) \tag{4.11}$$

$$(\mathbf{B}_{22} + j\omega\mathbf{C}_{22})\begin{bmatrix} \dot{\Theta}_{rel,1} \\ \dot{\Theta}_{rel,2} \end{bmatrix} = \hat{\mathbf{F}}_{wave,2} + \hat{\mathbf{U}} - (\mathbf{B}_{21} + j\omega\mathbf{C}_{21})\begin{bmatrix} \dot{Z}^b_{i,b_2} \\ \dot{\Theta}_2 \end{bmatrix} \tag{4.12}$$

where $\mathbf{Z}_f = \mathbf{B}_{11} + j\omega\mathbf{C}_{11}$ and $\mathbf{T} = \mathbf{B}_{12} + j\omega\mathbf{C}_{12}$. Substituting equation (4.11) into equation (4.12) yields the following equivalent reduced model for the relative pitch rotations:

$$\mathbf{A}_{eq}\hat{\mathbf{V}}_{eq} = \hat{\mathbf{F}}_{eq} + \hat{\mathbf{U}} \tag{4.13}$$

where:

$$\hat{\mathbf{V}}_{eq} = \begin{bmatrix} \dot{\Theta}_{rel,1} \\ \dot{\Theta}_{rel,2} \end{bmatrix} \tag{4.14}$$

$$\mathbf{A}_{eq} = \mathbf{B}_{22} - \mathbf{B}_{21}\mathbf{Z}_f^{-1}\mathbf{T} + j\omega\left(\mathbf{C}_{22} - \mathbf{C}_{21}\mathbf{Z}_f^{-1}T\right) \tag{4.15}$$

$$\hat{\mathbf{F}}_{eq,wave} = \hat{\mathbf{F}}_{wave,2} - j\omega\mathbf{C}_{2,1}\mathbf{Z}_f^{-1}\hat{\mathbf{F}}_{wave,1} - \mathbf{B}_{2,1}\mathbf{Z}_f^{-1}\hat{\mathbf{F}}_{wave,1} \tag{4.16}$$

As shown in equation (4.13), the equivalent reduced model is described in terms of the relative

pitch rotations only. In order to express the dynamic model in equation (4.13) in the time domain, the equivalent added mass at infinity and inertia matrix are computed. If $\mathbf{A}_{eq}$ in Equation (4.14) is written as follows:

$$\mathbf{A}_{eq} = \mathbf{B}_{eq,rad} + \mathbf{B}_{eq,visc} + j\omega\left(\mathbf{M}_{eq,in} + \mathbf{M}_{eq,a} - \frac{\mathbf{G}_{eq}}{\omega^2}\right) \tag{4.17}$$

where $\mathbf{B}_{eq,rad}$ is the equivalent radiation damping matrix, $\mathbf{B}_{eq,visc}$ is the equivalent viscous damping matrix, $\mathbf{M}_{eq,in}$ is the equivalent inertia matrix, $\mathbf{M}_{eq,a}$ is the equivalent added mass matrix and $\mathbf{G}_{eq}$ is the equivalent stiffness matrix. Therefore, the equivalent added mass at infinite frequency and the inertia matrix are given as follows:

$$\lim_{\omega\to\infty} \frac{\Im\mathbf{A}_{eq}}{\omega} = \mathbf{M}_{eq,in} + \mathbf{M}_{eq,\inf} \tag{4.18}$$

where $\mathbf{M}_{eq,\inf}$ is the equivalent added mass at infinite frequency. The equivalent stiffness matrix is given as follows:

$$\lim_{\omega\to 0} \omega\Im\mathbf{A}_{eq} = -\mathbf{G}_{eq} \tag{4.19}$$

Finally, the equivalent reduced model, expressed in the time domain, is given as:

$$\dot{\mathbf{q}}_{eq} = \mathbf{v}_{eq} \tag{4.20}$$

$$\mathbf{M}_{eq,tot}\dot{\mathbf{v}}_{eq} + \mathbf{B}_{eq,visc}\mathbf{v}_{eq} + \mathbf{G}_{eq}\mathbf{q}_{eq} + .. \int_0^t \mathbf{K}_{eq,rad}(t-\tau)\mathbf{v}_{eq}, d\tau = \mathbf{f}_{eq,wave} + \mathbf{u} \tag{4.21}$$

where $\mathbf{q}_{eq} \in \mathbb{R}^{n_c\times 1}$ is the equivalent position vector, $\mathbf{v}_{eq} \in \mathbb{R}^{n_c\times 1}$ is the equivalent velocity vector, $\mathbf{u} \in \mathbb{R}^{n_c\times 1}$ is the control force vector, $\mathbf{M}_{eq,tot} = \mathbf{M}_{eq,in} + \mathbf{M}_{eq,\inf}$, $\mathbf{k}_{eq,rad}$ is the kernel function matrix of the equivalent radiation forces and $\mathbf{f}_{eq,wave}$ is the equivalent wave excitation force vector. Each element of the matrix $k_{eq,rad_{ii}}$ can be obtained from the corresponding element of the equivalent radiation damping matrix $B_{eq,rad_{ii}}$ as follows [10]:

$$\mathbf{k}_{eq,rad_{ii}} = \frac{2}{\pi}\int_0^\infty \mathbf{B}_{eq,rad_{ii}}(\omega)cos(\omega t)d\omega \tag{4.22}$$

with $ii = 1,2$.

4.3 Pseudo-spectral control with Fourier basis functions of a three-body hinge-barge device

This section describes the direct transcription of the optimal control problem in the time domain for a three-body hinge barge device [47]. For a three-body hinge-barge device, the vector of control variables is considered to be $\mathbf{u} = [\tau_1\ \tau_2]^T$, where τ_1 is the torque applied by the PTO connecting

body 2 and 1, while τ_2 is the torque applied by the PTO connecting body 2 and 3. In contrast to the PTOs considered in Section 3.5.1 and 3.5.2 , the torque applied by each PTO are not linearly dependent on the relative pitch velocity between the connected bodies.

The average power absorbed by the PTOs, over the time interval $[0,T]$, is given as:

$$J = \frac{1}{T}\int_0^T \mathbf{v}^T \mathbf{F}_p \mathbf{u} dt \tag{4.23}$$

where $\mathbf{v}$ is the vector of the velocities of the device, $\mathbf{u}$ is the control force vector and $\mathbf{F}_p$ is the configuration matrix. The configuration matrix $\mathbf{F}_p$ in equation (4.23) is used in order to combine, in different ways, the manipulated control forces [47]. Therefore, the configuration matrix $\mathbf{F}_p$ depends on the PTO structure used. The optimal control problem consists of computing the vector of PTO torques that maximize the cost function in equation (4.23), subject to the equations of motion (3.13)-(3.15), (3.32)-(3.33) and (4.20)-(4.21), for the DAE, ODE formulations and the equivalent reduced model, respectively. Additional constraints on the applied torques and relative pitch velocity between the bodies can be considered in the optimal control formulation.

For the discretization of the control problem, the control torques can be approximated with a linear combination of basis functions. Given the periodic nature of the variables associated with the problem, non-zero mean trigonometric polynomials (truncated Fourier series) represent a sensible choice for the control torques. Therefore, the pth component of the control torque vector can be approximated as follows:

$$\tau_p(t) \approx \tau_p^{N_x}(t) = \sum_{k=1}^{N_x} u_{p,k}^c cos(k\omega_0 t) + u_{p,k}^s sin(k\omega_0 t) = \mathbf{\Phi}(t)\hat{\mathbf{u}}_p \tag{4.24}$$

with $p = 1,2$. The vector of the coefficients $\hat{\mathbf{u}}_p$ is given as follows:

$$\hat{\mathbf{u}}_p = \left[u_{p,1}^c \; u_{p,1}^s \; .. \; u_{p,N_x}^c \; u_{p,N_x}^s\right]^T \tag{4.25}$$

where N_x is the order of expansion of the PS Fourier methods. In the remainder of this section, three different PS control frameworks are derived based on the formulation used to describe the dynamics of the device: DAE PS control, ODE PS control and reduced equivalent model PS control.

4.3.1 DAE Fourier PS control

For the DAE formulation, the configuration matrix $\mathbf{F}_p$ in equation (4.23) is given as:

$$\mathbf{F}_p = \begin{bmatrix} 0 & 0 \\ 1 & 0 \\ 0 & 0 \\ -1 & -1 \\ 0 & 0 \\ 0 & 1 \end{bmatrix} \tag{4.26}$$

By substituting the approximated velocities and control torques defined in equations (3.44) and (4.24), respectively, into equation (4.23), the cost function can be written as:

$$\begin{aligned} J^M &= \frac{1}{T}\int_0^T \mathbf{\Phi}(t)^T(\ \mathbf{X}^V\mathbf{F}_p\mathbf{U}^T)\ \mathbf{\Phi}(t)dt \\ &= \frac{1}{2}(\ \hat{\mathbf{u}}_1^T(\hat{\mathbf{x}}_2^v-\hat{\mathbf{x}}_4^v)+\hat{\mathbf{u}}_2^T(\hat{\mathbf{x}}_6^v-\hat{\mathbf{x}}_4^v)) \\ &= \frac{1}{4}\mathbf{x}^T\mathbf{H}_{DAE}\mathbf{x} \end{aligned} \tag{4.27}$$

where:

$$\mathbf{X}^V = [\ \hat{\mathbf{x}}_1^v,..,\hat{\mathbf{x}}_6^v] \tag{4.28}$$

$$\mathbf{U} = [\ \hat{\mathbf{u}}_1\ \ \hat{\mathbf{u}}_2] \tag{4.29}$$

$$\mathbf{x} = [\ \hat{\mathbf{x}}^{q,T}\ \hat{\mathbf{x}}^{v,T}\ \hat{\mathbf{u}}^T]^T \tag{4.30}$$

$$\mathbf{H}_{DAE} = \begin{bmatrix} \mathbf{0}_{6\times 2N_x,6\times 2N_x} & \mathbf{0}_{6\times 2N_x,6\times 2N_x} & \mathbf{0}_{6\times 2N_x,2\times 2N_x} \\ \mathbf{0}_{6\times 2N_x,6\times 2N_x} & \mathbf{0}_{6\times 2N_x,6\times 2N_x} & \mathbf{H}_1 \\ \mathbf{0}_{2\times 2N_x,6\times 2N_x} & \mathbf{H}_2 & \mathbf{0}_{2\times 2N_x,2\times 2N_x} \end{bmatrix} \tag{4.31}$$

$$\mathbf{H}_1 = \begin{bmatrix} \mathbf{0}_{2N_x,2N_x} & \mathbf{0}_{2N_x,2N_x} \\ \mathbf{I}_{2N_x,2N_x} & \mathbf{0}_{2N_x,2N_x} \\ \mathbf{0}_{2N_x,2N_x} & \mathbf{0}_{2N_x,2N_x} \\ -\mathbf{I}_{2N_x,2N_x} & -\mathbf{I}_{2N_x,2N_x} \\ \mathbf{0}_{2N_x,2N_x} & \mathbf{0}_{2N_x,2N_x} \\ \mathbf{0}_{2N_x,2N_x} & \mathbf{I}_{2N_x,2N_x} \end{bmatrix} \tag{4.32}$$

$$\mathbf{H}_2 = \mathbf{H}_1^T \tag{4.33}$$

Thus, for the DAE formulation, the optimal control problem defined by the maximization of the cost function (4.23), subject to the dynamic constraints (3.13)-(3.15) is transformed into a finite dimensional optimization problem with cost function (4.27), and dynamic constraints (3.65)-(3.67). Note that, the cost function in equation (4.27) is quadratic, but non-convex, due to the negative eigenvalues of the matrix $\mathbf{H}_{DAE}$. Therefore, with a non-convex quadratic cost function, a global optimal solution cannot be guaranteed. Additional inequality constraints, on the applied PTO torques and relative pitch velocity between the bodies, can also be considered in the optimization problems as:

$$\mathbf{g}(\hat{\mathbf{x}}_i^q,\hat{\mathbf{x}}_i^v,\hat{\mathbf{u}}_p) \leq 0 \tag{4.34}$$

with $i = 1,..,6$ and $p = 1,2$.

4.3.2 ODE Fourier PS control

For the ODE formulation, the configuration matrix $\mathbf{F}_p$ in equation (4.23) is given as:

$$\mathbf{F}_p = \begin{bmatrix} 0 & 0 \\ 0 & 0 \\ 1 & 0 \\ 0 & 1 \end{bmatrix} \tag{4.35}$$

Similar to the development presented in Section 4.3.1 for the DAE formulation, the cost function in equation (4.23), for the ODE case, can be written as:

$$\begin{aligned} J^M &= \frac{1}{2}(\hat{\mathbf{u}}_1^T \hat{\mathbf{x}}_3^v + \hat{\mathbf{u}}_2^T \hat{\mathbf{x}}_4^v) \\ &= \frac{1}{2}\mathbf{x}^T \mathbf{H}_{ODE} \mathbf{x} \end{aligned} \tag{4.36}$$

where:

$$\mathbf{X}^V = [\, \hat{\mathbf{x}}_1^v, .., \hat{\mathbf{x}}_4^v] \tag{4.37}$$

$$\mathbf{U} = [\, \hat{\mathbf{u}}_1 \;\; \hat{\mathbf{u}}_2] \tag{4.38}$$

$$\mathbf{x} = [\, \hat{\mathbf{x}}^{q,T} \;\; \hat{\mathbf{x}}^{v,T} \;\; \hat{\mathbf{u}}^T]^T \tag{4.39}$$

$$\mathbf{H}_{ODE} = \begin{bmatrix} \mathbf{0}_{4\times 2N_x,4\times 2N_x} & \mathbf{0}_{4\times 2N_x,4\times 2N_x} & \mathbf{0}_{4\times 2N_x,2\times 2N_x} \\ \mathbf{0}_{4\times 2N_x,4\times 2N_x} & \mathbf{0}_{4\times 2N_x,4\times 2N_x} & \mathbf{H}_1 \\ \mathbf{0}_{2\times 2N_x,4\times 2N_x} & \mathbf{H}_2 & \mathbf{0}_{2\times 2N_x,2\times 2N_x} \end{bmatrix} \tag{4.40}$$

$$\mathbf{H}_1 = \begin{bmatrix} \mathbf{0}_{2N_x,2N_x} & \mathbf{0}_{2N_x,2N_x} \\ \mathbf{0}_{2N_x,2N_x} & \mathbf{0}_{2N_x,2N_x} \\ \mathbf{I}_{2N_x,2N_x} & \mathbf{0}_{2N_x,2N_x} \\ \mathbf{0}_{2N_x,2N_x} & \mathbf{I}_{2N_x,2N_x} \end{bmatrix} \tag{4.41}$$

$$\mathbf{H}_2 = \mathbf{H}_1^T \tag{4.42}$$

Thus, for the ODE formulation, the optimal control problem defined by the maximization of the cost function (4.23), subject to the dynamic constraints (3.32)-(3.33) is transformed into a finite dimensional optimization problem with cost function (4.36), and dynamic constraints (3.68)-(3.69). As for the DAE formulation in Section 4.3.1, the cost function in equation (4.36) is quadratic, but non-convex, due to the negative eigenvalues of the matrix $\mathbf{H}_{ODE}$.

4.3.3 Reduced equivalent model Fourier PS control

For the reduced equivalent model, the configuration matrix $\mathbf{F}_p$ in equation (4.23) becomes:

$$\mathbf{F}_p = \begin{bmatrix} 1 & 0 \\ 0 & 1 \end{bmatrix} \tag{4.43}$$

Similar to the development presented in Section 4.3.1 for the DAE formulation, the cost function in equation (4.23), for the reduced model case, can be written as:

$$\begin{aligned} J^M &= \frac{1}{2}(\ \hat{\mathbf{u}}_1^T \hat{\mathbf{x}}_1^v + \hat{\mathbf{u}}_2^T \hat{\mathbf{x}}_2^v) \\ &= \frac{1}{2}\mathbf{x}^T \mathbf{H}_{Red} \mathbf{x} \end{aligned} \tag{4.44}$$

where:

$$\mathbf{X}^V = [\ \hat{\mathbf{x}}_1^v \ \ \hat{\mathbf{x}}_2^v] \tag{4.45}$$

$$\mathbf{U} = [\ \hat{\mathbf{u}}_1 \ \ \hat{\mathbf{u}}_2] \tag{4.46}$$

$$\mathbf{x} = [\ \hat{\mathbf{x}}^{q,T} \ \hat{\mathbf{x}}^{v,T} \ \hat{\mathbf{u}}^T]^T \tag{4.47}$$

$$\mathbf{H}_{Red} = \begin{bmatrix} \mathbf{0}_{2\times 2N_x,2\times 2N_x} & \mathbf{0}_{2\times 2N_x,2\times 2N_x} & \mathbf{0}_{2\times 2N_x,2\times 2N_x} \\ \mathbf{0}_{2\times 2N_x,2\times 2N_x} & \mathbf{0}_{2\times 2N_x,2\times 2N_x} & \mathbf{H}_1 \\ \mathbf{0}_{2\times 2N_x,2\times 2N_x} & \mathbf{H}_2 & \mathbf{0}_{2\times 2N_x,2\times 2N_x} \end{bmatrix} \tag{4.48}$$

$$\mathbf{H}_1 = \begin{bmatrix} \mathbf{I}_{2N_x,2N_x} & \mathbf{0}_{2N_x,2N_x} \\ \mathbf{0}_{2N_x,2N_x} & \mathbf{I}_{2N_x,2N_x} \end{bmatrix} \tag{4.49}$$

$$\mathbf{H}_2 = \mathbf{H}_1^T \tag{4.50}$$

Substituting the approximated states (3.43), (3.44) and their time derivatives (3.48), (3.49) into the equations of motion (4.20)-(4.21), yields the following equations of motion in residual form:

$$r_i^q(t) = \mathbf{\Phi}(t)\mathbf{D}_\phi \hat{\mathbf{x}}_i^q - \mathbf{\Phi}(t)\hat{\mathbf{x}}_i^v \tag{4.51}$$

$$\begin{aligned} r_i^v(t) = &\sum_{p=1}^{n_c} B_{eq,visc_{i,p}} \mathbf{\Phi}(t)\hat{\mathbf{x}}_p^v \ + \sum_{p=1}^{n_c} G_{eq_{i,p}} \mathbf{\Phi}(t)\hat{\mathbf{x}}_p^q + \sum_{p=1}^{n_c} \mathbf{\Phi}(t)\mathbf{G}_{eq,rad_{i,p}}\hat{\mathbf{x}}_p^v \\ &- f_{eq,wave_i}(t) - \sum_{p=1}^{n_c} F_{p_{i,p}} u_p(t) \end{aligned} \tag{4.52}$$

where $i = 1,..,n_c$, and $B_{eq,visc_{i,p}}$, $G_{eq_{i,p}}$, $K_{eq,rad_{i,p}}$ and $F_{p_{i,p}}$ are the elements of the matrix $\mathbf{B}_{eq,visc}$, $\mathbf{G}_{eq}$, $\mathbf{K}_{eq,rad}$ and $\mathbf{F}_p$, respectively. Thus, for the reduced equivalent model, the optimal control problem defined by the maximization of the cost function (4.23), subject to the dynamic constraints (4.20)-(4.21) is transformed into a finite dimensional optimization problem with cost function (4.44), and dynamic constraints (4.51)-(4.52). As for the DAE formulation in Section 4.3.1, the cost function in equation (4.44) is quadratic, but non-convex, due to the negative eigenvalues of the matrix $\mathbf{H}_{Red}$. In Section 4.3.3.1, a finite dimensional optimization problem with convex quadratic cost function based on the reduced equivalent model is proposed.

4.3.3.1 Convex cost function

On average, the power given by the excitation force is dissipated by the PTOs, radiated waves and viscous forces due to the motion of the device in the water [10]. Therefore, the maximization of the cost function (4.23) is equivalent to the maximization of the difference between the excitation force power and the dissipated power due to the radiated waves and viscous forces [76].

Thus, the cost function in (4.23) can be rewritten as:

$$\begin{aligned} J &= \frac{1}{T}\int_0^T \left(\mathbf{v}_{eq}^T \mathbf{f}_{eq,wave} - \mathbf{v}_{eq}^T \mathbf{B}_{eq,visc} \mathbf{v}_{eq} - \mathbf{v}_{eq}^T \left(\int_{-\infty}^{t} \mathbf{k}_{eq,rad}(t-\tau)\mathbf{v}_{eq} d\tau \right) \right) dt \\ &= \frac{1}{T}\int_0^T \left(\mathbf{\Phi}(t)^T \mathbf{X}^V \mathbf{X}^{ex,T} \mathbf{\Phi}(t) - \mathbf{\Phi}(t)^T \mathbf{X}^V \mathbf{B}_{eq,visc} \mathbf{X}^{V,T} \mathbf{\Phi}(t) - \mathbf{\Phi}(t)^T \mathbf{X}^V \mathbf{X}^{rad,T} \mathbf{\Phi}(t) \right) d\tau \\ &= \frac{1}{2}\mathbf{x}^{ex,T}\mathbf{x} - \frac{1}{2}\mathbf{x}^T \tilde{\mathbf{H}}_{Red} \mathbf{x} \end{aligned} \tag{4.53}$$

where:

$$\mathbf{X}^V = [\, \hat{\mathbf{x}}_1^v \; \hat{\mathbf{x}}_2^v] \tag{4.54}$$

$$\mathbf{X}^{ex} = [\, \hat{\mathbf{x}}_1^{ex} \; \hat{\mathbf{x}}_2^{ex}] \tag{4.55}$$

$$\mathbf{x}^{ex} = [\, \mathbf{0}_{1,2\times 2N_x} \; \hat{\mathbf{x}}^{ex,T} \; \mathbf{0}_{1,2\times 2N_x}]^T \tag{4.56}$$

$$\mathbf{X}^{rad} = [\, \hat{\mathbf{x}}_1^{rad} \; \hat{\mathbf{x}}_2^{rad}] \tag{4.57}$$

$$\hat{\mathbf{x}}^{rad} = \mathbf{G}_{eq,rad} \hat{\mathbf{x}}^v \tag{4.58}$$

$$\tilde{\mathbf{H}}_{Red} = \begin{bmatrix} \mathbf{0}_{2\times 2N_x,2\times 2N_x} & \mathbf{0}_{2\times 2N_x,2\times 2N_x} & \mathbf{0}_{2\times 2N_x,2\times 2N_x} \\ \mathbf{0}_{2\times 2N_x,2\times 2N_x} & \mathbf{G}_{rad} + \mathbf{D}_{visc} & \mathbf{0}_{2\times 2N_x,2\times 2N_x} \\ \mathbf{0}_{2\times 2N_x,2\times 2N_x} & \mathbf{0}_{2\times 2N_x,2\times 2N_x} & \mathbf{0}_{2\times 2N_x,2\times 2N_x} \end{bmatrix} \tag{4.59}$$

$$\mathbf{D}_{visc} = \begin{bmatrix} B_{eq,visc_{1,1}} \mathbf{I}_{2N_x} & B_{eq,visc_{1,2}} \mathbf{I}_{2N_x} \\ B_{eq,visc_{2,1}} \mathbf{I}_{2N_x} & B_{eq,visc_{2,2}} \mathbf{I}_{2N_x} \end{bmatrix} \tag{4.60}$$

where $\hat{\mathbf{x}}_i^{rad}$ are the PS coefficients of the ith component of radiation force vector. In contrast to the cost function (4.44), the cost function (4.53) is quadratic and convex. The cost function (4.53) is convex since all the eigenvalues of the matrix $\tilde{\mathbf{H}}_{Red}$ are positive. Therefore, the solution to the optimization of cost function (4.53), subject to the dynamic constraints (4.51)-(4.52), is unique and globally optimal.

4.4 Maximum theoretical average power for a three-body hinge-barge device

In [10], a theory for the calculation of the maximum power absorption of a generic multibody WEC is presented. The theory is formulated in the frequency domain, and it computes the optimal

trajectory of the velocities of the bodies and PTO forces under the assumption of reactive control, with no constraints on the amplitude of displacements, velocities and PTO forces. Reactive control requires a PTO that can deliver power from the grid to the device, as well as absorbing power from the device.

Given the reduced equivalent model in the frequency domain in equation (4.13), the instantaneous power absorbed by the PTOs is given as follows:

$$p_u(t) = \mathbf{u}(t)^T \mathbf{v}_{eq}(t) \tag{4.61}$$

$$= \frac{1}{4}(\hat{\mathbf{U}} e^{j\omega t} + \hat{\mathbf{U}}^* e^{-j\omega t})^T (\hat{\mathbf{V}}_{eq} e^{j\omega t} + \hat{\mathbf{V}}^*_{eq} e^{-j\omega t}) \tag{4.62}$$

$$= \frac{1}{4}(\hat{\mathbf{U}}^T \hat{\mathbf{V}}^*_{eq} + \hat{\mathbf{U}}^{*,T} \hat{\mathbf{V}}_{eq} + \mathbf{U}^T \hat{\mathbf{V}}_{eq} e^{j2\omega t} + \hat{\mathbf{U}}^{*,T} \hat{\mathbf{V}}^*_{eq} e^{-j2\omega t}) \tag{4.63}$$

where the symbol * represents the complex conjugate operator. The average absorbed power is obtained by taking the time average of the power in equation (4.63):

$$P_u = \overline{p}_u(t) = \frac{1}{4}(\mathbf{U}^T \hat{\mathbf{V}}^*_{eq} + \mathbf{U}^{*,T} \hat{\mathbf{V}}_{eq}) \tag{4.64}$$

$$= \frac{1}{2} \Re(\mathbf{U}^{*,T} \hat{\mathbf{V}}_{eq}) \tag{4.65}$$

The last two terms in equation (4.63) are neglected, since their time average is zero. The total fluid forces acting on the device, in the frequency domain, are given as follows:

$$\hat{\mathbf{F}}_f = \hat{\mathbf{F}}_{eq,wave} - \mathbf{B}_{eq,rad} \hat{\mathbf{V}}_{eq} - \mathbf{B}_{eq,visc} \hat{\mathbf{V}}_{eq} - j\omega \left(\mathbf{M}_{eq,in} + \mathbf{M}_{eq,a} - \frac{\mathbf{G}_{eq}}{\omega^2} \right) \hat{\mathbf{V}}_{eq} \tag{4.66}$$

The instantaneous power due to the fluid forces acting on the device is given as follows:

$$p_f(t) = \mathbf{f}_f(t)^T \mathbf{v}_{eq}(t) \tag{4.67}$$

$$= \frac{1}{4}(\hat{\mathbf{F}}^T_f \hat{\mathbf{V}}^*_{eq} + \hat{\mathbf{F}}^{*,T}_f \hat{\mathbf{V}}_{eq} + \hat{\mathbf{F}}^T_f \hat{\mathbf{V}}_{eq} e^{j2\omega t} + \hat{\mathbf{F}}^{*,T}_f \hat{\mathbf{V}}^*_{eq} e^{-j2\omega t}) \tag{4.68}$$

The average absorbed power is obtained by taking the time average of the power in equation (4.68):

$$P_f = \overline{p}_f(t) = \frac{1}{2} \Re(\hat{\mathbf{F}}^{*,T}_f \hat{\mathbf{V}}_{eq}) \tag{4.69}$$

$$= \frac{1}{2} \Re(\hat{\mathbf{F}}^{*,T}_{eq,wave} \hat{\mathbf{V}}_{eq}) - \frac{1}{2} \Re(\hat{\mathbf{V}}^{*,T}_{eq} (\mathbf{B}_{eq,rad} + \mathbf{B}_{eq,visc}) \hat{\mathbf{V}}_{eq}) \tag{4.70}$$

$$= P_{ex} - P_{loss} \tag{4.71}$$

where P_{ex} is the average excitation power due to the action of the waves and P_{loss} is the average lost power due to the motion of the device. On average, the absorbed power by the PTO is equal to the difference between the excitation power and the lost power:

$$P_u = P_{ex} - P_{loss} \tag{4.72}$$

If the matrix $\mathbf{B}_{eq,rad} + \mathbf{B}_{eq,visc}$ is non-singular, the maximum theoretical average power that can be absorbed by the device is [10]:

$$P_{u,max} = \frac{1}{8}(\hat{\mathbf{F}}^{*,T}_{eq,wave}(\mathbf{B}_{eq,rad} + \mathbf{B}_{eq,visc}) ^{-1}\hat{\mathbf{F}}_{eq,wave}) \tag{4.73}$$

The optimal velocity vector, which gives the maximum average power, is given as follows:

$$\hat{\mathbf{V}}_{eq,opt} = \frac{1}{2}(\mathbf{B}_{eq,rad} + \mathbf{B}_{eq,visc}) ^{-1}\hat{\mathbf{F}}_{eq,wave} \tag{4.74}$$

Given the frequency domain model in equation (4.13), the optimal PTO force vector is given as follows:

$$\hat{\mathbf{U}}_{opt} = \frac{1}{2} j\omega \left(\mathbf{M}_{eq,in} + \mathbf{M}_{eq,a} - \frac{\mathbf{G}_{eq}}{\omega^2} \right) (\mathbf{B}_{eq,rad} + \mathbf{B}_{eq,visc}) ^{-1}\hat{\mathbf{F}}_{eq,wave} - \frac{1}{2}\hat{\mathbf{F}}_{eq,wave} \tag{4.75}$$

In Figure 4.2, the maximum average theoretical power for a $1/25th$ scale three-body hinge-barge device is shown for regular waves of frequency $2 \leq \omega \leq 8$ rad/s and amplitude of 0.02 m. In Figure 4.3, the magnitudes of the optimal relative pitch angles, relative pitch angles velocities and PTO torques are shown for regular waves of frequency $2 \leq \omega \leq 8$ rad/s and amplitude of 0.02 m.

4.5 Results

In this section, the performances of PS optimal control with Fourier basis functions applied to a $1/25th$ scale three-body hinge-barge device, are compared to a standard control strategy based on optimal linear damping. The comparison between PS optimal control and the optimal linear damping strategy is carried out for both monochromatic and polychromatic waves. In order to get more meaningful results of PS optimal control applied to a $1/25th$ scale three-body hinge-barge device, the dynamic model tuned in subsection 3.5.3.2 is used for the formulation of the optimal control. In Figure 4.2, the dynamic model identified in subsection 3.5.3.2 shows a good agreement with the tank data in terms of average absorbed power.

4.5.1 Monochromatic wave results

In this section, PS control applied to a $1/25th$ scale three-body hinge-barge device is compared to standard control strategy based on optimal linear damping for regular waves.

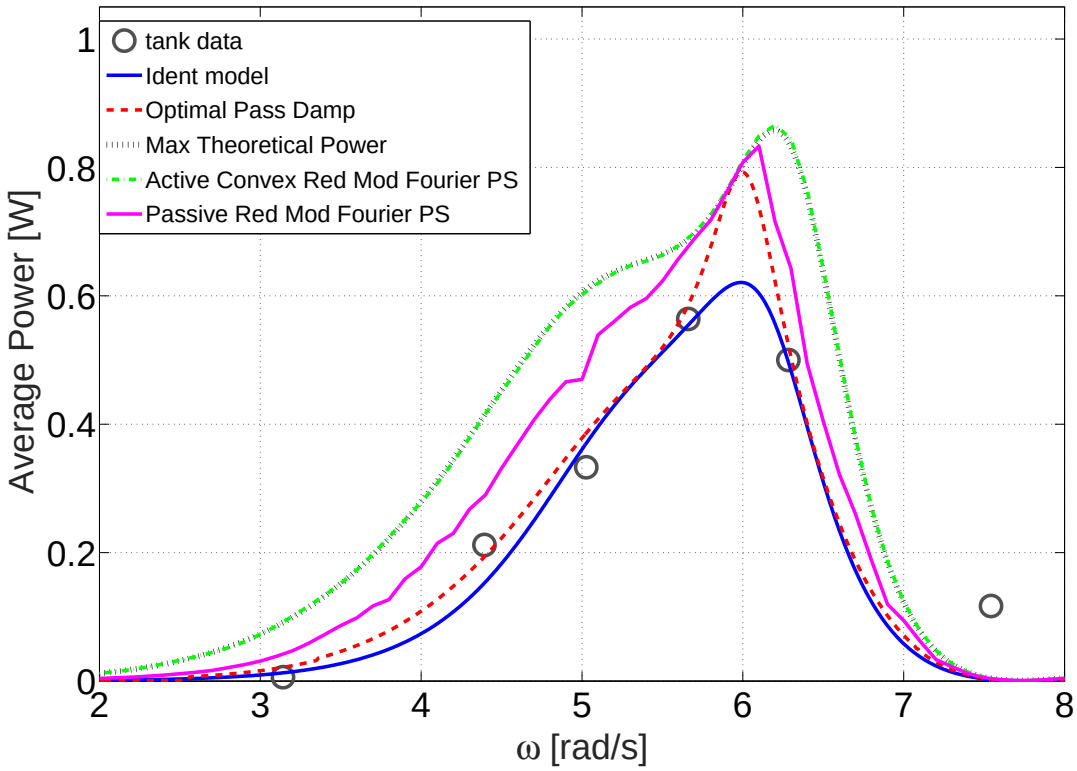

Figure 4.2: Comparison between the average power given by the tank data, identified model, max theoretical power, optimal linear damping control, convex active reduced model PS control and non-convex passive reduced model PS control of a $1/25th$ scale three-body hinge-barge device for different frequencies of a regular wave of amplitude A = 2 cm.

4.5.1.1 Optimal linear passive dampers

An alternative strategy to PS methods is to consider a linear model of the WEC in the frequency domain, and compute the optimal linear damping coefficients of the PTOs that maximize the energy absorption for each incoming wave frequency [10]. The average power absorbed by linear passive PTOs is given as follows:

$$P_u = \frac{1}{2}\Re(\ \hat{\mathbf{V}}_s^{*,T}\mathbf{K}_{pto}\hat{\mathbf{V}}_s) \tag{4.76}$$

where the matrix $\mathbf{K}_{pto,s}$ is given as follows:

$$\mathbf{K}_{pto} = \begin{bmatrix} 0 & 0 & 0 & 0 \\ 0 & 0 & 0 & 0 \\ 0 & 0 & a^2 c_{pto,1} & 0 \\ 0 & 0 & 0 & a^2 c_{pto,2} \end{bmatrix} \tag{4.77}$$

with the coefficients of the PTOs, $c_{pto,1}$ and $c_{pto,2}$, that satisfy the following conditions:

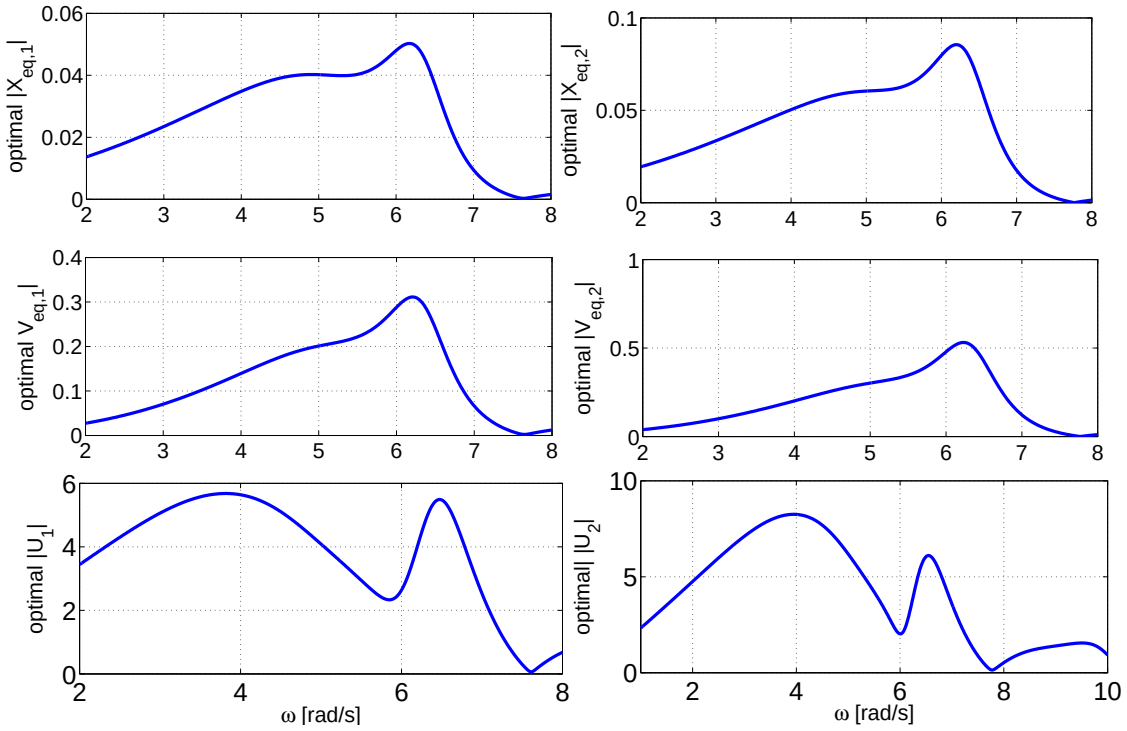

Figure 4.3: Magnitudes of the optimal relative pitch angles, relative pitch angles velocities and PTO torques of a $1/25th$ scale three-body hinge-barge device for different frequencies of a regular wave of amplitude A = 2 cm.

$$c_{pto,1} \geq 0 \tag{4.78}$$

$$c_{pto,2} \geq 0 \tag{4.79}$$

Therefore, the optimal linear passive dampers are obtained by maximization of the cost function (4.76) subject to the frequency domain model expressed in equation (4.4) and the passivity condition on the PTO coefficients (4.78)-(4.79).

In Figure 4.2, the average power given by the dynamic model with optimal linear damping coefficients for the PTOs is shown. As shown in Figure 4.2, the strategy with optimal passive dampers provides a small increase of the absorbed power with respect to the particular coefficients of the PTOs deployed during the tank tests. However, at the resonant frequency of the device, the optimal passive dampers greatly improve the power absorption, with an average power equal to the maximum theoretical power. At resonance, no reactive power is expected to be delivered by the PTOs [10].

4.5.1.2 Active PS control

An active controller is computed with PS methods, where the flow of power is considered to be bi-directional, so that power from the grid can be injected into the device. The active controller

is based on the reduced equivalent model with a convex cost function (4.53). In Figure 4.2, the average absorbed power with an active controller is shown. The order of expansion N_x for the positions, velocities and control torques is set equal to 1, according to the monochromatic wave conditions.

As shown in Figure 4.2, the average power computed with the active controller reaches the maximum theoretical power that can be absorbed by the device given by equation (4.73). Note that, for the active controller, the average powers, computed with the DAE formulation, ODE formulation, convex and non-convex reduced equivalent model, are identical. In fact, if the dynamic model of the device is linear and the incoming wave is monochromatic, the solution to the active control problem is unique [10].

While active control with the convex reduced equivalent model is computed analytically, an active-set algorithm [84] is used for the computation of the PS active control with the DAE formulation, ODE formulation and non-convex reduced equivalent model. By a way of example, in Figures 4.4 and 4.6, the optimal torques and relative pitch velocities computed by the active controller are shown for a regular wave of amplitude A=0.02 m and frequencies $\omega = 3$ rad/s and $\omega = 6.5$ rad/s, respectively. In Figures 4.5 and 4.7, the instantaneous and average absorbed power computed by the active controller are shown for a regular wave of amplitude A=0.02 m and frequencies $\omega = 3$ rad/s and $\omega = 6.5$ rad/s, respectively.

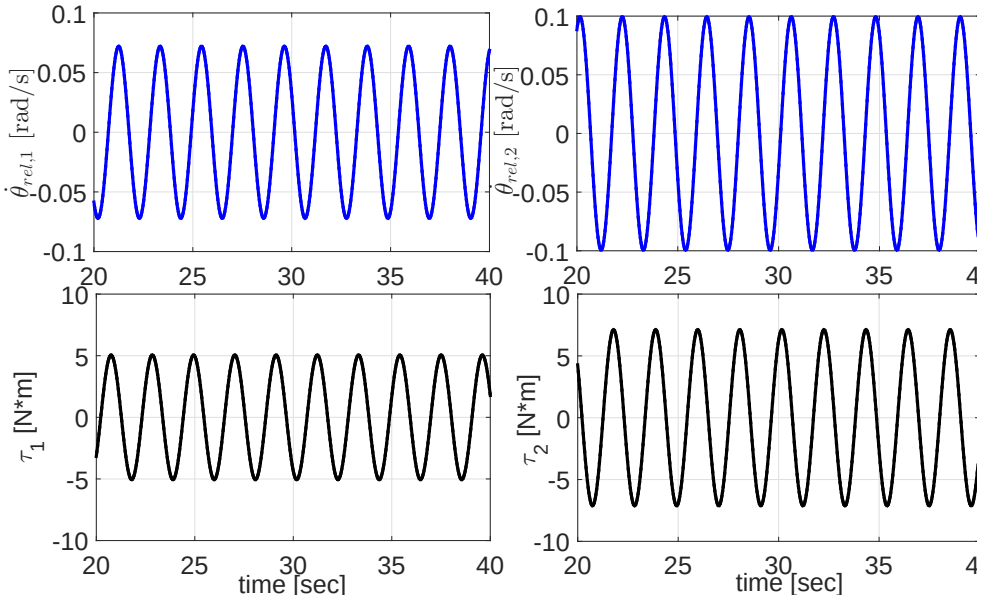

Figure 4.4: Optimal relative pitch angle velocities and PTO torques computed by active controller for regular wave of frequency $\omega = 3$ rad/s and amplitude A = 2 cm.

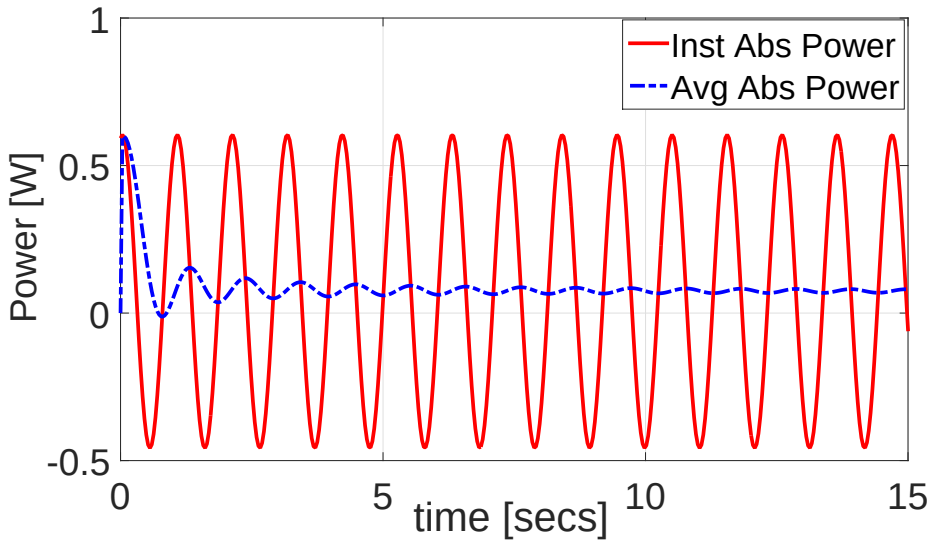

Figure 4.5: Instantaneous and average absorbed power computed by active controller for regular wave of frequency $\omega = 3$ rad/s and amplitude A = 2 cm.

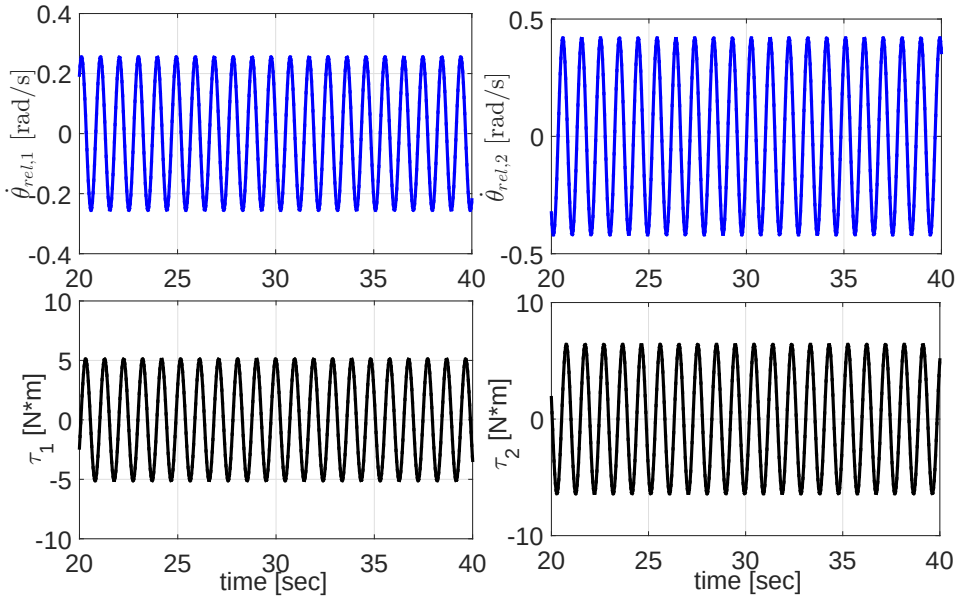

Figure 4.6: Optimal relative pitch angle velocities and PTO torques computed by active controller for regular wave of frequency $\omega = 6.5$ rad/s and amplitude A = 2 cm.

4.5.1.3 Passive PS control

Next, a passive controller (i.e. only positive power flow *from* the device) is computed with PS methods. While the torques applied by the PTOs, for a strategy based on optimal passive dampers presented in subsection 4.5.1.1, are linearly dependent on the relative pitch velocities between the bodies, the PTO torques computed by PS passive control are not linearly dependent of the relative pitch velocity between the bodies. While the computational time required by the passive controller based on the reduced equivalent model with a convex cost function (4.53) is of the order

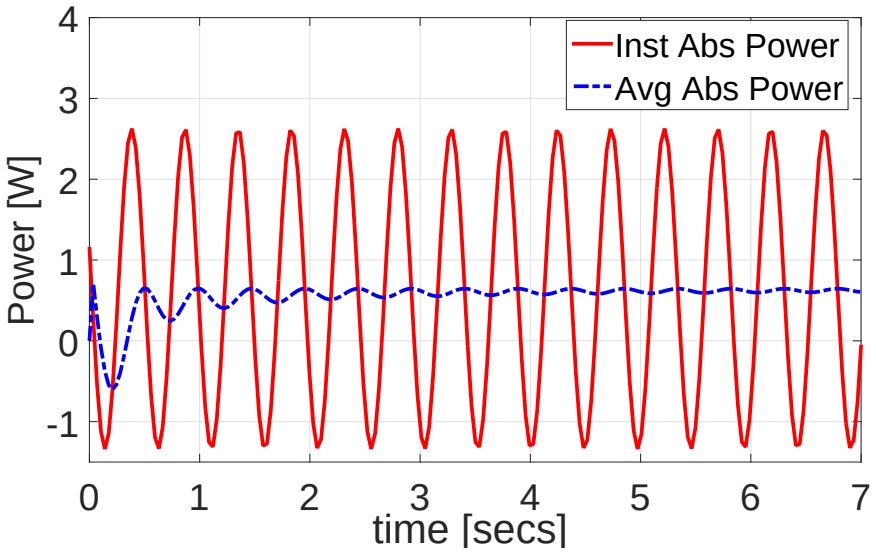

Figure 4.7: Instantaneous and average absorbed power computed by active controller for regular wave of frequency $\omega = 6.5$ rad/s and amplitude A = 2 cm.

of seconds, the computational time required to compute the passive control with DAE and ODE formulation is of the order of minutes, with no benefits in terms of absorbed power with respect to the passive controller based on the reduced equivalent model. Therefore, the passive controller is based on the reduced equivalent model, given its computational advantages with respect to the DAE and ODE formulations.

The passive control satisfies the passivity condition expressed by the following constraints on the instantaneous absorbed power from the PTOs:

$$\hat{\mathbf{x}}_1^{v,T} \mathbf{Q}_{PTO_{t_p}} \hat{\mathbf{u}}_1^T \geq 0 \tag{4.80}$$

$$\hat{\mathbf{x}}_2^{v,T} \mathbf{Q}_{PTO_{t_p}} \hat{\mathbf{u}}_2^T \geq 0 \tag{4.81}$$

with $t_p = 1,..,n_p$, where n_p is the number of time instants where the passivity condition is satisfied. The number of time instants n_p is generally greater than the number of collocation points where the dynamics of the device is satisfied. The matrix $\mathbf{Q}_{PTO_{t_p}}$ is given as:

$$\mathbf{Q}_{PTO_{t_p}} = \mathbf{\Phi}(t_p)\mathbf{\Phi}(t_p)^T \tag{4.82}$$

The quadratic forms in equation (4.80)-(4.81) are non-convex and, therefore, the optimal passive control problem can be considered as a nonconvex quadratically constrained quadratic program [85]. Therefore, a globally optimal solution cannot be guaranteed for the passive controller. In Figure 4.2, the average absorbed power with a passive controller is shown. The choice of the order of expansion N_x for the positions, velocities and control torques plays an important role in the maximization of the absorbed power with the passive controller. In Figure 4.8, the absorbed power and the computational time of the passive controller is shown for different values of N_x for a

regular wave of frequency $\omega = 6$ rad/s and amplitude A = 2 cm. An order $N_x = 3$ is chosen for the passive controller, as provides a trade-off between the computational time and the maximization of the absorbed power. An interior-point algorithm [86] is used to compute the PS passive control, since the computational time required with an active-set algorithm and an interior-point algorithm is of the order of minutes and seconds, respectively.

As shown in Figure 4.2, the average power with the passive controller is greater than the average power obtained with a strategy based on optimal passive dampers. In fact, while the torques applied by the PTOs with optimal passive dampers are linearly proportional to the relative pitch velocities, no explicit dependency is involved between the PTO's torques and relative pitch velocities for the passive controller. Therefore, the passive controller is less constrained than a strategy based on optimal passive dampers in the computation of the torques applied by the PTOs and, therefore, the passive control can achieve a greater average absorbed power than the power absorbed with optimal passive dampers. As a way of example, in Figure 4.9 and 4.11, the optimal torques and relative pitch velocities computed by the passive controller are shown for a regular wave of amplitude A=0.02 m and frequency $\omega = 3$ rad/s and $\omega = 6.5$ rad/s, respectively. In Figure 4.10 and 4.12, the instantaneous and average absorbed power computed by the passive controller are shown for a regular wave of amplitude A=0.02 m and frequency $\omega = 3$ rad/s and $\omega = 6.5$ rad/s, respectively.

In Figure 4.13, the Peak to Average Power Ratio (PAPR) given by an active and passive controller are compared. As shown in Figure 4.13, the passive controller shows a PAPR which is approximately constant and significantly lower than the PAPR given the active controller across the range of frequencies of the regular wave. Therefore, the passive controller applied to a 1/25th scale three-body hinge-barge device requires a significantly lower power electronics rating than the power electronics rating required by an active controller [87].

4.5.2 Polychromatic wave results

For polychromatic waves, the maximum theoretical average power that can be absorbed by the device under reactive control is given as follows:

$$P_{poly,max} = \sum_{k=1}^{n_f} P_{u,max}(\omega_k)|_{\eta=1} |\hat{\eta}(\omega_k)|^2 \tag{4.83}$$

where $P_{u,max}(\omega_k)|_{\eta=1}$ is the maximum theoretical power for a regular wave of amplitude A=1 m at the frequency ω_k rad/s and $|\hat{\eta}(\omega_k)|$ is the magnitude of the spectrum of the incoming wave at the frequency ω_k.

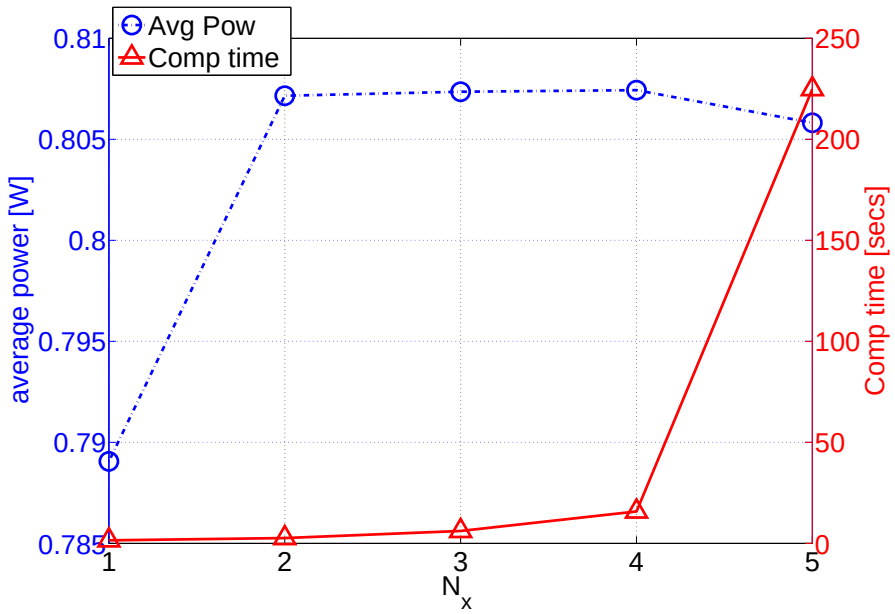

Figure 4.8: Absorbed power and computational time of the passive control for different values of N_x for a regular wave of frequency $\omega = 6$ rad/s and amplitude A = 2 cm.

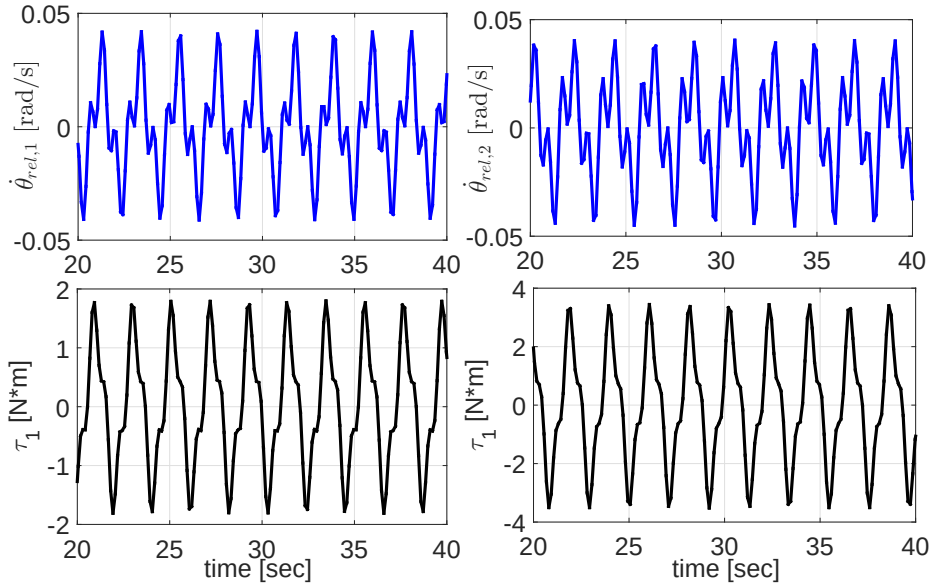

Figure 4.9: Optimal relative pitch angle velocities and PTO torques computed by passive controller for regular wave of frequency $\omega = 3$ rad/s and amplitude A = 2 cm.

4.5.2.1 Active PS control

In Figure 4.14, a comparison between the maximum theoretical power and the average power absorbed with the optimal linear damping control and PS active control is shown for a polychromatic wave over a time horizon of $T_{horiz} = 30$ s. The polychromatic wave is made with a JONSWAP spectrum with a significant wave height H_s = 15 cm and peak period T_p = 1.276 s. The PS active

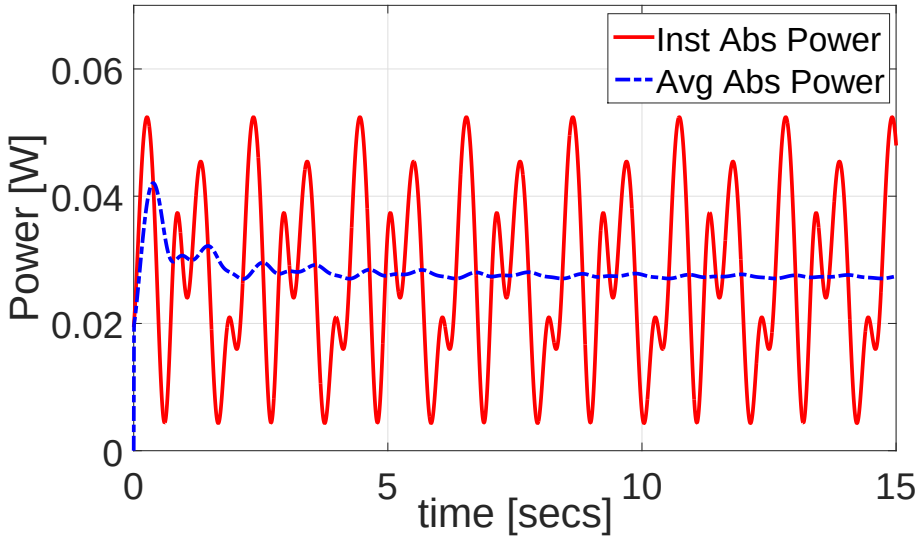

Figure 4.10: Instantaneous and average absorbed power computed by passive controller for regular wave of frequency $\omega = 3$ rad/s and amplitude A = 2 cm.

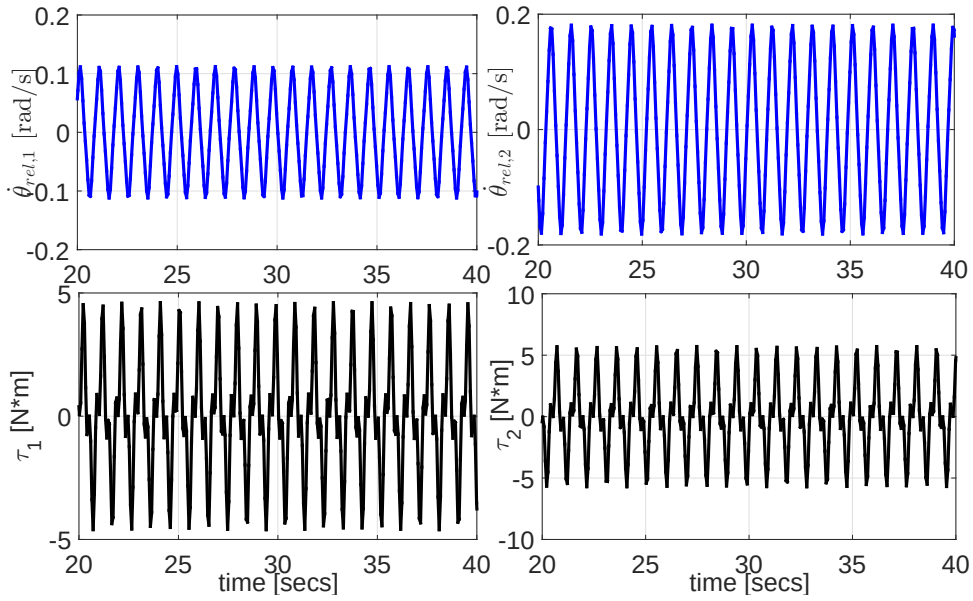

Figure 4.11: Optimal relative pitch angle velocities and PTO torques computed by passive controller for regular wave of frequency $\omega = 6.5$ rad/s and amplitude A = 2 cm.

control is based on the reduced equivalent model with convex cost function (4.53). Note that, for the active controller, the average power computed with the DAE formulation, ODE formulation, convex and non-convex reduced equivalent model, are identical.

Given that the dynamic model of the device derived in Section 3.5.1 and Section 3.5.2 is linear, the range of frequencies for the position and velocity spectra is the same as the range of frequencies of the spectrum of the incident wave. Therefore, for a fundamental frequency $\omega_0 = 2\pi/T_{horiz} = 2\pi/30 = 0.2$ rad/s and a maximum frequency of the spectrum of the incoming

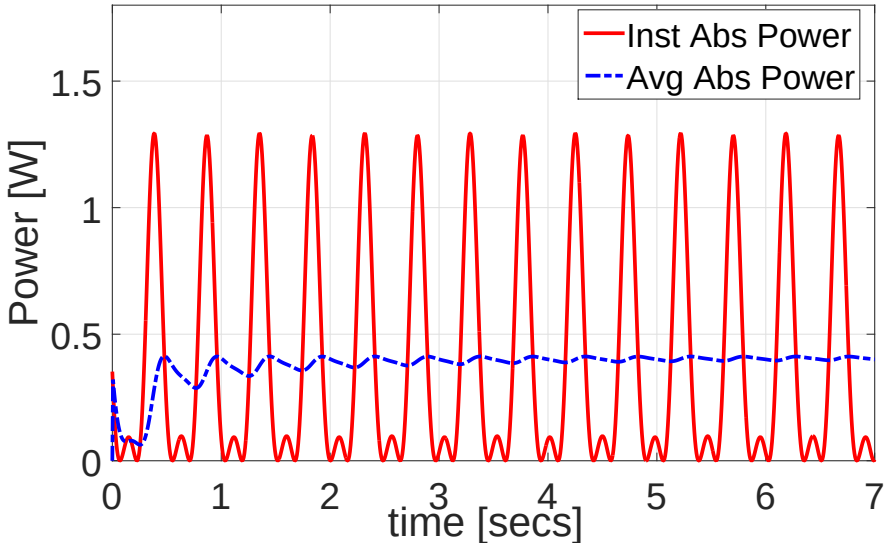

Figure 4.12: Instantaneous and average absorbed power computed by passive controller for regular wave of frequency $\omega = 6.5$ rad/s and amplitude A = 2 cm.

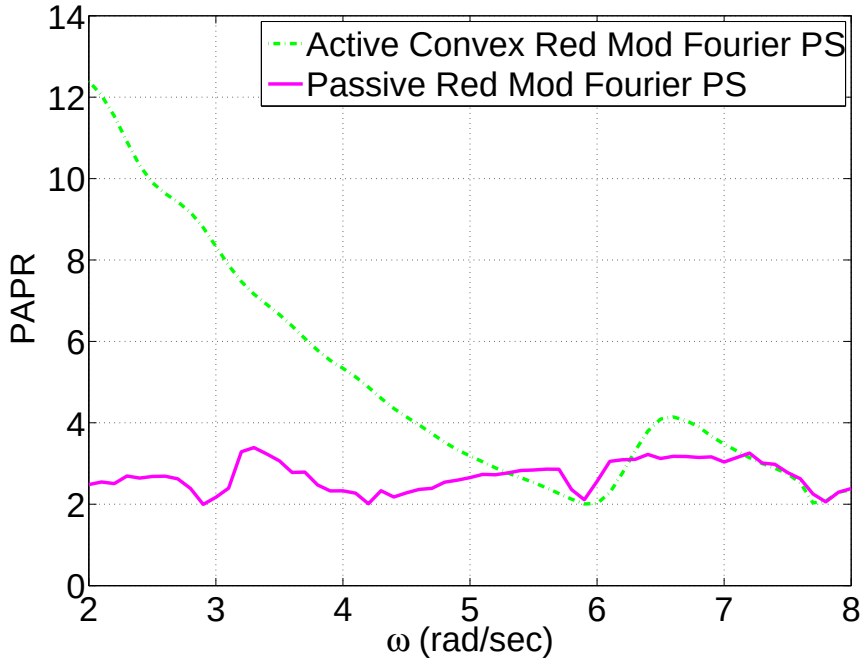

Figure 4.13: Comparison between the Peak to Average Power Ratio (PAPR) given by an active and passive controller for a $1/25th$ scale three-body hinge-barge device for different frequencies of a regular wave of amplitude A = 2 cm.

wave of $\omega_{max} = 10$ rad/s, the order of expansion for the positions, velocities and PTO torques is $N_x = \omega_{max}/\omega_0 = 50$. While the PS active maximizes the average absorbed power over the entire time horizon, the coefficients of dash-pot systems of the optimal linear damping control are set equal to their optimal values at the peak frequency of the spectrum of the incoming wave. As

shown in Figure 4.14, the PS active control outperforms the optimal linear damping control. In particular, the PS active controller compute an average power which is around 1.7 times greater than the power computed with the optimal linear damping. By a way of example, in Figure 4.15, the optimal torques and relative pitch velocities computed by the active controller controller are shown for a polychromatic wave made using JONSWAP spectrum with a significant wave height H_s = 15 cm and peak period T_p = 1.276 s.

4.5.2.2 Passive PS control

In Figure 4.14, the average power absorbed with PS passive control is shown for a polychromatic wave over a time horizon of $T_{horiz} = 30$ s. The passive controller is computed with the reduced equivalent model only, since the computational time required with the ODE and DAE formulations is of the order of hours. As for the regular wave case, an interior-point algorithm is used to compute the PS passive control. As for the PS active controller, the order of expansion for the positions, velocities and PTO torques is $N_x = 50$. As for the PS active controller, the PS passive controller maximizes the average absorbed power over the entire time horizon, and outperforms the optimal linear damping control. In particular, the PS passive controller compute an average power which is around 1.4 times greater than the power computed with the optimal linear damping. By a way of example, in Figure 4.16, the optimal torques and relative pitch velocities computed by the passive controller controller are shown for a polychromatic wave made using JONSWAP spectrum with a significant wave height H_s = 15 cm and peak period T_p = 1.276 s.

4.6 Computational considerations

In this Table 4.1, the comparison between the computational time required by PS methods with Fourier basis functions to compute the active and passive controller for different time horizons is presented. The comparison is made for a polychromatic wave from a JONSWAP spectrum with a significant wave height H_s = 15 cm and peak period T_p = 1.276 s. As shown in Table 4.1, the active controller is computed with the ODE formulation, DAE formulation, non-convex and convex reduced equivalent model. As shown in Table 4.1, the computational time required to compute the active controller with the reduced equivalent model is 4 times and 20 times smaller than the computational time required by the ODE and DAE formulations, respectively. Therefore, the reduced equivalent model is an efficient formulation which reduces the computational burden required to the solve the optimal control problem. As shown in Table 4.1, the computational time required to compute the passive control is considerably high. However, PS control with Fourier basis function is used to assess the power absorption achievable by the device at steady-state, rather than provide a framework for the real-time control of the device. Note that, the passive controller is based on the reduced equivalent model only, since the computational time required

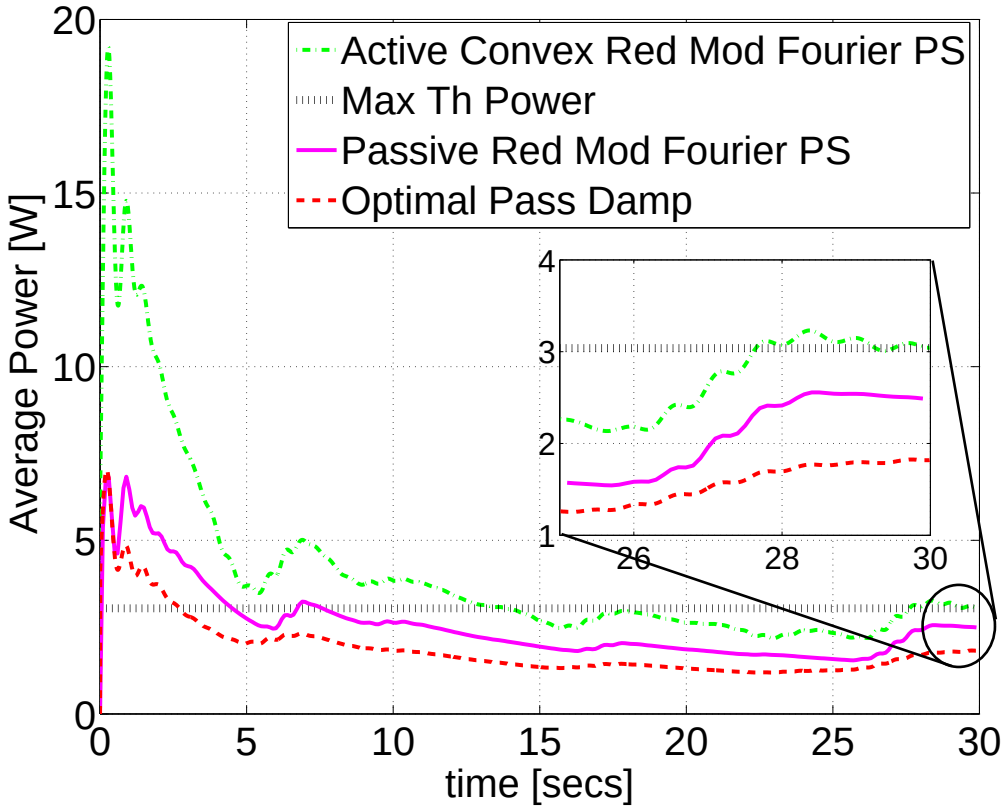

Figure 4.14: Time domain comparison between the max theoretical power and the average power given by optimal linear damping control, convex active reduced model PS control and non-convex passive reduced model PS control for a polychromatic wave made using JONSWAP spectrum with a significant wave height H_s = 15 cm and peak period T_p = 1.276 s.

with the ODE and DAE formulations is around 10 times the computational time required with the reduced model.

4.7 Conclusions

This chapter shows the benefits of PS active and passive control with respect to a strategy based on optimal linear passive dampers for the maximization of the energy extracted by a three-body hinge-barge device. In particular, for regular waves, the average absorbed power with PS active and passive control is approximately 1.5 times greater than the average absorbed power with optimal linear passive dampers around the resonance of the device. For irregular waves, a similar increase of the average power can be achieved with PS active and passive control with respect to optimal linear dampers. The main advantage of PS passive control over a strategy based on optimal linear passive dampers is that the PTO's torques are not linearly dependent on the relative pitch velocities between the bodies.

The results also show that the average absorbed power computed by PS passive control is

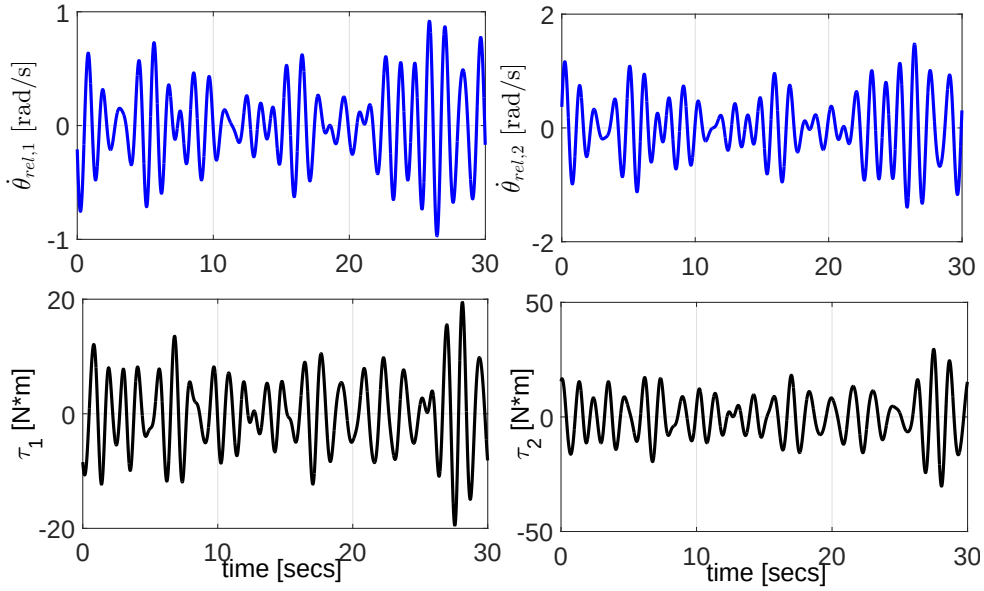

Figure 4.15: Optimal relative pitch angle velocities and PTO torques computed by active controller for a polychromatic wave made using JONSWAP spectrum with a significant wave height H_s = 15 cm and peak period T_p = 1.276 s.

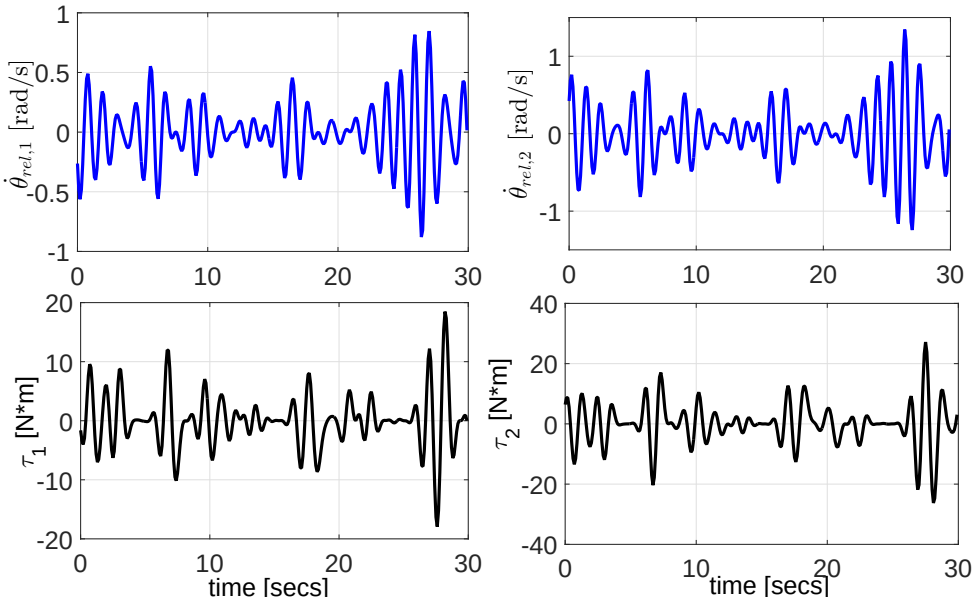

Figure 4.16: Optimal relative pitch angle velocities and PTO torques computed by passive controller for a polychromatic wave made using JONSWAP spectrum with a significant wave height H_s = 15 cm and peak period T_p = 1.276 s.

comparable to the average absorbed power computed by PS active control for both regular and irregular waves. However, considering a realistic PTO efficiency [88], a reduction of the benefits of using a reactive control is expected. Also, the costs involved with the use of a bi-directional PTO can exceed the increment in the value of absorbed power that can be achieved with respect to

$\mathbf{T_{horiz}}$ [s]	**Active Control**				**Passive Control**
	DAE [s]	**ODE** [s]	**Non-conv Red Mod** [s]	**Conv Red Mod** [s]	**Non-conv Red Mod** [s]
20	1.29	0.26	0.063	0.04	1800
25	2.62	0.51	0.11	0.07	3700
30	4.09	0.78	0.18	0.1	8800

Table 4.1: Computational time in seconds required to compute the active and passive controller for a polychromatic wave made using JONSWAP spectrum with a significant wave height H_s = 15 cm and peak period T_p = 1.276 s for different time horizons.

a simpler passive PTO [13].

The complexity of PS optimal control is greatly reduced by using the reduced equivalent dynamic model presented in Section 4.2, instead of a fully dynamic model, for the description of the dynamics of the device. The reduced equivalent model is described in terms of the relative pitch rotations only, which are the modes that are used to extract energy from the device. In particular, the computational time required to compute the active controller by the reduced equivalent model is 4 times and 20 times smaller than the computational time required by the ODE and DAE formulations, respectively. For the passive control, the computational time required to compute an optimal solution is considerably high, due to the passivity condition on the absorbed power, which greatly increases the complexity of PS optimal control.

While the optimization problems for the active control with the ODE and DAE formulations are non-convex, a convex optimization problem for the active control with the reduced equivalent model can be found, which guarantees a globally optimal solution. However, with the reduced equivalent model, no constraints on the heave and absolute pitch rotation of the central barge can be enforced, as the reduced equivalent model is described in terms of the relative pitch rotations only.

Chapter 5

Real-time pseudo-spectral optimal control of a three-body hinge-barge device

5.1 Introduction

In chapter 4, an optimal PS control of a three-body hinge-barge device, based on Fourier-series basis functions, is considered for a finite time horizon. However, Fourier-series basis functions can only represent the steady-state response of the device. Therefore, with Fourier-series basis functions, the motion of the device is considered to be periodic and the transient effects of the dynamics of the device are neglected. This chapter addresses Receding Horizon (RH) real-time optimal control of a three-body hinge-barge device that maximizes the energy extracted by a WEC at each time step over a moving control horizon T_0. In contrast to the RH control, PS methods with Fourier basis functions maximize the energy extracted by the device only once over a finite time horizon.

Traditionally, MPC is adopted for RH control of a WEC, where a local approximation, based on Zero Order Holder (ZOH) basis functions, is used to approximate the control input at each time step over the entire control horizon T_0 [76],[89]. As shown in Figure 5.1, MPC computes the optimal trajectories of position, velocity and control input at the time step t_0 that maximize the energy extracted by the device over the time interval $[t_0, t_0 + T_0]$. Then, the first optimal control input computed by MPC at time step t_0, is applied to the device. At the new time step $t_0^* = t_0 + T_s$, where T_s is the sampling period, a new measurement on position and velocity is available, and the computation of the optimal trajectories of positions, velocities and control inputs is repeated. Usually, for MPC, the time period for the update of the control input is equal to the sampling period T_s.

As presented in Section 4.1, both MPC and RHPSC are valid control strategies that maximize the energy extracted by a WEC over a moving control horizon T_0, considering the limitations on the motion and the PTO force. In this chapter, PS control based on the Half-Range Chebyshev-Fourier

(HRCF) basis functions [90] is presented. Unlike ZOH basis functions, HRCF basis functions are globally defined over the entire control horizon T_0. HRCF basis functions are well suited for the approximation of non-periodic signals, allowing the representation of both the transient and steady-state response of the device. HRCF functions represent a Fourier extension for nonperiodic signals and, therefore, are especially suited for the wave energy field, since wave elevation and fluidstructure interaction forces are all well described using Fourier analysis. As shown in Figure 5.2, PS control based on HRCF basis functions computes the optimal trajectories of position, velocity and control input at the time step t_0 that maximize the energy extracted by the device over the time interval $[t_0, t_0 + T_0]$. In contrast to MPC, PS control based on HRCF basis functions computes a control input which is continuous over the time interval $[t_0, t_0 + T_0]$. Therefore, in theory, the time period for the update of the control input computed by PS control with HRCF basis functions can be longer than the sampling period T_s. However, in practice, in order to retain the properties of robustness of the control with respect to uncertainty on the dynamics of the WEC, the computation of the control input is repeated at each time a new measurement on position and velocity is available.

While in [80], PS with HRCF basis functions is applied to a flap device, in [58], PS shows advantageous computational properties with respect to MPC.

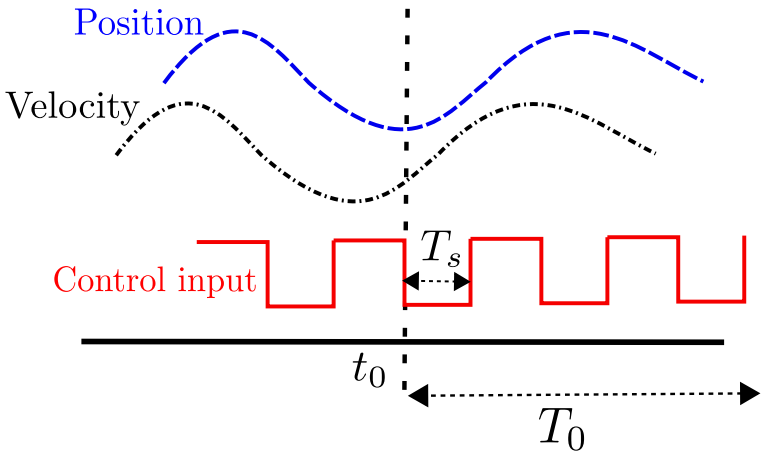

Figure 5.1: Moving control horizon principle of MPC for the computation of the optimal trajectories of position, velocity and control input at the time step t_0 that maximize the energy extracted by the device over the time interval $[t_0, t_0 + T_0]$.

In Figure 5.3, a general hierarchical digital control scheme for a multibody WEC is shown. The control scheme is composed of two different control levels: the high-level control which is based on a PS control with HRCF basis functions, and the low-level control that manipulates the control input vector of the WEC. At the time instant k, PS control with HRCF basis functions takes as inputs the prediction of the future excitation forces vector $\hat{\mathbf{f}}_{wave}(k+L|k)$, the current positions vector $\mathbf{x}(k)$ and velocities vector $\mathbf{v}(k)$, and computes the optimal reference for the velocity vector $\mathbf{v}_{ref}(k)$. The reference velocity vector $\mathbf{v}_{ref}(k)$ is tracked by the low-level control by manipulating

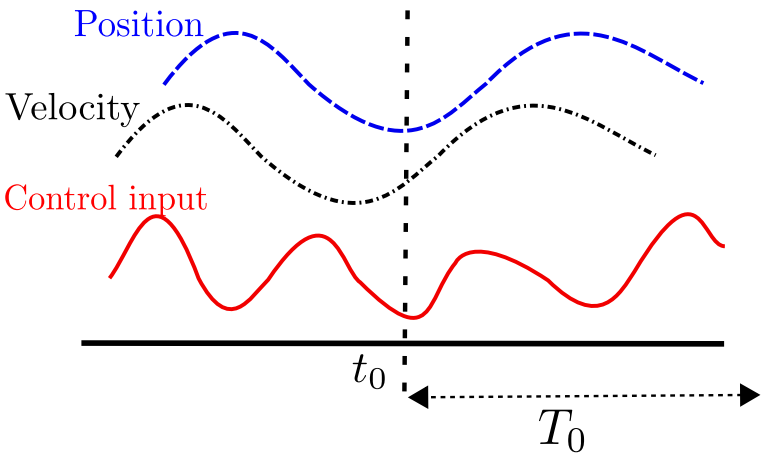

Figure 5.2: Moving control horizon principle of RHPSC control based on HRCF basis functions for the computation of the optimal trajectories of position, velocity and control input at the time step t_0 that maximize the energy extracted by the device over the time interval $[t_0, t_0 + T_0]$.

the control input vector of the WEC $\mathbf{u}(k)$. The objective of this chapter is to asses the value of PS control with HRCF basis functions applied to a three-body hinge-barge device, with the assumption that the low-level control can track the optimal reference velocity vector $\mathbf{v}_{ref}(k)$ computed by PS control with HRCF basis functions. In Section 5.6, a general outline of the possible control schemes that can be adopted for the low-level control are presented.

Note that the DAE formulation is not further considered in the implementation of PS control with HRCF basis functions, given that it requires a considerable computational time to compute the PS control with Fourier basis functions with respect to the ODE formulation and reduced equivalent model, as presented in Table 4.1. In fact, the objective of this chapter is to obtain a computationally efficient real-time controller and, therefore, the DAE formulation is not further considered in this chapter.

The remainder of this chapter is organized as follows: in Section 5.2, the HRCF basis functions are introduced, while, in Section 5.3, PS control with HRCF basis functions is applied to a three-body hinge-barge device. In Section 5.4, PS methods with HRCF basis functions, are compared to a standard optimal controller and PS methods with Fourier basis functions, for both monochromatic and polychromatic waves. In Section 5.5, considerations on the computational time required by PS methods with HRCF basis functions, to compute the active and passive control of the device, are presented, while, in Section 5.6, a general outline of the possible control schemes that can be adopted for the low-level control are presented. Finally, overall conclusions are drawn in Section 5.7.

5.2 Half-range Chebyshev-Fourier basis functions

For the approximation of nonperiodic functions, Fourier basis functions generate boundary discontinuities with the consequent emergence of the Gibbs phenomenon. On the other hand, HRCF

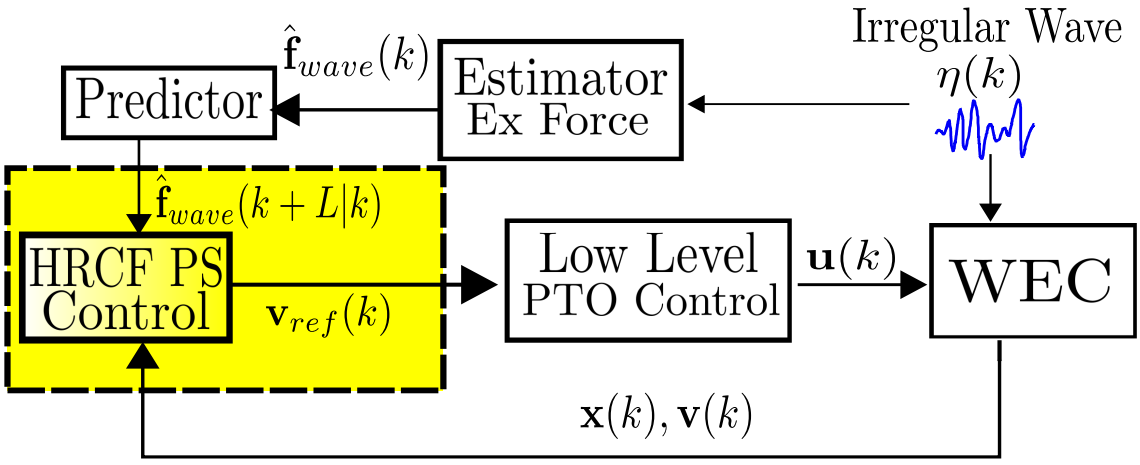

Figure 5.3: RHPSC scheme with low-level control of the PTO for a generic multibody WEC in the discrete time domain

functions are well suited for the approximation of nonperiodic functions. An orthogonal basis for nonperiodic functions is determined based on half-range Chebyshev polynomials of the first and the second kind. Half-range Chebyshev polynomials of the first and the second kind of order k, T_k^h and U_k^h , respectively, are orthogonal with lower order monomials with respect to the weights $1/(1-y^2)^{1/2}$, for the first kind, and $(1-y^2)^{1/2}$, for the second kind, on the interval [0, 1]. Definitions of T_k^h and U_k^h are given in [91] based on [90]:

Definition 1: Let $T_k^h(y)$ be the unique normalized sequence of orthogonal polynomials satisfying:

$$\int_0^1 T_k^h(y) y^l \frac{1}{(1-y^2)^{1/2}} dy = 0, l = 0,..,k-1 \tag{5.1}$$

$$\frac{4}{\pi}\int_0^1 T_k^h(y)^2 \frac{1}{(1-y^2)^{1/2}} dy = 1 \tag{5.2}$$

The set $T_k^h|$ with $k = 0,..,\infty$ is a set of half-range Chebyshev polynomials of the first kind.

Definition 2: Let $U_k^h(y)$ be the unique normalized sequence of orthogonal polynomials satisfying:

$$\int_0^1 U_k^h(y) y^l (1-y^2)^{1/2} dy = 0, l = 0,..,k-1 \tag{5.3}$$

$$\frac{4}{\pi}\int_0^1 U_k^h(y)^2 (1-y^2)^{1/2} dy = 1 \tag{5.4}$$

The set $U_k^h|$ with $k = 0,..,\infty$ is a set of half-range Chebyshev polynomials of the second kind. In Figure 5.4, Half-range Chebyshev polynomials of the first kind $T_k^h(y)$ and second kind $U_k^h(y)$, with $k = 0,..,5$, are shown.

In Figure 5.5a, a given nonperiodic function f defined over the interval $T \in [0,3]$ is approx-

imated by using different basis functions: Fourier, HRCF and ZOH functions. The function f is made of the summation of 3 sinusoidal components of different period, amplitude and phase. The number of basis functions used to approximate the function f is 23 for the Fourier, HRCF and ZOH approximation. In Figure 5.5b, the approximation error of the Fourier, HRCF and ZOH approximation is shown for different numbers of basis functions. As shown in Figure 5.5a, while the approximation with HRCF basis functions is almost indistinguishable from the original function f, the approximation with Fourier and ZOH basis functions do not provide satisfactory approximation. In particular, the approximation with Fourier basis functions shows boundary discontinuities and the emergence of the Gibbs phenomenon. Regarding the ZOH approximation, as shown in Figure 5.5b, a comparatively large number of basis functions is needed to achieve the same approximation error provided by the HRCF approximation. For a standard MPC strategy based on ZOH basis functions, the use of a large number of basis functions requires a high computational time for the computation of the optimal trajectories of positions, velocities and control inputs. In [80], the HRCF approximation is compared to an approximation based on Legendre polynomials, and the results show that the HRCF functions provides smaller approximation errors than Legendre polynomials, for high numbers of basis functions.

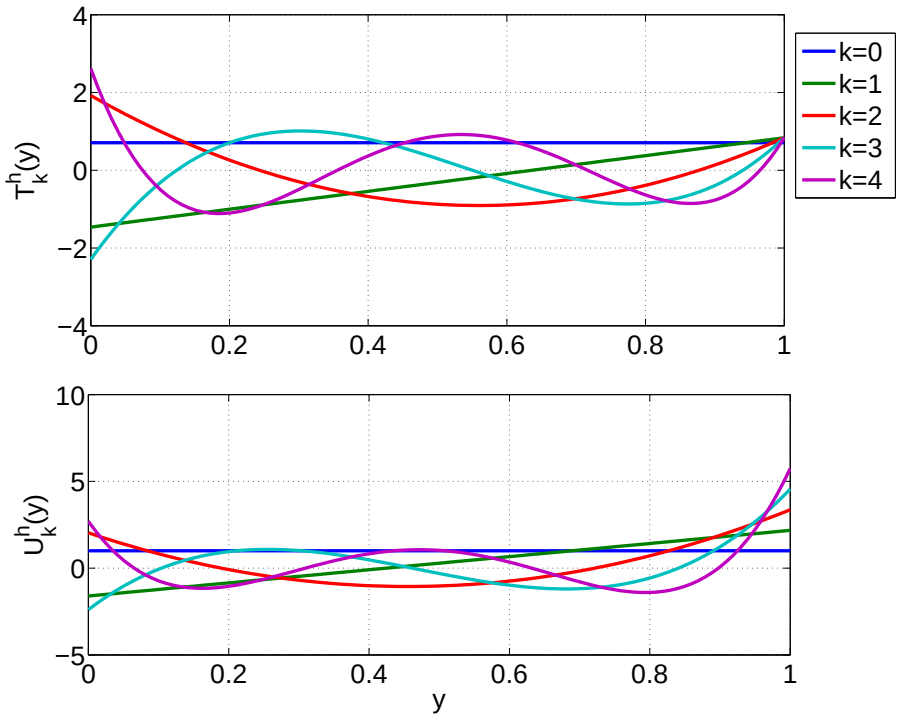

Figure 5.4: Half-range Chebyshev polynomials first kind $T_k^h(y)$ and second kind $U_k^h(y)$ with $k = 0,..,5$.

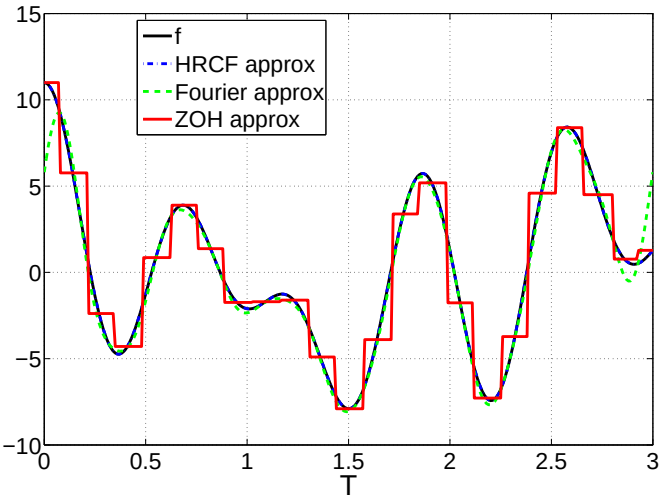

(a)

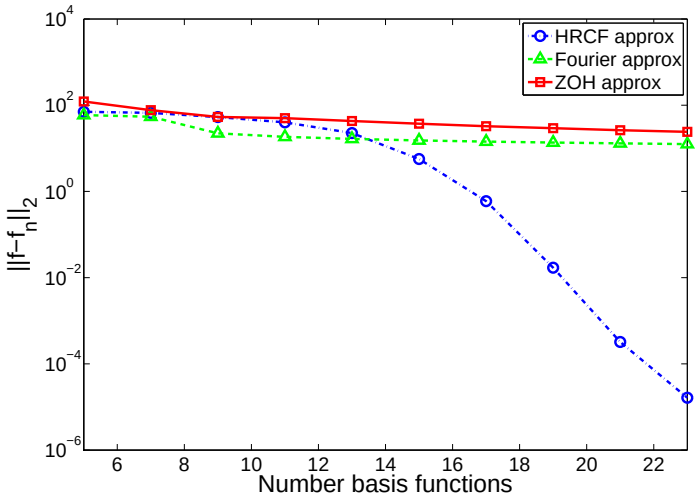

(b)

Figure 5.5: Approximation (a) and approximation error (b) of a nonperiodic function f with different basis functions: Fourier, HRCF and ZOH basis functions

5.3 Pseudo-spectral control with Half-Range Chebyshev-Fourier basis functions of a three-body hinge-barge device

This section describes the direct transcription, with HRCF basis functions, of the optimal control problem for a three-body hinge-barge device. The objective of the optimal control problem is to compute the trajectories of the PTO torques and velocities of the bodies of the device in order to maximize the energy absorbed by the device. The average power absorbed by the PTOs, over the

time interval $[t_0, t_0+T_0]$, is given as:

$$J = \frac{1}{T_0}\int_{t_0}^{t_0+T_0} \mathbf{v}^T \mathbf{F}_p \mathbf{u} dt \tag{5.5}$$

For simplicity, the time interval $[t_0, t_0+T_0]$ is mapped into the time interval $[-1,1]$ by using the following affine transformation $g : t \to \tau$:

$$\tau = g(t) = \frac{2}{T_0}(t-t_0) - 1 \tag{5.6}$$

where $t \in [t_0, t_0+T_0]$ and $\tau \in [-1,1]$. Using the affine transformation in equation (5.6), the average power absorbed by the PTOs, over the time interval $[-1,1]$, is given as:

$$J = \frac{1}{2}\int_{-1}^{1} \mathbf{V}^T \mathbf{F}_p \mathbf{U} d\tau \tag{5.7}$$

where $\circ$ is the composition operator, $\mathbf{V} = \mathbf{v} \circ g$ is the scaled velocity vector and $\mathbf{U} = \mathbf{u} \circ g$ is the scaled control force vector. For the discretization of the control problem, the positions, velocities and control forces can be approximated as a combination HRCF basis functions as follows [80]:

$$Q_i(\tau) \approx Q_i^M(\tau) = \sum_{k=0}^{M} x_{i,k}^{q,c} T_k^h\left(cos\frac{\pi}{2}\tau\right) + \sum_{k=0}^{M-1} x_{i,k}^{q,s} U_k^h\left(cos\frac{\pi}{2}\tau\right) sin\frac{\pi}{2}\tau = \mathbf{\Phi}(\tau)^T \hat{\mathbf{x}}_i^q \tag{5.8}$$

$$V_i(\tau) \approx V_i^M(\tau) = \sum_{k=0}^{M} x_{i,k}^{v,c} T_k^h\left(cos\frac{\pi}{2}\tau\right) + \sum_{k=0}^{M-1} x_{i,k}^{v,s} U_k^h\left(cos\frac{\pi}{2}\tau\right) sin\frac{\pi}{2}\tau = \mathbf{\Phi}(\tau)^T \hat{\mathbf{x}}_i^v \tag{5.9}$$

$$U_p(\tau) \approx U_p^M(\tau) = \sum_{k=0}^{M} u_{p,k}^{c} T_k^h\left(cos\frac{\pi}{2}\tau\right) + \sum_{k=0}^{M-1} u_{p,k}^{s} U_k^h\left(cos\frac{\pi}{2}\tau\right) sin\frac{\pi}{2}\tau = \mathbf{\Phi}(\tau)^T \hat{\mathbf{u}}_p \tag{5.10}$$

where $\mathbf{Q} = \mathbf{q} \circ g$ is the scaled position vector, M is the order of expansion of the approximation, $p = 1,..,2$, and $i = 1,..,4$ and $i = 1,..,2$ for the ODE and reduced equivalent model, respectively. The vector of the coefficients $\hat{\mathbf{x}}_i^q$, $\hat{\mathbf{x}}_i^v$ and $\hat{\mathbf{u}}_p$ of the approximated components of the position, velocity and control vectors, are given as follows:

$$\hat{\mathbf{x}}_i^q = \left[x_{i,0}^{q,c}\ x_{i,1}^{q,c}\ ..\ x_{i,M-2}^{q,s}\ x_{i,M-1}^{q,s}\right]^T \tag{5.11}$$

$$\hat{\mathbf{x}}_i^v = \left[x_{i,0}^{v,c}\ x_{i,1}^{v,c}\ ..\ x_{i,M-2}^{v,s}\ x_{i,M-1}^{v,s}\right]^T \tag{5.12}$$

$$\hat{\mathbf{u}}_p = \left[u_{p,0}^{c}\ u_{p,1}^{c}\ ..\ u_{p,M-2}^{s}\ u_{p,M-1}^{s}\right]^T \tag{5.13}$$

while the basis function vector $\mathbf{\Phi}(t)$ is given as follows:

$$\mathbf{\Phi}(\tau) = \left[T_0^h\left(cos\frac{\pi}{2}\tau\right)\ \ T_1^h\left(cos\frac{\pi}{2}\tau\right)\ ..\ T_M^h\left(cos\frac{\pi}{2}\tau\right)\ \ U_0^h\left(cos\frac{\pi}{2}\tau\right) sin\frac{\pi}{2}\tau\ \ ..\ \ U_{M-1}^h\left(cos\frac{\pi}{2}\tau\right) sin\frac{\pi}{2}\tau\right]^T \tag{5.14}$$

The derivatives of the ith components of the position and velocity vector are, respectively,

$$\dot{Q}_i^M(\tau) = \dot{\mathbf{\Phi}}(\tau)^T \hat{\mathbf{x}}_i^q = \mathbf{\Phi}(\tau)^T \mathbf{D} \hat{\mathbf{x}}_i^q \tag{5.15}$$

$$\dot{V}_i^M(\tau) = \dot{\mathbf{\Phi}}(\tau)^T \hat{\mathbf{x}}_i^v = \mathbf{\Phi}(\tau)^T \mathbf{D} \hat{\mathbf{x}}_i^v \tag{5.16}$$

where $\mathbf{D} \in \mathbb{R}^{2M+1 \times 2M+1}$ is a block diagonal matrix given as follows [91]:

$$\mathbf{D} = \frac{\pi}{2} \begin{bmatrix} \mathbf{0} & \mathbf{H}_1 \\ \mathbf{H}_2 & \mathbf{0} \end{bmatrix} \tag{5.17}$$

For the ODE formulation, the convolution integral in equation (3.33) can be expressed as a function of the PS coefficients $\hat{\mathbf{x}}_i^v$. The convolution integral of the element $K_{rad,s_{i,ii}}$ of the impulse response matrix $\mathbf{K}_{rad,s}$, with $i = 1,..n$ and $ii = 1,..n$, in equation (3.33) can be written as [80]:

$$\int_{-\infty}^{t} K_{rad,s_{i,ii}}(t-\tau) v_{ii}, d\tau = \int_0^t K_{rad_{i,ii}}(t-\tau) v_{ii} d\tau \tag{5.18}$$

$$= \int_{g(0)}^{\tau} k_{rad,s_{i,ii}}(\tau - s) V_{ii}(s) ds \tag{5.19}$$

$$= \int_{g(0)}^{-1} k_{rad,s_{i,ii}}(\tau - s) V_{ii}(s) ds + \int_{-1}^{\tau} k_{rad,s_{i,ii}}(\tau - s) V_{ii}(s) ds \tag{5.20}$$

$$= c_0(\tau) + c(\tau) \tag{5.21}$$

where $k_{rad,s_{i,ii}} = K_{rad,s_{i,ii}} \circ g$ is the scaled kernel function matrix of the radiation forces. The first part of the convolution integral $c_0(\tau)$ represents the memory effect of the radiation forces before t_0, and can be computed from the past values of the velocity $v_{ii}(t)$. The second part of the convolution integral $c(\tau)$ can be written as:

$$c(\tau) = \sum_{k=1}^{2M+1} c_k(\tau) \hat{x}_{i,k}^v \tag{5.22}$$

$$= \sum_{k=1}^{2M+1} \left(\int_{-1}^{\tau} k_{rad,s_{i,ii}}(\tau - s) \Phi_k(s) ds \right) \hat{x}_{i,k}^v \tag{5.23}$$

If the projection of $c_k(\tau)$ over each HRCF basis funtion $\Phi_j(\tau)$ is defined as:

$$p_{j,k} = \int_{-1}^{1} c_k(\tau) \Phi_j(\tau) d\tau \tag{5.24}$$

then, the matrix $\mathbf{P}_{rad,s_{i,ii}}$ of the convolution integral $c(\tau)$ in equation (5.22) is defined as follows:

$$\mathbf{P}_{rad,s_{i,ii}} = \begin{bmatrix} p_{1,1} & p_{1,2} & \cdots & p_{1,2M+1} \\ \cdots & \cdots & \cdots & \cdots \\ p_{2M+1,1} & p_{2M+1,2} & \cdots & p_{2M+1,2M+1} \end{bmatrix} \tag{5.25}$$

Therefore, $c(\tau)$ in equation (5.22) can be rewritten as:

$$c(\tau) = \mathbf{\Phi}(\tau)^T \mathbf{P}_{rad_{i,ii}} \hat{\mathbf{x}}_i^v \tag{5.26}$$

For the equivalent reduced model, a similar development can be carried out for the convolution integral of each element $K_{eq,rad_{i,ii}}$ of the impulse response matrix $\mathbf{K}_{eq,rad}$, with $i = 1,..n_c$ and $ii = 1,..n_c$, in equation (4.21).

In the remainder of this section, two different PS control frameworks are derived, based on the formulation used to describe the dynamics of the device: ODE HRCF PS control, and reduced equivalent model HRCF PS control. Similarly to PS control with Fourier basis functions presented in Chapter 4, while the optimization problem associated with the ODE HRCF PS control is non-convex, the optimization problem associated with the reduced equivalent model HRCF PS control can be either nonconvex or convex.

5.3.1 ODE HRCF PS control

By substituting the approximated velocities and control torques, defined in equations (5.9) and (5.10), respectively, into the expression for the absorbed power defined in equation (5.7), the approximated average absorbed power is given as:

$$\begin{aligned} J^M &= \frac{1}{2}\int_{-1}^{1} \mathbf{\Phi}(\tau)^T \mathbf{X}^V F_{p,s} \mathbf{U}^T \mathbf{\Phi}(\tau) d\tau \\ &= \frac{1}{2}(\hat{\mathbf{u}}_1^T \hat{\mathbf{x}}_3^v + \hat{\mathbf{u}}_2^T \hat{\mathbf{x}}_4^v) \\ &= \frac{1}{4}\mathbf{x}^T \mathbf{H}_{HRCF,ODE} \mathbf{x} \end{aligned} \tag{5.27}$$

where:

$$\mathbf{X}^V = [\,\hat{\mathbf{x}}_1^v, .., \hat{\mathbf{x}}_4^v] \tag{5.28}$$

$$\mathbf{U} = [\,\hat{\mathbf{u}}_1, .., \hat{\mathbf{u}}_2] \tag{5.29}$$

$$\mathbf{x} = [\,\hat{\mathbf{x}}^{q,T}\ \hat{\mathbf{x}}^{v,T}\ \hat{\mathbf{u}}^T]^T \tag{5.30}$$

$$\mathbf{H}_{HRCF,ODE} = \begin{bmatrix} \mathbf{0}_{4\times M_x,4\times M_x} & \mathbf{0}_{4\times M_x,4\times M_x} & \mathbf{0}_{4\times M_x,2\times M_x} \\ \mathbf{0}_{4\times M_x,4\times M_x} & \mathbf{0}_{4\times M_x,4\times M_x} & \mathbf{H}_1 \\ \mathbf{0}_{2\times M_x,4\times M_x} & \mathbf{H}_2 & \mathbf{0}_{2\times M_x,2\times M_x} \end{bmatrix} \tag{5.31}$$

$$\mathbf{H}_1 = \begin{bmatrix} \mathbf{0}_{M_x,M_x} & \mathbf{0}_{M_x,M_x} \\ \mathbf{0}_{M_x,M_x} & \mathbf{0}_{M_x,M_x} \\ \mathbf{I}_{M_x,M_x} & \mathbf{0}_{M_x,M_x} \\ \mathbf{0}_{M_x,M_x} & \mathbf{I}_{M_x,M_x} \end{bmatrix} \tag{5.32}$$

$$\mathbf{H}_2 = \mathbf{H}_1^T \tag{5.33}$$

with $M_x = 2M+1$. Using the affine transformation in equation (5.6), equations (3.32) and (3.33) can be written as:

$$\dot{\mathbf{Q}}_s = \frac{T}{2}\mathbf{V}_s \tag{5.34}$$

$$\dot{\mathbf{V}}_s = \frac{T}{2}(\,\mathbf{M}_s + \mathbf{M}_{\infty,s})^{-1}\Big(-\mathbf{B}_{visc,s}\mathbf{V}_s - \mathbf{G}_s\mathbf{Q}_s - \int_{g^{-1}(0)}^{\tau} \mathbf{k}_{rad,s}(\tau - s + g(0)^{-1})\mathbf{V}_s ds + \mathbf{F}_{wave,s} + F_{p,s}\mathbf{U}\Big) \tag{5.35}$$

where $\mathbf{F}_{wave,s} = \mathbf{f}_{wave,s} \circ g$ is the scaled excitation force vector. Substituting the approximated states (5.8), (5.9) and their time derivatives (5.15), (5.16) into the equations of motion (5.34)-(5.35) yields the following equations of motion in residual form:

$$r_i^q(\tau) = \mathbf{\Phi}(\tau)^T\mathbf{D}\hat{\mathbf{x}}_i^q - \mathbf{\Phi}(\tau)^T\hat{\mathbf{x}}_i^v \tag{5.36}$$

$$\begin{aligned} r_i^v(\tau) = {} & \sum_{p=1}^{4}\frac{2}{T}(\,M_{s_{i,p}+} + M_{\infty,s_{i,p}})\,\mathbf{\Phi}(\tau)^T\mathbf{D}\hat{\mathbf{x}}_p^v + \sum_{p=1}^{4} B_{visc,s_{i,p}}\mathbf{\Phi}(\tau)^T\hat{\mathbf{x}}_p^v + \sum_{p=1}^{4} G_{s_{i,p}}\mathbf{\Phi}(\tau)^T\hat{\mathbf{x}}_p^q + .. \\ & \sum_{p=1}^{4}\mathbf{\Phi}(\tau)^T\mathbf{P}_{rad_{i,p}}\hat{\mathbf{x}}_p^v - F_{wave,s_i}(\tau) - \sum_{p=1}^{2} F_{p,s_{i,p}}\mathbf{\Phi}(\tau)^T\hat{\mathbf{u}}_p \end{aligned} \tag{5.37}$$

where $i = 1, .., 4$. The optimal control problem defined by the maximization of the cost function (5.7), subject to the dynamic constraints (5.34)-(5.35), is transformed into a finite dimensional optimization problem with cost function (5.27), and dynamic constraints (5.36)-(5.37). Note that the cost function in equation (5.27) is quadratic, but non-convex and, therefore, a solution to the optimization problem can be locally optimal.

5.3.2 Reduced equivalent model HRCF PS control

By substituting the approximated velocities and control torques, defined in equations (5.9) and (5.10), respectively, into the expression for the absorbed power, defined in equation (5.7), the approximated average absorbed power is given as:

$$\begin{aligned} J^M &= \frac{1}{2}\int_{-1}^{1} \mathbf{\Phi}(\tau)^T \mathbf{X}^V \mathbf{U}^T \mathbf{\Phi}(\tau) d\tau \\ &= \frac{1}{2}(\ \hat{\mathbf{u}}_1^T \hat{\mathbf{x}}_1^v + \hat{\mathbf{u}}_2^T \hat{\mathbf{x}}_2^v) \\ &= \frac{1}{4}\mathbf{x}^T \mathbf{H}_{HRCF,Red}\mathbf{x} \end{aligned} \tag{5.38}$$

where:

$$\mathbf{X}^V = [\ \hat{\mathbf{x}}_1^v, .., \hat{\mathbf{x}}_{n_c}^v\ ] \tag{5.39}$$

$$\mathbf{U} = [\ \hat{\mathbf{u}}_1, .., \hat{\mathbf{u}}_{n_c}] \tag{5.40}$$

$$\mathbf{x} = [\ \hat{\mathbf{x}}^{q,T}\ \hat{\mathbf{x}}^{v,T}\ \hat{\mathbf{u}}^T\ ]^T \tag{5.41}$$

$$\mathbf{H}_{HRCF,Red} = \begin{bmatrix} \mathbf{0}_{2\times M_x,2\times M_x} & \mathbf{0}_{2\times M_x,2\times M_x} & \mathbf{0}_{2\times M_x,2\times M_x} \\ \mathbf{0}_{2\times M_x,2\times M_x} & \mathbf{0}_{2\times M_x,2\times M_x} & \mathbf{H}_1 \\ \mathbf{0}_{2\times M_x,2\times M_x} & \mathbf{H}_2 & \mathbf{I}_N \end{bmatrix} \tag{5.42}$$

$$\mathbf{H}_1 = \begin{bmatrix} \mathbf{I}_{M_x} & \mathbf{0}_{M_x} \\ \mathbf{0}_{M_x} & \mathbf{I}_{M_x} \end{bmatrix} \tag{5.43}$$

$$\mathbf{H}_2 = \mathbf{H}_1^T \tag{5.44}$$

Using the affine transformation in equation (5.6), equations (4.20) and (4.21) can be written as:

$$\dot{\mathbf{Q}}_{eq} = \frac{T}{2}\mathbf{V}_{eq} \tag{5.45}$$

$$\dot{\mathbf{V}}_{eq} = \frac{T}{2}\mathbf{M}_{eq,tot}^{-1}\Big(-\mathbf{B}_{eq,visc}\mathbf{V}_{eq} - \mathbf{G}_{eq}\mathbf{Q}_{eq} - \int_{g^{-1}(0)}^{\tau} \mathbf{k}_{eq,rad}(\tau - s + g(0)^{-1})\mathbf{V}_{eq} ds + \mathbf{F}_{eq,wave} + \mathbf{U}\Big) \tag{5.46}$$

where $\mathbf{K}_{eq,rad} = \mathbf{k}_{eq,rad} \circ g$ is the scaled kernel function matrix of the radiation forces and $\mathbf{F}_{eq,wave} = \mathbf{f}_{eq,wave} \circ g$. Substituting the approximated states (5.8), (5.9) and their time derivatives (5.15), (5.16) into the equations of motion (5.45)-(5.46) yields the following equations of motion in residual form:

$$r_i^q(\tau) = \mathbf{\Phi}(\tau)^T \mathbf{D}\hat{\mathbf{x}}_i^q - \mathbf{\Phi}(\tau)^T \hat{\mathbf{x}}_i^v \tag{5.47}$$

$$\begin{aligned} r_i^v(\tau) = &\sum_{p=1}^{n_c} \frac{2}{T} M_{eq,tot_{i,p}} \mathbf{\Phi}(\tau)^T \mathbf{D}\hat{\mathbf{x}}_p^v + \sum_{p=1}^{n_c} B_{eq,visc_{i,p}} \mathbf{\Phi}(\tau)^T \hat{\mathbf{x}}_p^v + \sum_{p=1}^{n_c} G_{eq_{i,p}} \mathbf{\Phi}(\tau)^T \hat{\mathbf{x}}_p^q + .. \\ &\sum_{p=1}^{n_c} \mathbf{\Phi}(\tau)^T \mathbf{P}_{eq,rad_{i,p}} \hat{\mathbf{x}}_p^v - F_{eq,wave_i}(\tau) - \mathbf{\Phi}(\tau)^T \hat{\mathbf{U}}_i \end{aligned} \tag{5.48}$$

where $i = 1,..,2$. The optimal control problem defined by the maximization of the cost function (5.7), subject to the dynamic constraints (5.45)-(5.46), is transformed into a finite dimensional optimization problem with cost function (5.38), and dynamic constraints (5.47)-(5.48). Note that, the cost function in equation (5.38) is quadratic, but non-convex and, therefore, a solution to the optimization problem can be locally optimal. In Section 5.3.2.1, a convex cost function is proposed, which guarantees that the solution to the optimization problem is globally optimal.

5.3.2.1 Convex cost function

The cost function in (5.7) can be rewritten as:

$$\begin{aligned} J &= \frac{1}{2}\int_{-1}^{1} \left(\mathbf{V}_{eq}^T \mathbf{F}_{eq,wave} - \mathbf{V}_{eq}^T \mathbf{B}_{eq,visc} \mathbf{V}_{eq} - \mathbf{V}_{eq}^T \left(\int_{g(0)^{-1}}^{\tau} \mathbf{K}_{eq,rad}(\tau - s + g(0)^{-1}) \mathbf{V}_{eq} d\tau \right) \right) d\tau \\ &= \frac{1}{2}\int_{-1}^{1} \Big(\mathbf{\Phi}(\tau)^T \mathbf{X}^V \mathbf{X}^{ex,T} \mathbf{\Phi}(\tau) - \mathbf{\Phi}(\tau)^T \mathbf{X}^V \mathbf{B}_{eq,visc} \mathbf{X}^{V,T} \mathbf{\Phi}(\tau) - \mathbf{\Phi}(\tau)^T \mathbf{X}^V \mathbf{X}^{rad,T} \mathbf{\Phi}(\tau) \Big) d\tau \\ &= \frac{1}{2}\mathbf{x}^{ex,T}\mathbf{x} - \frac{1}{2}\mathbf{x}^T \tilde{\mathbf{H}} \mathbf{x} \end{aligned} \tag{5.49}$$

where:

$$\mathbf{X}^{ex} = [\, \hat{\mathbf{x}}_1^{ex} \; \hat{\mathbf{x}}_2^{ex}] \tag{5.50}$$

$$\mathbf{x}^{ex} = [\, \mathbf{0}_{1,2\times M_x} \; \hat{\mathbf{x}}^{ex,T} \; \mathbf{0}_{1,2\times M_x}]^T \tag{5.51}$$

$$\mathbf{X}^{rad} = [\, \hat{\mathbf{x}}_1^{rad} \; \hat{\mathbf{x}}_2^{rad}] \tag{5.52}$$

$$\hat{\mathbf{x}}^{rad} = \mathbf{P}_{eq,rad} \hat{\mathbf{x}}^v \tag{5.53}$$

$$\tilde{\mathbf{H}} = \begin{bmatrix} \mathbf{0}_{2\times M_x,2\times M_x} & \mathbf{0}_{2\times M_x,2\times M_x} & \mathbf{0}_{2\times M_x,2\times M_x} \\ \mathbf{0}_{2\times M_x,2\times M_x} & \mathbf{P}_{eq,rad} + \mathbf{D}_{visc} & \mathbf{0}_{2\times M_x,2\times M_x} \\ \mathbf{0}_{2\times M_x,2\times M_x} & \mathbf{0}_{2\times M_x,2\times M_x} & \mathbf{0}_{2\times M_x,2\times M_x} \end{bmatrix} \tag{5.54}$$

$$\mathbf{D}_{visc} = \begin{bmatrix} B_{eq,visc_{1,1}} \mathbf{I}_{M_x} & B_{eq,visc_{1,2}} \mathbf{I}_{M_x} \\ B_{eq,visc_{2,1}} \mathbf{I}_{M_x} & B_{eq,visc_{2,2}} \mathbf{I}_{M_x} \end{bmatrix} \tag{5.55}$$

with $\mathbf{P}_{eq,rad} \in \mathbb{R}^{N,N}$ is the matrix used to compute the HRCF coefficients of the radiation forces,

given the HRCF coefficients of the velocities. In contrast to the cost function in equation (5.38), the cost function in equation (5.49) is convex and, therefore, the solution to the optimization problem is a global optimal solution.

5.4 Results

In this Section, the performance of RH control based on PS optimal control with HRCF basis functions applied to a $1/25th$ scale three-body hinge-barge device is compared to the optimal linear damping strategy presented in subsection 4.5.1.1, and PS control with Fourier basis functions as presented in Chapter 4. The comparison between PS optimal control with HRCF basis functions, PS optimal control with Fourier basis functions and the optimal linear damping strategy is carried out for both monochromatic and polychromatic waves. In order to get more meaningful results of PS optimal control with HRCF basis functions applied to a $1/25th$ scale three-body hinge-barge device, the dynamic model tuned in subsection 3.5.3.2 is used for the formulation of the optimal control.

5.4.1 Monochromatic wave results

In this section, PS control with HRCF basis functions applied to a 1/25th scale three-body hinge-barge device is compared to standard control strategy based on optimal linear damping, and PS control with Fourier basis functions, for regular waves.

5.4.1.1 Active HRCF PS Control

An active controller, based on the ODE formulation and the reduced equivalent model, is computed with HRCF PS methods. The active controller, based on the reduced equivalent model, is computed with both non-convex and convex cost function, given in equation (5.38) and (5.49), respectively. For the PS active control, the choice of number of HRCF basis functions M, in the approximation of positions, velocities and control forces, plays an important role in the maximization of the absorbed power. In Figure 5.6, the absorbed power and the computational time of the active controller with HRCF basis function is shown for different values of M for a regular wave of frequency $\omega = 5$ rad/s and amplitude A = 2 cm. An order $M = 9$ is chosen for the passive controller, as provides a trade-off between the computational time and the maximization of the absorbed power. In Figure 5.7, the average absorbed power, given by the HRCF PS control based on the ODE formulation, and the reduced equivalent model with both non-convex and convex cost functions, is shown for regular waves.

As Figure 5.7 shows, the PS active control, based on the ODE formulation, computes a negative average absorbed power for a range of frequencies from 2.5 rad/s to 3 rad/s, which means that the PTOs *supply energy* to the device rather than absorb energy. For a range of frequencies from 2.5 rad/s to 3 rad/s, the PS active control based on the ODE formulation computes a negative power, as cannot find the optimally global solution to the energy maximization problem, due

the non-convexity of the cost function in equation (5.27). However, for a range of frequencies greater than 3 rad/s, the PS active control based on the ODE formulation computes an average absorbed power which is close to the maximum theoretical power. As Figure 5.7 shows, both the PS active controller, based on the reduced equivalent model, with convex and nonconvex cost functions, show similar performances, and compute an absorbed power which is close the maximum theoretical average power. While the active control with the convex reduced equivalent model is computed analytically, an active-set algorithm [84] is used for the computation of the HRCF PS active control with the ODE formulation and non-convex reduced equivalent model.

Now, a comparison between PS active control with HRCF basis functions and Fourier basis functions, as presented in Section 4.5, is made. In Figure 5.8, a comparison between PS active control with HRCF basis functions and Fourier basis functions is shown for regular waves. As shown in Figure 5.8, PS active control, with Fourier basis functions, slightly absorbs more power than PS active control with HRCF basis functions around the natural resonant frequency of the device.

In Figure 5.9 and 5.11, a comparison between the optimal torques and relative pitch velocities computed by the active controller, with HRCF basis functions and Fourier basis functions, is shown for a regular wave of amplitude A=0.02 m and frequency $\omega = 3$ rad/s and $\omega = 6.5$ rad/s, respectively. As shown in Figure 5.9 and 5.11, the optimal torques and relative pitch velocities computed by the active controller, with HRCF basis functions, converge to the optimal torques and relative pitch velocities computed by the active controller with Fourier basis functions. In Figure 5.10 and 5.12, the average absorbed power achieved by the active controller with HRCF basis functions is compared to the average absorbed power achieved by the active controller with Fourier basis functions for a regular wave of amplitude A=0.02 m and frequency $\omega = 3$ rad/s and $\omega = 6.5$ rad/s, respectively. As shown in Figure 5.10 and 5.12, the average power absorbed by the active controller with HRCF basis functions converge to the average power absorbed by the active controller with Fourier basis functions.

5.4.1.2 Passive HRCF PS Control

A passive controller is computed with PS methods based on HRCF basis functions. The passive controller is based on the reduced equivalent model with convex cost function (5.49), since the computational time required to compute the passive control with the ODE formulation is excessive. For the PS passive control, the choice of number of HRCF basis functions M in the approximation of positions, velocities and control forces plays an important role in the maximization of the absorbed power. In Figure 5.13, the absorbed power and the computational time of the passive controller with HRCF basis function is shown for different values of M for a regular

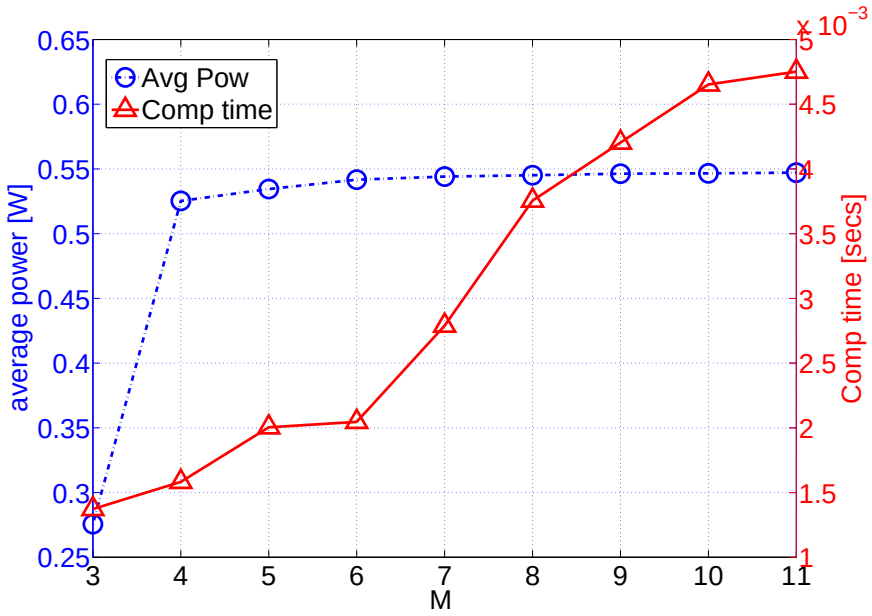

Figure 5.6: Absorbed power and computational time of the active control for different values of M for a regular wave of frequency $\omega = 5$ rad/s and amplitude A = 2 cm.

wave of frequency $\omega = 5$ rad/s and amplitude A = 2 cm. An order $M = 6$ is chosen for the passive controller, as provides a trade-off between the computational time and the maximization of the absorbed power.

Note that, for the PS passive control, the passivity condition introduces a non-convex quadratic inequality constraint to the optimization problem given by the cost function (5.49). Therefore, a globally optimal solution cannot be guaranteed for passive control formulation. An interior-point algorithm [86] is used to compute the PS passive control, since the computational time required with an active-set algorithm is of the order of minutes. As Figure 5.7 shows, the power absorbed with the PS passive control is higher than the power absorbed with a control strategy based on optimal linear damping coefficients.

Now, a comparison between PS passive control, with HRCF basis functions and Fourier basis functions, as presented in Section 4.5, is made. In Figure 5.8, a comparison between the PS passive control, with HRCF basis functions and Fourier basis functions, is shown for regular waves. As shown in Figure 5.8, PS passive control with Fourier basis functions absorbs a greater average power that the average power with PS passive control with HRCF basis functions, across all the range of frequencies considered. The discrepancy between the average absorbed power for the PS passive control with Fourier and HRCF basis functions is due to the nonconvexity of the passive control problem, which does not guarantee an unique solution to the optimization problem.

In Figure 5.14 and 5.16, a comparison between the optimal torques and relative pitch veloci-

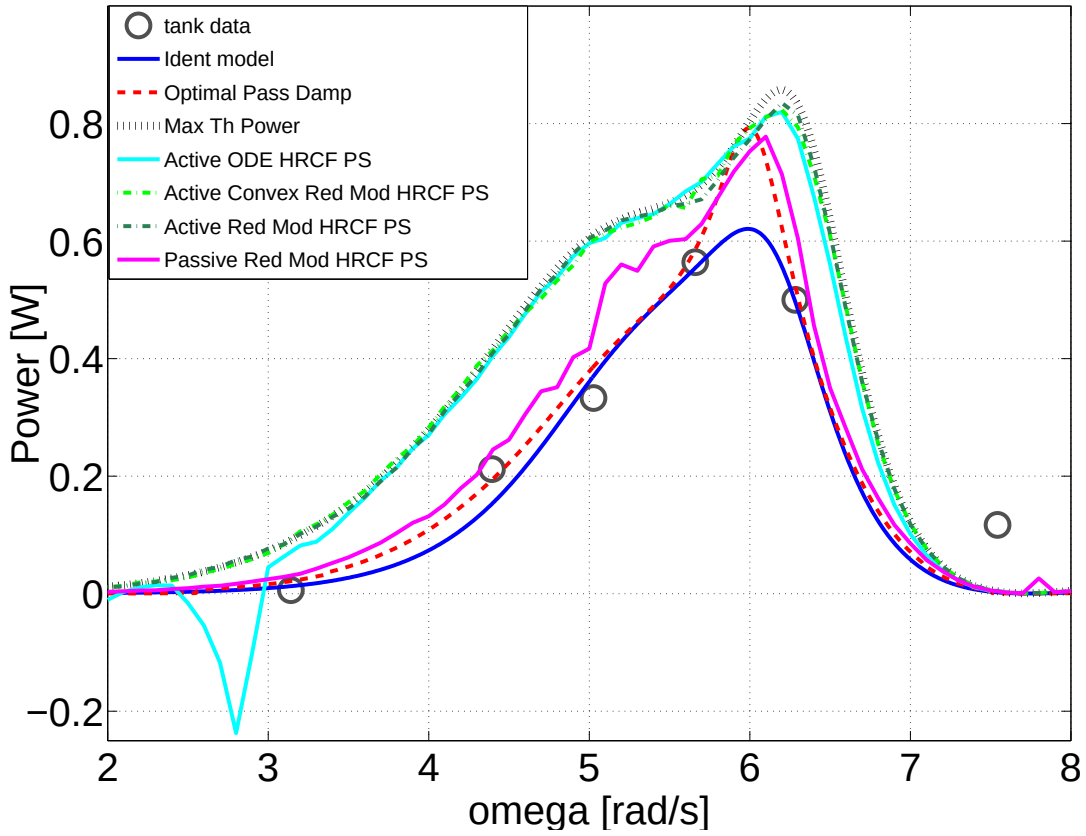

Figure 5.7: Comparison between the average power given by the tank data, identified model, max theoretical power, optimal linear damping control, non-convex active ODE HRCF PS control,convex active reduced model HRCF PS control and non-convex passive reduced model HRCF PS control for different frequencies of a regular wave of amplitude A = 2 cm.

ties computed by the passive controller, with HRCF basis functions and Fourier basis functions, is shown for a regular wave of amplitude A=0.02 m, and frequency $\omega = 3$ rad/s and $\omega = 6.5$ rad/s, respectively. As shown in Figures 5.14 and 5.16, the optimal torques and relative pitch velocities computed by the passive controller, with HRCF basis functions, do not converge to the optimal torques and relative pitch velocities computed by the passive controller with Fourier basis functions. However, the optimal trajectories of positions, velocities and control torques computed by the PS passive control with HRCF and Fourier basis functions show a similar phase delay, with a difference between their peak values.

In Figure 5.15 and 5.17, the average power absorbed with the passive controller with HRCF basis functions is compared to the average power absorbed with the passive controller with Fourier basis functions for a regular wave of amplitude A=0.02 m and frequency $\omega = 3$ rad/s and $\omega = 6.5$ rad/s, respectively. As shown in Figure 5.15 and 5.17, the average power absorbed with the passive controller, with HRCF basis functions, is less than the average powe absorbed with the passive controller with Fourier basis functions. The passive controller, with HRCF basis functions, shows worse power performance than the passive controller with Fourier basis functions due to the nonconvexity of the passive control problem, which strongly affects the convergence to the global

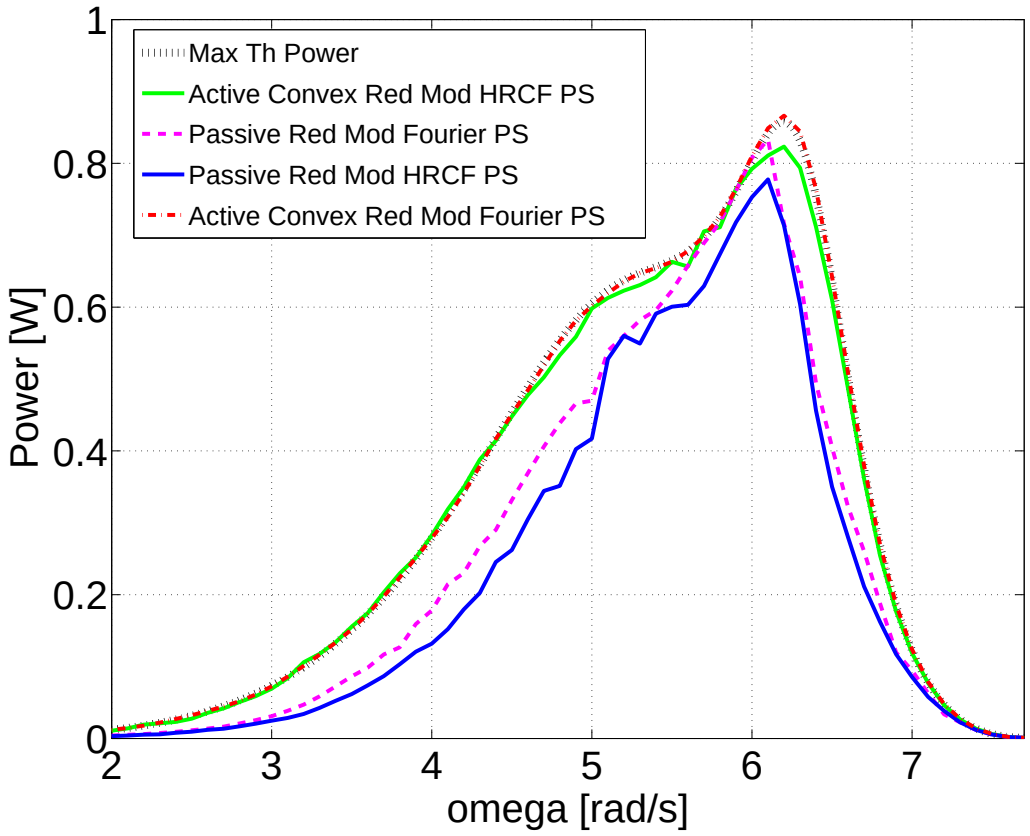

Figure 5.8: Comparison between max theoretical power, convex active reduced model Fourier PS control, convex active reduced model HRCF PS control, passive reduced model Fourier PS control and passive reduced model HRCF PS control for different frequencies of a regular wave of amplitude $A = 2$ cm.

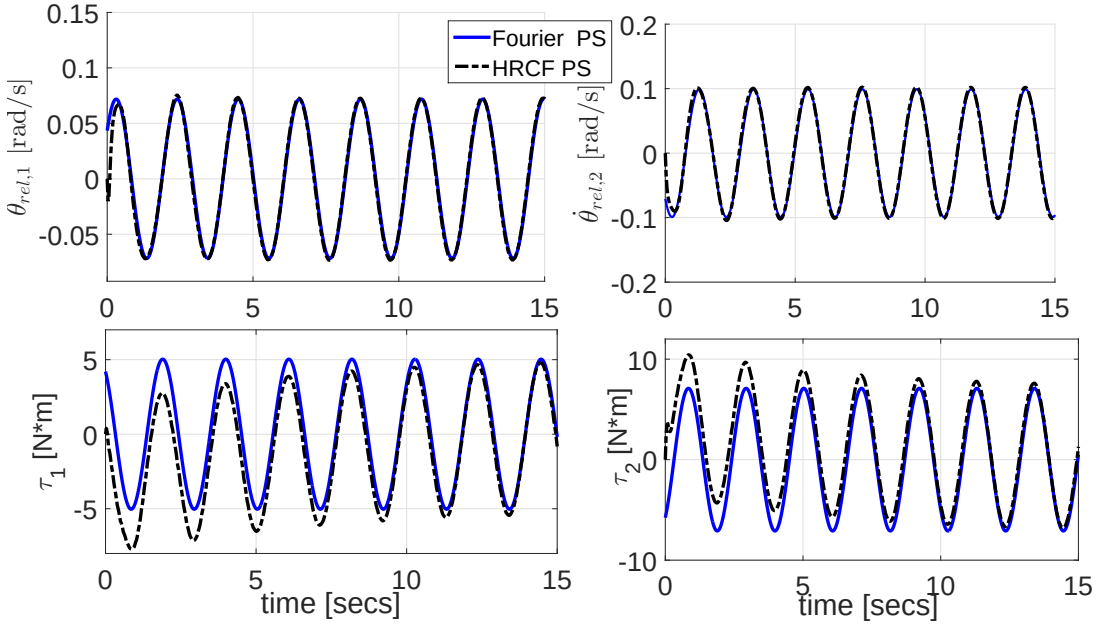

Figure 5.9: Comparison between optimal relative pitch angle velocities and PTO torques computed by active controller with HRCF and Fourier basis functions for regular wave of frequency $\omega = 3$ rad/s and amplitude A = 2 cm.

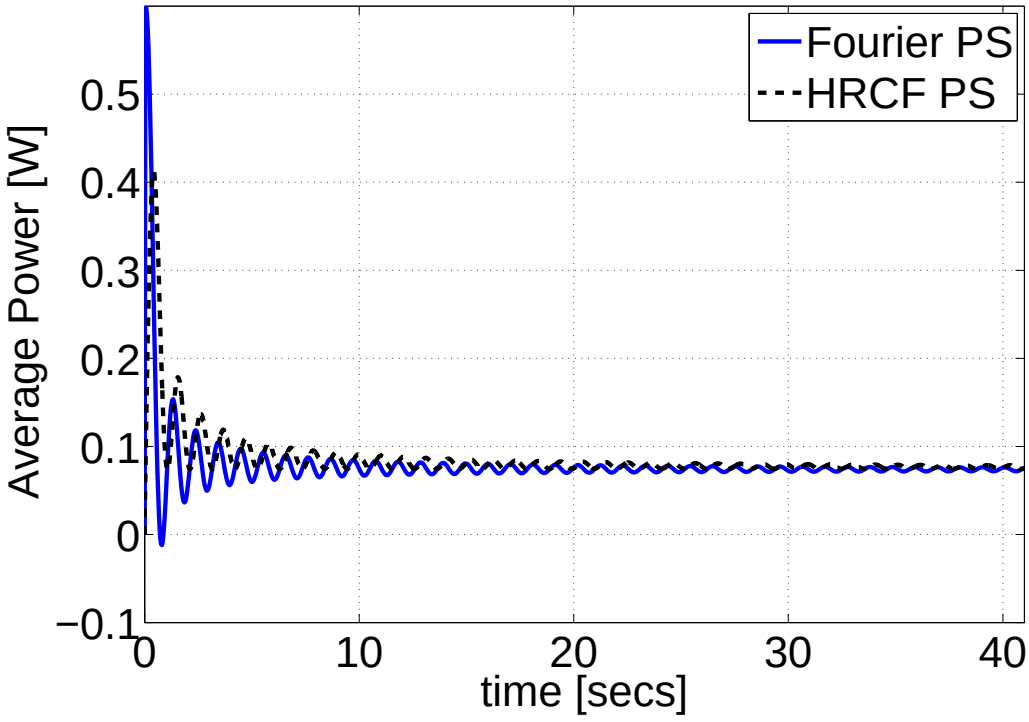

Figure 5.10: Comparison between the average absorbed power computed by active controller with HRCF and Fourier basis functions for regular wave of frequency $\omega = 3$ rad/s and amplitude A = 2 cm.

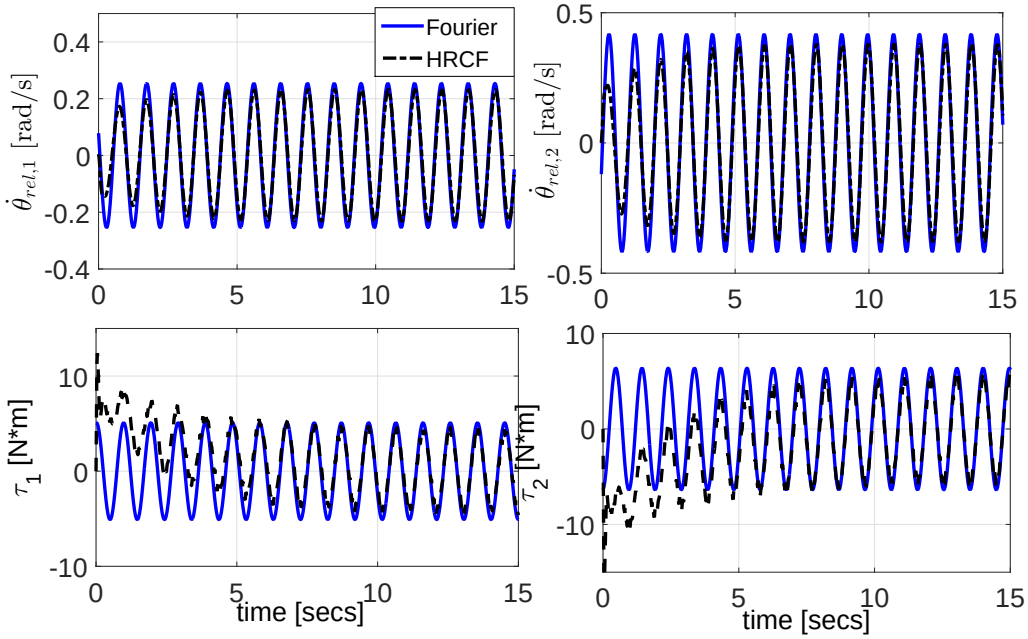

Figure 5.11: Comparison between optimal relative pitch angle velocities and PTO torques computed by active controller with HRCF and Fourier basis functions for regular wave of frequency $\omega = 6.5$ rad/s and amplitude A = 2 cm.

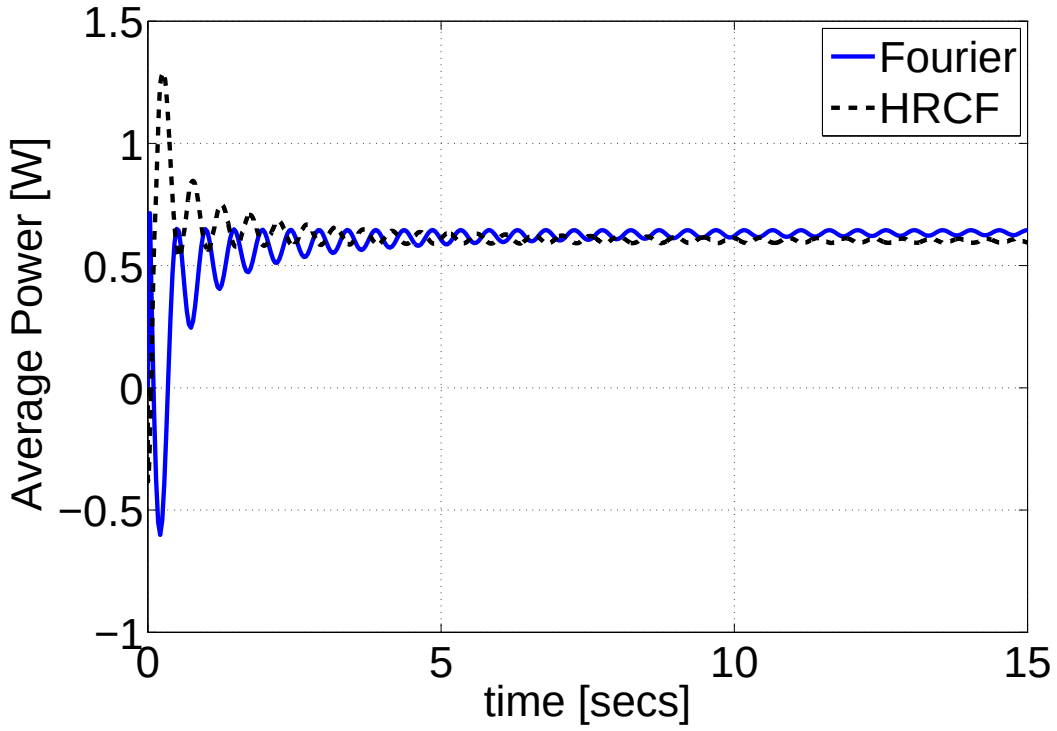

Figure 5.12: Comparison between the average absorbed power computed by active controller with HRCF and Fourier basis functions for regular wave of frequency $\omega = 6.5$ rad/s and amplitude A = 2 cm.

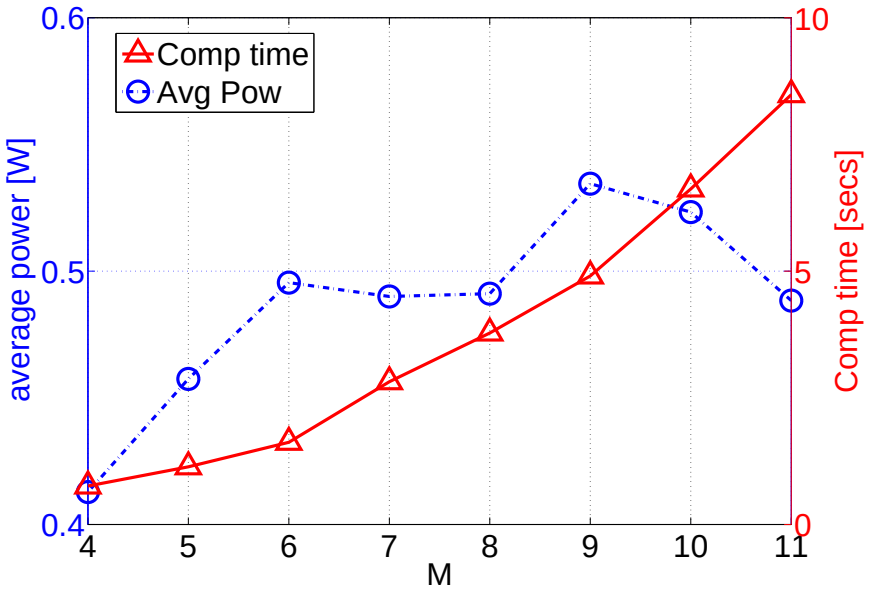

Figure 5.13: Absorbed power and computational time of the passive control for different values of M for a regular wave of frequency $\omega = 5$ rad/s and amplitude A = 2 cm.

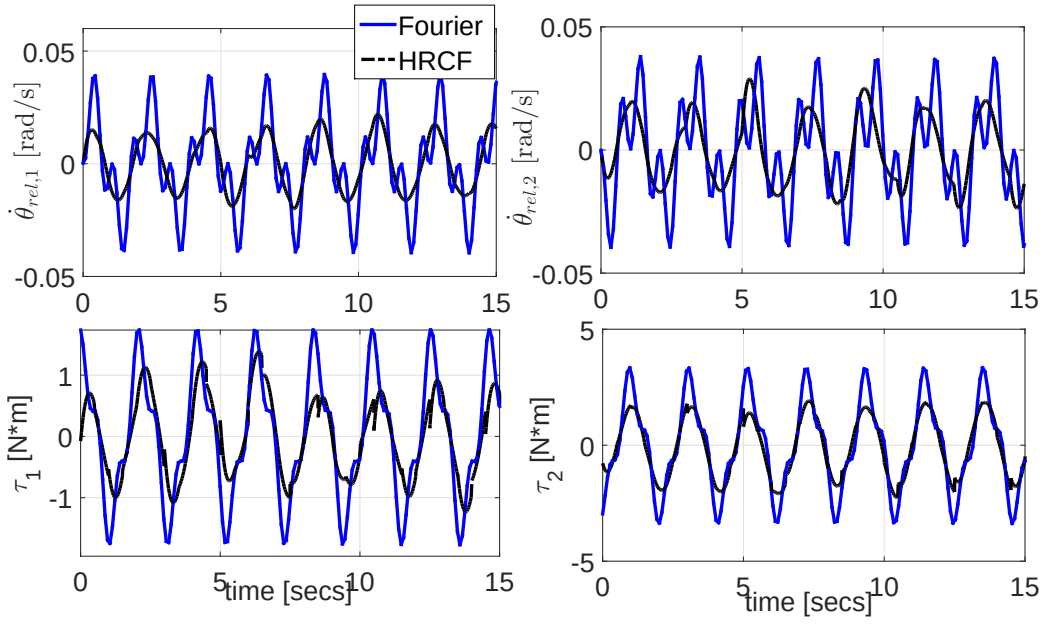

Figure 5.14: Comparison between optimal relative pitch angle velocities and PTO torques computed by passive controller with HRCF and Fourier basis functions for regular wave of frequency $\omega = 3$ rad/s and amplitude A = 2 cm.

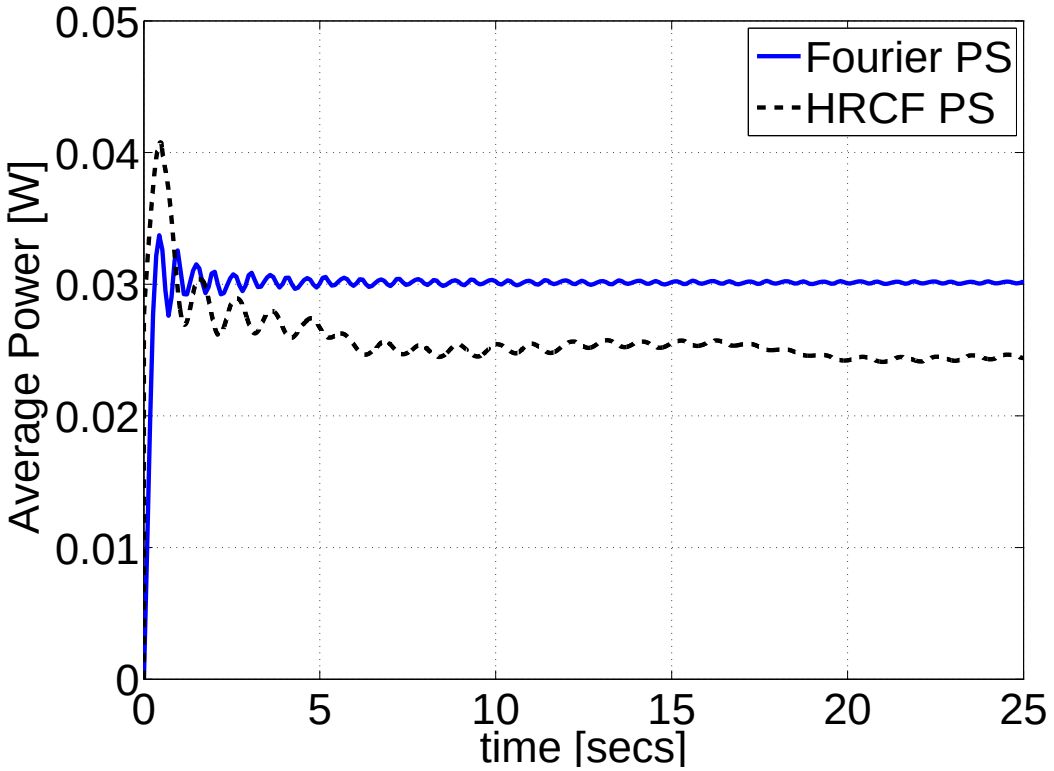

Figure 5.15: Comparison between the average absorbed power computed by passive controller with HRCF and Fourier basis functions for regular wave of frequency $\omega = 3$ rad/s and amplitude A = 2 cm.

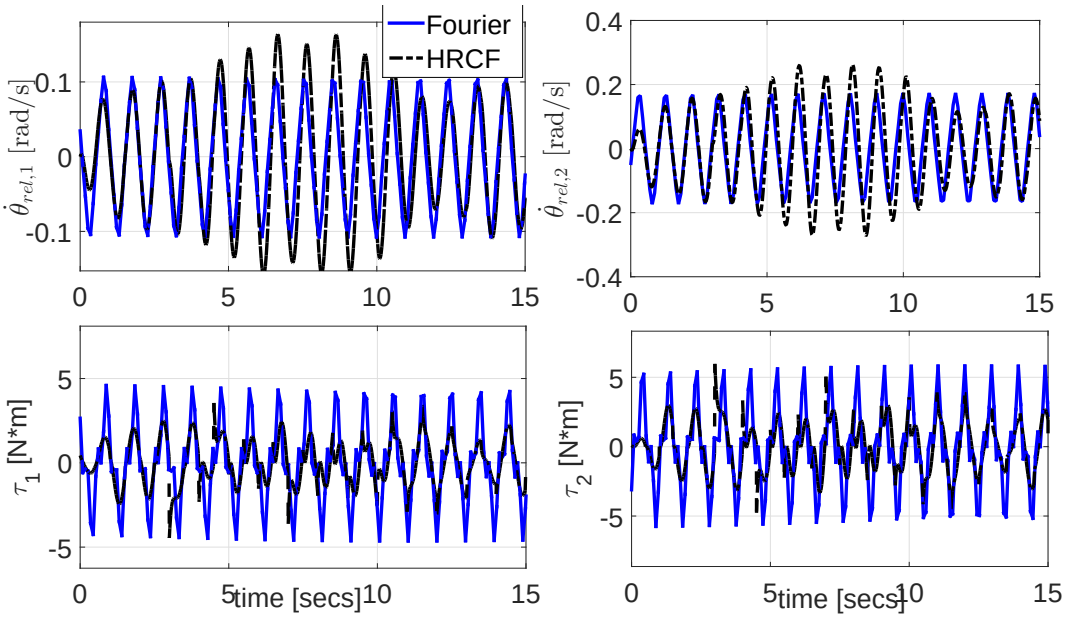

Figure 5.16: Comparison between optimal relative pitch angle velocities and PTO torques computed by passive controller with HRCF and Fourier basis functions for regular wave of frequency $\omega = 6.5$ rad/s and amplitude A = 2 cm.

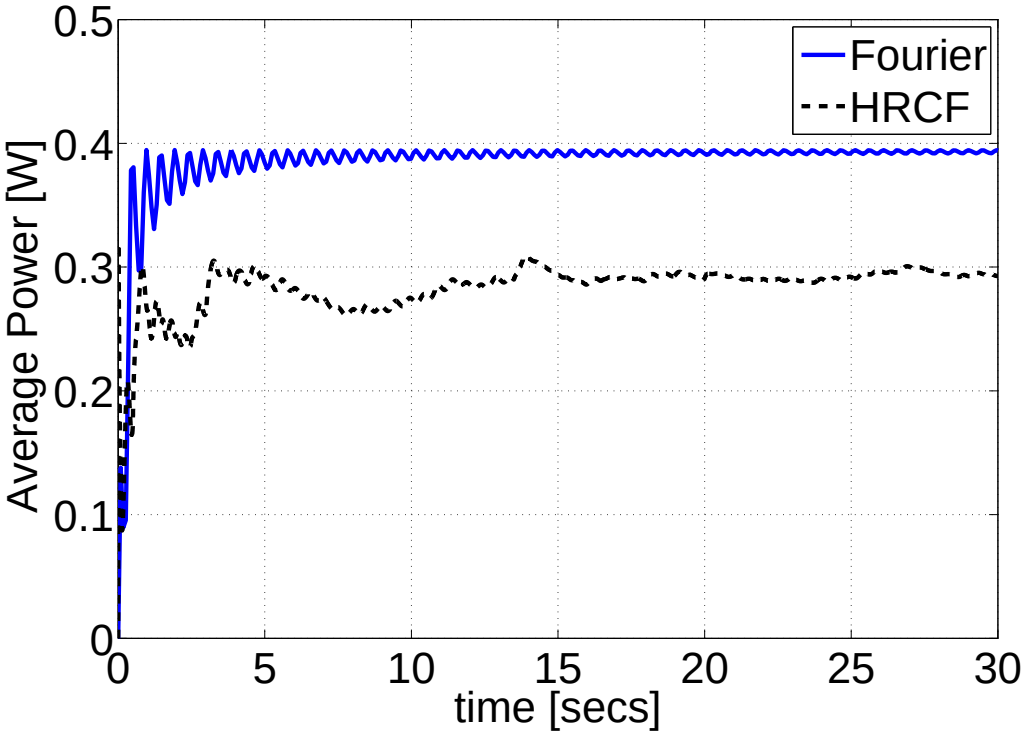

Figure 5.17: Comparison between the average absorbed power computed by passive controller with HRCF and Fourier basis functions for regular wave of frequency $\omega = 6.5$ rad/s and amplitude A = 2 cm.

optimal solution. However, for a number of HRCF basis functions $M > 6$ in the approximation of positions, velocities and control force, improves the power absorption achievable by the the passive controller with HRCF basis functions.

5.4.2 Polychromatic wave results

For polychromatic waves, under the assumption of the linear superposition of the hydrodynamic loads given by the individual frequency components of the incoming wave, the maximum theoretical average power is given as:

$$\overline{P}_{th,max} = \sum_{i}^{N_f} \overline{P}_{th,i} A_i^2 \tag{5.56}$$

where N_f is the number of frequency components of the incoming waves, A_i is the amplitude of the i frequency component and $\overline{P}_{th,i}$ is maximum theoretical average power computed for the i frequency component with unitary amplitude.

5.4.2.1 Active HRCF PS Control

In Figure 5.18, a comparison between the maximum theoretical average power and the average power absorbed with the optimal linear damping control, PS active convex and non-convex control with HRCF basis functions is shown for a polychromatic wave over a simulation time of 100 s. The polychromatic wave is from a JONSWAP spectrum with a significant wave height $H_s = 15$ *cm* and peak period $T_p = 1.1$ *s*. While the PS active control maximize the average absorbed power over the entire time horizon, the coefficients of dash-pot systems of the optimal linear damping control are set equal to their optimal values at the peak frequency of the spectrum of the incoming wave. As shown in Figure 5.18, the PS active convex and non-convex control compute an average power which asymptotically converges to the maximum theoretical power. As for regular wave case, a number of HRCF basis functions $M = 9$ is considered in the approximation of positions, velocities and control forces, for the PS active control. By a way of example, in Figure 5.19, the optimal torques and relative pitch velocities computed by the active controller are shown for a polychromatic wave made using JONSWAP spectrum with a significant wave height H_s = 15 cm and peak period T_p = 1.1 s.

In Figure 5.21, a comparison between the PS active control with HRCF basis functions, and the PS active with Fourier basis functions is shown for a polychromatic wave over a simulation time of 30 s. The polychromatic wave is from a JONSWAP spectrum with a significant wave height $H_s = 15$ *cm* and significant period $T = 1.1$ *s*. As Figure 5.21 shown, PS active control with HRCF basis functions converge to an average absorbed power which is the same as the average absorbed power computed with PS active control with Fourier basis functions. In contrast to the case with regular waves, for irregular waves, although the average absorbed power computed by active HRCF and Fourier PS control is the same, the optimal trajectories of the relative velocities and torques computed by the active HRCF and Fourier PS control are different.

5.4.2.2 Passive HRCF PS Control

In Figure 5.18, the average power absorbed with PS passive control with HRCF basis functions is shown for a polychromatic wave over a simulation time of 100 s. As for the PS active control, the PS passive control maximize the average absorbed power over the entire time horizon. Furthermore, as shown in Figure 5.18, the passive PS control shows better performances than the optimal linear damping control. As for regular wave case, a number of HRCF basis functions $M = 6$ is considered in the approximation of positions, velocities and control forces, for the PS passive control. By a way of example, in Figure 5.20, the optimal torques and relative pitch velocities computed by the active controller are shown for a polychromatic wave made using JONSWAP spectrum with a significant wave height H_s = 15 cm and peak period T_p = 1.1 s.

In Figure 5.21, a comparison between the PS passive control with HRCF basis functions, and the PS passive control with Fourier basis functions is shown for a polychromatic wave over a simulation time of 30 s. As shown in Figure 5.21, PS passive control with HRCF basis functions achieve an average absorbed power which is the less than the average absorbed power computed

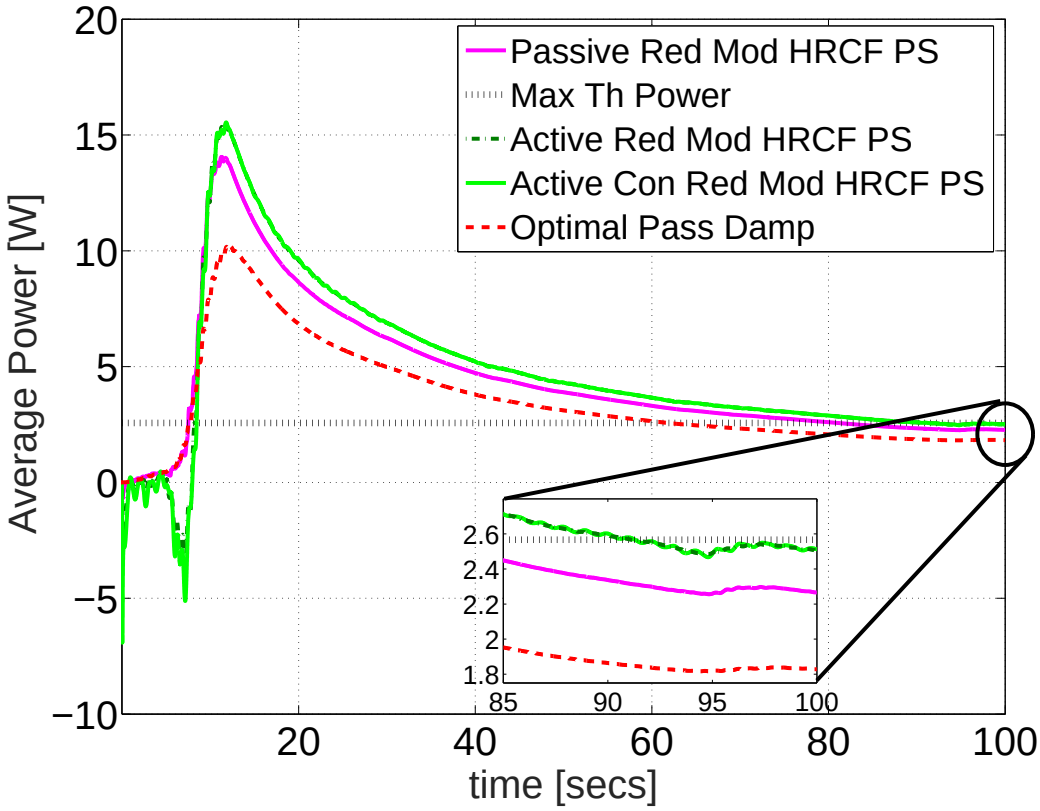

Figure 5.18: Comparison between the asymptotic maximum average power and the average power given by the optimal linear damping control, non-convex active reduced model HRCF PS control, convex active reduced model HRCF PS control and passive reduced model HRCF PS control for a polychromatic wave made from a Jonswap spectrum with $H_s = 15$ cm and $T_p = 1.1$ s.

with PS passive control with Fourier basis functions. As in the case of PS passive control with HRCF basis functions for regular waves presented in Section 5.4.1.2, the PS passive control with HRCF functions for irregular waves cannot find the global optimal solution, due to the nonconvexity of the passive control problem. As for the active control problem, the optimal trajectories of the relative velocities and torques computed by the passive HRCF and Fourier PS control are different.

5.5 Computational considerations

In this section, a comparison between the computational time required by PS methods with HRCF and Fourier basis functions to compute the active and passive controller is made. While PS methods with HRCF basis functions are used solve the optimal control problem over the control horizon at each time step, PS methods with Fourier basis functions are used to solve the optimal control

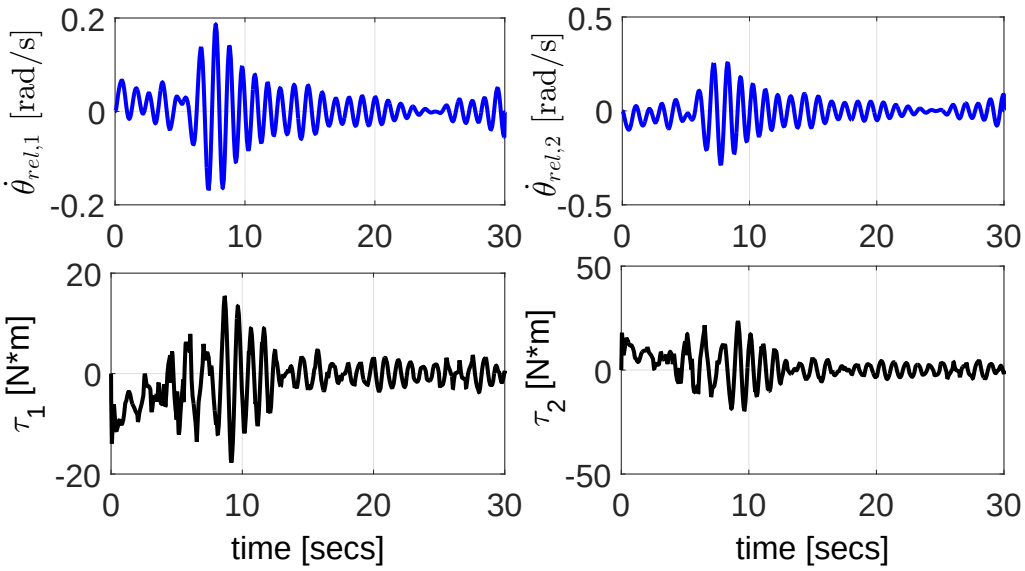

Figure 5.19: Optimal relative pitch angle velocities and PTO torques computed by active controller with HRCF basis functions for a polychromatic wave made using JONSWAP spectrum with a significant wave height H_s = 15 cm and peak period T_p = 1.1 s.

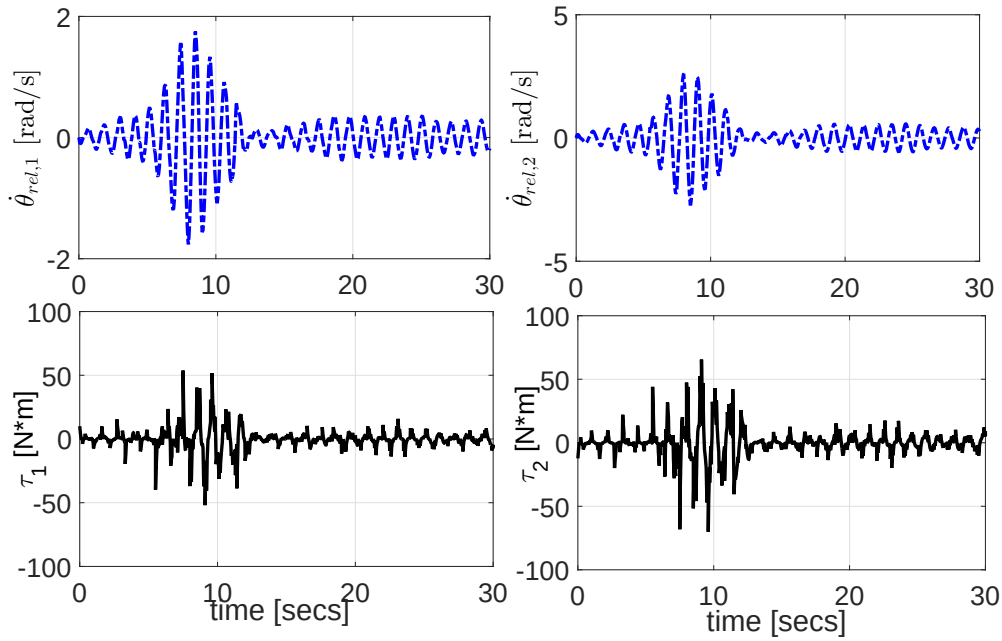

Figure 5.20: Optimal relative pitch angle velocities and PTO torques computed by passive controller with HRCF basis functions for a polychromatic wave made using JONSWAP spectrum with a significant wave height H_s = 15 cm and peak period T_p = 1.1 s.

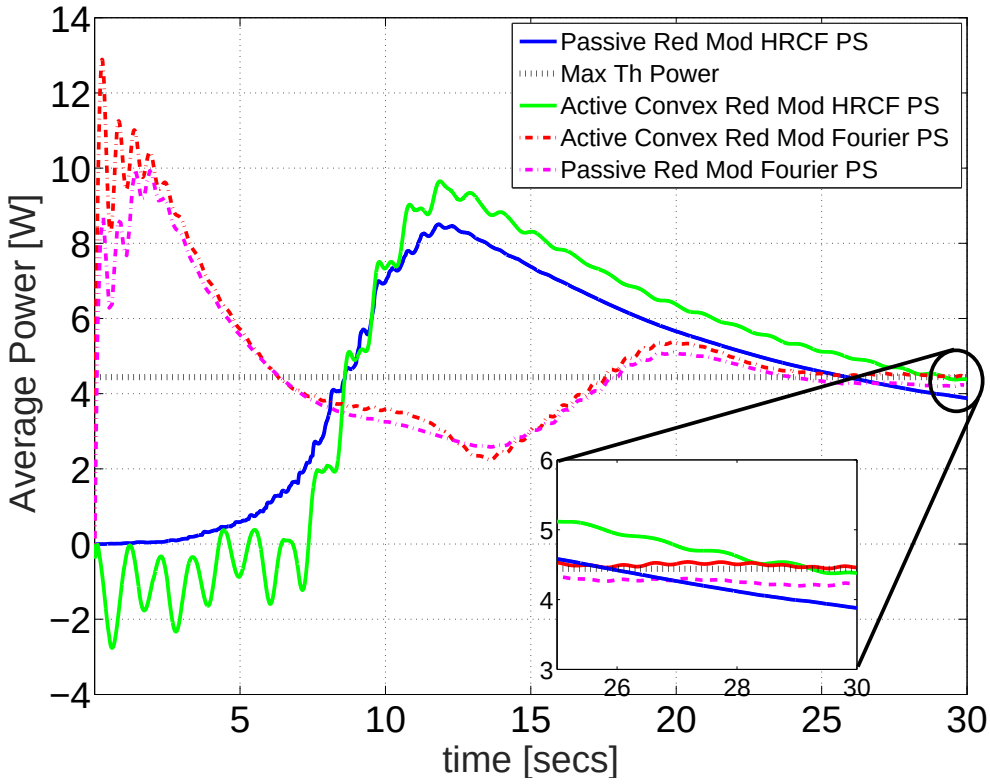

Figure 5.21: Comparison between max theoretical power, convex active reduced model Fourier PS control, convex active reduced model HRCF PS control, passive reduced model Fourier PS control and passive reduced model HRCF PS control for a polychromatic wave made from a Jonswap spectrum with $H_s = 15$ cm and $T_p = 1.1$ s.

problem only once over a finite time horizon. Therefore, given the different nature of the control strategies with PS methods with HRCF and Fourier basis functions, a comparison between the computational time required by PS methods with HRCF and Fourier basis functions cannot be made with respect to the time horizon. Instead, PS methods with HRCF and Fourier basis functions can be compared in terms of number of basis functions involved in the approximation of positions, velocities and control inputs.

In Table 5.1, the comparison between the computational time required by PS methods with Fourier and HRFC basis functions to compute the active and passive controller for different numbers of basis functions is presented. The comparison is made for a regular wave of frequency ω=4 rad/s and amplitude 0.02 m, since the number of basis functions required by PS methods with Fourier basis functions for irregular waves greatly exceeds the maximum number of basis functions that can be used by PS methods with HRCF basis functions. As shown in Table 5.1, for the computation of the active controller with the ODE formulation and nonconvex reduced equivalent model, the computational time required by PS methods with HRCF basis functions is less than the computational time required by PS methods with Fourier basis functions. However, for the computation of the active controller with the convex reduced equivalent model and passive control with nonconvex reduced equivalent model, the computational time required by PS methods with HRCF basis functions is greater than the computational time required by PS methods with Fourier basis functions. Therefore, the complexity of PS methods with HRCF and Fourier basis functions depends on the nature of the controller, whether active or passive, and the formulation used to describe the dynamic model of the device. Overall, Table 5.1 shows that there are no computational disadvantages in using HRCF basis functions, as opposed to Fourier basis functions, for the formulation of the optimal control problem.

5.6 Low-level control

As shown in Figure 5.3, the reference velocity vector $\mathbf{v}_{ref}$computed by the high-level control based on PS control with HRCF basis functions is tracked by a low-level control, which manipulates the control input vector of the WEC. Therefore, the low-level control acts on the PTO force vector so that the velocity vector $\mathbf{v}$ of the WEC follows the reference $\mathbf{v}_{ref}$. Usually, the low-level control is based on a feedback controller, as shown in Figure 5.22. In [11], a feedback controller based on the concept of Internal Model Control (IMC) [92] is proposed. In [93], IMC is also proposed for the Archimed Wave Swing WEC. In [80], a feedback control based on a backstepping method [94] is proposed.

Alternatevely, for the case of a WEC with a hydraulic PTO, a feedforward control can be adopted for the low-level control, as shown in Figure 5.23. In case of a hydraulic PTO, the damping force exerted by the PTO can be varied by acting on the opening of the valves that regulate the flow of a hydraulic fluid. As shown in Figure 5.23, the reference velocity vector $\mathbf{v}_{ref}(k)$ and control vector $\mathbf{u}_{s,ref}(k)$, computed by PS control based on HRCF basis functions, are used to

Number Functions	Active Control						Passive Control	
	Fourier			HRCF				
	ODE [s]	**Non-conv Red Mod** [s]	**Conv Red Mod** [s]	**ODE** [s]	**Non-conv Red Mod** [s]	**Conv Red Mod** [s]	**Fourier Non-Conv Red Mod** [s]	**HRCF Non-Conv Red Mod** [s]
9	0.0067	0.0049	$1 \cdot 10^{-6}$	0.0029	$1.5 \cdot 10^{-3}$	$2.7 \cdot 10^{-4}$	0.85	0.85
11	0.0076	0.0052	$1 \cdot 10^{-6}$	0.0035	$2.1 \cdot 10^{-3}$	$3.2 \cdot 10^{-4}$	0.87	1.42
13	0.0081	0.0071	$1 \cdot 10^{-6}$	0.0042	$2.7 \cdot 10^{-3}$	$5.3 \cdot 10^{-4}$	1.80	2.11
15	0.0088	0.0082	$1 \cdot 10^{-6}$	0.0050	$3.1 \cdot 10^{-3}$	$6.1 \cdot 10^{-4}$	2.16	3.4
17	0.0100	0.0093	$1 \cdot 10^{-6}$	0.0060	$3.5 \cdot 10^{-3}$	$6.5 \cdot 10^{-4}$	3.35	4.1
19	0.0290	0.0150	$1 \cdot 10^{-6}$	0.0070	$3.7 \cdot 10^{-3}$	0.001	4.58	5.12

Table 5.1: Computational time in seconds required to compute the active and passive controller with Fourier and HRCF basis functions for a regular wave of frequency ω=4 rad/s and amplitude 0.02 m.

determine the optimal passive damping for the PTOs. Then, given a static mapping between the PTOs damping and opening of the valves, as shown in Figure 5.23, the opening of the valves is changed accordingly by the feedforward control. A feedforward control of a passive PTO is proposed for the optimal control of a 1/20th scale three-body hinge-barge device in Chapter 7.

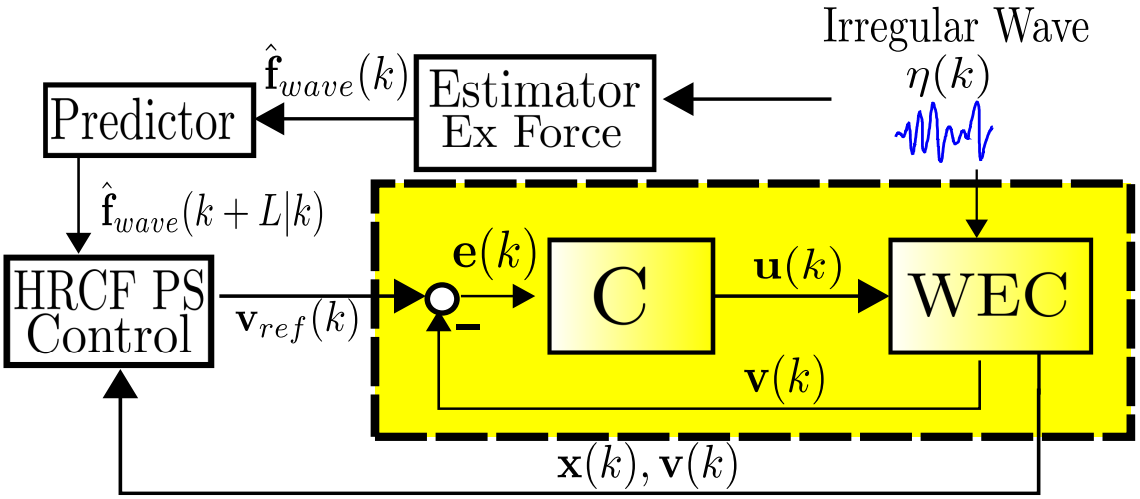

Figure 5.22: RHPSC scheme with low-level control of the PTO based on a feedback controller for a generic multibody WEC in the discrete time domain

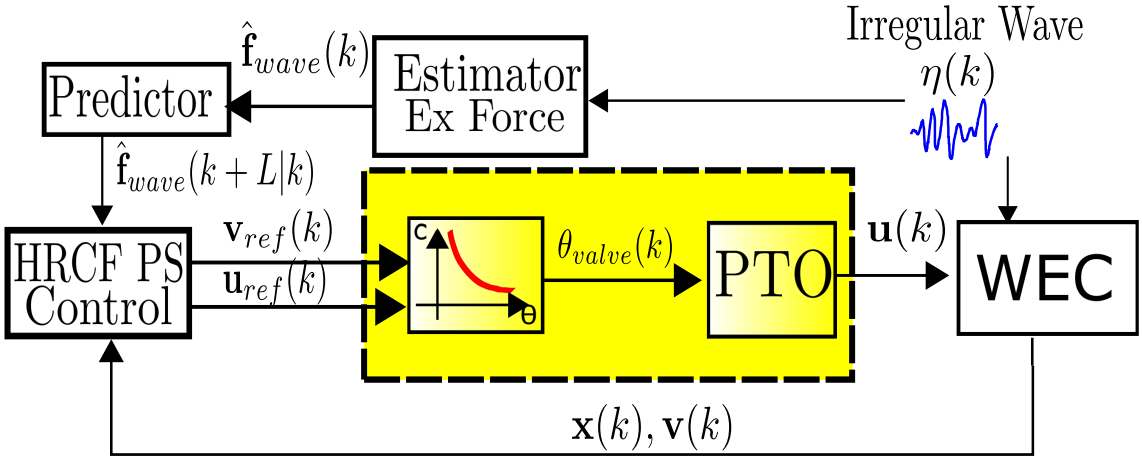

Figure 5.23: RHPSC scheme with low-level control of the PTO based on a feedforward controller for a generic multibody WEC in the discrete time domain

5.7 Conclusions

This chapter assess the value of receding horizon PS control with HRCF basis functions for the maximization of the energy extracted by a three-body hinge-barge device. In contrast to the optimal control strategy presented in Chapter 4, which computes a steady-state solution to the optimal control problem, receding horizon PS control with HRCF basis functions can be used for real-time control of the device. In fact, given a dynamic model of the device and the initial conditions on positions, velocities and control torques, the receding horizon PS control computes the optimal trajectories of positions, velocities and control torques that maximize the energy extracted by the device over a time horizon in the future at each time step. For the optimal control with Fourier basis functions presented in Chapter 4, the variables associated with the control problem are assumed to be periodic, and no initial conditions on positions, velocities and control torques can be specified.

In terms of power absorption performance, the PS active control with HRCF basis functions achieves the same average absorbed power as PS active control with Fourier basis functions, for both regular and irregular waves. Furthermore, for regular waves, the optimal trajectories of positions, velocities and control torques computed with PS active control, with HRCF basis functions, converge to the optimal steady-state solutions computed with PS active control, with Fourier basis functions. For irregular waves, PS active control with HRCF and Fourier basis functions compute different trajectories of positions, velocities and control torques. For PS passive control with regular and irregular waves, the average power absorbed with HRCF basis functions is lower than the average power achieved with Fourier basis functions. The difference between the average power computed by the PS passive control with HRCF and Fourier basis functions is due to the non-convexity associated with the optimal passive control problem, which does not guarantee that a solution to the optimization problem is a global optimal solution. However, for regular waves, the optimal trajectories of positions, velocities and control torques computed by the PS passive

control with HRCF and Fourier basis functions show a similar phase delay, with a difference between their peak values. As for the PS active control, for irregular waves, the PS passive control with HRCF and Fourier basis functions compute different trajectories of positions, velocities and control torques.

As in the case of PS control with Fourier basis functions, the use of the reduced equivalent model presented in Section 4.2 greatly reduces the computational effort required by the controller with HRCF basis functions to compute the optimal solution. As shown in Table 5.1, the computational time required by PS methods, with HRCF basis functions, to compute the active controller with the reduced equivalent model is 2 times smaller than the time required with the ODE formulation. Furthermore, while the optimization problem for the active control with the ODE is non-convex, a convex optimization problem for the active control with the reduced equivalent model can be found, which guarantees a globally optimal solution. For the comparison between the computational effort required by PS methods with HRCF and Fourier basis functions, as shown in Table 5.1, the complexity of PS methods depends on the nature of the controller, whether active or passive, and the formulation used to describe the dynamic model of the device. Overall, Table 5.1 shows that there are no computational disadvantages in using HRCF basis functions, rather than Fourier basis functions, for the formulation of the optimal control problem.

In terms of formulation used to describe the dynamics of the device, the DAE formulation is not considered in the implementation of the PS control with HRCF basis functions, given that it requires a relatively high computational time to compute the PS control with Fourier basis functions, compared to the ODE formulation and reduced equivalent model, as presented in Table 4.1. Therefore, the DAE formulation is not a suitable candidate for the real-time control of the device, as it does not represent a computationally efficient formulation for the optimal control problem. Regarding the ODE formulation, the nonconvexity associated with the PS active control problem strongly influences the convergence to the optimal global solution. In fact, for regular waves, the PS active control, based on the ODE formulation, cannot compute the global solution for a range of frequencies from 2.5 rad/s to 3 rad/s. However, for a range of frequencies greater than 3 rad/s, the PS active control based on the ODE formulation computes an average absorbed power which is close to the maximum theoretical power. For irregular waves, the PS active control based on the ODE formulation diverges from the global optimal solution, and computes a negative average power. Therefore, the reduced equivalent model is more suitable for the real-time control of a three-body hinge-barge device than a full dynamic model, as it always provides the global optimal solution to the PS active control problem, and reduces the complexity of the controller.

Chapter 6

Excitation force estimation

In Chapter 5, a real-time optimal controller, for the maximization of the energy extracted by a three-body hinge-barge WEC, is presented. In the wave energy scenario, several control strategies have been developed to maximize the energy extracted by a WEC. However, most of the control strategies, including the real-time optimal controller developed in Chapter 5, require knowledge of the current and future wave excitation force acting upon the wet surface of the device. It has been proven that the effectiveness of different real-time control strategies depends on the prediction of the future wave elevation or wave excitation force acting on the device [95], [96], [11], [97], [9]. Some others developed sub-optimal control schemes that minimize or eliminate the need for knowledge of the future excitation force [98]. Nevertheless, for the vast majority of WEC controllers, future knowledge of the wave excitation force is an essential requirement, to maximize the energy extraction from the WEC. Optimal energy extraction is mandatory in order to reach the economic viability of wave energy [12], [15], reaching a commercial state.

6.1 Review of excitation force estimation

The wave excitation force acting upon a WEC can be estimated with two different estimator types: feedback and feedforward. As shown in Figure 6.1a, the feedback estimator is based only on the measurement of the position and velocity of the WEC, in addition to the control input to the WEC. The feedback estimator computes an estimate of the excitation force, based on a dynamic model of the WEC, and knowledge of the control input. Then, the estimate of the excitation force is corrected by using the measurements of the position and velocity of the WEC. For the implementation of the feedback estimator, only sensors for the measurement of position and velocity of the WEC are required, which are already available by virtue of the optimal control of the WEC.

As shown in Figure 6.1b, the feedforward estimator is based on the measurement of the wave elevation up-wave of the WEC. The feedforward estimator computes an estimate of the excitation force, based on a transfer function between the wave elevation up-wave of the WEC, and the excitation force. The transfer function between the wave elevation up-wave of the WEC, and the excitation force, can be determined with two different approaches. For the first approach,

the transfer function between the wave elevation up-wave of the WEC, and the excitation force, is computed by using linear potential theory [99]. For the second approach, the transfer function between the wave elevation up-wave of the WEC, and the excitation force, is experimentally determined from observations of the position of the WEC, and of the wave elevation up-wave elevation, as presented in Section 3.5.3.2.

The feedback estimator is naturally robust to uncertainty on the parameters of the dynamic model of WEC, as the feedback on the position and velocity of the WEC corrects the estimates of the excitation force computed based on the dynamic model of the device only. However, the feedforward estimator computes the excitation force purely on the basis of the transfer function between the wave elevation up-wave of the WEC, and the excitation force. Therefore, a small variation of the parameters of the transfer function, between the wave elevation up-wave of the WEC and the excitation force, results into a large decrease in the performance of the feedforward estimator.

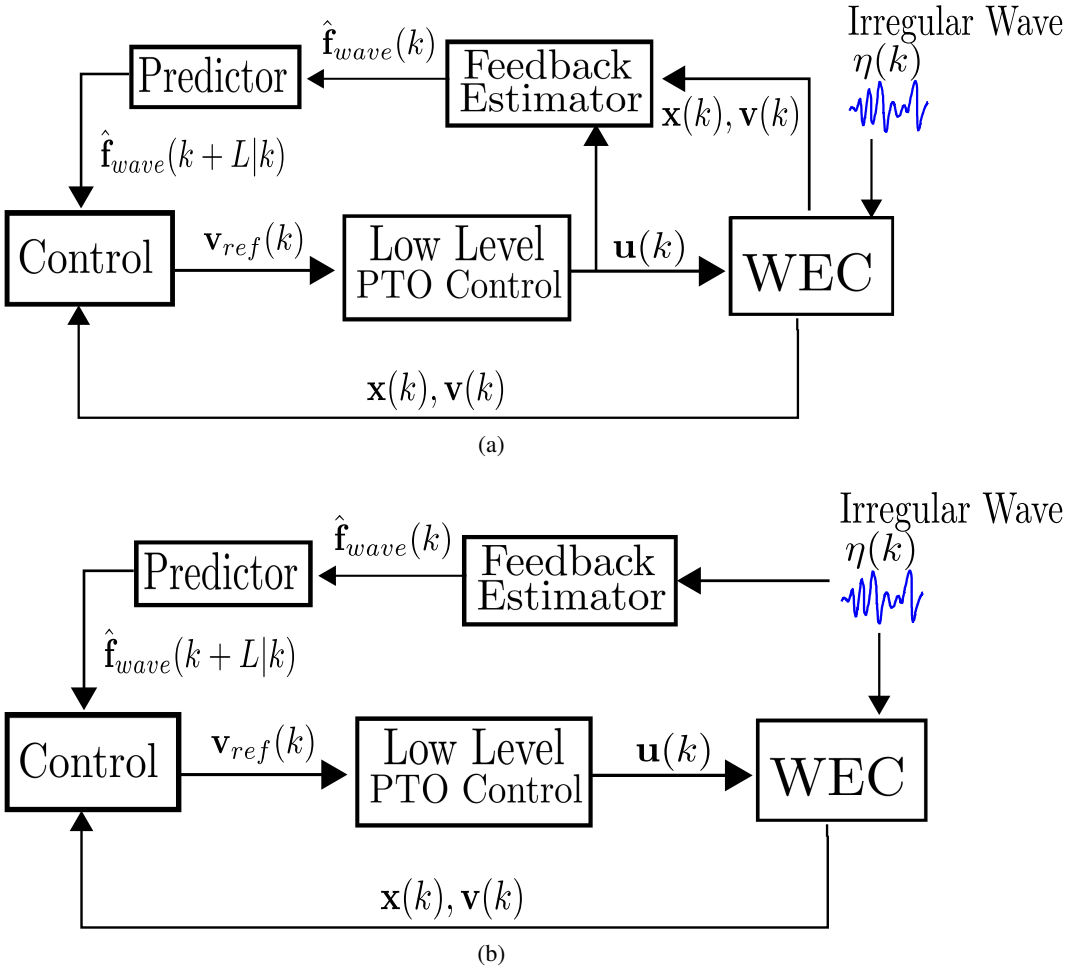

Figure 6.1: Feedback estimator (a) and feedforward estimator (b) of the excitation force of a WEC.

Regarding the feedback estimation of the excitation force, a feedback estimator based on the

measurement of the position and velocity of a heaving buoy, and on pressure measurements at 9 points on the surface of the WEC, is considered in [100]. The feedback estimator is based on a state-space model of the WEC, whose state vector X comprises the position and velocity of the WEC, in addition to the amplitudes, frequencies and phases associated with N dominating frequency components of the wave elevation. The outputs of the state-space model are the position and velocity of the WEC, and the pressure at the points on the surface of WEC, where the pressure measurements are taken. The total force acting on the buoy surface, which includes the excitation force, hydrostatic force, radiation force and viscous damping force, can be computed in terms of the state vector X, using potential flow theory. Furthermore, the pressure on the surface of the WEC can be also computed in terms of the state vector X, using potential flow theory. Therefore, the resulting state-space model is nonlinear with respect to the state vector X, due to the nonlinear relationship between the state vector X, and the pressure on the surface of the WEC and the excitation force. An Extended Kalman Filter (EKF) is used in [100] to compute an estimate of the state vector X, based on a linearization of the state-space model, at each sampling period.

In [101], the wave excitation force of a heaving buoy is estimated by using a feedback estimator, which is based on the observation of the position and velocity of WEC, without any extra wave measurements. The feedback estimator is based on a nonlinear state-space model of the buoy coupled with a Tubular Permanent Magnet Linear Generator (TPMLG). The dynamics of the buoy coupled with TPMLG is nonlinear due to the nonlinear relationship between the currents of the TPMLG and the force applied by the TPMLG on the WEC. The instantaneous estimate of the wave excitation force, in the nonlinear state space model, is obtained via a nonlinear adaptive observer, which is inspired by the Fast Adaptive Fault Estimation (FAFE) technique addressed in [102]. The adaptive observer uses proportional and integral terms of the state estimation error in order to ensure fast and accurate estimation of the wave excitation force, which is considered as an unknown input signal.

In [103], the wave excitation force of a heaving buoy is estimated using a feedback estimator, which is based on observation of position and velocity of the WEC. The feedback estimator is based on a linear state-space model of the WEC, where the radiation force is linearly proportional to the velocity of the WEC. The excitation force in the linear state-space model is estimated using a Kalman filter.

Regarding the feedforward estimation of the excitation force, in [104], the wave excitation forces of a two-body WEC are estimated using a feedforward estimator, based on the measurement of the wave elevation up-wave of the WEC. The Fourier transform of the wave elevation up-wave of the WEC is computed and, then, the excitation forces of the WEC are calculated by using the transfer functions between the wave elevation up-wave of the WEC and the excitation forces. The transfer functions between the wave elevation up-wave of the WEC and the excitation forces, are obtained using linear potential theory [99].

For the *prediction* of the excitation force, an Auto-Regressive (AR) model can be applied ([105]). The forecasting horizon required by the real-time control depends on the characteristics of the impulse response of the radiation damping of the device [12]. Many researches have worked

on the prediction of future wave elevation, rather than the prediction of the excitation force [11]. In [106], adaptive filters, based on autoregressive models for wave prediction, are employed. In [107], a robust control strategy, for wave energy devices, based on the prediction of wave elevation, is implemented. For wave prediction, a hybrid Kautz/AR predictive model, as well as a purely predictive Kautz model, are proposed. In [108], neural networks were trained, for the estimation of the wave excitation force, and results compared to other methods.

In this chapter, a feedback and feedforward estimators, for the estimation of the excitation forces of a three-body hinge-barge device, are developed. The feedback estimator is based on a linear dynamic model of the device, and on measurement of position and velocity of the device, with the excitation forces considered to be unknown inputs. The excitation forces, in the linear dynamic model of the WEC, are estimated by using a Kalman filter. The dynamic model of the device is described by using the reduced equivalent model, since the reduced equivalent model is computationally faster than the ODE formulation, for the implementation of the real-time optimal controller, as shown in Table 5.1. Furthermore, as shown in Figure 5.7, PS control with the reduced equivalent model shows convexity properties that guarantee the convergence to the global optimal solution, as opposed to PS control based on ODE formulation, which cannot converge to an acceptable solution for regular waves with a frequency range from 2.5 rad/s to 3 rad/s.

The feedforward estimator is formulated in the frequency domain, and is based on the transfer functions between the wave elevation up-wave of the WEC, and the excitation forces. The transfer functions between the wave elevation up-wave of the WEC, and the excitation forces, are computed from the measurement of the position of the device and the surface elevation up-wave of the device, as presented in Section 3.5.3.2. The transfer functions between the wave elevation up-wave of the WEC and the excitation forces are derived from the reduced equivalent model.

In this chapter, for the *prediction* of the excitation forces, an AR model is fitted to the estimated excitation force given by the feedback and feedforward estimators, and used to predict its future values.

The remainder of this chapter is organized as follows: in Section 6.2, a feedback estimator for the excitation forces of a three-body hinge-barge device is presented, while, in Section 6.3, a feedforward estimator for the excitation forces of the device is derived. In Section 6.4, an AR model for the prediction of the excitation forces based on the estimated excitation forces, given by the feedback and feedforward estimators, is developed. In Section 6.5, the results of the feedback estimator, feedforward estimator and AR model applied to a 1/25th scale three-body hinge-barge device, under both regular and irregular waves, are presented. Finally, in Section 6.6, overall conclusions are drawn.

6.2 Feedback estimation of excitation forces

In this section, a feedback estimator for the excitation forces acting on a three-body hinge-barge device is formulated in the time-domain, and is based on the measurements of the variables that are affected by the excitation forces, e.g. position and velocity of the device. The feedback estimator

is based on a Kalman Filter, which makes use of measurements of position and velocity of the device for estimating the excitation forces acting on the wet surface of the WEC. In Figure 6.2, the Kalman filter scheme for the estimation of the excitation forces acting on a generic multibody WEC in the discrete time domain is shown. The Kalman filter takes, as inputs, the control forces, and computes, as outputs, an estimation of the excitation forces, positions and velocities based on an linear model of the WEC. Then, the estimates of the excitation forces, positions and velocities are corrected by using the available measurements of position and velocities.

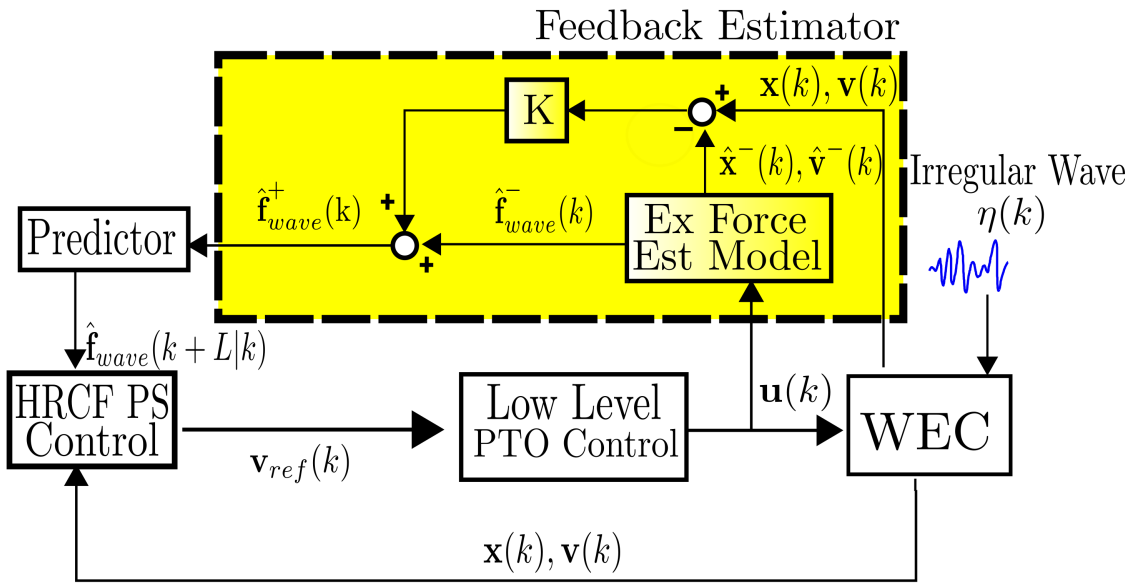

Figure 6.2: Kalman filter scheme for the estimation of the excitation forces acting on a generic multibody WEC in the discrete time domain

In Section 6.2.1, an overview of the Kalman filter is presented, while, in Section 6.2.2, a linear dynamic model of the WEC, for the Kalman filter, is developed.

6.2.1 Kalman filter

The Kalman filter is an optimal linear estimator which estimates the states of a linear dynamic system. In this work, the formulation of the Kalman filter is based on [109], and the dynamical model used by the filter is described as follows:

$$\hat{\mathbf{s}}_{k+1} = \mathbf{A}_d \hat{\mathbf{s}}_k + \mathbf{B}_d \mathbf{u}_k + \mathbf{G}_d w_k \tag{6.1}$$

$$\mathbf{y}_k = \mathbf{H}_d \hat{\mathbf{s}}_k + \mathbf{v}_k \tag{6.2}$$

$$\mathbf{w}_k \sim (0, \mathbf{Q}) \tag{6.3}$$

$$\mathbf{v}_k \sim (0, \mathbf{R}) \tag{6.4}$$

where $\hat{\mathbf{s}}_k$ represents the estimated states, $\mathbf{u}_k$ represents the control vector states, $\mathbf{y}_k$ is the measurement vector, $\mathbf{w}_k$ and $\mathbf{v}_k$ are the white noise present in the process and in the measurements, respectively, with both noise signals assumed to be stationary. The matrix $\mathbf{A}_d$ is the dynamic matrix, $\mathbf{B}_d$ is the input matrix, $\mathbf{H}_d$ is the measurement matrix, $\mathbf{G}_d$ is the weighting matrix for the state errors, while $\mathbf{Q}$ and $\mathbf{R}$ represents the covariance matrices of the white noise considered in the process and the measurements, respectively.

The Kalman filter is based on two steps [109]: the prediction or time update (TU), and the correction or measurement-update (MU). In the TU step, the algorithm estimates the state variables with some uncertainty $\mathbf{P}_{KF}$, which is the effect of the system dynamics. Then, the estimate of the state vector computed during the TU step is improved by using the measurements provided by the sensors. The TU and MU steps are detailed as follows:

KF *a priori* recursive step (TU):

$$\mathbf{P}^{-}_{KF,k+1} = \mathbf{A}_d \mathbf{P}_{KF,k} \mathbf{A}_d^T + \mathbf{G}_d \mathbf{Q} \mathbf{G}_d^T \tag{6.5}$$

$$\hat{\mathbf{s}}^{-}_{k+1} = \mathbf{A}_d \hat{\mathbf{s}}_k \tag{6.6}$$

KF *a posteriori* recursive step (MU):

$$\mathbf{K}_{KF,k+1} = \mathbf{P}^{-}_{KF,k+1} \mathbf{H}_d^T (\mathbf{H}_d \mathbf{P}^{-}_{KF,k+1} \mathbf{H}_d^T + \mathbf{R})^{-1} \tag{6.7}$$

$$\mathbf{P}_{KF,k+1} = (\mathbf{I} - \mathbf{K}_{KF,k+1} \mathbf{H}_d) \mathbf{P}^{-}_{KF,k+1} \tag{6.8}$$

$$\hat{\mathbf{s}}_{k+1} = \hat{\mathbf{s}}^{-}_{k+1} + \mathbf{K}_{KF,k+1} (\mathbf{y}_{k+1} - \mathbf{H}_d \hat{\mathbf{s}}^{-}_{k+1}) \tag{6.9}$$

In equation (6.7), the Kalman gain $\mathbf{K}_{KF,k+1}$ is the residual weighting coefficient, which provides an optimal weight between the estimates of the outputs based on the dynamics of the system and the measurements. The TU step generally increases the covariance error $\mathbf{P}_{KF}$ due to the uncertainty introduced by the process noise $\mathbf{w}_k$, whereas the MU step decreases the error covariance $\mathbf{P}_{KF}$ by adding the measurement information.

6.2.2 Kalman filter estimation model

In this section, a continuous-time dynamic model for a three-body hinge-barge device, which can be used by the Kalman filter, is derived. The excitation forces are considered to be unknown inputs, and are included in the state variable vector as additional state variables to be estimated, in addition to positions and velocities. The dynamic model of the Kalman filter is described in terms of the dynamics of the WEC and the excitation forces. The dynamic model of the WEC is based on the reduced equivalent model, which is presented in Section 4.2. A linear dynamic reduced equivalent model is considered, where the convolution integral of the radiation forces is replaced with a radiation force composed of a term that is linearly proportional to the velocity

of the WEC, and another term that is linearly proportional to the acceleration of the WEC. The terms of the radiation force that are linearly proportional to the velocity and acceleration have a proportionality constant equal to the radiation damping and added mass, respectively. While, for regular waves, the radiation damping and the added mass are taken at the frequency of the incoming wave, for irregular waves, the radiation damping and the added mass are taken at the peak frequency of the incoming wave. Given that the excitation forces have an oscillating nature, a harmonic oscillator model with assumed wave frequencies ω_i is used to describe the excitation forces. Thus, the continuous-time dynamic WEC model for the Kalman filter is given as follows:

$$\begin{aligned}\begin{bmatrix} \dot{\hat{\mathbf{x}}} \\ \ddot{\hat{\mathbf{x}}} \\ \dot{\hat{\mathbf{f}}}_{eq,wave} \\ \ddot{\hat{\mathbf{f}}}_{eq,wave} \end{bmatrix} &= \begin{bmatrix} \mathbf{0}_{2,2} & \mathbf{I}_{2,2} & \mathbf{0}_{2,n_{KF,f}} & \mathbf{0}_{2,n_{KF,f}} \\ -\mathbf{M}_{eq,tot}^{-1}\mathbf{G}_{eq} & -\mathbf{M}_{eq,tot}^{-1}\mathbf{B}_{eq,tot} & \mathbf{M}_{eq,tot}^{-1}\mathbf{E} & \mathbf{0}_{2,n_{KF,f}} \\ \mathbf{0}_{n_{KF,f},2} & \mathbf{0}_{n_{KF,f},2} & \mathbf{0}_{n_{KF,f},n_{KF,f}} & \mathbf{I}_{n_{KF,f},n_{KF,f}} \\ \mathbf{0}_{n_{KF,f},2} & \mathbf{0}_{n_{KF,f},2} & -\mathbf{\Omega}^2 & \mathbf{0}_{n_{KF,f},n_{KF,f}} \end{bmatrix} \begin{bmatrix} \hat{\mathbf{x}} \\ \dot{\hat{\mathbf{x}}} \\ \hat{\mathbf{f}}_{eq,wave} \\ \dot{\hat{\mathbf{f}}}_{eq,wave} \end{bmatrix} + \dots \\ &+ \begin{bmatrix} \mathbf{0}_{2,2} \\ \mathbf{I}_{2,2} \\ \mathbf{0}_{n_{KF,f},2} \\ \mathbf{0}_{n_{KF,f},2} \end{bmatrix} \mathbf{u} + \begin{bmatrix} \mathbf{0}_{2,2} & \mathbf{0}_{2,2} & \mathbf{0}_{2,n_{KF,f}} & \mathbf{0}_{2,n_{KF,f}} \\ \mathbf{0}_{2,2} & \mathbf{0}_{2,2} & \mathbf{0}_{2,n_{KF,f}} & \mathbf{0}_{2,n_{KF,f}} \\ \mathbf{0}_{n_{KF,f},2} & \mathbf{0}_{n_{KF,f},2} & \mathbf{I}_{n_{KF,f},n_{KF,f}} & \mathbf{0}_{n_{KF,f},n_{KF,f}} \\ \mathbf{0}_{n_{KF,f},2} & \mathbf{0}_{n_{KF,f},2} & \mathbf{0}_{n_{KF,f},n_{KF,f}} & \mathbf{I}_{n_{KF,f},n_{KF,f}} \end{bmatrix} \mathbf{w} \end{aligned} \tag{6.10}$$

$$\mathbf{y} = \begin{bmatrix} \mathbf{I}_{2,2} & \mathbf{0}_{2,2} & \mathbf{0}_{2,n_{KF,f}} & \mathbf{0}_{2,n_{KF,f}} \\ \mathbf{0}_{2,2} & \mathbf{I}_{2,2} & \mathbf{0}_{2,n_{KF,f}} & \mathbf{0}_{2,n_{KF,f}} \end{bmatrix} \begin{bmatrix} \hat{\mathbf{x}} \\ \dot{\hat{\mathbf{x}}} \\ \hat{\mathbf{f}}_{eq,wave} \\ \dot{\hat{\mathbf{f}}}_{eq,wave} \end{bmatrix} + \mathbf{v} \tag{6.11}$$

where $\hat{\mathbf{x}}$ is the estimated position vector, $\hat{\mathbf{f}}_{eq,wave}$ is the estimated equivalent excitation force vector, $n_{KF,f} = 2 \times n_f$, n_f is the number of frequencies of the excitation forces, $\mathbf{M}_{eq,tot} = \mathbf{M}_{eq,in} + \mathbf{M}_{eq,a}$ and $\mathbf{B}_{eq,tot} = \mathbf{B}_{eq,rad} + \mathbf{B}_{eq,visc}$.

The matrix $\mathbf{\Omega}$ is given as follows:

$$\mathbf{\Omega} = \begin{bmatrix} diag(\boldsymbol{\omega}) & \mathbf{0}_{n_f,n_f} \\ \mathbf{0}_{n_f,n_f} & diag(\boldsymbol{\omega}) \end{bmatrix} \tag{6.12}$$

where the vector of excitation force frequencies $\boldsymbol{\omega}$ is given as follows:

$$\boldsymbol{\omega} = [\, \omega_1, .., \omega_{n_f}]^{\,T} \tag{6.13}$$

The matrix $\mathbf{E}$ in equation (6.10) is given as follows:

$$\mathbf{E} = \begin{bmatrix} \mathbf{1}_{1,n_f} & \mathbf{0}_{1,n_f} \\ \mathbf{0}_{1,n_f} & \mathbf{1}_{1,n_f} \end{bmatrix} \tag{6.14}$$

The accuracy of the estimation of the equivalent excitation force $\hat{\mathbf{f}}_{eq,wave}$ depends on the number of frequencies n_f considered in the estimator model. The more frequencies considered, the

more accurate is the estimate $\hat{\mathbf{f}}_{eq,wave}$. However, the complexity of the estimation problem increases with n_f. The number of frequencies n_f is related to the nature of the spectrum of the incoming wave. A narrow spectrum requires a smaller number of fixed frequencies, compared to a broad spectrum.

Note that equations (6.10)-(6.11) must be discretized in the time domain in order to implement equations (6.5)-(6.9). For the initialization of the matrix P_{KF}, the initial values of the excitation force covariance errors are high, since the initial estimate of the excitation forces contain a high degree of uncertainty. For this work, while the initial value for each of the covariance errors of the excitation forces is 10, the initial value for each of the covariance errors of position and velocities is 0.

The estimation accuracy can be measured with the Goodness of Fit (GoF) index, which is defined as follows:

$$GoF_{est} = \left(1 - \frac{\sqrt{\sum_{k=1}^{N_1}(f_{eq,wave_{real}}(k) - \hat{f}_{eq,wave}(k))^2}}{\sqrt{\sum_{k=1}^{N_1} f_{eq,wave_{real}}(k)^2}}\right) \cdot 100 \tag{6.15}$$

where N_1 is a set of data, $f_{eq,wave_{real}}$ and $\hat{f}_{eq,wave}$ are the real and estimated excitation force vector, respectively. Obtaining a value of $GoF_{est} = 100\%$ means that the excitation force has been perfectly estimated.

6.3 Feedforward estimation of excitation force

In this section, the excitation forces acting on a three-body hinge-barge device are estimated with a feedforward estimator from the measurements of the surface elevation up-wave of the device. Compared to the feedback estimation of the excitation forces presented in Section 6.2, which is based in the time-domain, the feedforward estimator is formulated in the frequency-domain, and requires knowledge of the incoming wave elevation. In Figure 6.3, a scheme for the feedforward estimation of the excitation forces acting on a generic multibody WEC in the discrete time domain is shown.

The feedforward estimator is based on frequency-domain identification of the transfer function $\mathbf{H}(\omega)$ between the wave elevation and the positon of the DoF of the device as defined in equation (3.104). The transfer function $\mathbf{H}(\omega)$ can be identified from the motion of the device under irregular waves, via equation (3.105). The peak period of the spectrum of the irregular waves needs to be close to the resonant period of the device, and the spectrum has to be sufficiently broad in order to cover the bandwidth of the device. Then, from equation (3.104), the transfer function $\mathbf{H}_{wave,s}(\omega)$ between the wave elevation and the excitation force vector is estimated, in the frequency domain, using the identified transfer function $\mathbf{H}(\omega)$, as follows:

$$\hat{\mathbf{H}}_{wave,s}(\omega_i) = \left(-\omega^2(\mathbf{M}_s + \mathbf{M}_{a,s}(\omega_i)) + j\omega(\mathbf{B}_{visc,s} + \mathbf{B}_{rad,s}(\omega_i)) + \mathbf{G}_s\right)\mathbf{H}(\omega_i) \tag{6.16}$$

where $i = 1,..,N_f$ and N_f is the number of discrete frequencies considered in the identification of the transfer function $\mathbf{H}_{wave,s}(\omega)$. Note that N_f for the feedforward estimator is different from n_f for the feedback estimator. If the vector $\mathbf{H}_{wave,s}$ is partitioned as follows:

$$\hat{\mathbf{H}}_{wave,s}(\omega) = \begin{bmatrix} \hat{\mathbf{H}}_{wave,1}(\omega) \\ \hat{\mathbf{H}}_{wave,2}(\omega) \end{bmatrix} \tag{6.17}$$

then, the transfer function between the wave elevation and the equivalent excitation forces can be derived, from equation (4.16), as follows:

$$\hat{\mathbf{H}}_{eq,wave}(\omega_i) = \hat{\mathbf{H}}_{wave,2}(\omega_i) - j\omega\mathbf{C}_{2,1}\mathbf{Z}_f^{-1}\hat{\mathbf{H}}_{wave,1}(\omega_i) - \mathbf{B}_{2,1}\mathbf{Z}_f^{-1}\hat{\mathbf{H}}_{wave,1}(\omega_i) \tag{6.18}$$

Finally, the estimated excitation forces are computed in the time-domain as a summation of N_f sinusoidal components:

$$\hat{f}_{eq,wave_p}(k) = \sum_{i=1}^{N_f} |\hat{H}_{eq,wave_p}(\omega_i)||\hat{\eta}(\omega_i)|cos(\omega_i t_k + \angle\hat{H}_{eq,wave_p}(\omega_i)) \tag{6.19}$$

with $p = 1,2$.

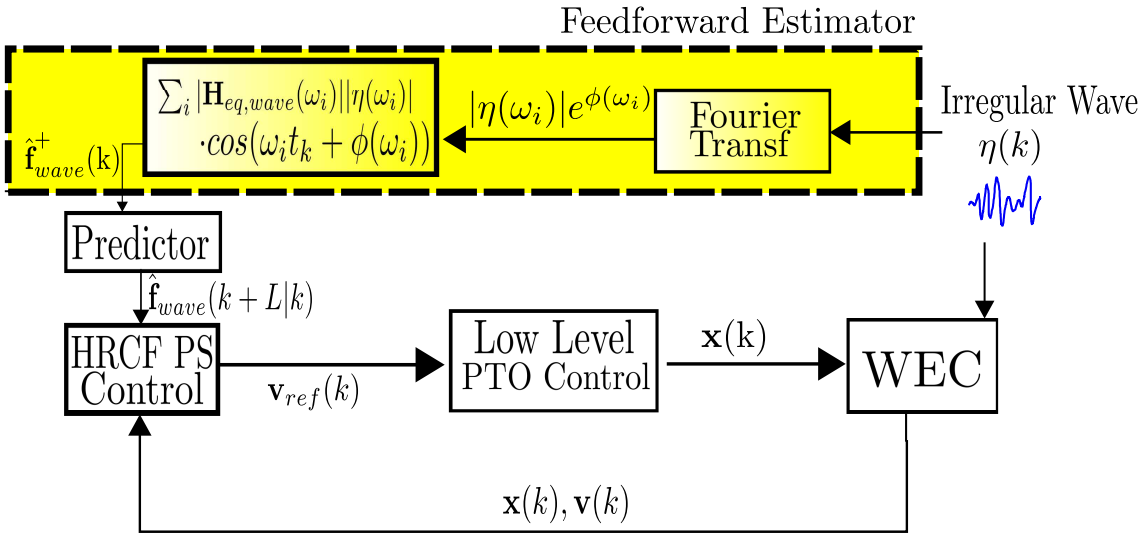

Figure 6.3: Feedforward estimator for excitation forces acting on a generic multibody WEC in the time-domain.

The estimation accuracy of feedforward estimator can be measured with the GoF index defined in equation (6.15).

6.4 Prediction of excitation force

In this section, a model for forecasting the excitation forces, based on their past history, is presented. In particular, an AR model [105] is proposed which assumes that the excitation forces at time instant k are linearly dependent on a number n_a of their past values. Thus, the forecasting model considered is of the form:

$$\hat{f}_{eq,wave_p}(k) = \sum_{i=1}^{n_a} \alpha_i \hat{f}_{eq,wave_p}(k-i) + \xi(k) \tag{6.20}$$

with $p = 1,2$ and ξ is white noise with zero mean and variance σ. Given a set of parameters α_i, from equation (6.20) the l-step ahead prediction $\tilde{f}_{eq,wave_p}$ is given as follows:

$$\tilde{f}_{eq,wave_p}(k+l|k) = \sum_{i=1}^{n_a} \alpha_i \tilde{f}_{eq,wave_p}(k+l-i|k) \tag{6.21}$$

where $\tilde{f}_{eq,wave_p}(k+l-i|k) \equiv \hat{f}_{eq,wave_p}(k+l-i)$ if $k+l-i \leq k$, since the information is already available and there is no need to have a prediction [105]. The coefficients α_i in equation (6.20) of the AR model are estimated by minimizing the following cost function:

$$J_{LS} = \sum_{k=1}^{N_1} (\hat{f}_{eq,wave_p}(k+1) - \hat{f}_{eq,wave_p}(k+1|k))^2 \tag{6.22}$$

where N_1 is a set of training data. The cost function in equation (6.22) is a linear Least Squares (LS) problem. For estimation of the model parameters, a different cost function, referred to as Long Range Predictive Identification (LRPI) [110] was considered, with an initial value of the parameter estimates given by the minimization of (6.22). Since the minimization of the LPRI cost function for different forecasting horizons did not yield a significantly different value of the parameters compared to their initial estimates, the LPRI cost function was not further considered.

The prediction accuracy, for every forecasting horizon l, can be measured with the following GoF index:

$$GoF_{pred}(l) = \left(1 - \frac{\sqrt{\sum_{k=1}^{N_2} (f_{eq,wave_p}(k+l) - \tilde{f}_{eq,wave_p}(k+l|k))^2}}{\sqrt{\sum_{k=1}^{N_2} f_{eq,wave_p}(k+l)^2}}\right) \cdot 100 \tag{6.23}$$

where N_2 is a set of validation data. Obtaining a value of $GoF_{pred}(l) = 100\%$ means that the excitation force has been perfectly predicted l steps into the future. The accuracy of the prediction is higher when the bandwidth of the excitation force is narrow ([105]).

6.5 Estimation and prediction results

In this section, a comparison between the performance of the feedback and feedforward estimators applied to a $1/25th$ scale three-body hinge-barge device is made for both regular and irregular waves. Regarding the prediction of the future excitation forces, an AR model as presented in

Section 6.4 is used. In order to obtain realistic performance of the feedback and feedforward estimator, the motion of the device is based on the dynamic model identified in subsection 3.5.3.2, with the convolution integral of the radiation forces approximated with a state-space model. The measurements of positions and velocities of the device are affected by white noise with zero mean and given variance.

The feedback estimator is based on a linear reduced equivalent dynamic model, where the convolution integral of the radiation forces is replaced a radiation force that is composed of a term that is linearly proportional to the velocity of the WEC, and another term that is linearly proportional to the acceleration of the WEC. The estimator makes use of the measurements of positions and velocities of the device, in order to estimate the equivalent excitation forces acting upon the device.

The feedforward estimator makes use of the measurements of positions and wave elevation in order to estimate the transfer functions of equivalent excitation force $\hat{\mathbf{H}}_{eq}(\omega)$, and then computes the equivalent excitation forces in the time-domain. Note that the transfer function $\hat{\mathbf{H}}_{eq}(\omega)$ can only be identified by using a set of irregular waves, since an incoming wave with a sufficiently broad spectrum is needed to excite all the frequency components of the transfer function $\hat{\mathbf{H}}_{eq}(\omega)$.

6.5.1 Feedback and Feedforward estimation with regular waves

For the estimation of excitation forces in regular waves with the feedback estimator, a number of frequencies $n_f = 1$ is chosen, given the monochromatic nature of the incoming waves. The frequency of the estimator model ω_1 is chosen equal to the frequency of the incoming wave.

For the feedforward estimator, the transfer function $\hat{\mathbf{H}}_{eq}(\omega)$ is estimated with a set of irregular waves, as presented in Section 6.5.2.2, and then used to compute the equivalent excitation forces at the particular frequency of the incoming regular wave. A number of discrete frequencies $N_f = 100$ is chosen, as it provides a good GoF_{est}, as shown in Figure 6.12.

By way of example, the real and estimated equivalent excitation forces, with the feedback and feedforward estimators, are shown for regular waves of frequency $\omega = 3$ rad/secs in Figure 6.4, frequency $\omega = 5$ rad/secs in Figure 6.5 and frequency $\omega = 7$ rad/secs in Figure 6.6. As shown in Figures 6.4, 6.5 and 6.6, both feedback and feedforward estimators provide a good estimate of the excitation forces for different regular wave frequencies. Therefore, for the feedback estimator, the linear radiation forces represent a good approximation of the radiation forces in the estimator model.

As shown in Figures 6.4, 6.5 and 6.6, the equivalent excitation forces estimated by the feedback estimator converge to the real equivalent excitation force after a certain transient time. The transient time is needed by the KF to correct the estimates of the equivalent excitation forces by using the measurements of the motion of the device. The speed of convergence of the equivalent excitation forces estimated by the feedback estimator depends on the values of the matrices $\mathbf{Q}$ and $\mathbf{R}$, in equations (6.3) and (6.4). The $\mathbf{Q}$ and $\mathbf{R}$ matrixes are chosen in order to provide a trade-off between the accuracy and the noise level of the estimation of the excitation force. Small values

for the matrix **R** increase the converge speed of the estimation of the excitation force to the real excitation force, but the noise level in the estimation is increased too. On the other hand, a small **Q** decreases the noise level in the estimation, but the convergence speed is also decreased. While the values of the matrix **Q** are equal to the variance of the noise on the measurements of position and velocity, the values for the matrix **Q** are appropriately tuned so that the noise level in the estimation of the excitation force is acceptable and the estimation rapidly converges to the real value of the excitation force.

As shown in Figures 6.4, 6.5 and 6.6, the equivalent excitation forces estimated by the feedforward estimator do not show any transient behavior, as they are composed of a single frequency component with amplitude and phase delay given by the estimated transfer function $\hat{\mathbf{H}}_{eq}$ at the frequency of the incoming wave, as shown in equation (6.19).

In Figures 6.7a and 6.7b, the GoF_{est} of the estimates of the equivalent excitation forces given by the feedback estimator is shown for a range of regular wave frequencies from 3 rad/s to 8 rad/s. As Figure 6.7a and 6.7b show, the performance of the feedback estimator is quite good, with values of the GoF_{est} above 70% across all the range of considered frequencies. In Figure 6.8a and 6.8b, the GoF_{est} of the estimates of the equivalent excitation forces given by the feedforward estimator is shown for regular wave frequencies from 3 rad/s to 8 rad/s. As Figure 6.8a and 6.8b show, the performance of the feedforward estimator is slightly worse than the performance of the feeback estimator, with a GoF_{est} of the estimated equivalent excitation forces that have a value of 60% for frequencies of the incoming wave around 7 rad/s. Overall, the performance of both feedback and feedforward estimator, for regular waves, is acceptable. Regarding the prediction of excitation forces for regular waves, given that the excitation forces are sinusoidal, the excitation forces can be easily predicted into the future with the same accuracy achieved by the estimator.

6.5.2 Excitation forces estimation with irregular waves

6.5.2.1 Wave spectrum

For irregular waves, the wave conditions are represented a realization of a JONSWAP spectrum, which is given as follows [34]:

$$S(\omega) = \frac{\alpha g^2}{\omega^M} e^{-\frac{M}{N}\left(\frac{\omega_p}{\omega}\right)^N} \gamma^a \tag{6.24}$$

where $M = 5$, $N = 4$ and:

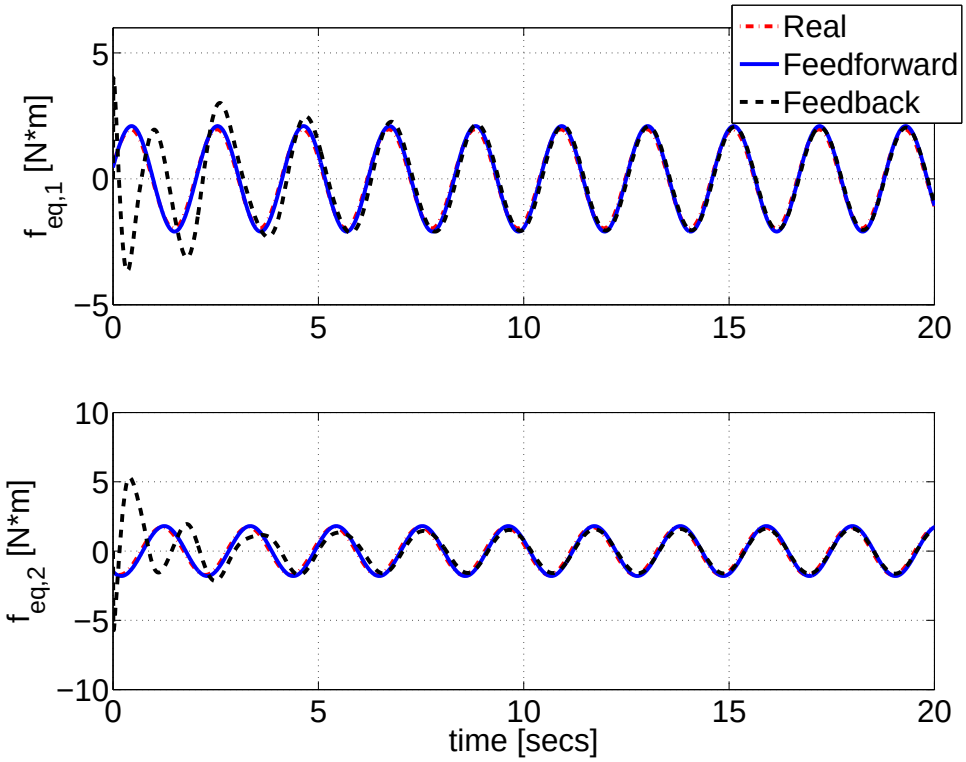

Figure 6.4: Real and estimated equivalent excitation forces for a 1/25th scale three-body hinge-barge device with feedback and feedforward estimator for a regular wave of frequecy $\omega = 3$ rad/s amplitude A = 2 cm.

$$\sigma = \begin{cases} 0.07 & if\ \omega < \omega_p \\ 0.09 & if\ \omega \geq \omega_p \end{cases} \tag{6.25}$$

$$\alpha = 5.061 \frac{H_s^2}{T_p^4} (\ 1 - 0.287\, ln(\gamma)) \tag{6.26}$$

$$a = e^{\frac{-(\omega/\omega_p - 1)^2}{2\sigma^2}} \tag{6.27}$$

For realistic sea-states, the peak shape parameter $\gamma = 3.3$ [111], [112] for Pico Island, which has a narrow frequency spectrum. For a $1/25th$ scale three-body hinge-barge device, a JONSWAP spectrum for the incoming wave with peak period $T_p = 1.25$ and significant wave height $H_s = 15$ cm is considered, and is shown in Figure 6.9.

6.5.2.2 Feedback and Feedforward estimation with irregular waves

Regarding the feedback estimator, the choice of the number of frequencies n_f and the frequencies values ω_i, with $i = 1,..,n_f$, in the feedback estimator model, play a fundamental role in the

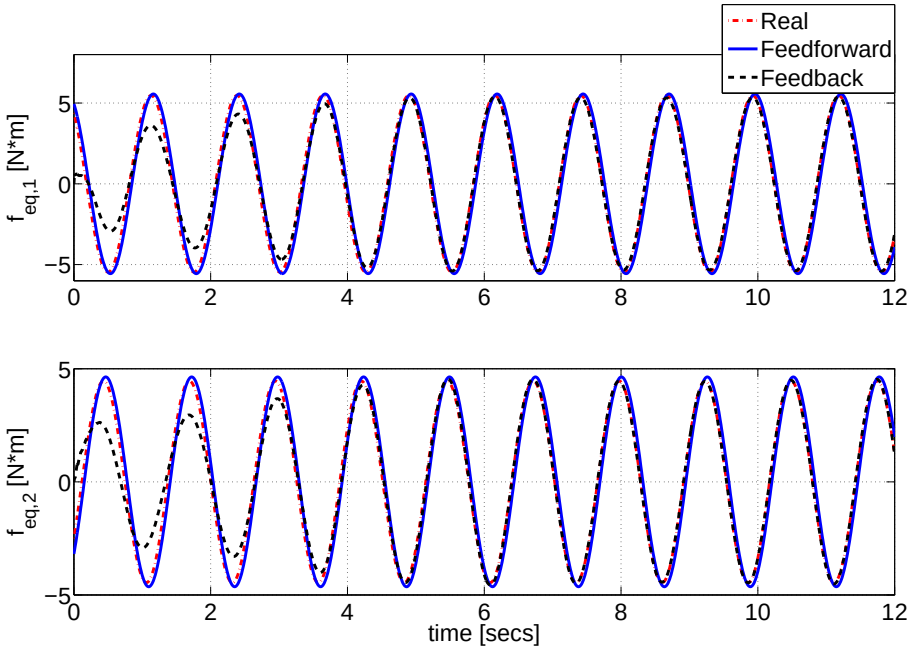

Figure 6.5: Real and estimated equivalent excitation forces for a 1/25th scale three-body hinge-barge device with feedback and feedforward estimator for a regular wave of frequecy $\omega = 5$ rad/s amplitude A = 2 cm.

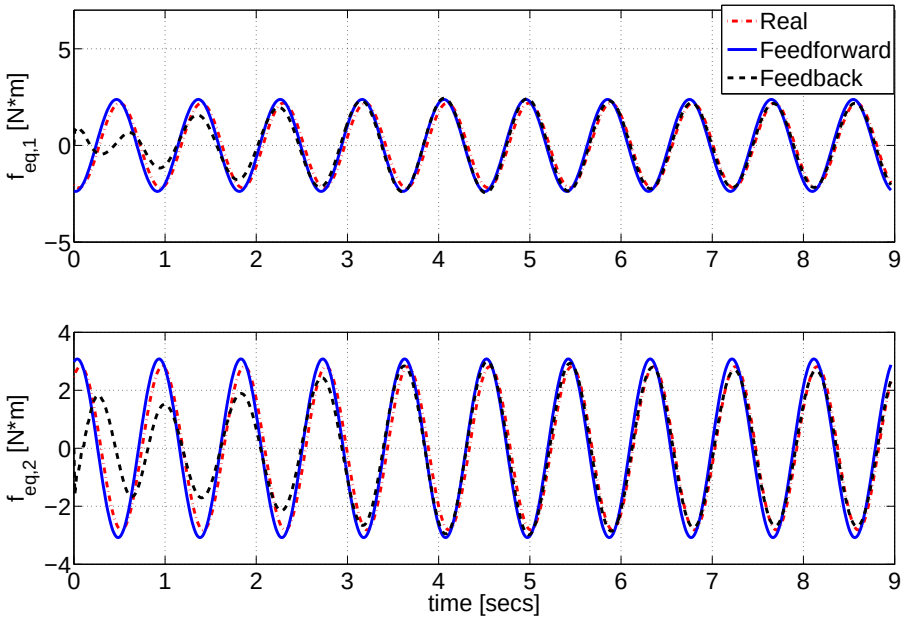

Figure 6.6: Real and estimated equivalent excitation forces for a 1/25th scale three-body hinge-barge device with feedback and feedforward estimator for a regular wave of frequecy $\omega = 7$ rad/s amplitude A = 2 cm.

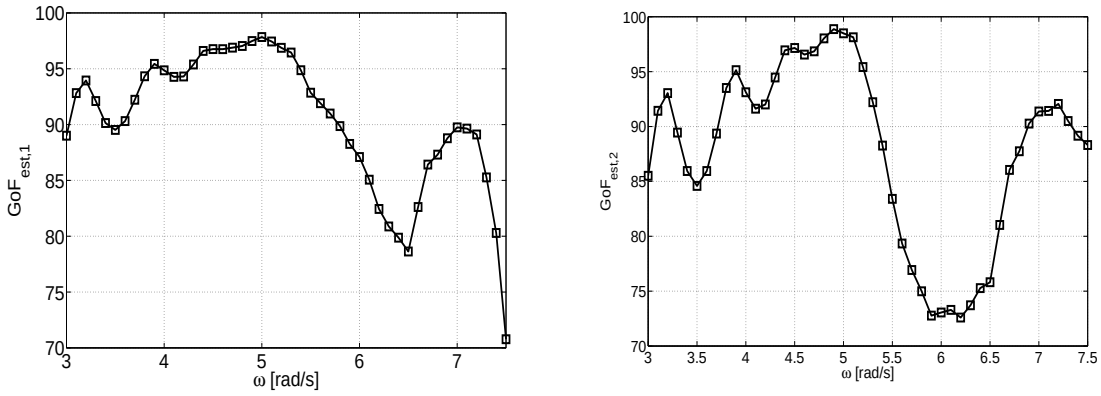

(a) (b)

Figure 6.7: GoF of first estimated equivalent excitation force (a) and second estimated equivalent excitation force (b) for a 1/25th scale three-body hinge-barge device computed by the feedback estimator for regular waves of amplitude A=2 cm and range of frequencies from 3 rad/s to 8 rad/s.

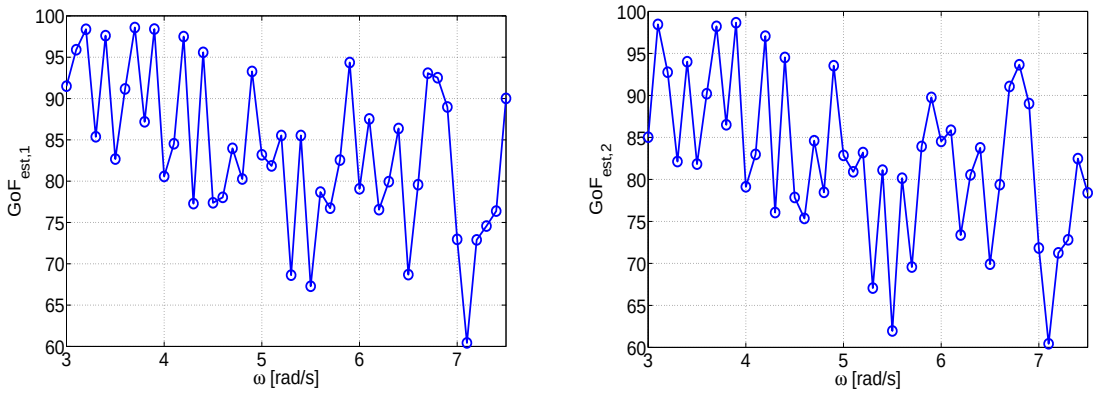

(a) (b)

Figure 6.8: GoF of first estimated equivalent excitation force (a) and second estimated equivalent excitation force (b) for a 1/25th scale three-body hinge-barge device computed by the feedforward estimator for regular waves of amplitude A=2 cm and range of frequencies from 3 rad/s to 8 rad/s.

performance of the estimator. Given a fixed number of frequencies n_f, the frequencies ω_i are chosen in order to maximize the GoF_{est} index as defined in equation (6.15). Given the spectrum of the incoming wave shown in Figure 6.9, a frequency range from 2 rad/s to 10 rad/s is considered in the choice of the frequencies ω_i. The algorithm for the optimal choice of the frequencies ω_i, for a given number of frequencies n_f, is presented in Algorithm 1. As shown in Algorithm 1, a frequency vector $\overline{\omega}$ is defined which takes values from a frequency range from 2 rad/s to 10 rad/s with a frequency resolution $\Delta\omega$. Then, the i-th component of the frequency vector of the excitation forces ω in the estimator model is assigned with each ii-th component of the frequency vector $\overline{\omega}$. Given the vector ω and batch of data of dimension N_1, the GoF_{est} index given in equation (6.15) is computed, and the ii-th component of the frequency vector $\overline{\omega}$ that gives the maximum GoF_{est}

index is selected as the optimal frequency for the i-th component of the frequency vector $\boldsymbol{\omega}$.

In Table 6.1, the optimal frequencies ω_i that maximize the GoF_{est} index, as defined in equation (6.15), are presented for a number of frequencies n_f from 1 to 9. In Figure 6.11, the GOF_{est} of the equivalent excitation forces is shown for different numbers of frequencies n_f. Note that, in Figure 6.11, for every number of frequencies n_f, the frequencies ω_i are chosen according to Algorithm 1. As Figure 6.11 shows, a number of frequencies n_f greater than 5 guarantees a GoF_{est} that is greater than 85 % and 65 % for the first and second equivalent excitation force, respectively.

Regarding the feedforward estimator, the choice of the number of frequencies N_f plays a fundamental role in the estimation of the excitation forces. A low number of frequencies N_f does not provide a sufficiently accurate frequency resolution for the estimation of the transfer function of the equivalent excitation force $\hat{\mathbf{H}}_{eq}(\omega)$. On the other hand, a large number of frequencies N_f results in a high frequency resolutions $\Delta\omega$ for the estimated transfer function $\hat{\mathbf{H}}_{eq}(\omega)$, which requires a large observation time T_{obsv} for the motion of the device. In fact, the frequency resolution of the transfer function $\hat{\mathbf{H}}_{eq}(\omega)$ is given as $\Delta\omega = 1/T_{obsv}$. In Figure 6.12, the GOF_{est} of the equivalent excitation forces is shown for different numbers of frequencies N_f. As Figure 6.12 shows, a number of frequencies N_f greater than 100 guarantees a GoF_{est} greater than 80 %, for both the first and second equivalent excitation force. In Figures 6.10a and 6.10b, the modulus and phase of the real and estimated transfer function computed with $N_f = 100$, for the first equivalent excitation force and second equivalent excitation force, are shown, respectively.

By way of example, in Figure 6.13, the real and estimated equivalent excitation forces with the feedback and feedforward estimator are shown for an irregular wave made using a JONSWAP spectrum with a significant wave height H_s = 15 cm and peak period T_p = 1.25 s. In Figure 6.13, the number of frequencies for the feeback and feedforward estimator are $n_f = 5$ and $N_f = 100$, respectively. As shown in Figure 6.13, the feedback and feedforward estimators provide a similar estimation of the first equivalent force. However, for the second equivalent excitation force, the feedforward estimator provides a more accurate estimation than the feedback estimator. While the feedforward estimator provides a GoF_{est}=85% for both excitation forces, the feedback estimator provides a GoF_{est}=85% and GoF_{est}=65% for the first and second equivalent excitation force, respectively.

6.5.3 Excitation forces prediction with irregular waves

The equivalent excitation force estimated by the feedback and feedforward estimators, with a number of frequencies $n_f = 5$ and $N_f = 100$, respectively, derived in Section 6.5.2, are predicted into the future with an AR model defined as in equation (6.20). In particular, an AR model is designed for each equivalent excitation force, which depends on estimates provided either by the

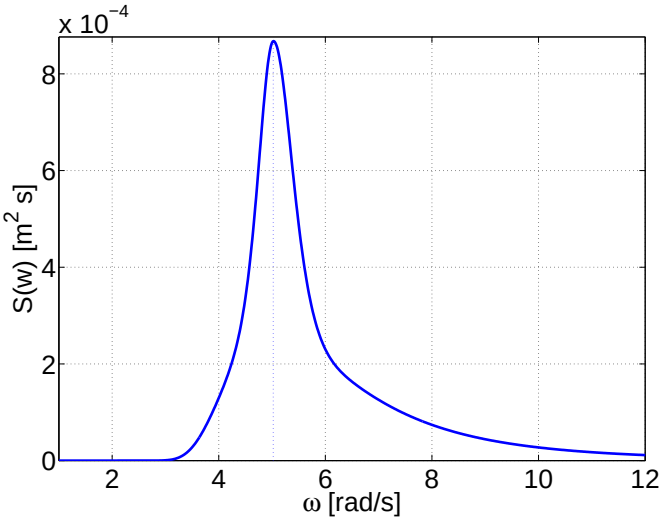

Figure 6.9: JONSWAP spectrum with peak period $T_p = 1.25$ and significant wave height $H_s = 15$ cm.

Algorithm 1 Optimal Selection Estimator Model Frequencies

$\Delta\omega \leftarrow 0.1$ rad/s
$\overline{\omega} \leftarrow 2 : \Delta\omega : 10$
$\boldsymbol{\omega} \leftarrow$ empty array
for $i = 1, .., n_f$ **do**
  for $ii = 1, .., length(\overline{\omega})$ **do**
    $\boldsymbol{\omega}[i] \leftarrow \overline{\omega}[ii]$
    $\mathbf{GoF}_{est}[ii] \leftarrow ComputeGoF_{est}(\boldsymbol{\omega})$
  end for
  $index \leftarrow GetIndexMax(\mathbf{GoF}_{est})$
  $\boldsymbol{\omega}[i] \leftarrow \overline{\omega}[index]$
end for

feedback and feedforward estimator. Therefore, two different AR models are derived: an AR model based on the estimates provided by the feedback estimator, and an AR model based on the estimates provided by the feedforward estimator.

Low-pass filtering of the estimated excitation forces is carried out in order to focus the prediction of the future excitation forces only on the low-frequency components [105]. In fact, the low-frequency components of the incoming wave spectrum carry out most of the wave energy and, therefore, it is reasonable to predict the low-frequency components of the excitation forces only. Furthermore, focusing the prediction on the low-frequency components of the excitation forces improves the accuracy of the prediction and extends the achievable prediction horizon with a sufficiently accurate prediction. Given the spectrum of the incoming waves shown in Figure 6.9, an ideal zero-phase low-pass Chebyshev filter, of the 6nd order with cut-off frequency of 7 rad/s, is chosen. It is important to highlight that the use of a zero-phase low-pass filter requires the filtering to be carried out off-line. However, for real-time applications, where the filtering is carried out online, the filtering introduces a phase delay which depends on the cut-off frequency and the type

$n_f = 1$ [rad/s]	ω_1=5								
$n_f = 2$ [rad/s]	ω_1=4.9	ω_2=7							
$n_f = 3$ [rad/s]	ω_1=4.8	ω_2=5	ω_3=6.6						
$n_f = 4$ [rad/s]	ω_1=4.1	ω_2=4.7	ω_3=5	ω_4=6.5					
$n_f = 5$ [rad/s]	ω_1=4.5	ω_2=4.7	ω_3=5.1	ω_4=6.5	ω_5=6.6				
$n_f = 6$ [rad/s]	ω_1=3.6	ω_2=4.2	ω_3=4.5	ω_4=5.1	ω_5=6.4	ω_6=6.6			
$n_f = 7$ [rad/s]	ω_1=2	ω_2=4.2	ω_3=4.5	ω_4=5.1	ω_5=6.4	ω_6=6.6	ω_7=7.2		
$n_f = 8$ [rad/s]	ω_1=2	ω_2=4.2	ω_3=4.3	ω_4=4.5	ω_5=5.1	ω_6=6.4	ω_7=6.6	ω_2=7.2	
$n_f = 9$ [rad/s]	ω_1=4.2	ω_2=4.7	ω_3=4.8	ω_4=4.9	ω_5=5.1	ω_6=6.4	ω_7=6.5	ω_8=6.6	ω_9=7.2

Table 6.1: Estimator model optimal frequencies ω_i, with $i = 1,..,n_f$, computed with Algorithm 1 for different numbers of frequencies n_f.

of filter used.

The forecasting horizon $T_{horizon}$ required to maximize the energy extracted by a WEC depends on the properties of the impulse response functions of the radiation damping [10], [12]. In particular, the forecasting horizon is equivalent to the time needed by the impulse response of the radiation damping to reach a zero value. In Figure 6.14, the impulse responses of the radiation damping matrix of the reduced equivalent model of a $1/25$th scale three-body hinge-barge device is shown. As shown in Figure 6.14, the impulse response functions decay to zero in approximately 3 seconds. Therefore, a forecasting horizon $T_{horizon} = 3$ seconds is considered for the prediction of the excitation forces.

An important element of the identification of the AR model in equation (6.20), with cost function (6.22), is the order n_a. Note that, in order to reduce the complexity of the AR model, the estimated excitation forces are re-sampled with a sampling time $T_{samp} = 0.1$ seconds. The objective is to identify a model that guarantees accurate fitting of the training data without incurring in the so-called "over-fitting", or rather the identification of an over-parametrized model which also interpolates the stochastic noise presents in the measurements. In order to select the best order n_a that avoids over-fitting the data, AR models of different orders n_a are trained and validated. Given a set of estimated excitation force data of dimension N_1, the training of the AR models is carried out with cost function in equation 6.22). Then, given a previously unseen batch of validation data of dimension N_2, the GoF_{pred} index given in equation (6.23), for a forecasting horizon of 3 seconds, is computed for different orders n_a.

In Figure 6.15, for a forecasting horizon of $T_{horizon} = 3$ seconds, the GoF_{pred} index given in equation (6.23), for each equivalent excitation force, is computed for different orders n_a of the AR model, based on the feedback and feedforward estimators. As shown in Figure 6.15, an order $n_a = 30$ is chosen as the optimal value that maximizes the $GoF_{pred}(l)$, with $l = T_{horizon}/T_{samp} = 3/0.1 = 30$, for both the excitation forces provided by the AR model, based on the feedback and

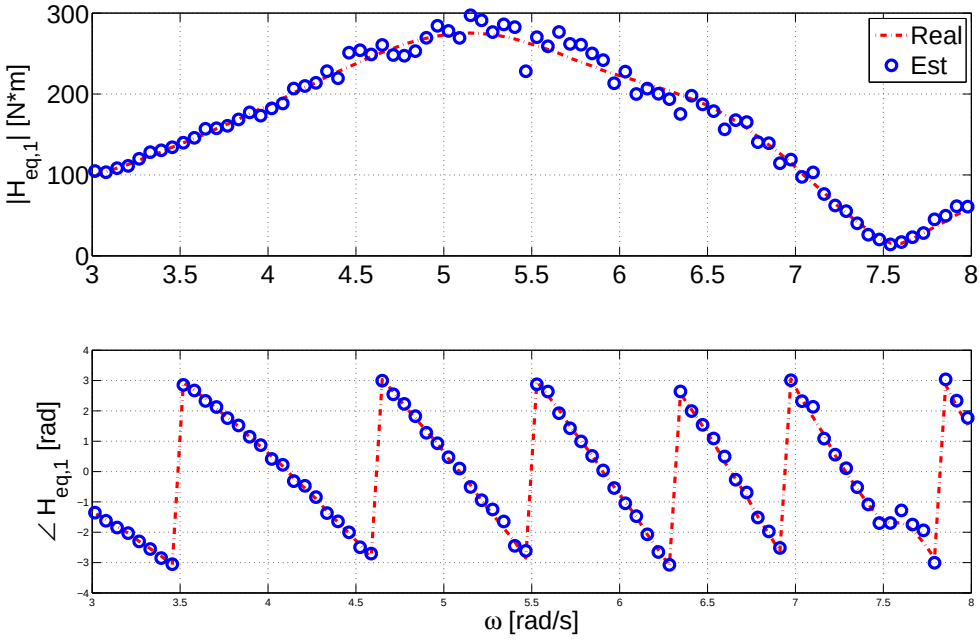

(a)

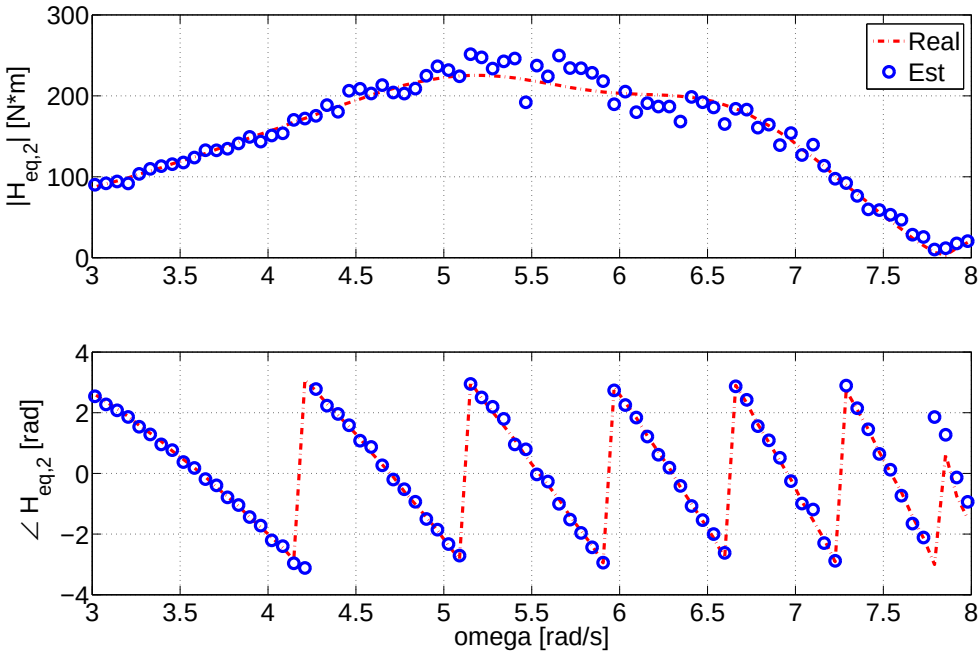

(b)

Figure 6.10: Module and phase of the real and estimated transfer function for first equivalent excitation force (a) and second equivalent excitation force (b).

feedforward estimator. Furthermore, as shown in Figure 6.15, the GoF_{pred} index provided by the

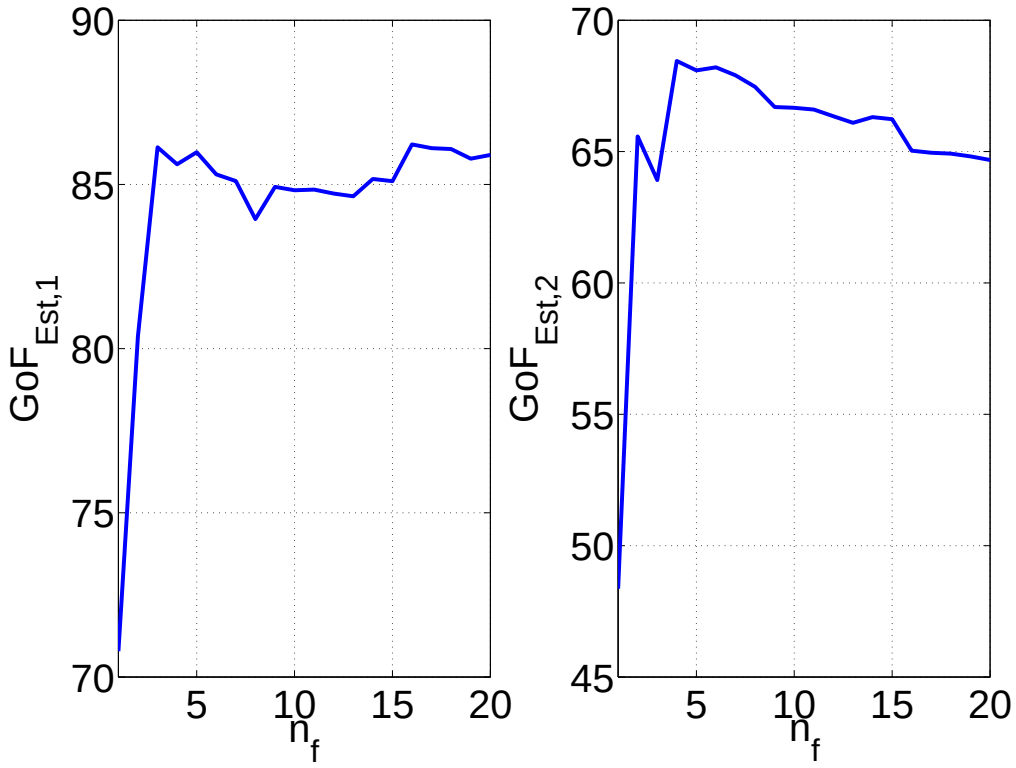

Figure 6.11: GoF of the estimation of the equivalent excitation forces for different values of the number of frequencies n_f in the feedback estimator.

AR model, based on the feedback estimator, is lower than the GoF_{pred} provided by the AR model based on the feedforward estimator, for both equivalent excitation forces, due to the more accurate estimates provided by the feedforward estimator. In particular, the GoF_{pred} index provided by the AR model based on the feedforward estimator is 10% and 15% higher than the GoF_{pred} provided by the AR model based on feedback estimator, for the first and second equivalent excitation force, respectively.

In Figure 6.16, the GoF_{pred} index given in equation (6.23) for each equivalent excitation force, is computed for different forecasting horizons $T_{horizon}$ and different orders of the AR model, based on the feedback estimator. In Figure 6.17, the GoF_{pred} index given in equation (6.23) for each equivalent excitation force, is computed for different forecasting horizons $T_{horizon}$ and different orders of the AR model, based on the feedforward estimator. As shown in Figures 6.16 and 6.17, the GoF_{pred}, for the first equivalent excitation force, given by the AR model based on the feedback estimator, is similar to the GoF_{pred} given by the AR model based on the feedforward estimator, across all the range of forecasting horizons $T_{horizon}$ considered. However, the GoF_{pred} for the second equivalent excitation force, given by the AR model based on the feedback estimator, is worse than the GoF_{pred} given by the AR model based on the feedforward estimator, across all the range of forecasting horizons $T_{horizon}$ considered. In particular, for the second equivalent excitation force, the AR model based on the feedforward estimator computes a GoF_{pred} which is

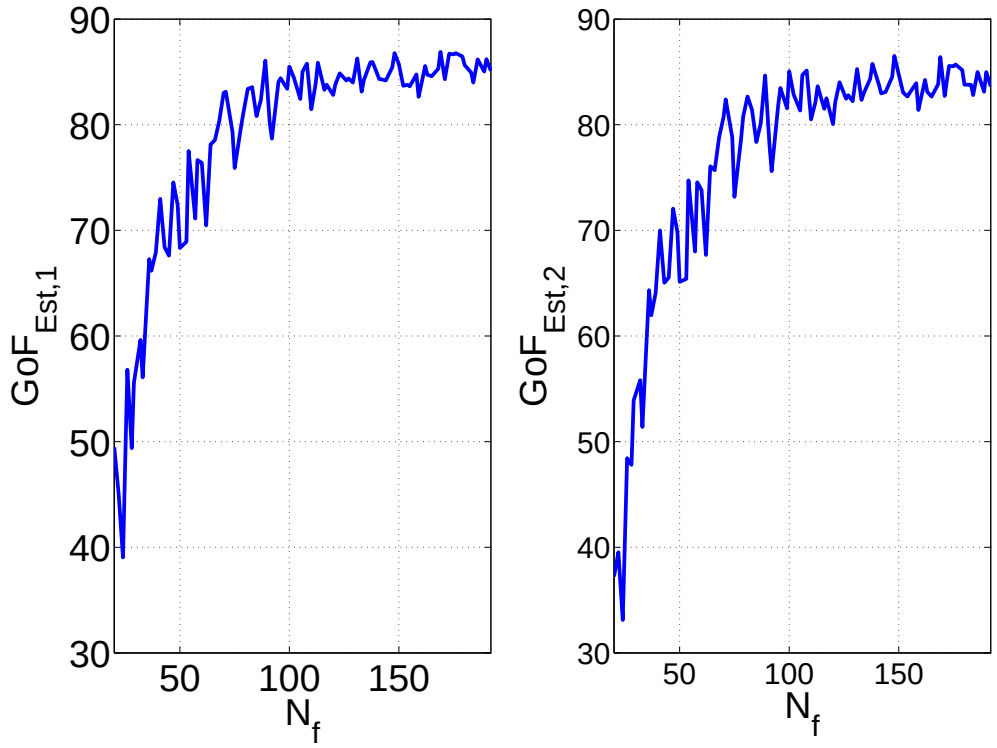

Figure 6.12: GoF of the estimation of the equivalent excitation forces for different values of the number of frequencies N_f in the feedforward estimator.

approximately 10% higher than the GoF_{pred} computed by the AR model based on the feedback estimator, for every forecasting horizon $T_{horizon}$ considered.

By way of example, in Figure 6.18, the real and predicted equivalent excitation forces for a forecasting horizon $T_{horizon} = 3$ seconds, given by the AR model with $n_a = 30$, based on the feedback and feedforward estimator, are shown for an irregular wave from a JONSWAP spectrum with a significant wave height H_s = 15 cm and peak period T_p = 1.25 s. As shown in Figure 6.18, the AR model, based on the feedback estimator, provides a prediction of the first equivalent force that is similar to the prediction provided by the AR model based on the feedforward estimator. However, for the second equivalent excitation force, the AR model based on the feedforward estimator provides a more accurate prediction than the AR model based on the feedback estimator. While the AR model based on the feedforward estimator provides a GoF_{pred}=70% for both excitation forces, the AR model based on the feedback estimator provides a GoF_{pred}=70% and GoF_{est}=60% for the first and second equivalent excitation force, respectively.

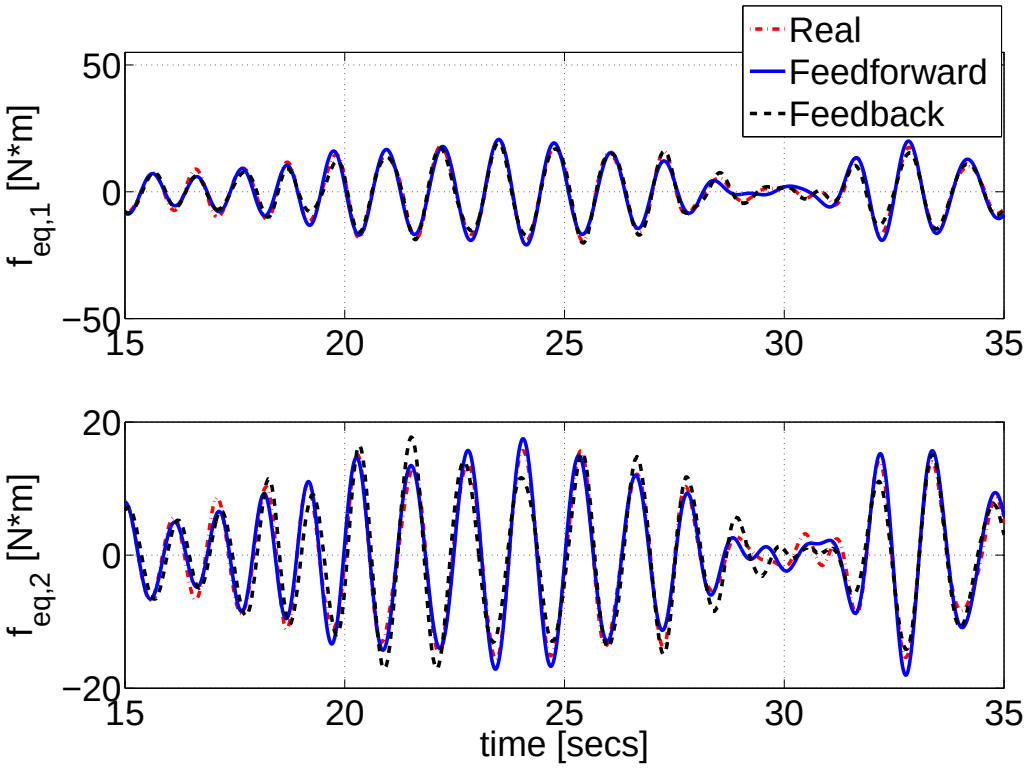

Figure 6.13: Real and estimated equivalent excitation forces with a number of frequencies in the estimator model $n_f = 15$ for an irregular wave made using a JONSWAP spectrum with a significant wave height H_s = 15 cm and peak period T_p = 1.25 s.

6.6 Conclusions

In this chapter, two different estimators for the excitation forces acting on a three-body hinge-barge devices are presented: feedback and feedforward estimators. The feedback estimator is formulated in the time domain, and is based on a Kalman filter which takes, as inputs, the position and the velocity of the DoF of the device. In contrast, the feedforward estimator is formulated in the frequency domain, and is based on frequency domain identification of the transfer function between the wave elevation up-wave of the device, and the position of the DoF of the device. Both estimators are based on the reduced equivalent model derived in Section 4.2, as it provides a computationally efficient formulation for the solution of the optimal control problem.

While the feedback estimator only requires information on the motion of the device, the feedforward estimator requires the information of both the motion of the device and wave elevation up-wave of the device. Therefore, the feedback estimator is simpler to implement than the second algorithm, as only motion sensors deployed on the device are required, without the need to deploy a wave gauge for the measurement of the wave elevation up-wave of the device. Furthermore, for the feedforward estimator, a long observation time of the motion of the device and wave elevation up-wave of the device is needed in order to achieve a small frequency resolution of the transfer function between the wave elevation up-wave of the device, and the position of the DoF of the

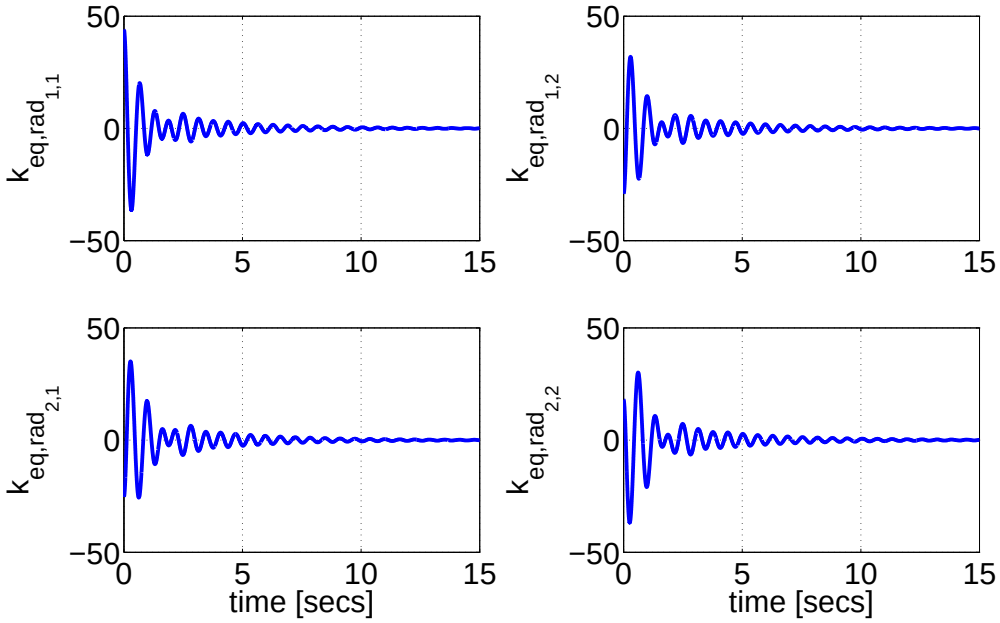

Figure 6.14: Impulse responses of the radiation damping matrix of the reduced equivalent model of a $1/25$th scale three-body hinge-barge device.

device. In particular, a small frequency resolution of the transfer function guarantees an accurate estimation of the equivalent excitation forces. For the feedback estimator, the Kalman filter converges to an accurate estimate of the equivalent excitation force after a transient time which is 4 times shorter than the observation time required by the feedforward estimator. The time needed by the feedback estimator to accurately estimate the equivalent excitation forces depends on weight matrices $\mathbf{Q}$ and $\mathbf{R}$ of the Kalman filter.

Results of the feedback and feedforward estimator, applied to a 1/25th scale three-body hinge-barge device, for the estimation of the equivalent excitation forces, show that both estimators estimate the first equivalent excitation force with the same accuracy. However, for the second equivalent excitation force, the feedforward estimator performs slightly better than the feedback estimator, with an accuracy of the estimation of the second equivalent excitation force that is 20% higher than the accuracy of the estimation given by the feedback estimator.

Note that, for this work, both estimators are based on perfect knowledge of the dynamic model of the device. It is expected that, in a more realistic scenario, where the knowledge of the parameters of the dynamic model is affected by a certain degree of uncertainty, the feedback is likely to perform better than the feedforward estimator. In fact, the feedback estimator is naturally robust to uncertainty in the parameters of the dynamic model, as the feedback on the position and velocity of the DoF of the device corrects the estimates of the excitation forces computed based on the dynamic model of the device only. In contrast, the feedforward estimates the equivalent excitation forces purely on the basis of the dynamic model of the device. Therefore, a small variation of the parameters of the dynamic model of the device could potentially lead to a large decrease of the

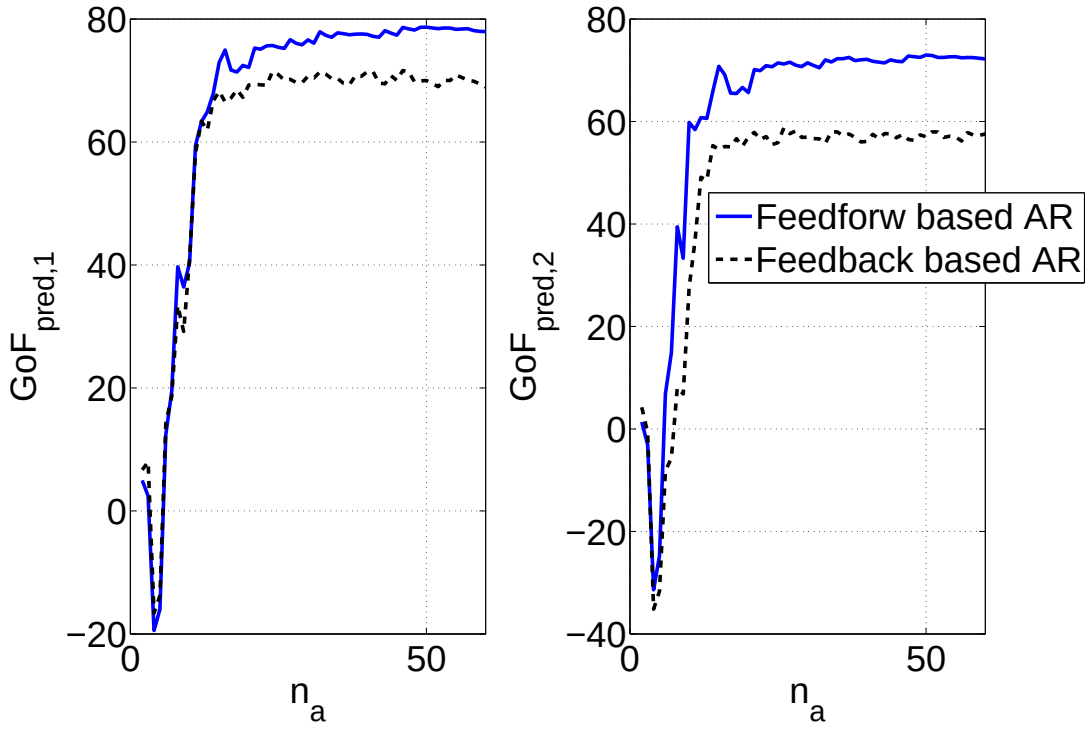

Figure 6.15: GoF of the prediction of the excitation forces for a forecasting horizon of 3 s as a function of the order n_a of the AR model based on the estimates given by the feedback and feedforward estimator.

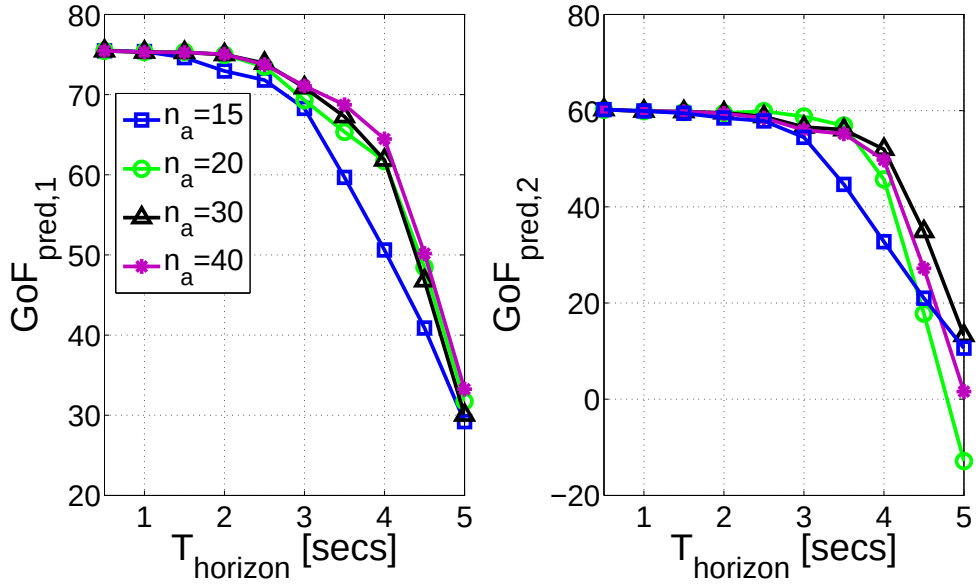

Figure 6.16: GoF of the prediction of the excitation forces as a function of the forecasting horizon $T_{horizon}$ and order n_a of the AR model based on the estimates given by the feedback estimator.

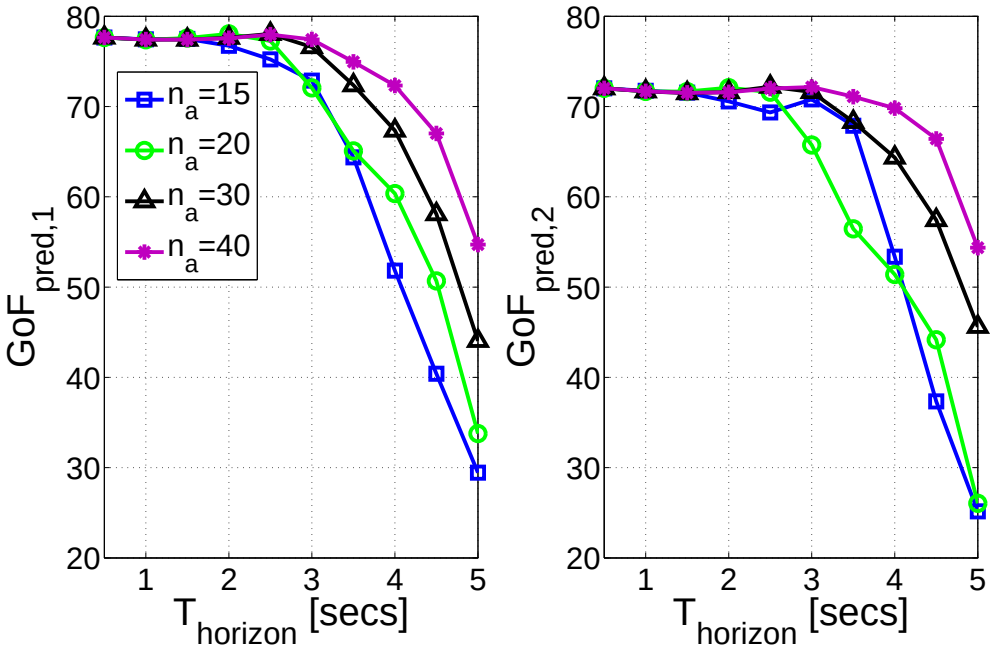

Figure 6.17: GoF of the prediction of the excitation forces as a function of the forecasting horizon $T_{horizon}$ and order n_a of the AR model based on the estimates given by the feedforward estimator.

performance of the feedforward estimator.

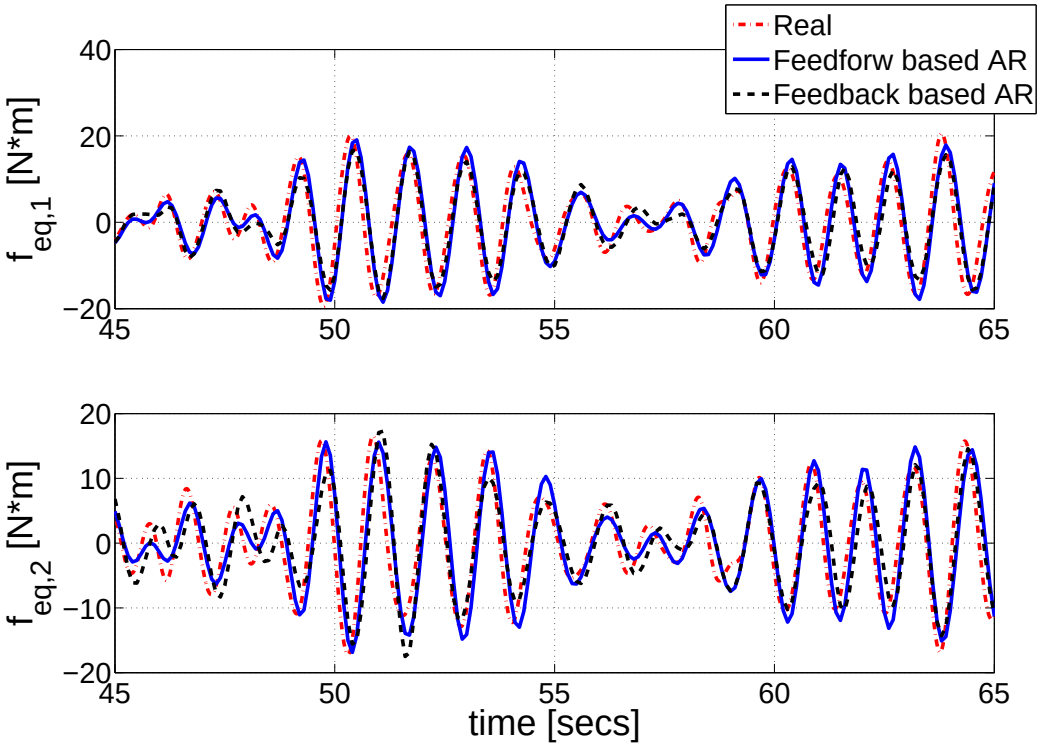

Figure 6.18: Comparison between real and predicted equivalent excitation forces for a forecasting horizon $T_{horizon} = 3$ seconds given by the AR model with $n_a = 30$ based on the feedback and feedforward estimator for an irregular wave made using a JONSWAP spectrum with a significant wave height H_s = 15 cm and peak period T_p = 1.25 s.

Chapter 7

System set-up for wave-tank testing

7.1 Introduction

In Section 3.5, a dynamic model of a three-body hinge-barge WEC is derived, while, in Chapter 5, a real-time optimal controller, that maximizes the energy extracted by the WEC, is presented. The power absorption performance of the real-time optimal controller heavily depends on the quality of the dynamic model that is used to evaluate the response of the WEC to the waves. In this chapter, a system set-up for wave-tank testing of a 1/20th scale three-body hinge barge WEC, is presented. The wave-tank tests of a 1/20th scale three-body hinge barge WEC can be used to validate the dynamic model of the WEC, and experimentally evaluate the performance of the real-time optimal controller and of a control strategy based on optimal linear damping coefficients of passive PTOs. The scale model device has been provided by Wave Energy Conversion Corporation of America (WECCA) [113], and the tank tests carried out on the scale model device, are presented in Chapter 9.

The results from wave-tank tests, carried out on a small scale device, can be scaled for a full scale device. It is important to highlight that the influence of some forces, on the motion of the small scale device, can be different from the influence of the same forces on the full scale device. For example, the influence of friction effects, at the hinges between the barges, on the motion of the device, is higher for the small scale device than the full scale device. Also, the problem of the design of a PTO, for a small scale device, is considerably more challenging than for a full scale device, due to the increased effects of friction and backlash between moving parts of the PTO, on the motion of the small scale device.

A picture of the 1/20th scale three-body hinge-barge WEC in the wave-tank is shown in Figure 7.1a showing the WEC structure composed of fore, central and aft barges. A damping plate is attached to the central barge in order to reduce the heave motion of the central barge, and increase the relative pitch motion of the fore and aft barge with respect to the central barge. As shown in Figure 7.1a, the device is moored with 4 compliant moorings connected to the central barge. The moorings were kindly provided by Sea Power Ltd [20]. In Figure 7.2, the configuration of the moorings, connected to one side of the central barge, is shown. As shown in Figure 7.2, each

mooring is composed of a chain, with one end anchored to the bottom of the tank, and the other end connected to a buoy. Then, the buoy is connected to the central barge via an elastic string. While the surge motion of the central barge is constrained by the compliant moorings, the central barge is free to move in heave. As shown in Figure 7.1a, the device is equipped with a fore and aft encoder at the hinge-point to measure the relative pitch motion of the fore and aft barge with respect to the central barge, respectively. The surface elevation of the incoming wave is measured via a wave gauge situated 1.2 m in front of the device, as shown in Figure 7.1b.

As shown in Figure 7.1a, the central barge is also equipped with an Inertial Measurement Unit (IMU) which, together with ultrasound sensors, provides a measurement of the motion of the central barge. The ultrasound sensors are mounted on the ceiling above the wave-tank, as shown in Figure 7.1c. The measurements provided by the ultrasound sensors and IMU are optimally combined together with a Extended Kalman Filter (EKF), to compute the motion of the central barge. Full details on the motion capture system, based on ultrasound sensors and an IMU, are presented in Chapter 8.

Also shown in Figure 7.1a are two hydraulic dampers, which are connect the central barge to the fore and aft barges. The relative pitch motion between the fore and aft barge, with respect to the central barge, drives the hydraulic dampers, which dissipate the mechanical energy of the device. Therefore, the hydraulic dampers act as PTOs, which convert the energy of the waves into mechanical energy. The flow of the hydraulic fluid, in each hydraulic damper, is regulated using a flow control valve, whose opening is controlled with a stepper motor. The force exerted by each hydraulic damper on the device is measured using a load cell, and the force can be changed by varying on the opening of the flow control valve. Therefore, the hydraulic dampers, with the flow control valves, represent passive PTOs with adjustable damping. The damping of the hydraulic dampers is varied by an optimal control strategy that computes the optimal profile of the damping of each PTO in order to maximize the energy extracted by the device, as shown by the control scheme in Figure 5.23.

A functional scheme of the system set-up for wave tank testing of a 1/20th scale device is shown in Figure 7.3, with the system composed of 3 functional parts: control, actuators and sensors. The sensor suite comprises the fore and load cells, the fore and aft encoders, the ultrasound sensors and the IMU, and the wave gauge. The actuators are comprised of the fore and aft motors, the fore and aft valves and the fore and aft hydraulic dampers. The control part comprises an Arduino board, and a PC running a Matlab script which implements an EKF to compute the motion of the central barge, and the HRCF PS control for maximization of the energy extracted by the device. The EKF optimally combines the information provided by the ultrasound sensors and IMU in order to compute the motion of the central barge. Full details on the EKF for the motion capture system are presented in Chapter 8. Also, the Matlab script implements HRCF PS control for maximization of the energy extracted by the device. The HRCF PS control is presented in Chapter 5, and computes the optimal damping profile for the hydraulic dampers, based on the optimal trajectories of relative torques and pitch rotational velocities between the fore and aft barge, with respect to the central barge. The Ardunino board plays the role of an interface

between the PC, the sensors and the actuators. The signals provided by the sensors are processed by the Arduino board, and the processed data is then streamed to the PC. The data provided by the ultrasound sensors and IMU are directly sent to the PC through a dongle. Given the optimal damping profile for the hydraulic dampers, computed by the HRCF PS control, the Arduino board changes the opening of the flow control valve accordingly, using the stepper motors.

A major issue of the system set-up, shown in Figure 7.3, is the synchronization of the data provided by the ultrasound sensors and IMU streamed through the dongle, and the data provided by the sensors streamed through the Arduino board. The data provided by the Arduino board, and the dongle, are transmitted to the PC running the Matlab script, via serial ports. However, the PC running the Matlab script is equipped with only one controller of the serial bus and, therefore, the dongle and the Arduino board cannot simultaneously stream data. Thus, at a certain time step, while the PC running the Matlab script retrieves the data provided by the dongle, the data provided by the Arduino board are buffered. Then, once the data provided by the dongle are retrieved, the PC running the Matlab scripts empties the buffer in order to retrieve the data provided by the Arduino at the same time step at which the data provided by the dongle are retrieved. While the dongle and Arduino board can independently stream data with a sampling frequency of 15 Hz and 1 kHz, respectively, the need for synchronization of data provided by both the dongle and Arduino board significantly reduces the achievable sampling frequency. In particular, the maximum sampling frequency achievable by the set-up in Figure 7.3, is only 5 Hz. However, as shown in Figure 3.10, given that the fastest dynamics of a 1/25th scale three-body hinge-barge device are around 1.3 Hz, a sampling frequency of 5 Hz satisfies the Nyquist criterion, which requires a sampling frequency that is, at least, twice the maximum frequency present in the signal.

The remainder of this Chapter is organized as follows: in Section 7.2, the wave-tank used to carried out the tank tests is described in detail while, in Section 7.3, the wave gauge for the measurement of the incoming wave is described. In Section 7.4, the load cells for the measurement of the forces applied by the hydraulic dampers are presented while, in Section 7.5, the encoders for the relative rotation of the fore and aft barge with respect to the central barge is described. In Section 7.6, the hydraulic dampers with variable damping are characterized and, finally, in Section 7.7, conclusions are drawn.

7.2 Wave Tank

A graphical representation of the wave tank, used for the wave-tank testing of the device, is shown in Figure 7.4, together with the ultrasound sensors for the motion capture system placed above the central section of the tank. The tank is produced by OMEY labs [114], which offers a modular design for the wave tank, where each module is 2.5 m wide, 2 m long and 1.3 m deep. The assembly of different modules allows wave tanks of any length to be built and, therefore, provides a low-cost customized solution that is affordable by small to medium size wave energy companies,

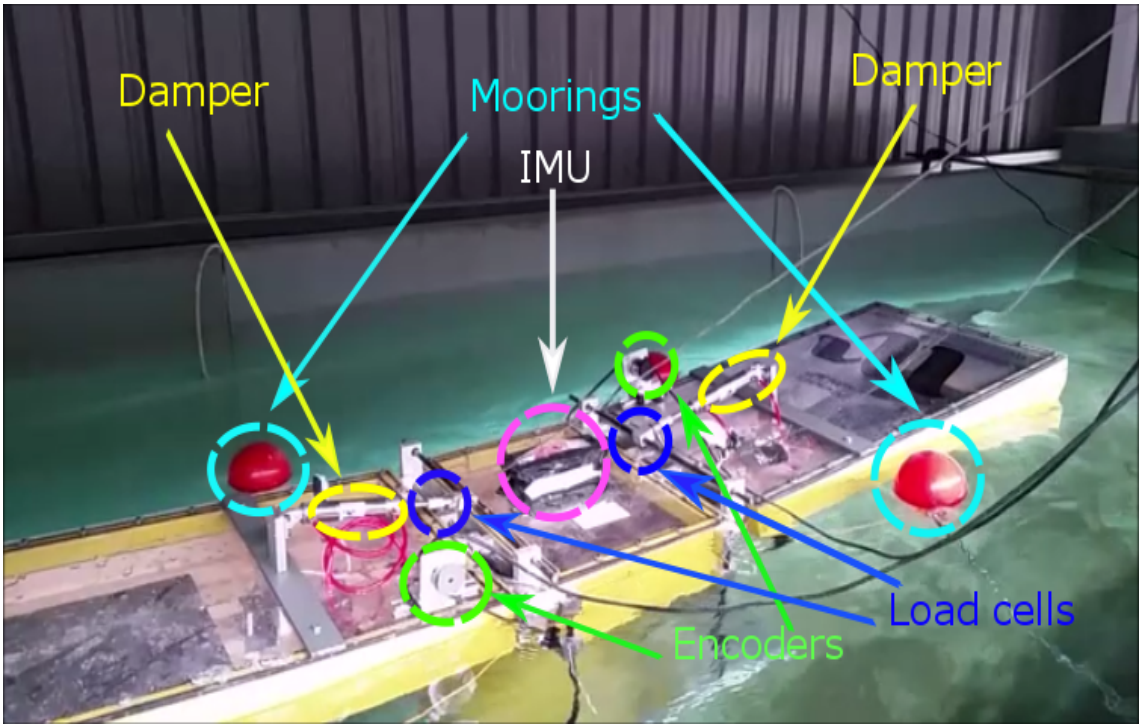

(a)

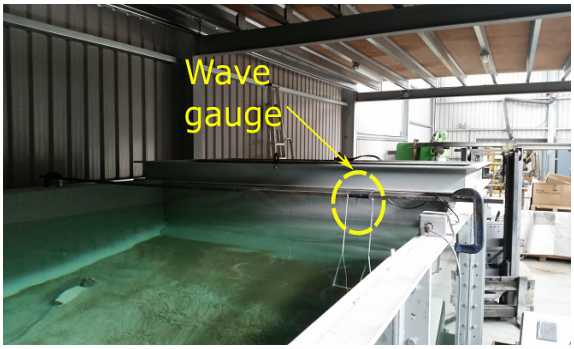

(b)

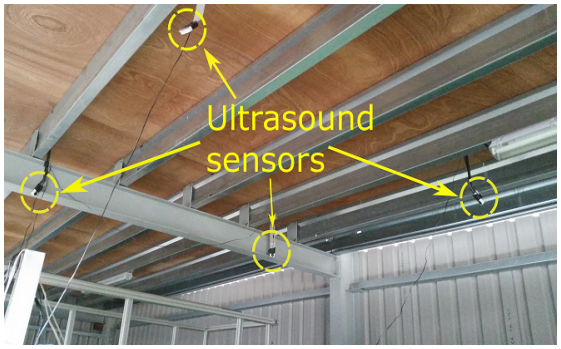

(c)

Figure 7.1: Picture of the 1/20th scale three-body hinge-barge in the wave-tank (a), wave gauge for the measurement of the incident wave elevation (b), and ultrasound sensors mounted on the ceiling above the wave-tank (c).

eliminating the need to resort to high-end wave tanks characterized by high daily costs. For this study, the tank is composed of 5 modules, for an overall length of 10 m. The tank is also equipped with a bottom-hinged paddle wave maker which can create planar regular and irregular waves, and a parabolic passive beach, for wave absorption. The wave maker is set-up to generate regular waves with a specific wave height and period, and irregular waves with a specific significant wave height and peak period, using a Bretschneider spectrum.

In Figure 7.5, the operational range of the wave maker is shown, in terms of the maximum wave height at each wave period. For example, the maximum wave height that can be generated at a period of $T = 1.25$ seconds is 0.16 m. For wave periods less than $T = 1.25$ seconds, the wave

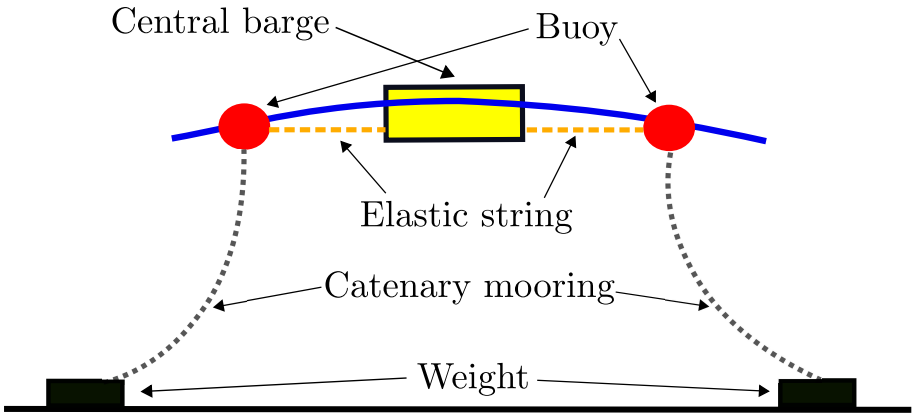

Figure 7.2: Illustrative scheme of the moorings connected to one side of the central barge of a three-body hinge-barge device.

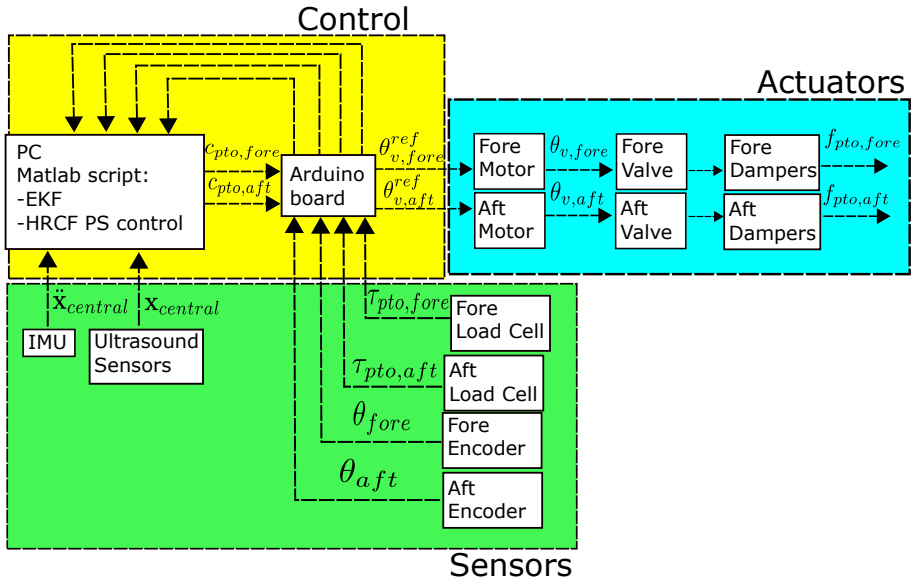

Figure 7.3: Functional scheme of the system set-up for wave tank testing of the 1/20th scale device composed of control part, sensors and actuators.

height is limited by wave breaking. In order to determine the maximum wave height for each wave period smaller than $T = 1.25$ seconds, the wave height was increased for each wave period with an increment of 0.01 m until wave breaking occurred [115]. The maximum wave height for wave periods less than $T = 1.25$ seconds is determined visually as the wave height just before wave breaking, or ripples on the top of the wave crests occurred.

As shown in Figure 7.5, the smallest period achievable by the tank is $T = 0.5$ seconds. For wave periods less than $T = 0.5$ seconds, the size of the cross waves generated in the tank have comparable or even larger size than the size of the longitudinal wave generated by the wave maker. The size of the cross waves decreases with an increase of the wave period. For each wave period, the cross waves become less significant, if the waves generated by the wave maker have a small wave height. For waves of period longer than $T = 1.25$ seconds, the wave height is limited by the

stroke of the wave maker.

Given that the depth of the tank is 1.3 m and the operational range of the wave maker goes from 0.5 to 3 seconds, as shown in Figure 7.5, the tank tests are carried out under the assumption of deep water. As the 3-body hinge-barge device is classified as an attenuator, the full scale 3-body hinge-barge WEC is designed to operate offshore [2] and, therefore, the assumption of deep water for the tank tests if justified. Given a geometric scale ratio between the 1/20th scale and the full scale model of $\lambda = 20$, the resonant period of the 1/20th scale model device is given as follows:

$$T_{n,dev} = T_{n,scale}\sqrt{\lambda} \tag{7.1}$$

where $T_{n,scale}$ and $T_{n,dev}$ are the resonant period of the scale model and full scale device, respectively. Therefore, given that the wave makers generate a spectrum of the waves with peak period around 1.4 seconds, the peak period of the full scale device is around 6 seconds. For a spectrum of the waves with a peak period $T_p = 6$ seconds and significant wave height $H_s = 2$ m, the wave power level is given as follows [10]:

$$J = \frac{\rho g^2}{32\pi} T_p H_s^2 \cong 23kW/m \tag{7.2}$$

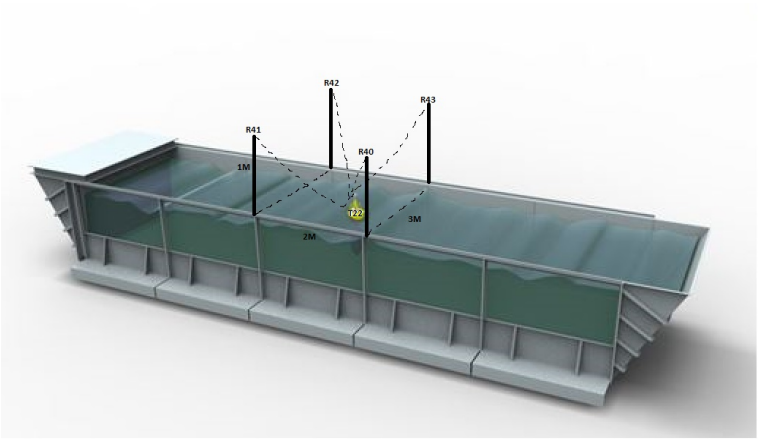

Figure 7.4: OMEY labs wave tank with ultrasound receivers placed above the middle section of the tank.

7.3 Wave gauge

The waves incident on a device can be measured by using two different types of wave gauges: resistive and capacitive. Resistive wave gauges are composed of two metal rods, where the resistance between the rods changes with the water elevation [116]. Capacitive wave gauges change their capacitance as the water level varies, and they are generally more accurate and expensive than resistive gauges. The accuracy of resistive gauges can be improved by using an artificial neural

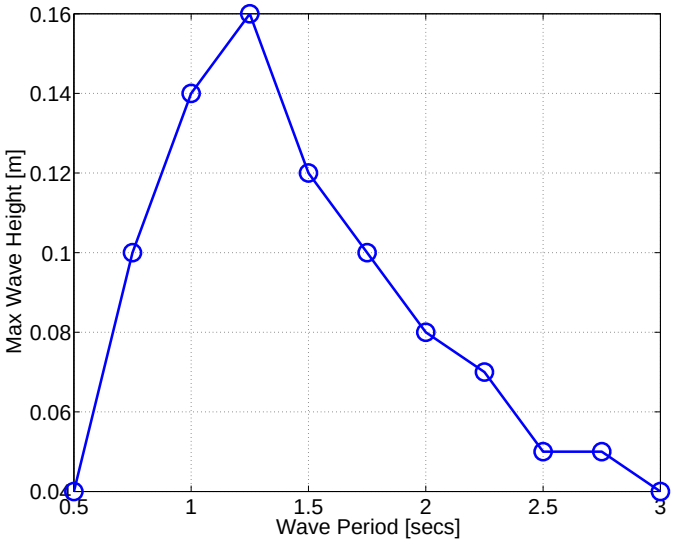

Figure 7.5: OMEY labs wave maker operational range.

network trained with data from capacitive gauges [117]. In this study, a capacitive wave gauge WG-55 from RBR Limited is used [118], and is placed 1.2 m up-wave of the front barge of the device.

In the remainder of this section, the static calibration of the wave gauge and the measurement of regular and irregular waves are presented.

7.3.1 Wave gauge static calibration

The output of the wave gauge is a voltage which is linearly proportional to the water level. In order to statically calibrate the wave gauge, 5 tests, with different water levels, were performed, with an increase of 22.8 mm of the water level between each test. The output voltage given by the wave gauge, for each test, is shown in Figure 7.6, together with the linear calibration curve that best fits the output voltage. The linear calibration curve is used for the subsequent measurement of water elevation for the wave-tank tests, with regular and irregular waves, with or without the device in the tank.

7.3.2 Regular wave measurement

In this section, the measurement of the wave elevation for regular waves with a wave height of 0.04 m, and different periods, is presented. In Figures 7.7, 7.8, 7.9 and 7.10, the wave elevation, measured by the calibrated wave gauge, is shown for regular waves of wave height 0.04 m and period $T = 0.5$ seconds, $T = 1$ seconds, $T = 1.5$ seconds and $T = 2$ seconds, respectively. As shown in Figures 7.7 and 7.8, for small wave periods, the wave height is close to desired value, but is not constant. For small wave periods, the cross waves generated in the tank interfere with

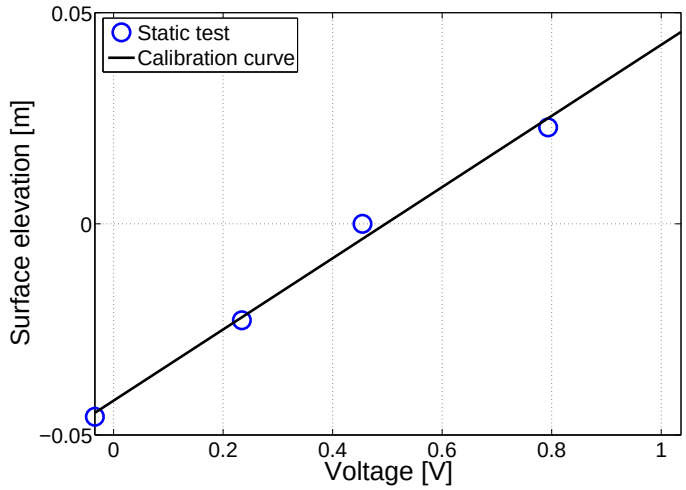

Figure 7.6: Static calibration wave gauge with 5 tests of different water levels.

the longitudinal waves generated by the wave maker, resulting into the formation of ripples on the top of the wave crests. Also, at the end of each test with regular waves, the waves are not fully absorbed by the passive beach, with reflected waves traveling back along the tank. Therefore, the measurement of the wave elevation, for a certain test with regular waves, is corrupted by the reflected waves generated at the end of the previous test. As shown in Figures 7.9 and 7.10, for long wave periods, the wave height is more constant than for small wave periods, but is about 25% higher than the desired value. A more extensive study on the measurement of the wave elevation at OMEY labs can be found in [115].

7.3.3 Irregular wave measurement

In this section, the measurement of the wave elevation for irregular waves generated using a Bretschneider spectrum with a significant wave height of 0.18 m, and different peak periods, is presented. In Figures 7.11, 7.13 and 7.15, the wave elevation measured by the calibrated wave gauge is shown for irregular waves made using a Bretschneider spectrum with a significant wave height 0.18 m and peak period $T_p = 1.0$ seconds, $T_p = 1.25$ seconds and $T_p = 1.5$ seconds, respectively. In Figures 7.12, 7.14 and 7.16, the spectrum of the wave elevation measured by the calibrated wave gauge is shown for irregular waves, generated using a Bretschneider spectrum, with a significant wave height 0.18 m and peak period $T_p = 1.0$ seconds, $T_p = 1.25$ seconds and $T_p = 1.5$ seconds, respectively. As shown in Figures 7.12, 7.14 and 7.16, the peak frequencies of the irregular waves are the same as the desired peak frequencies. Given the spectrum of an irregular wave $S(\omega)$, the significant wave height, for an irregular wave, can be calculated as follows

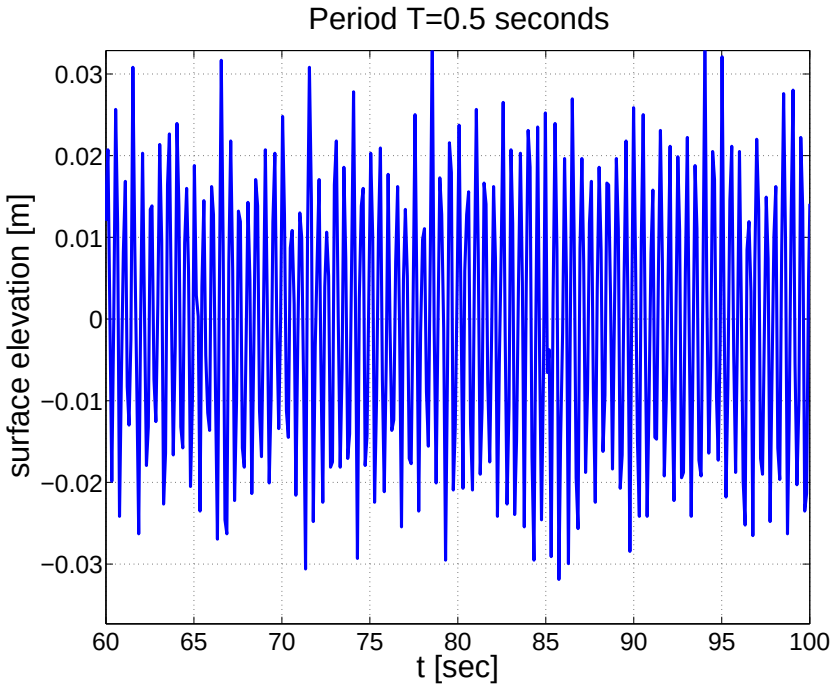

Figure 7.7: Measured wave elevation for regular wave with period $T = 0.5$ seconds and desired wave height of 0.04 m.

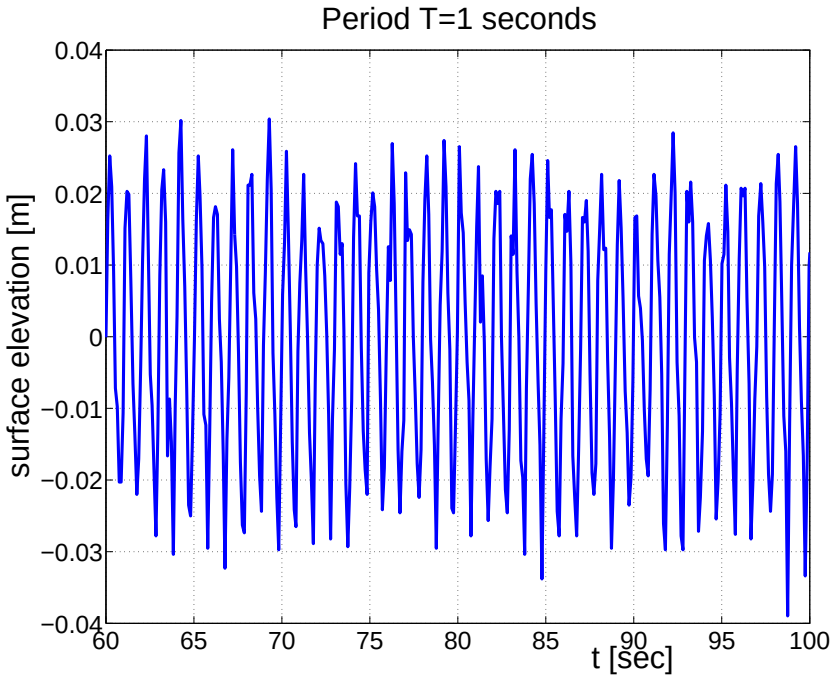

Figure 7.8: Measured wave elevation for regular wave with period $T = 1$ seconds and desired wave height of 0.04 m.

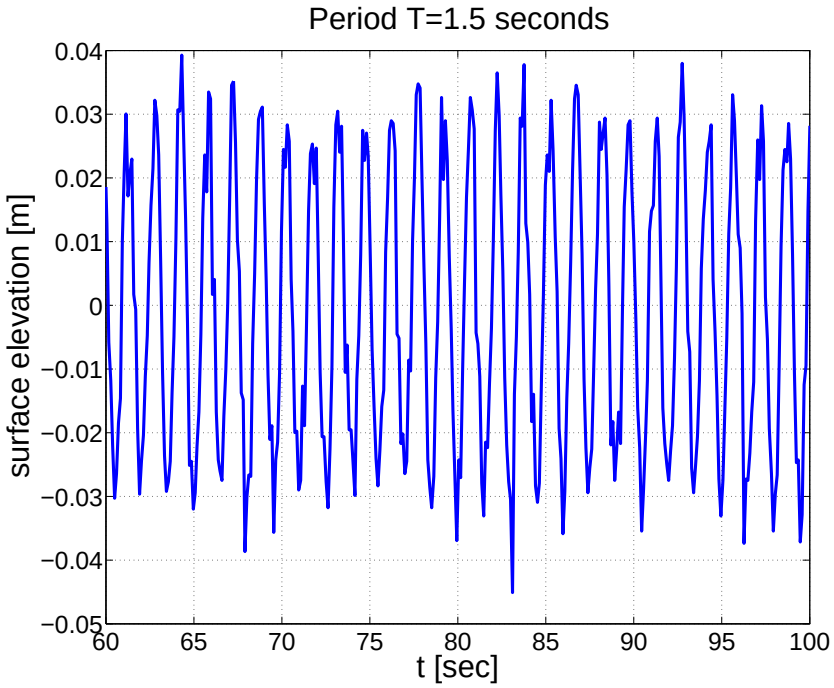

Figure 7.9: Measured wave elevation for regular wave with period $T = 1.5$ seconds and desired wave height of 0.04 m.

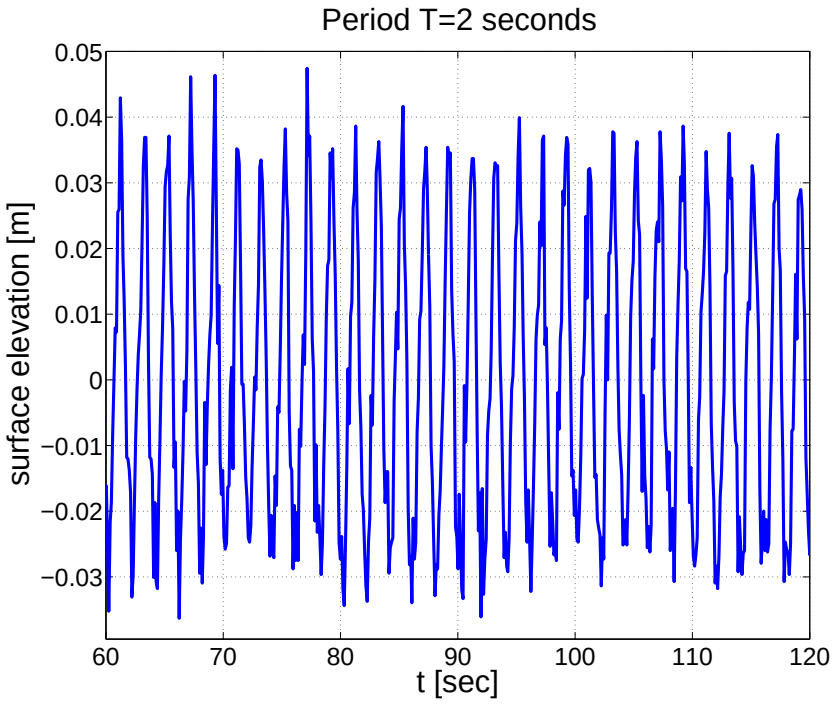

Figure 7.10: Measured wave elevation for regular wave with period $T = 2$ seconds and desired wave height of 0.04 m.

[34]:

$$H_s = 4\sqrt{m_0} = 4\sqrt{\int_0^\infty S(\omega)d\omega} \tag{7.3}$$

For the irregular waves measured in this study, an average significant wave height $H_s = 0.048$ m is found, which is 70% smaller than the desired significant wave height $H_s = 0.18$ m.

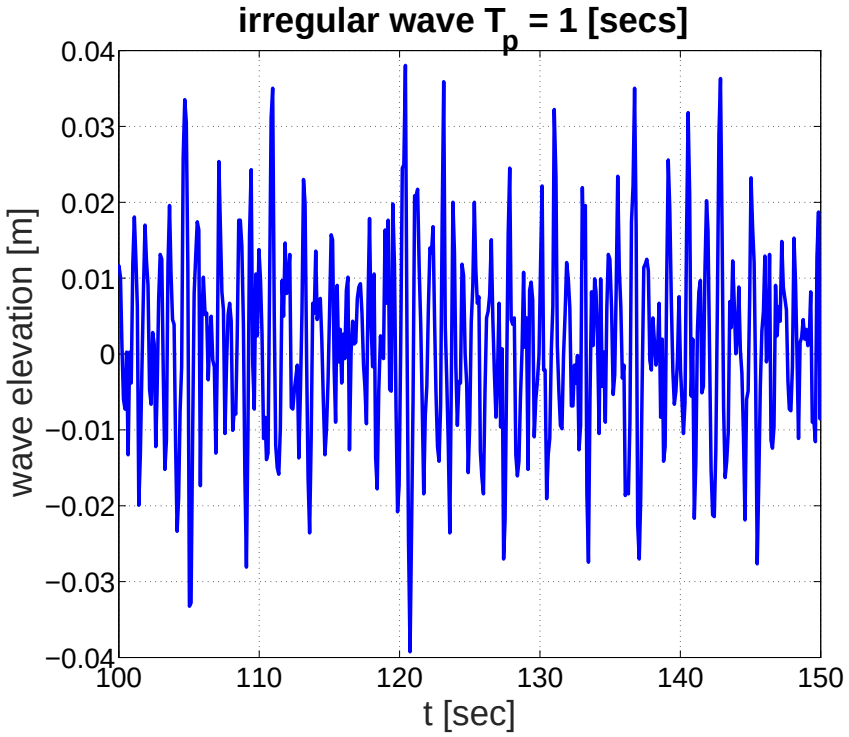

Figure 7.11: Measured wave elevation for irregular wave made using a BRETSCHNEIDER spectrum with a significant wave height 0.18 m and peak period $T_p = 1.0$ seconds.

7.4 Load cells

The fore and aft load cells, for measurement of the forces exerted by each hydraulic damper on the device, are LCM 300 models from Futek [119]. The LCM 300 load cell can measure both tensile and compressive loads. The output of each load cell is a voltage which is linearly proportional to the applied load. In order to statically calibrate each load cell, 21 tests with different applied loads are performed, with an increase of 1.08 N of the applied load between each test. The output voltage, given by the fore load cell for each test, is shown in Figure 7.17, together with the linear calibration curve that best fits the output voltage. The output voltage given by the aft load cell,

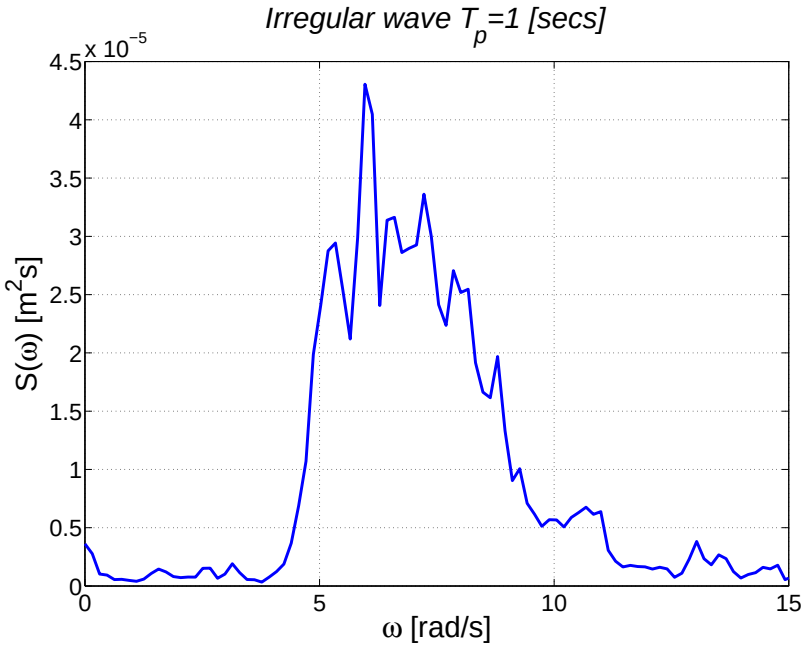

Figure 7.12: Spectrum of measured wave elevation for irregular wave made using a BRETSCHNEIDER spectrum with a significant wave height 0.18 m and peak period $T_p = 1.0$ seconds.

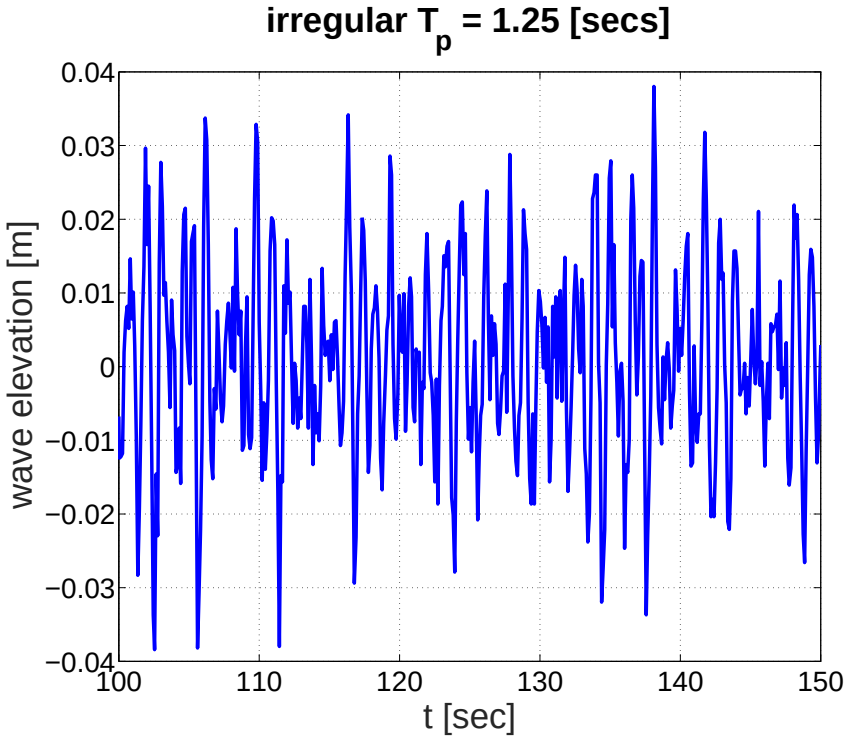

Figure 7.13: Measured wave elevation for irregular wave made using a BRETSCHNEIDER spectrum with a significant wave height 0.18 m and peak period $T_p = 1.25$ seconds.

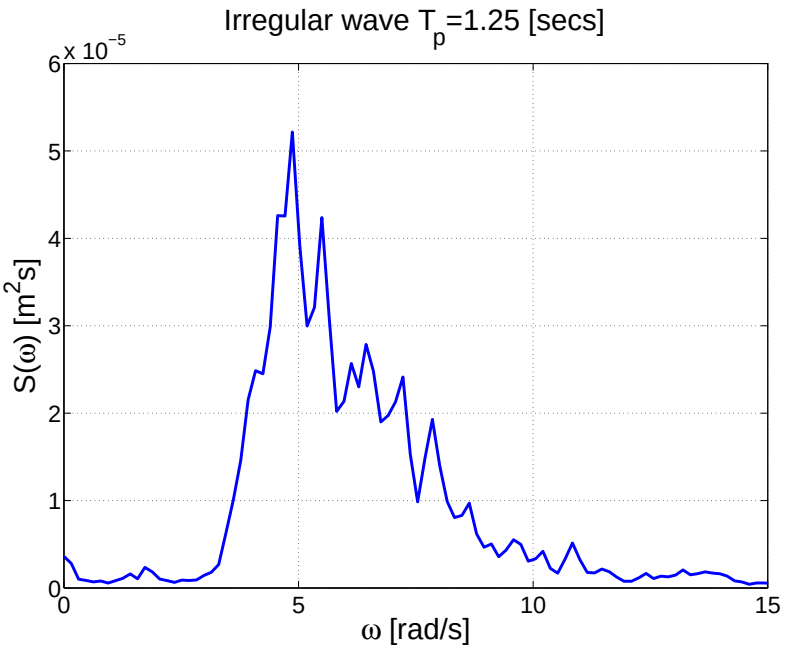

Figure 7.14: Spectrum of measured wave elevation for irregular wave made using a BRETSCHNEIDER spectrum with a significant wave height 0.18 m and peak period $T_p = 1.25$ seconds.

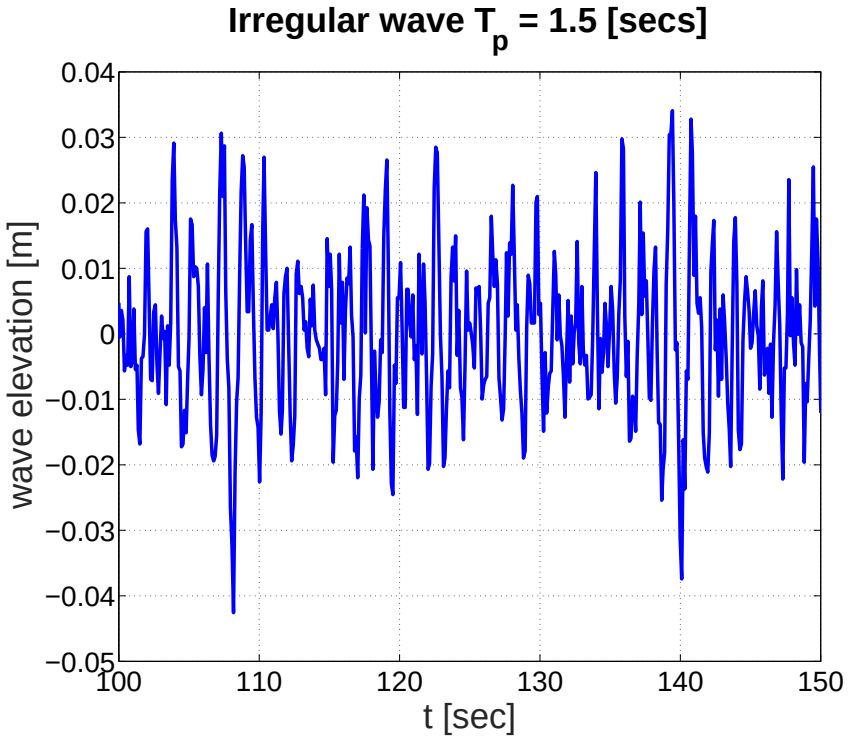

Figure 7.15: Measured wave elevation for irregular wave made using a BRETSCHNEIDER spectrum with a significant wave height 0.18 m and peak period $T_p = 1.5$ seconds

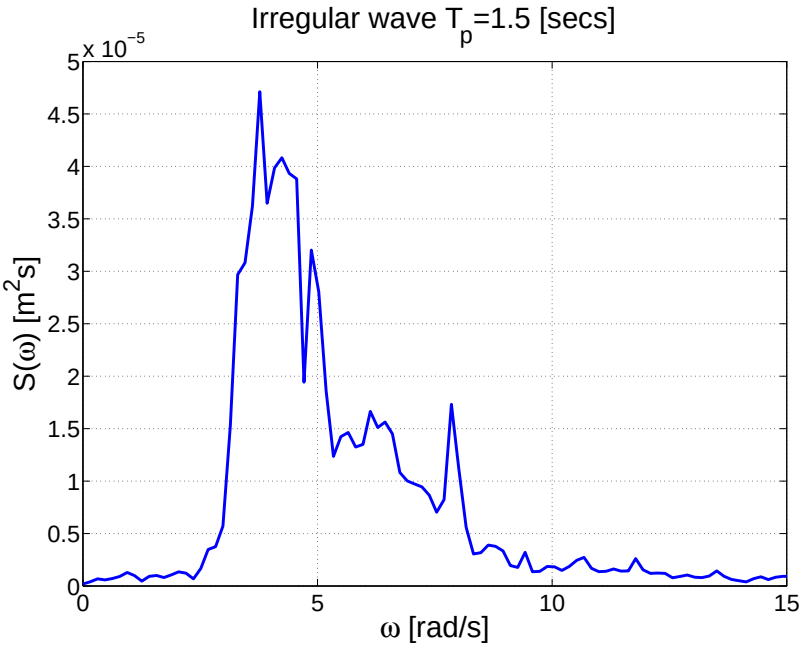

Figure 7.16: Spectrum of measured wave elevation for irregular wave made using a BRETSCHNEIDER spectrum with a significant wave height 0.18 m and peak period $T_p = 1.5$ seconds

for each test, is shown in Figure 7.18, together with the linear calibration curve that best fits the output voltage.

7.5 Rotational encoders

The fore and aft encoders, for the measurement of relative pitch rotation of the fore and aft barge with respect to the central barge, are rotary incremental encoders of the series TRDA-2E [120]. As shown in Figure 7.19, the rotary incremental encoder is composed of a rotating disk connected to a shaft, a light source, and two photo detectors A and B. The rotating disk contains two patterns of alternating opaque and transparent sectors which intermittently block the light emitted by the light source, as the disk rotates. A pulse signal for the photo detectors A and B is therefore generated. An example of the pulse signals generated by the photo detectors A and B is shown in Figure 7.19. As shown in Figure 7.19, both the rotational position and direction of the disk can be measured. The rotational position of the disk can be measured by counting the number of pulses generated by the photo detectors. Regarding the direction of the rotation of the disk, if the pulse signal from the photo detector A leads the pulse signal from the photo detector B, the disk is rotating in a clockwise direction. Viceversa, if the pulse signal from the photo detector B leads the pulse signal from the photo detector A, then the disk is rotating in a counter-clockwise direction. The encoders used in this work have a resolution of the rotational position of 0.09°.

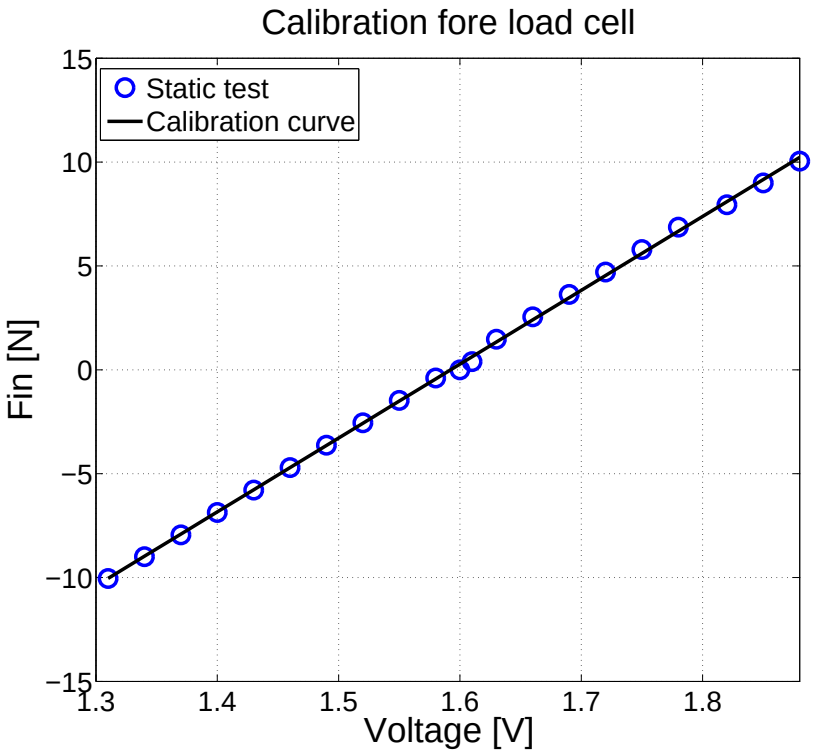

Figure 7.17: Static calibration fore load cell with 21 tests of different applied loads.

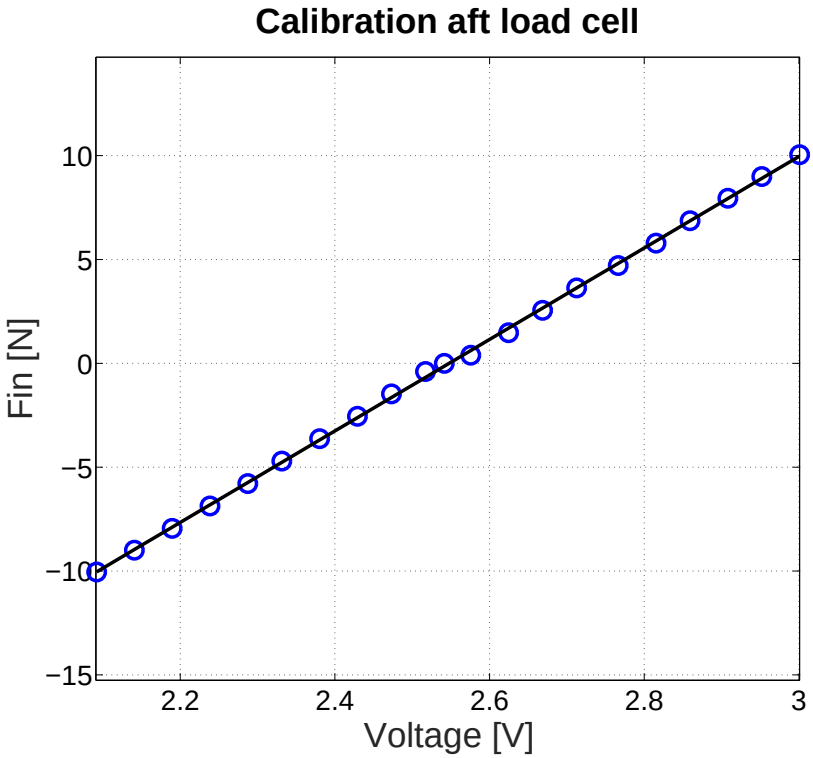

Figure 7.18: Static calibration aft load cell with 21 tests of different applied loads.

In order to statically calibrate each encoder, 9 tests with different static rotation of the fore and aft barges are performed, with an increase of 5°in the rotation of the fore and aft barges between each test. The rotation measured by the fore encoder, for each test, is shown in Figure 7.20, together with the linear calibration curve that best fits the rotation measured by the encoder. The rotation by the aft encoder for each test is shown in Figure 7.21, together with the linear calibration curve that best fits the rotation measured by the encoder.

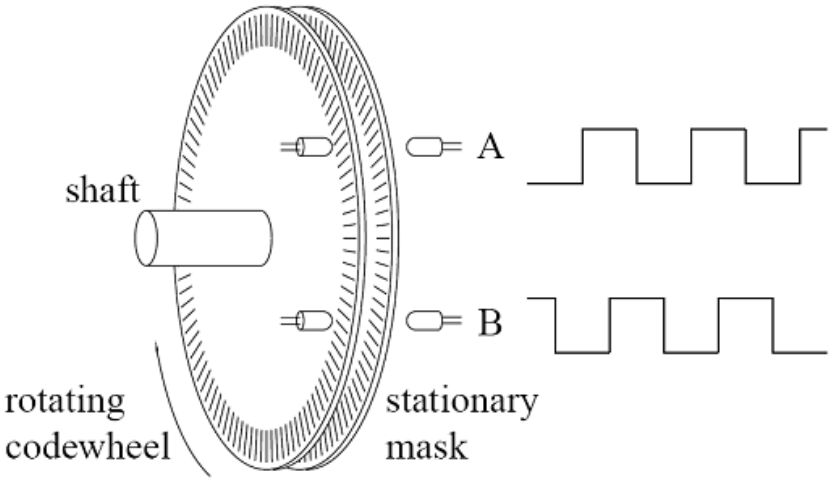

Figure 7.19: Scheme of rotary incremental encoder [121].

7.6 Hydraulic pistons with variable damping

Each hydraulic damper that converts the energy of the waves into mechanical energy is composed of a double acting cylinder, with a flow control valve that regulates the flow of the hydraulic fluid circulating outside the cylinder. The opening of the flow control valve can be changed via a stepper motor. In Figure 7.22, a schematic of the hydraulic damper, together together with the flow control valve and stepper motor, is shown. The hydraulic dampers are of the NITRA series from NITRA Pneumatics [120], the flow control valve is a high-precision flow-adjustment valve from McMASTER-CARR [122] and the stepper motor is a STP-MTR-17040 from [120]. The resolution of the stepper motor is $1.8\ ^\circ/step$ and the maximum motor speed is 13 rps. The choice of the stepper motor for the actuation of the flow control valve plays a critical role in the implementation of the real-time optimal control of the device. In fact, most of the control strategies presented in Section 4.1, that maximize the energy extracted by the device, such as latching, MPC and RHPSC, require an opening of the flow control valve from 0% to 100% instantaneously. For the flow control valve chosen in this study, 20 full rotations of the stepper motor are needed to open the flow control valve from 0% to 100% and, therefore, given a maximum speed of the stepper motor of 13 rps, the time needed by the motor to fully close the flow control valve is around 1.5

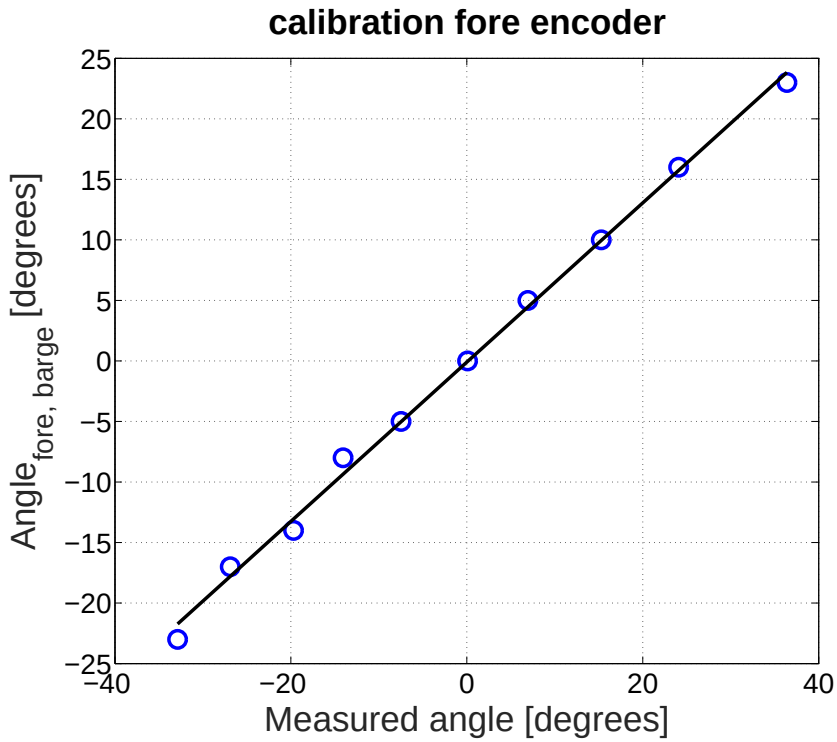

Figure 7.20: Static calibration fore encoder with 9 tests with different static rotation of the fore barge.

seconds, which is not an acceptable actuation time for real-time control of the device. In fact, an actuation time of 1.5 seconds is well beyond the maximum computational time allowed for the real-time controller of the device, which depends on the fastest dynamics of a 1/20th scale three-body hinge-barge device. As shown in Figure 3.10, given that the fastest dynamics of a 1/25th scale three-body hinge-barge device are around 0.8 seconds, a reasonable computational time available to the real-time controller is around 0.2 seconds. Thus, with the stepper motor chosen for this study, the maximum variation of the opening of the valve that can be achieved in real-time is around 10%, which requires an actuation time of 0.2 seconds. Obviously, a maximum variation of the opening of the valve of 10% greatly reduces the power absorption that can be achieved by real-time control, with respect to the control strategy based on optimal constant damping for the dampers presented in Section 4.5.1.1.

In order to characterize the hydraulic dampers, a series of wave-tank tests, with a regular wave of period $T = 1.5$ seconds and amplitude of 0.025 m were performed . The opening of the flow control valve of the fore and aft hydraulic damper was varied from 0% to 100%, with a 10% increment. The forces applied by the hydraulic dampers, measured by the load cells, together with the relative pitch rotation of the fore and aft barge measured by the encoders, were recorded during each test. From equation (3.91), the damping of each hydraulic damper can be computed as:

$$c_{pto,i} = \frac{F_{s,i}}{\dot{l}_i} \tag{7.4}$$

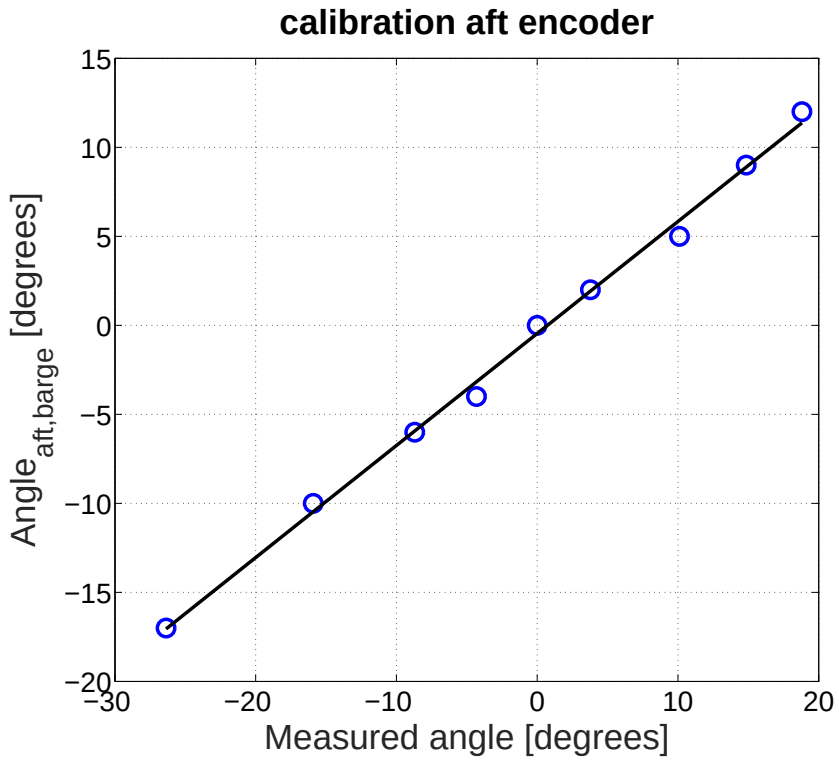

Figure 7.21: Static calibration aft encoder with 9 tests with different static rotation of the aft barge.

with $i = 1,2$ for the fore and aft damper, respectively, while $F_{s,i}$ and $\dot{l}_i$ are the force and time derivative of the displacement of the hydraulic damper, respectively. For this study, the derivative of the displacement of the hydraulic damper $\dot{l}_i$ is not directly measured, but can be approximated from equation (7.5) as follows:

$$\dot{l}_i = a\dot{\theta}_{rel,i} \tag{7.5}$$

where a represents the vertical distance between the line of action of the damper force and the center-line of the device, and $\dot{\theta}_{rel,i}$, with $i = 1$ and $i = 2$, is the relative pitch velocity between the fore and aft barge with respect to the central barge, respectively.

By way of example, for a regular wave of period $T = 1.5$ seconds and amplitude of 0.025 m, in Figures 7.23, 7.24 and 7.25, the measured force exerted by the fore and aft hydraulic dampers is compared to the approximated forces given by equation (3.91) for a valve's opening of 10%, 50 % and 70%, respectively. As shown in Figures 7.23, 7.24 and 7.25, the forces given by equation (3.91) provide a quite accurate approximation of the measured forces exerted by the fore and aft hydraulic damper. Furthermore, as shown in Figures 7.23, 7.24 and 7.25, the magnitude of the force on the fore hydraulic damper, for an opening of the flow control valves of 10%, is very similar to the magnitude of the force on the fore hydraulic damper, for an opening of the flow control valves of 50% and 70%. However, the magnitude of the force on the aft hydraulic damper, for an opening of the flow control valves of 10%, is twice the magnitude of the force on the

aft hydraulic damper, for an opening of the flow control valves of 50% and 70%. Furthermore, as shown in Figures 7.24 and 7.25, the force on the aft hydraulic damper shows an asymmetric response, with the absolute value of the negative peaks larger than the absolute value of the positive peaks.

The response of the forces of the hydraulic dampers is asymmetric since the flow of the hydraulic fluid is different depending on the direction of the movement of the ram of the dampers. Therefore, the hydraulic dampers introduce nonlinear effects to the dynamics of the device. In order to characterize the nonlinearities introduced by the hydraulic dampers, in Figure 7.26, the forces of the hydraulic dampers are plotted against the derivative of the displacements of the hydraulic dampers for a valve's opening of 10%. In Figure 7.27, the forces of the hydraulic dampers are plotted against the derivative of the displacements of the the hydraulic dampers for a valve's opening of 50%. As shown 7.26 and 7.27, a significant number of points deviate from the linear function of the derivative of the displacements that best fits the measured forces. In particular, for a valve's opening of 10%, the square of the correlation, between the measured values and the predicted values given by the linear function, R^2 is 0.91 and 0.92 for the force of the fore and aft damper, respectively. For a valve's opening of 50%, the square of the correlation, between the measured values and the predicted values given by the linear function, R^2 is 0.8 and 0.92 for the force of the fore and aft damper, respectively.

Another issue that occurred with the hydraulic dampers used in this study is the compressibility of the hydraulic fluid introduced by the air-bubbles trapped inside the hydraulic fluid. Therefore, the use of hydraulic dampers for the extraction of the energy from the device involves different issues that strongly affect the performance of the real-time control of the damping, and the control strategy based on optimal constant damping for the dampers.

In Figures 7.28 and 7.29, the damping computed with equation (7.4) is shown for the fore and aft hydraulic damper, respectively. The damping of the fore and aft hydraulic cylinder is computed for an opening of the flow control valves that varies from 0% to 100%. In Figures 7.28 and 7.29, the damping is interpolated with a quadratic curve. As shown in Figures 7.28 and 7.29, the damping of the aft hydraulic damper is higher than the damping of the fore hydraulic damper for each opening of the flow control valves. The quadratic interpolation curve shown in Figures 7.28 and 7.29 can be used by the feedforward controller shown in Figure 5.23, to compute the optimal opening of the flow control valves, given the optimal damping computed by the PS with HRCF basis functions.

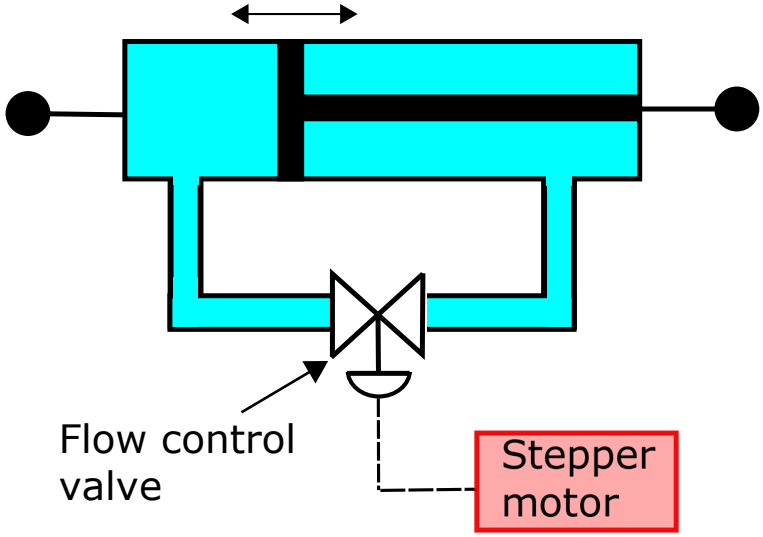

Figure 7.22: Schematic of the hydraulic damper together with the flow control valve actuated by stepper motor.

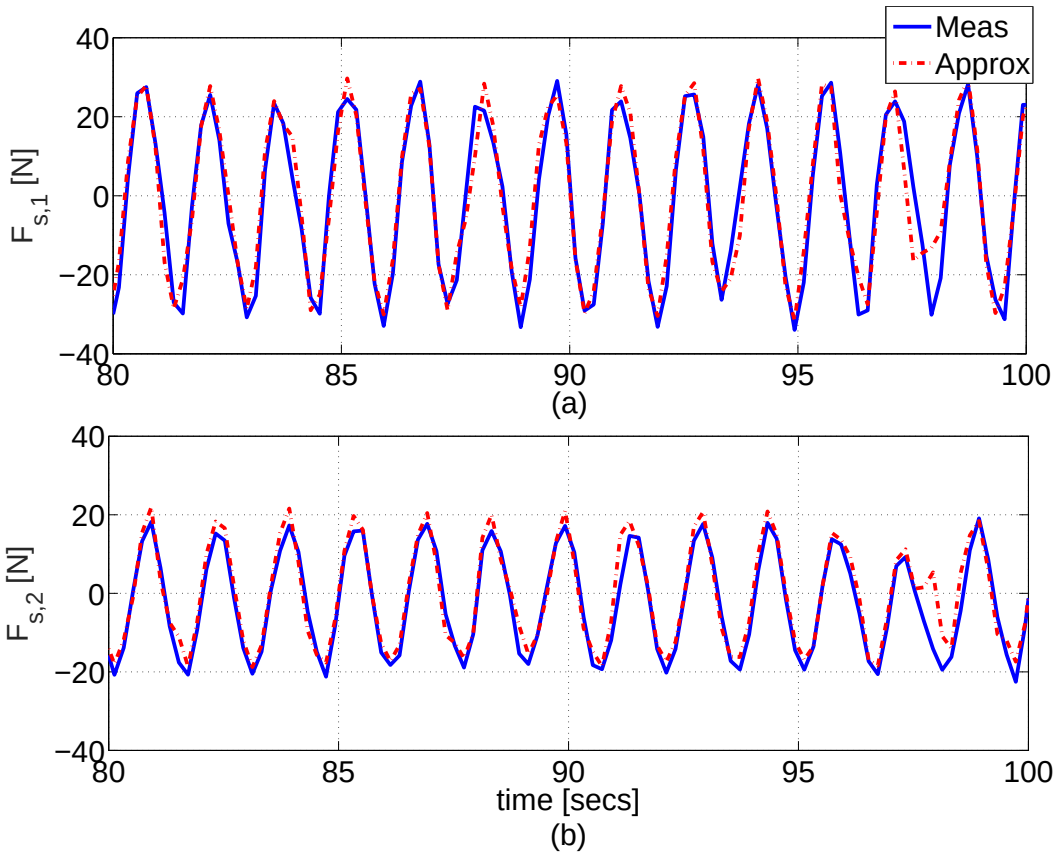

Figure 7.23: Measured and approximated forces exerted by the fore (a) and aft (b) hydraulic damper with an opening of the flow control valves of 10% for a regular wave of period 1.5 seconds and amplitude 0.025 m.

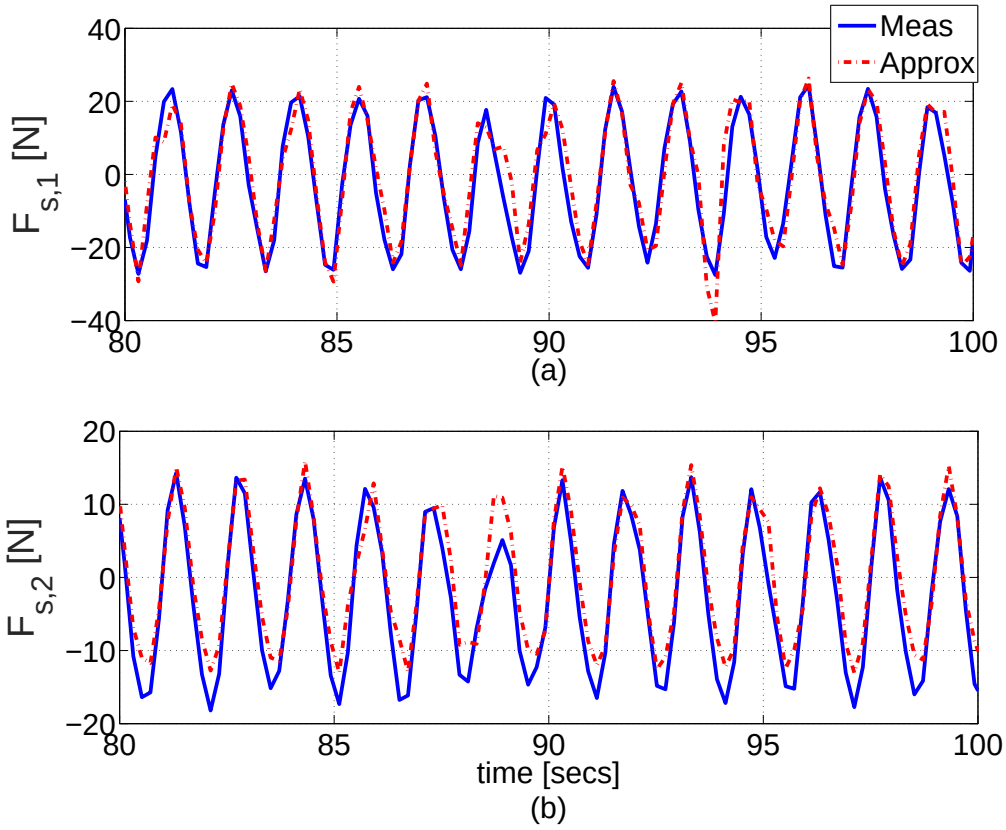

Figure 7.24: Measured and approximated forces exerted by the fore (a) and aft (b) hydraulic damper with an opening of the flow control valves of 50% for a regular wave of period 1.5 seconds and amplitude 0.025 m.

7.7 Conclusions

In this chapter, the system set-up for wave-tank testing of a 1/20th scale three-body hinge-barge, is presented. The wave-tank testing of a small scale WEC is important for the evaluation of the response of the WEC to the waves, and the assessment of power production. Furthermore, measurements from wave tank tests can also be used to validate the dynamic model of the device, which can be used for the implementation of energy-maximising control strategies.

The acquisition of data from the sensors, and the energy-maximising control strategy, are mainly implemented in a PC running Matlab, with an Arduino board acting as an interface between the PC and the signals provided by the encoders, load cells and wave gauge. The signals provided by the motion capture system are directly sent to the PC through a dongle.

The major issues associated with the system set-up for the wave-tank testings, in this work, are:

- The low maximum sampling frequency of the signals provided by the sensors, due to required synchronization of the streamed data from the Ardunio board and the motion capture system.

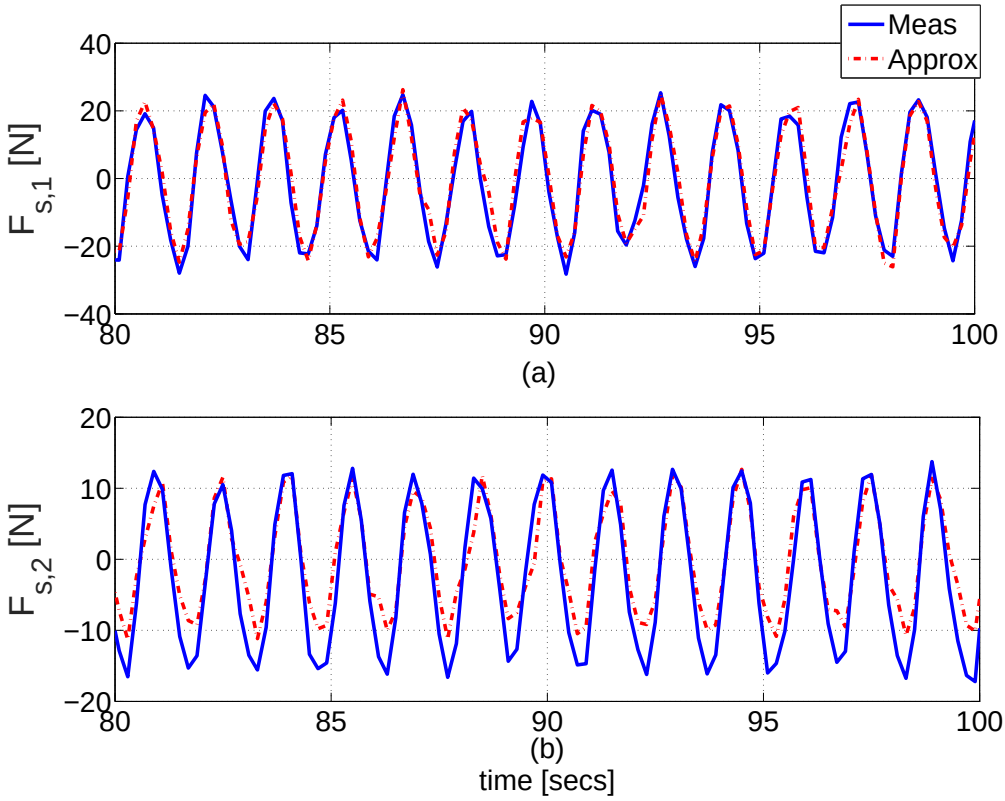

Figure 7.25: Measured and approximated forces exerted by the fore (a) and aft (b) hydraulic damper with an opening of the flow control valves of 70% for a regular wave of period 1.5 seconds and amplitude 0.025 m.

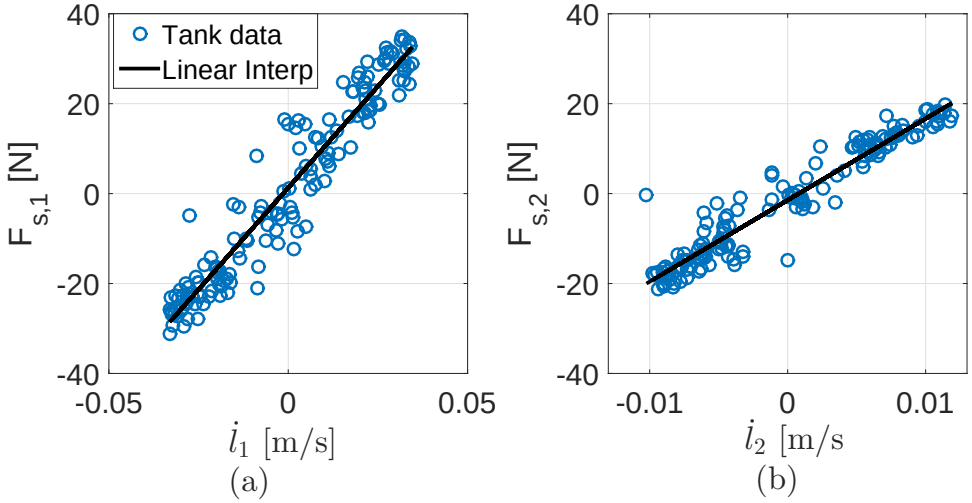

Figure 7.26: Measured force of the fore damper (a) and aft damper (b) plotted against the derivative of the displacements with an opening of the flow control valves of 10% for a regular wave of period 1.5 seconds and amplitude 0.025 m.

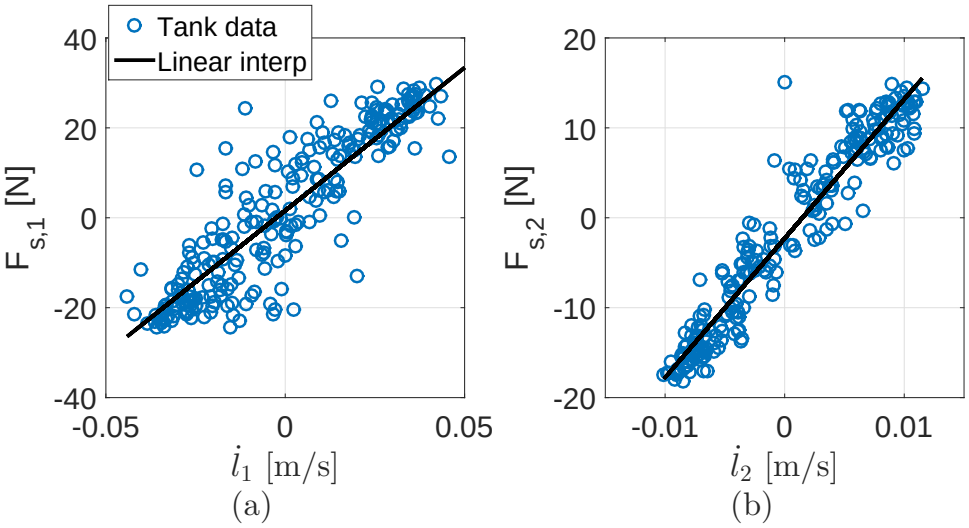

Figure 7.27: Measured force of the fore damper (a) and aft damper (b) plotted against the derivative of the displacements with an opening of the flow control valves of 50% for a regular wave of period 1.5 seconds and amplitude 0.025 m.

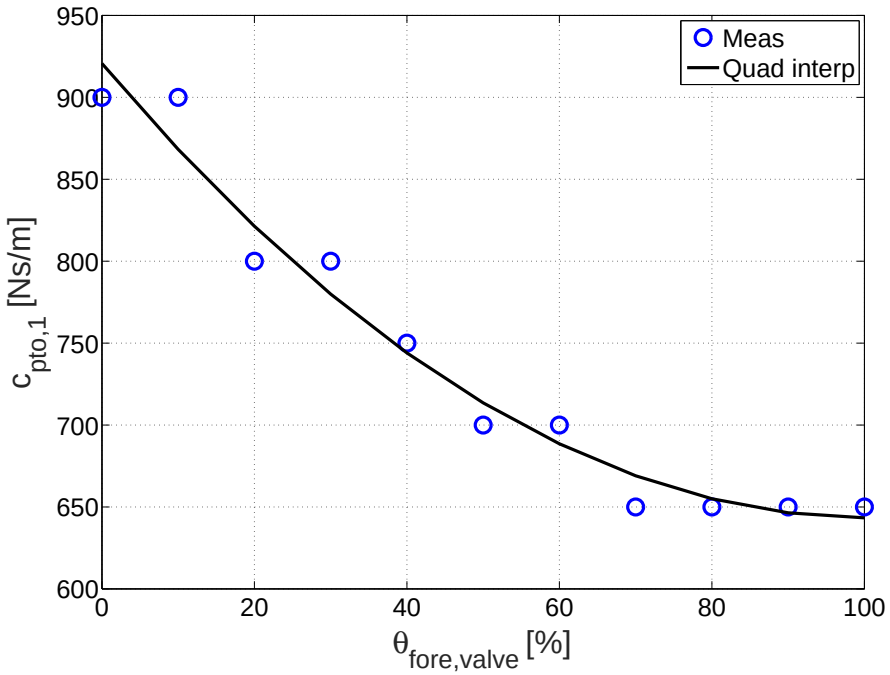

Figure 7.28: Damping of the fore hydraulic cylinder for an opening of the flow control valve that varies from 0% to 100%.

- The wave heights of regular waves of small period, generated by the wave maker, is not constant.
- There is a slow dynamic response of the stepper motors for the control of the flow control valves of the hydraulic dampers.

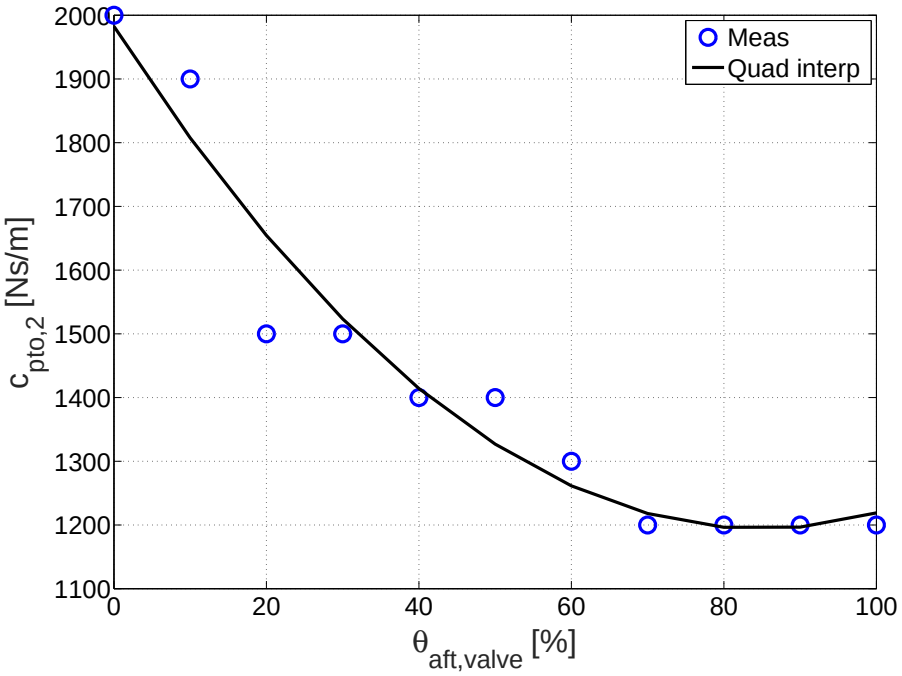

Figure 7.29: Damping of the aft hydraulic cylinder for an opening of the flow control valve that varies from 0% to 100%.

- Only a small variation of the damping force on the fore and aft dampers, for different values of the opening of the control valves, is achievable.
- The hydraulic dampers introduce nonlinearities to the dynamics of the device as the forces applied by the dampers are asymmetric due the flow of the hydraulic fluid which is different depending on the direction of the movement of the ram of the dampers.

The maximum sampling frequency achievable by the system set-up for wave-tank testing is only 5 Hz, due to the synchronization requirement of the streamed data from the Ardunio board, and the motion capture system, through the serial ports of the PC. In fact, the PC is equipped with only one serial bus controller and, therefore, at each time step, the PC retrieves the data from the motion capture system, and the data provided by the Arduino board are buffered. After the data from the motion capture system are retrieved, the buffer with the data from the Arduino board is emptied, in order to retrieve the data from the sensors at the same time step at which the data from the motion capture system were retrieved.

Although a sampling frequency of 5 Hz satisfies the Nyquist criterion, which requires a sampling frequency that is, at least, twice the maximum frequency presents in the signals, a faster sampling frequency is desirable, in order to more accurately represent the high-frequency components of the signals. A faster sampling frequency can be achieved by using only one interface for data streaming from all the sensors to the PC, or by using a PC with 2 different controllers for the serial bus, which can retrieve the data from the Arduino board and the motion capture system,

independently.

Regarding the wave maker, for regular wave small periods, the height of the wave is close to desired value, but is not constant. In contrast, for regular wave long periods, the height of the wave is 25% higher than the desired value, but is more constant than for small periods. For regular wave small periods, a non-constant wave height is problematic, as the response of the device is not regular, and validation of the dynamic model of the device, which takes as input a regular wave of constant wave height, against the tank tests, can be difficult. However, for regular wave long periods, the fact that the wave height is higher than the desired value, but is constant, is not an issue, as the dynamic model can take, as input, a regular wave with actual wave height of the regular waves generated in the wave-tank.

For implementation of energy-maximising control strategies, the most critical point of the system set-up for wave tank testing is the slow dynamic response of the stepper motors for the control of the opening of the flow control valves of the hydraulic dampers. In fact, with the stepper motors selected for this study, a maximum variation of the opening of the valve of only 10% is allowed in real-time. Obviously, a maximum variation of the opening of the valve of 10% greatly reduces the power absorption that can be achieved by real-time control, with respect to the control strategy based on optimal constant damping for the dampers, presented in Section 4.5.1.1. An obvious solution, to the slow dynamic response of the stepper motor, is to select different stepper motors which allow faster rotational speed. Alternatively, the dynamic response of the stepper motors chosen for the system set-up in this work can be faster, if the supplied voltage to the motor is increased.

The small variation of the damping force on the fore and aft dampers, for different value of the opening of the control valves, strongly affects the power absorption performance of both the real-time control of the damping, and the control strategy based on optimal constant damping for the dampers. A solution to the small variation of the damping of the dampers is to select different dampers which allows a greater range of damping than the damping range of the dampers used in this work.

Chapter 8

Motion capture system for wave-tank testing

In Chapter 7, the system set-up for wave-tank testing of a 1/20th scale three-body hinge barge WEC, is presented. Wave-tank tests are fundamental to asses the response of the WEC to the action of waves, and to experimentally evaluate the power absorption performance of the WEC. The system set-up for wave-testing of the WEC features a motion capture system, which is described in detail in this chapter. While the motion capture system measures the motion of the central barge of the WEC, the relative pitch motion of the fore and aft barge, with respect to the central barge, is measured by using rotational incremental encoders, as described in Chapter 7. The wave-tank tests carried out on the scale model device, are presented in Chapter 9.

8.1 Review on motion capture systems

Usually, the motion of a small scale wave energy converter in a tank-testing environment is tracked using an optical motion capture system which is composed of several cameras positioned around the device [116]. The optical motion capture system can measure the 6 degrees of freedom of a body in a 3D space, i.e. surge, sway, heave, roll, pitch and yaw. Reflective markers are mounted at different points on the body, and the cameras track their motion with high-precision and a high sampling rate. The use of reflective markers minimizes the amount of instrumentation needed on the device and, in general, does not affect the motion of the device. In [123], a tank test facility with an optical motion capture system with a position accuracy of 0.9 mm at 480 Hz sample rate is presented. In [124], tank tests are carried out with the Qualisys Motion Capture System [125], which is a popular system for motion capture in wave tanks.

The principal drawback of optical motion capture systems is their cost, which can be high and, therefore, the overall cost for wave tank testing is increased. Furthermore, for the test of a full scale device in sea trials, on-board sensors should be used instead of an optical motion capture system [126].

In this chapter, a low-cost motion capture system, based on a optimal combination of an Inertial

Navigation System (INS) with ultrasound sensors, is proposed. The INS is based on an Inertial Measurement Unit (IMU) which is mounted on the device and measures the accelerations and angular velocities of the device. Given the initial values on position, velocity and orientation of the body with respect to the fixed reference frame, the accelerations and angular velocities provided by the IMU can be integrated in order to determine position, velocity and orientation at any time instant [127]. However, due to low-frequency noise and bias in the IMU, the integration process can lead to drift in the position and orientation with an unbounded error that grows with time [128].

The ultrasonic measurement system is composed of a set of receivers placed around the device and a transmitter which is mounted on the same point of the device where the IMU is placed. The transmitter emits an ultrasonic signal which is then processed by the receivers. Given the sound speed and the travel time of the ultrasonic signal to reach the receivers, the distance of an object from each receiver can be obtained. The ultrasound sensors measure the absolute position of the device with respect to a fixed reference frame. For the study in this chapter, the ultrasound sensor provides measurements at lower sampling rates than the IMU. On the other hand, the position provided by the ultrasound sensor is characterized by long-term stability, as opposed to the position obtained through the integration of the IMU outputs.

Therefore, the INS and ultrasound sensor have complementary strengths, which make the integration of the two systems desirable [129]. In [130], a motion capture system based on an INS, aided by ultrasound sensors, for an augmented reality system is presented. For maritime and aviation applications, the INS is usually aided by radio sensors, the Global Position System (GPS) or ground-based radar [131].

The data provided by the INS and ultrasound sensors can be optimally combined in order to obtain a motion capture system with a higher update rate for the position than the stand-alone ultrasound receivers, and with bounded errors for the orientation of the body. Several integration approaches have been developed for aiding the INS by an external global measurement system: uncoupled, loosely coupled, tightly coupled and ultra-tightly coupled systems [131]. In this chapter, a loosely coupled ultrasound sensor aided INS with an Extended Kalman Filter (EKF) is proposed [132]. In a loosely coupled method, the difference between the estimated position given by the INS and ultrasound sensors is used to drive an EKF, whose model represents the propagation of the errors of the INS with time. Then, the estimated errors, computed by the EKF, are used to correct the position, velocity and orientation provided by the INS.

The remainder of the chapter is organized as follows: in Section 8.2, the ultrasound sensors and IMU are presented while, in Section 8.3, the operational space for the motion of different types of 1/20th scale WEC models is calculated. In Section 8.4, a sensor fusion algorithm, based on the EKF, is designed in order to optimally combine the data provided by the INS and ultrasound sensors while, in Section 8.5, a protocol and results on the validation of the fusion algorithm is presented. Finally, overall conclusions are drawn in Section 8.6.

8.2 Proposed sensor suite

The motion capture system of the WEC, which is the focus of this chapter, is composed of an IMU and an ultrasound measurement system from Hexamite [133]. In the remainder of this section, the two type of sensors are explained in more detail.

8.2.1 Ultrasound sensors

The sampling frequency of the ultrasound system is 15 Hz. The ultrasound system is composed of 4 ultrasound receivers positioned around the device and one ultrasound transmitter which is attached to the top of the WEC, as shown in Figure 8.1. As shown in Figure 8.1, the receivers are positioned on a plane 2.5 m wide and 2 m long at 2.0 m above the equilibrium free surface elevation. The ultrasound measures the absolute position of the WEC with respect to a fixed reference frame X_g, Y_g, Z_g located at the position of one of the receivers. Given the speed of sound, the distance of the WEC from each receiver is obtained by measuring the travel time needed by the ultrasonic signal emitted by the transmitter to reach each receiver. As shown in Figure 8.2, the global coordinates x_T^g, y_T^g, z_T^g of the WEC can be computed, through trilateration, as follows:

$$x_T^g = \frac{r_1^2 - r_2^2 + d^2}{2d} \tag{8.1}$$

$$y_T^g = \frac{r_1^2 - r_3^2 + B^2 + C^2}{2C} - \frac{B}{C} x^g \tag{8.2}$$

$$z_T^g = \pm\sqrt{r_1^2 - (x^g)^2 - (y^g)^2} \tag{8.3}$$

where r_1, r_2 and r_3 are the distances of the WEC from receivers $R1$, $R2$ and $R3$, respectively. The parameter d is the distance of receiver $R2$ from receiver $R1$ along the X_g axis, while the parameters B and C are the coordinates of receiver $R3$ along the X_g and Y_g axis, respectively. For redundancy, four receivers are used so that if one fails, the position of the transmitter can still be recovered from the remaining three receivers.

8.2.2 Inertial measurement unit

The IMU is composed of 3 accelerometers and 3 gyroscopes. As shown in Figure 8.1, the IMU is placed at the same point as the ultrasound transmitter. The accelerometer measures the acceleration along the 3 axis of translation X_b, Y_b and Z_b, while the gyroscope measures the angular velocities around the same axes. The sampling frequency of the IMU is 30 Hz.

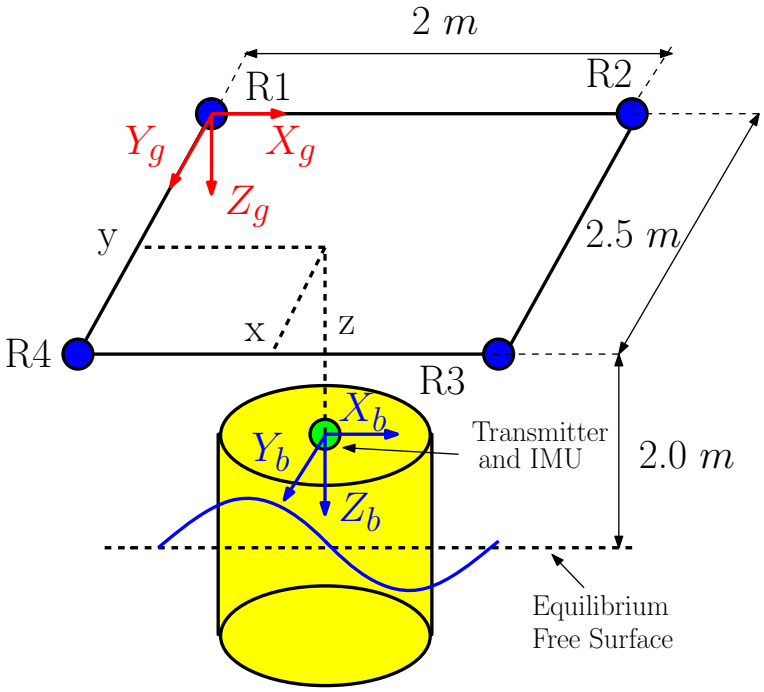

Figure 8.1: Set-up ultrasound measurement system and IMU for measurement of the WEC motion

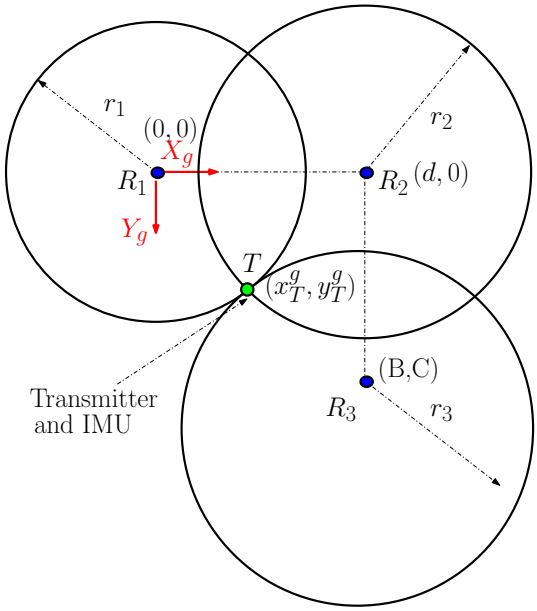

Figure 8.2: Intersection of the spheres centered at the location of the receivers $R1, R2, R3$ at the plane $Z_g = 0$

8.3 Calculation of operational space for motion

In this section, the operational space for the motion of a 1/20th scale model device for 4 different WEC types, as shown in Figure 8.3, is considered. The devices selected are: a self-reacting point absorber, a sphere, a flap and a hinge-barge. As shown in Figure 8.3, each device is connected to a

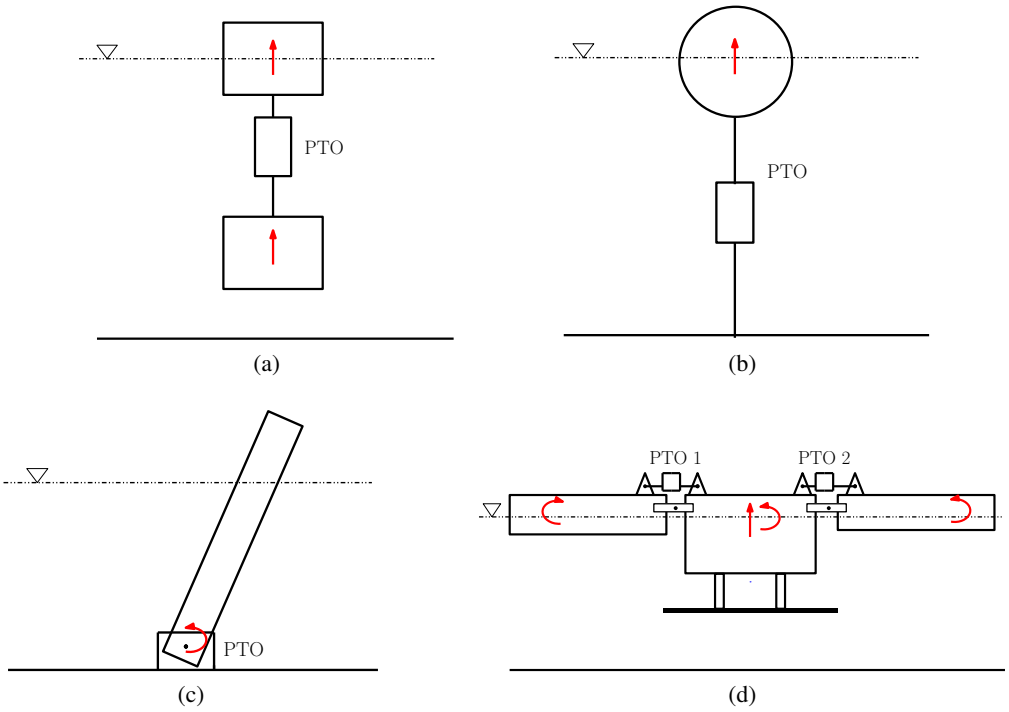

Figure 8.3: Different type of WECs: self-reacting point aborber (a), sphere (b), flap (c) and hinge-barge (d)

Power Take Off (PTO) system, which extracts the mechanical energy of the device. The analysis of the motion is restricted to the plane longitudinal to the wave directions, since the wavemaker can only generate planar waves. Therefore, the motions of interest for this study are surge, heave and pitch. In the available literature, several studies address the motion of full scale devices. In order to scale the results from full scale to 1/20th, the Froude similarity is applied, since the gravitational and inertial forces are considered to be the predominant forces [134]. Given a geometric scale ratio between the 1/20th scale and the full scale model of $\lambda = 20$, the resonant period of the 1/20th scale model device is given as follows:

$$T_{n,scale} = \frac{T_{n,dev}}{\sqrt{\lambda}} \tag{8.4}$$

where $T_{n,dev}$ is the resonant period of the full scale device. In Table 8.1, the operational space for the motion is shown for the maximum values of position, velocity, acceleration, angular position and angular velocity of each type of device, with and without control. The control maximizes the energy extracted by the PTO by increasing the motion of the device. Different control strategies for WECs have been developed and, for this chapter, the controllers considered are: complex-conjugate control, latching and Pseudo-Spectral (PS) control [9]. The last column in Table 8.1 shows the maximum value of each motion quantity among all the devices. In the remainder of this section, the operational space of each device is investigated in detail.

8.3.1 Self-reacting point absorber

For the self-reacting point absorber, a floating two-body heaving converter, inspired by the Wavebob WEC, is considered. The device mainly operates in heave, and it is composed of a spar and a torus sliding relative to each other [5]. The IMU and the ultrasound transmitter are placed on the spar, while the relative heave motion of the torus is measured by a linear potentiometer. Regarding the heaving motion of the spar, the modelling and control of the full scale device is carried out in both the time and frequency domain in [135]. In particular, for control, the PTO parameters are optimized at each frequency of the incoming regular wave in order to maximize power absorption. With non-optimized PTO parameters, the Response Amplitude Operator (RAO) for the heave motion of the spar shows a maximum value of $RAO_{max,h} = 2.5\ m/m$ at the natural resonant period of the device $T_{n,dev} = 10$ seconds. The resonant period $T_{n,scale}$ of the 1/20th scale model device is given from equation (8.4), and is 2.23 s. Given the operational range of the tank in Figure 7.5, for a regular wave with a period of 2.23 s, the maximum wave height is $H_{max} = 0.08\ m$ and, therefore, the maximum heave displacement for the 1/20th scale model device is given as follows:

$$p_{max,h} = RAO_{max,h} \cdot H_{max}/2 = 0.1\ m \tag{8.5}$$

At the resonant frequency $\omega_{n,scale} = 2\pi/T_{n,scale} = 2.8\ rad/s$, the maximum heave velocity and acceleration are computed as follows:

$$v_{max,h} = \omega_{n,scale} \cdot p_{max} = 0.28\ m/s \tag{8.6}$$

$$a_{max,h} = \omega^2_{n,scale} \cdot p_{max} = 0.78\ m/s^2 \tag{8.7}$$

With optimized PTO parameters, a complex-conjugate control system is considered, and the RAO for the heave motion of the spar shows a maximum value $RAO_{contr,h} = 10\ m/m$ around the natural resonant period of the full scale device. Therefore, the maximum heave displacement, velocity and acceleration are given as follows:

$$p_{contr,h} = RAO_{contr,h} \cdot H_{max}/2 = 0.4\ \ m \tag{8.8}$$

$$v_{contr,h} = \omega_{n,scale} \cdot p_{contr,h} = 1.12\ \ m/s \tag{8.9}$$

$$a_{contr,h} = \omega^2_{n,scale} \cdot p_{contr,h} = 3.13\ \ m/s^2 \tag{8.10}$$

Although a self-reacting point absorber is designed to mainly operate in heave, the device can also experience a parametric resonance which induces large amplitudes in the pitch and roll motion [136]. The parametric resonance in the pitch and roll motion of a self-reacting point absorber is important for the study in this chapter, since it provides an upper bound on the angular motion that WECs can experience. A numerical and experimental analysis of the 1/17th scale model of a self-reacting point absorber is carried out in [136], where it is shown that parametric resonance

occurs at $T_{res} = 3\ s$. At the period of the parametric resonance, the pitch motion is greater than the roll motion, showing a maximum value for the RAO of the pitch motion $RAO_{max,p}$ =221.7 $^\circ/m$. Given the operational space of the tank in Figure 7.5, for a regular wave with a period of 3 s, the maximum wave height is $H_{max} = 0.04\ m$ and, therefore, the maximum pitch rotation is given as follows:

$$p_{max,p} = RAO_{max,p} \cdot H_{max}/2 = 4.42\ ^\circ \tag{8.11}$$

At wave frequency $\omega_{res} = 2\pi/T_{res} = 2\ rad/sec$, the maximum pitch velocity is computed as follows:

$$v_{max,p} = \omega_{res} \cdot p_{max,p} = 8.8\ ^\circ/s \tag{8.12}$$

The study in [135] shows reduced pitch motion at parametric resonance than in [136], both for the uncontrolled and controlled device. Therefore, in order to evaluate the maximum range of motion of the device, only the study in [136] is considered for the evaluation of the pitch motion. However, in order to compute the maximum range of the pitch motion that can be achieved by the controlled device, a max value $p_{contr,p}$ =40° and $v_{contr,p}$ =80°/s are considered.

8.3.2 Sphere

The sphere is a device that operates in heave. The modelling and control of the device is considered in [137], where the diameter of device is 5 m, inspired by the WAVESTAR device [138]. A latching control strategy is applied in order to maximize power absorption. For the uncontrolled device, the RAO for heave motion shows a maximum value $RAO_{max,h} = 1.6\ m/m$ at the natural resonant period of the device $T_{n,dev} = 3\ s$. The resonant period $T_{n,scale}$ of the 1/20th scale model device is given from equation (8.4), and is 0.67 s. Given the operational range of the tank in Figure 7.5, for a regular wave with a period of 0.67 s, the maximum wave height is $H_{max} = 0.1\ m$ and, therefore, the maximum heave displacement for the 1/20th scale model device is given as follows:

$$p_{max,h} = RAO_{max,h} \cdot H_{max}/2 = 0.08\ m \tag{8.13}$$

At the resonant frequency $\omega_{n,scale} = 2\pi/T_{n,scale} = 9.37\ rad/s$, the maximum heave velocity and acceleration are computed as follows:

$$v_{max,h} = \omega_{n,scale} \cdot p_{max} = 0.74\ m/s \tag{8.14}$$

$$a_{max,h} = \omega^2_{n,scale} \cdot p_{max} = 7.02\ m/s^2 \tag{8.15}$$

The RAO for the heave motion with a latching control strategy shows a maximum value $RAO_{contr,h} = 2\ m/m$ at a period $T_{dev} = 6\ sec$. The corresponding period T_{scale} for the scale model device is obtained from equation (8.4), and it is equal to 1.35 secs. Given the operational range of

the tank in Figure 7.5, for a regular wave with period around 1.35 secs, the maximum wave height is $H_{max} = 0.16\ m$ and, therefore, the maximum heave displacement, velocity and acceleration for the 1/20th scale model device are given as follows:

$$p_{contr,h} = RAO_{contr,h} \cdot H_{max}/2 = 0.16\ \ m \tag{8.16}$$

$$v_{contr,h} = \omega_{scale} \cdot p_{contr,h} = 0.74\ \ m/s \tag{8.17}$$

$$a_{contr,h} = \omega_{scale}^2 \cdot p_{contr,h} = 3.45\ \ m/s^2 \tag{8.18}$$

where $\omega_{scale} = 2\pi/T_{scale} = 4.65\ rad/s$.

8.3.3 Flap

The flap is a device that pitches around a fixed axis close to the sea bottom with the top of the device piercing the water surface. The IMU cannot be placed at the bottom of the device and, therefore, the pitch motion is not directly measurable. Instead, the IMU and the ultrasound transmitter are placed at the top of the device, and the pitch motion can be measured from the measurements of the surge motion. The modelling and control of the full scale device is considered in [135]. In particular, for control, the influence of the PTO parameters on the RAO for the pitch motion and power output is investigated. For the uncontrolled device, the RAO for the pitch motion shows a maximum value of $RAO_{max,p} = 119.74\ ^\circ/m$ at the natural resonant period of the device $T_{n,dev} = 20\ s$. The resonant period $T_{n,scale}$ for the scale model device is obtained from equation (8.4), and is 4.47 s. Given the operational range of the tank, as shown in Figure 7.5, regular waves of period 4.47 s cannot be generated by the wave maker and, therefore, a lower period $T_{scale} = 3$ s is considered instead. A corresponding period for the full scale device $T_{dev} = 13\ s$ is obtained by using equation (8.4). The RAO for the pitch motion at a period $T_{n,dev} = 13\ s$ shows a value of $RAO_p = 49.84\ ^\circ/m$. Given the operational range of the tank in Figure 7.5, the maximum wave height is $H_{max} = 0.04\ m$ and, therefore, the maximum pitch displacement for the 1/20th scale model device is given as follows:

$$p_{max,p} = RAO_p \cdot H_{max}/2 = 1.03\ ^\circ \tag{8.19}$$

Given the height of the scale model device $h_{scale} = 1\ m$, a surge motion of amplitude $p_{max,s} = 0.018\ m$ is expected. At the resonant frequency $\omega_{scale} = 2\pi/T_{scale} = 2\ rad/s$, the maximum surge velocity and acceleration are computed as follows:

$$v_{max,s} = \omega_{scale} \cdot p_{max,s} = 0.036\ m/s \tag{8.20}$$

$$a_{max,s} = \omega_{scale}^2 \cdot p_{max,s} = 0.07\ m/s^2 \tag{8.21}$$

For the controlled device, at periods lower than the resonant period, increasing the PTO pa-

rameters yields an increase in power, with no significant changes for the RAO of the pitch motion.

8.3.4 Hinge-barge

The hinge-barge device is composed of several bodies interconnected together by hinges. The modelling and control of the 1/20th scale model device of a three-body hinge-barge is considered in [139]. The central body can move in heave and in pitch, while the end bodies pitch relative to the central body. The IMU and the ultrasound transmitter measure the motion of the central body, while the relative angular displacements of the end barges are measured by angular potentiometers. For the uncontrolled device, at the resonant period of the device of $T_{n,scale} = 1.5\ s$, the maximum heave and pitch displacements are $p_{max,h} = 0.025\ m$ and $p_{max,p} = 4.5\ ^\circ$, respectively. At the resonant frequency $\omega_{n,scale} = 2\pi/T_{n,scale} = 4.18\ rad/s$, the maximum heave velocity and acceleration are computed as follows:

$$v_{max,h} = \omega_{n,scale} \cdot p_{max,h} = 0.1\ \ m/s \tag{8.22}$$

$$a_{max,h} = \omega^2_{n,scale} \cdot p_{max,h} = 0.43\ \ m/s^2 \tag{8.23}$$

while the pitch velocity is given as follows:

$$v_{max,p} = \omega_{n,scale} \cdot p_{max,p} = 18.81\ \ ^\circ/s \tag{8.24}$$

For the case of the controlled device, PS control is applied in order to maximize the power production. The maximum heave displacement $p_{contr,h} = 0.04\ m$ is shown at the period $T_{scale} = 1.25\ s$. At the frequency $\omega_{scale} = 2\pi/T_{scale} = 5\ rad/s$, the maximum heave velocity and acceleration are computed as follows:

$$v_{contr,h} = \omega_{n,scale} \cdot p_{contr,h} = 0.2\ \ m/s \tag{8.25}$$

$$a_{contr,h} = \omega^2_{n,scale} \cdot p_{contr,h} = 1\ \ m/s^2 \tag{8.26}$$

The maximum pitch displacement $p_{contr,p} = 10.13\ ^\circ$ is developed at a period $T_{scale} = 1.75\ s$. At the frequency $\omega_{scale} = 2\pi/T_{scale} = 3.6\ rad/s$, the maximum pitch velocity is given as follows:

$$v_{contr,p} = \omega_{scale} \cdot p_{contr,p} = 36.66\ \ ^\circ/s \tag{8.27}$$

8.4 Sensor processing and optimal combination

In this section, the measurements from the ultrasound sensors are combined optimally with the measurements from the IMU through an EKF in order to obtain an accurate estimation of the

	Self-reacting point absorber	Sphere	Flap	Hinge-barge	Max Value
Max Position $[m]$	**0.4** [0.1]	**0.16** [0.08]	**0.018** [0.018]	**0.04** [0.025]	**0.4**
Max Velocity $[m/s]$	**1.12** [0.28]	**0.74** [0.74]	**0.036** [0.036]	**0.2** [0.1]	**1.12**
Max Acceleration $[m/s^2]$	**3.13** [0.78]	**3.45** [7.02]	**0.07** [0.07]	**1** [0.43]	7.02
Max Angle $[^\circ]$	**40** [4.0]	-	-	**10** [4.5]	40
Max Angular velocity $[^\circ/s]$	**80** [8.6]	-	-	**36** [18.81]	80

Table 8.1: Operational space for motion of different 1/20th scale model of wave energy converters with control applied (boldface values) and no control (values in brackets)

position, velocity and orientation of a WEC. For the position, the EKF estimates are updated using the measurements provided by the ultrasound sensors. Furthermore, since the accelerometer provides a measure of the gravity force vector, the static orientation of the IMU can be detected [140], while the transient orientation of the IMU is provided by the gyroscope. Therefore, the EKF computes the correct position, velocity and orientation from the fusion of the static measurements provided by the ultrasound sensors with the dynamic measurements provided by the IMU.

The INS is described by the inertial navigation equations, which are a set of nonlinear differential equations describing the relationship between the position, velocity and orientation of the WEC, and the outputs from the IMU, which are the accelerations and the angular velocities. The EKF is based on the navigation error equations, which represent a linearized model of the inertial navigation equations. The navigation error equations describe how the errors on the position, velocity and orientation of the WEC relate to the errors on the measured accelerations and angular velocities.

In the reminder of this section, the continuous-time inertial navigation and navigation error equations are obtained. Then, both navigation and navigation error equations are discretized with a zero order hold for the inputs. The discrete-time error navigation equations are suitable for the implementation of the EKF with the sampled measurements from both the ultrasound sensors and the IMU. Finally, the EKF is introduced in order to integrate the measurements provided by the ultrasound system with the positions, velocities and orientation computed by the INS.

8.4.1 Continuous-time inertial navigation equations

The continuous-time inertial navigation equations are given as follows [129]:

$$\dot{\mathbf{p}}^g = \mathbf{v}^g \tag{8.28a}$$

$$\dot{\mathbf{v}}^g = \mathbf{R}_b^g(\boldsymbol{\Theta})\mathbf{s}^b + \mathbf{g}^g \tag{8.28b}$$

$$\dot{\mathbf{R}}_b^g = \mathbf{R}_b^g(\boldsymbol{\Theta})\boldsymbol{\Omega}_{gb}^b \tag{8.28c}$$

where $\mathbf{p}^g$ and $\mathbf{v}^g$ are the global position and velocity vector of the WEC, respectively. The vector $\mathbf{g}^g$ represents the gravitational force per unit mass, while $\mathbf{s}^b$ represents the inertial force per unit mass expressed in the body frame. The matrix $\boldsymbol{\Omega}_{gb}^b$ is the skew-symmetric matrix of the angular velocities vector $\boldsymbol{\omega}^b = [\omega_{gb_x}^b \ \omega_{gb_y}^b \ \omega_{gb_z}^b]^T$ expressed in the body coordinate frame, and it is given as follows:

$$\boldsymbol{\Omega}_{gb}^b = \begin{bmatrix} 0 & -\omega_{gb_z}^b & \omega_{gb_y}^b \\ \omega_{gb_z}^b & 0 & -\omega_{gb_x}^b \\ -\omega_{gb_y}^b & \omega_{gb_x}^b & 0 \end{bmatrix} \tag{8.29}$$

The matrix $\mathbf{R}_b^g(\boldsymbol{\Theta})$, used for the transformation of coordinates from the body coordinate frame to the global coordinate frame, is a function of the vector of Euler angles $\boldsymbol{\Theta} = [\phi \ \theta \ \psi]^T$. The state space form of equations (8.28a)-(8.28b) can be expressed as:

$$\dot{\mathbf{x}} = \mathbf{A}\mathbf{d} + \mathbf{B}\mathbf{n} \tag{8.30}$$

where:

$$\mathbf{x} = [\mathbf{p}^{g,T} \ \mathbf{v}^{g,T}]^T \tag{8.31a}$$

$$\mathbf{n} = \mathbf{R}_b^g(\boldsymbol{\Theta})\mathbf{s}^b + \mathbf{g}^g \tag{8.31b}$$

$$\mathbf{A} = \begin{bmatrix} \mathbf{0}_3 & \mathbf{I}_3 \\ \mathbf{0}_3 & \mathbf{0}_3 \end{bmatrix} \tag{8.31c}$$

$$\mathbf{B} = \begin{bmatrix} \mathbf{0}_3 \\ \mathbf{I}_3 \end{bmatrix} \tag{8.31d}$$

8.4.2 Continuous-time navigation error equations

The continuous-time navigation error equations are obtained through linearization of the navigation equations around the estimated positions, velocities and orientation computed by the INS. The

estimated position, velocity and orientation are given as [129]:

$$\dot{\hat{\mathbf{p}}}^g = \hat{\mathbf{v}}^g \tag{8.32a}$$

$$\dot{\hat{\mathbf{v}}}^g = \hat{\mathbf{R}}_b^g(\boldsymbol{\Theta})\mathbf{s}^b + \hat{\mathbf{g}}^g \tag{8.32b}$$

$$\dot{\hat{\mathbf{R}}}_b^g = \hat{\mathbf{R}}_b^g(\boldsymbol{\Theta})\boldsymbol{\Omega}_{gb}^b \tag{8.32c}$$

where the notation $(\hat{\cdot})$ and $(\tilde{\cdot})$ represent estimated and measured quantities, respectively. The estimated rotation matrix $\hat{\mathbf{R}}_b^g(\boldsymbol{\Theta})$ is given as follows:

$$\hat{\mathbf{R}}_b^g(\boldsymbol{\Theta}) = (\mathbf{I} - \boldsymbol{\Omega}_{\boldsymbol{\epsilon}})\mathbf{R}_b^g \tag{8.33}$$

where $\boldsymbol{\Omega}_{\boldsymbol{\epsilon}}$ is the skew-symmetric matrix of the elements of the orientation angles error vector $\boldsymbol{\epsilon} = [\varepsilon_1\ \varepsilon_2\ \varepsilon_3]^T$, and is given as follows:

$$\boldsymbol{\Omega}_{\boldsymbol{\epsilon}} = \begin{bmatrix} 0 & -\varepsilon_3 & \varepsilon_2 \\ \varepsilon_3 & 0 & -\varepsilon_1 \\ -\varepsilon_2 & \varepsilon_1 & 0 \end{bmatrix} \tag{8.34}$$

Defining the errors on the estimated position and velocity as:

$$\delta\mathbf{p}^g = \mathbf{p}^g - \hat{\mathbf{p}}^g \tag{8.35}$$

$$\delta\mathbf{v}^g = \mathbf{v}^g - \hat{\mathbf{v}}^g \tag{8.36}$$

while the errors on the measured accelerations and angular velocities are given as:

$$\delta\mathbf{s}^b = \mathbf{s}^b - \tilde{\mathbf{s}}^b \tag{8.37}$$

$$\delta\boldsymbol{\omega}_{gb}^b = \boldsymbol{\omega}_{gb}^b - \tilde{\boldsymbol{\omega}}_{gb}^b \tag{8.38}$$

For the position errors, by substitution of equation (8.35) into equation (8.32a), the following linearized equation is obtained:

$$\delta\dot{\mathbf{p}}^g = \delta\mathbf{v}^g \tag{8.39}$$

For the velocity errors, by substitution of equation (8.36) into equation (8.32b), the following equation is obtained:

$$\dot{\mathbf{v}}^g - \delta\dot{\mathbf{v}}^g = (\mathbf{I} - \boldsymbol{\Omega}_{\boldsymbol{\epsilon}})\mathbf{R}_b^g(\mathbf{s}^b - \delta\mathbf{s}^b) + \hat{\mathbf{g}}^g \tag{8.40}$$

Neglecting the terms of second order yields the linearized velocity error equation:

$$\begin{aligned}\delta\dot{\mathbf{v}}^g &= \boldsymbol{\Omega}_{\boldsymbol{\epsilon}}\mathbf{R}_b^g\mathbf{s}^b + \mathbf{R}_b^g\delta\mathbf{s}^b \\ &= -\mathbf{S}^g\boldsymbol{\epsilon} + \mathbf{R}_b^g\delta\mathbf{s}^b\end{aligned} \tag{8.41}$$

where $\mathbf{S}^g$ is the skew-symmetric matrix of the elements of the inertial force per unit mass vector $\mathbf{s}^g = [s_x^g \; s_y^g \; s_z^g]^T$, and is given as follows:

$$\mathbf{S}^g = \begin{bmatrix} 0 & -s_z^g & s_y^g \\ s_z^g & 0 & -s_x^g \\ -s_y^g & s_x^g & 0 \end{bmatrix} \tag{8.42}$$

For the orientation angle errors, by differentiation of the right-hand side of equation (8.33) and substitution into equation (8.32c), yields to the following equation:

$$-\dot{\boldsymbol{\Omega}}_{\boldsymbol{\epsilon}}\mathbf{R}_b^g + (\mathbf{I} - \boldsymbol{\Omega}_{\boldsymbol{\epsilon}})\dot{\mathbf{R}}_b^g = \hat{\mathbf{R}}_b^g(\boldsymbol{\Theta})\tilde{\boldsymbol{\Omega}}_{gb}^b \tag{8.43}$$

By substitution of equations (8.33) and (8.38) into the right-hand side of equation (8.43), the following equation is obtained:

$$\dot{\boldsymbol{\Omega}}_{\boldsymbol{\epsilon}} = \mathbf{R}_b^g\delta\boldsymbol{\Omega}_{gb}^b\mathbf{R}_g^b \tag{8.44}$$

Equation (8.44) can be rewritten as [141]:

$$\dot{\boldsymbol{\epsilon}} = \mathbf{R}_b^g\delta\boldsymbol{\omega}_{gb}^b \tag{8.45}$$

Hence, the continuous-time navigation error equations are given as follows:

$$\delta\dot{\mathbf{p}}^g = \delta\mathbf{v}^g \tag{8.46a}$$

$$\delta\dot{\mathbf{v}}^g = -\mathbf{S}^g\boldsymbol{\epsilon} + \mathbf{R}_b^g\delta\mathbf{s}^b \tag{8.46b}$$

$$\dot{\boldsymbol{\epsilon}} = \mathbf{R}_b^g\delta\boldsymbol{\omega}_{gb}^b \tag{8.46c}$$

The system of equations in (8.46) describes how the evolution over time of the errors on the positions, velocities and orientations is related to the errors on the measured accelerations and angular velocities. If the errors on the accelerations and angular velocities are modeled as biases, the state space form of the system of equations in (8.46) is as follows:

$$\delta\dot{\mathbf{x}} = \mathbf{F}\delta\mathbf{x} + \mathbf{G}\mathbf{u} \tag{8.47}$$

where:

$$\delta\mathbf{x} = [\delta\mathbf{p}^{g,T}\ \delta\mathbf{v}^{g,T}\ \boldsymbol{\epsilon}^T\ \delta\mathbf{s}^{b,T}\ \ \delta\boldsymbol{\omega}_{gb}^{b,T}]^T \tag{8.48a}$$

$$\mathbf{u} = [\mathbf{w}_{acc}^T\ \mathbf{w}_{gyro}^T]^T \tag{8.48b}$$

$$\mathbf{F} = \begin{bmatrix} \mathbf{0}_3 & \mathbf{I}_3 & \mathbf{0}_3 & \mathbf{0}_3 & \mathbf{0}_3 \\ \mathbf{0}_3 & \mathbf{0}_3 & -\mathbf{S}^g & \mathbf{R}_b^g & \mathbf{0}_3 \\ \mathbf{0}_3 & \mathbf{0}_3 & \mathbf{0}_3 & \mathbf{0}_3 & \mathbf{R}_b^g \\ \mathbf{0}_3 & \mathbf{0}_3 & \mathbf{0}_3 & \mathbf{0}_3 & \mathbf{0}_3 \\ \mathbf{0}_3 & \mathbf{0}_3 & \mathbf{0}_3 & \mathbf{0}_3 & \mathbf{0}_3 \end{bmatrix} \tag{8.48c}$$

$$\mathbf{G} = \begin{bmatrix} \mathbf{0}_3 & \mathbf{0}_3 \\ \mathbf{R}_b^g & \mathbf{0}_3 \\ \mathbf{0}_3 & \mathbf{R}_b^g \\ \mathbf{0}_3 & \mathbf{0}_3 \\ \mathbf{0}_3 & \mathbf{0}_3 \end{bmatrix} \tag{8.48d}$$

(8.48e)

with $\mathbf{w}_{acc}$ and $\mathbf{w}_{gyro}$ denoting the accelerometer noise and gyroscope noise, respectively. The covariance matrix of the measurement noise $\mathbf{u}$ is:

$$\mathbf{Q} = \begin{bmatrix} \sigma_{acc}^2\mathbf{I}_3 & \mathbf{0}_3 \\ \mathbf{0}_3 & \sigma_{gyro}^2\mathbf{I}_3 \end{bmatrix} \tag{8.49}$$

8.4.3 Discrete time inertial navigation equations

The continuous-time inertial navigation equations in (8.30) are discretised to make them suitable for the implementation of the EKF with the sampled measurements from both the ultrasound sensors and IMU. Assuming that the input $\mathbf{n}$ in (8.30) is constant over a sampling period, the zero-order-hold sampling of the state space in (8.30) becomes [129]:

$$\mathbf{x}_{k+1} = \begin{bmatrix} \mathbf{0}_3 & T_s\mathbf{I}_3 \\ \mathbf{0}_3 & \mathbf{0}_3 \end{bmatrix} \mathbf{x}_k + T_s\mathbf{n}_k \tag{8.50}$$

where T_s is the sampling period. For the discretisation of the orientation equation in (8.28c), if the measured angular velocity $\boldsymbol{\Omega}_{gb}^b$ is constant over a sampling period, the discrete orientation equation is as follows:

$$\mathbf{R}_{b,k+1}^g = \mathbf{R}_{b,k}^g(2\mathbf{I}_3 + \boldsymbol{\Omega}_{gb,k}^b T_s)(2\mathbf{I}_3 - \boldsymbol{\Omega}_{gb,k}^b T_s)^{-1} \tag{8.51}$$

The vector of Euler angles $\boldsymbol{\Theta}_k$, used to represent the orientation of the body coordinate frame, can be computed from $\mathbf{R}_{b,k}$ [142].

8.4.4 Discrete time navigation error equations

The discrete-time inertial navigation error equations are derived from the continuous-time inertial navigation errors equations in (8.47). If the matrix $\mathbf{F}$ is constant over a sampling period, the discrete-time inertial navigation errors equations are given as follows [129]:

$$\delta\mathbf{x}_{k+1} = (\ \mathbf{I} + \mathbf{F}(kT_s)T_s)\ \delta\mathbf{x}_k + \mathbf{u}_k \tag{8.52}$$

where the covariance matrix of the discrete-time process noise $\mathbf{u}_k$ is given as [141]:

$$\mathbf{Q}_k = \mathbf{G}(kT_s)\mathbf{Q}\mathbf{G}(kT_s)^T T_s = \begin{bmatrix} \mathbf{0}_3 & \mathbf{0}_3 & \mathbf{0}_3 & \mathbf{0}_6 \\ \mathbf{0}_3 & \sigma^2_{acc}\mathbf{I}_3 & \mathbf{0}_3 & \mathbf{0}_6 \\ \mathbf{0}_3 & \mathbf{0}_3 & \sigma^2_{gyro}\mathbf{I}_3 & \mathbf{0}_6 \\ \mathbf{0}_6 & \mathbf{0}_6 & \mathbf{0}_6 & \mathbf{0}_6 \end{bmatrix} \tag{8.53}$$

8.4.5 Extended Kalman Filter

The EKF integrates the measurements provided by the ultrasounds system with the position, velocities and orientation computed by the INS. Equations (8.50) and (8.51) can be written as:

$$\mathbf{z}_{k+1} = \mathbf{c}(\mathbf{z}_k, \mathbf{a}_k) \tag{8.54}$$

where $\mathbf{z}_k = [\mathbf{x}_k\ \boldsymbol{\Theta}_k]^T$ and $\mathbf{a}_k = [\mathbf{s}^b_k\ \boldsymbol{\omega}^b_k]^T$. If the measurements from the ultrasound system are available, the estimates of the positions, velocities and orientation are given as [129]:

$$\hat{\mathbf{z}}_{k+1} = \hat{\mathbf{z}}^-_{k+1} + \delta\hat{\mathbf{z}}_{k+1} \tag{8.55a}$$
$$\hat{\mathbf{a}}_{k+1} = \tilde{\mathbf{a}}_{k+1} + \delta\hat{\mathbf{a}}_{k+1} \tag{8.55b}$$
$$\hat{\mathbf{z}}^-_{k+1} = \mathbf{c}(\hat{\mathbf{z}}_k, \hat{\mathbf{a}}_k) \tag{8.55c}$$
$$\delta\hat{\mathbf{z}}_{k+1} = [\delta\hat{\mathbf{x}}_{k+1}]_{1,..,9} \tag{8.55d}$$
$$\delta\hat{\mathbf{a}}_{k+1} = [\delta\hat{\mathbf{x}}_{k+1}]_{10,..,15} \tag{8.55e}$$
$$\delta\hat{\mathbf{x}}_{k+1} = \delta\hat{\mathbf{x}}^-_{k+1} + \mathbf{K}_{k+1}(\ \mathbf{y}_{k+1} - \mathbf{H}_k(\ \hat{\mathbf{z}}^-_{k+1} + \delta\hat{\mathbf{x}}^-_{k+1})\ ) \tag{8.55f}$$
$$\mathbf{K}_{k+1} = \mathbf{P}^-_{k+1}\mathbf{H}^T_k(\mathbf{H}_k\mathbf{P}^-_{k+1}\mathbf{H}^T_k + \mathbf{R}_k)^{-1} \tag{8.55g}$$
$$\mathbf{P}^-_{k+1} = (\ \mathbf{I} + \mathbf{F}(kT_s)T_s)\mathbf{P}_k(\ \mathbf{I} + \mathbf{F}(kT_s)T_s)^T + \mathbf{Q}_k \tag{8.55h}$$
$$\mathbf{P}_{k+1} = \mathbf{P}^-_{k+1} - \mathbf{K}_{k+1}\mathbf{H}_k\mathbf{P}^-_{k+1} \tag{8.55i}$$
$$\delta\hat{\mathbf{x}}^-_{k+1} = (\ \mathbf{I} + \mathbf{F}(kT_s)T_s)\delta\hat{\mathbf{x}}_k \tag{8.55j}$$

where $\mathbf{y}_{k+1}$ is the vector of the positions provided by the ultrasound system and static orientation measured by the accelerometer. The matrix $\mathbf{R}_k$ is the covariance matrix of the noise on position and static orientation. The matrix $\mathbf{H}_k \in \mathbb{R}^{6,15}$ is the measurement matrix, which is given

as follows:

$$\mathbf{H}_k = \begin{bmatrix} \mathbf{I}_{3,3} & \mathbf{0}_{3,3} & \mathbf{0}_{3,3} & \mathbf{0}_{3,6} \\ \mathbf{0}_{3,3} & \mathbf{0}_{3,3} & \mathbf{I}_{3,3} & \mathbf{0}_{3,6} \end{bmatrix} \tag{8.56}$$

If no ultrasound data are available, estimates of the positions, velocities and orientation are given as follows:

$$\hat{\mathbf{z}}_{k+1} = \hat{\mathbf{z}}^-_{k+1} + \delta\hat{\mathbf{z}}^-_{k+1} \tag{8.57a}$$
$$\hat{\mathbf{a}}_{k+1} = \tilde{\mathbf{a}}_{k+1} + \delta\hat{\mathbf{a}}^-_{k+1} \tag{8.57b}$$
$$\hat{\mathbf{z}}^-_{k+1} = \mathbf{c}(\hat{\mathbf{z}}_k, \hat{\mathbf{a}}_k) \tag{8.57c}$$
$$\delta\hat{\mathbf{z}}^-_{k+1} = [\delta\hat{\mathbf{x}}^-_{k+1}]_{1,..,9} \tag{8.57d}$$
$$\delta\hat{\mathbf{a}}^-_{k+1} = [\delta\hat{\mathbf{x}}^-_{k+1}]_{10,..,15} \tag{8.57e}$$
$$\mathbf{P}^-_{k+1} = (\,\mathbf{I} + \mathbf{F}(kT_s)T_s)\mathbf{P}_k(\,\mathbf{I} + \mathbf{F}(kT_s)T_s)^T + \mathbf{Q}_k \tag{8.57f}$$
$$\delta\hat{\mathbf{x}}^-_{k+1} = (\,\mathbf{I} + \mathbf{F}(kT_s)T_s)\delta\hat{\mathbf{x}}_k \tag{8.57g}$$

8.5 Validation sensor system with a 6-axis robotic manipulator

In order to validate the motion sensors proposed in Section 8.2 and the sensor fusion algorithm in Section 8.4, a series of experimental tests were carried out with a servo controlled six-axis robot arm at the Mobile and Marine Robotics Research Centre at the University of Limerick. The robot is a Stäubli TX Series 60 [143] which has a position repeatability at constant temperature of $\pm$ 0.02 *mm*, while the angular resolution for the wrist joint is 0.172 $^\circ$.

8.5.1 Validation protocol

In this section, a series of tests with the robot is proposed in order to cover the operational space in Table 8.1. The operational space described in Table 8.1 cannot be fully covered due to physical limitations of the robot. The setup of the sensors illustrated in Figure 8.1 was replicated by mounting the ultrasound receivers on a wall along a square of 2.3 m by 2.3 m, while the IMU, along with the ultrasound transmitter, was mounted on the end effector of the robot which is facing the ultrasound receivers. In Figure 8.4, the setup of the IMU and the global coordinate frame of the ultrasound sensors for the tests with the robot is shown. The motion of the robot arm is programmed with a high-level interface with no logging of the actual motion data performed by the robot. Therefore, the measurements performed with the motion capture system are compared to the set-points given to the robot through the high-level interface. In order to test the static performance of the motion capture system, the following *static tests* are proposed:

- Position measurements:

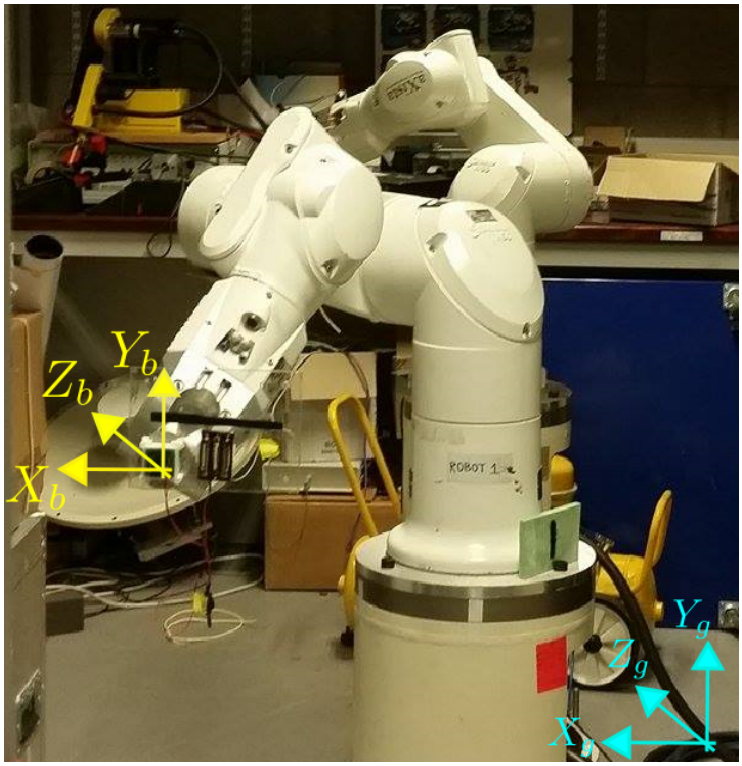

Figure 8.4: Set-up of the IMU and ultrasound coordinate frame X_g, Y_g, Z_g for the tests with the Stäubli robot

SPx Measurements of the positions given by the ultrasound sensors for a range of x from -0.4 m to 0.4 m, with an increment of 0.01 m between each measurement.

SPy Measurements of the positions given by the ultrasound sensors for a range of y from -0.4 m to 0.4 m, with an increment of 0.01 m between each measurement.

SPz Measurements of the positions given by the ultrasound sensors for a range of z from -0.4 m to 0.4 m, with an increment of 0.01 m between each measurement.

SP* Measurements of the positions given by the ultrasound sensors for the points of a cube of side 0.2 m, with a space of 0.1 m between each points.

- Rotation angle measurements

SRx Measurements of constant rotations around X_b within a range of values from -40° to 40°, with an increment of 2° between each measurement.

SRy Measurements of constant rotations around Y_b within a range of values from -40° to 40°, with an increment of 2° between each measurement.

SRz Measurements of constant rotations around Z_b within a range of values from -40° to 40°, with an increment of 2° between each measurement.

- Rotational velocity measurements

SWx Measurements of constant rotational velocities around X_b axis, within a range of values from -229°/s to 229°/s.

SWy Measurements of constant rotational velocities around Y_b axis, within a range of values from -229°/s to 229°/s.

SWz Measurements of constant rotational velocities around Z_b axis, within a range of values from -229°/s to 229°/s.

Given the operational space in Figure 8.3, and the operational range of the wave maker in Figure 7.5, the following *dynamic tests* are proposed:

- Position measurements

  DPx Measurements of sinusoidal positions for x with a peak to peak amplitude of 0.2 m and a range of periods from 1.25 s to 3 s.

  DPy Measurements of sinusoidal positions for y with a peak to peak amplitude of 0.2 m and a range of periods from 1.25 s to 3 s.

  DPz Measurements of sinusoidal positions for z with a peak to peak amplitude of 0.2 m and a range of periods from 1.25 s to 3 s.

- Rotation angle measurements

  DRx Measurements of sinusoidal rotations with amplitude of 20° around the axis X_b, with a range of periods from 1.25 s to 3 s

  DRy Measurements of sinusoidal rotations with amplitude of 20° around the axis Y_b, with a range of periods from 1.25 s to 3 s

  DRz Measurements of sinusoidal rotations with amplitude of 20° around the axis Z_b, with a range of periods from 1.25 s to 3 s

- Path trajectory

  DHelix Trajectory of the position along a helix of diameter 0.2 m and height 0.2 m

8.5.2 Validation results

8.5.2.1 Static tests

In this section, the results from the experimental tests with the robot are presented. In the upper part of Figure 8.5, the x-position from the ultrasound sensors X_{meas}, for the test SPx, are shown for different actual value of displacement X_{in}. In order to calibrate the ultrasound sensors along the x-axis, the measurements are interpolated with a polynomial. The degree of the polynomial is chosen as 5, as it provides a good trade-off between complexity and interpolation error. In the lower part of Figure 8.5, the absolute value of the error between X_{in} and the measurement X_{meas}

is compared to the absolute value of the error between X_{in} and the interpolant polynomial. As the lower part of Figure 8.5 shows, the interpolant polynomial provides a significantly lower position error than the measurements X_{meas}. The maximum error on x-position given by the interpolant polynomial is approximately 0.005 m.

In the upper part of Figure 8.6, the y-position from the ultrasound sensors Y_{meas}, for the test SPy, are shown together with a interpolant polynomial of degree 5 for different actual value of displacement Y_{in}. In the lower part of Figure 8.6, the absolute value of the error between Y_{in} and the measurement Y_{meas} is compared to the absolute value of the error between Y_{in} and the interpolant polynomial. The maximum error on y-position given by the interpolant polynomial is approximately 0.005 m.

In the upper part of Figure 8.7, the z-position from the ultrasound sensors Z_{meas}, for the test SPz, are shown together with a interpolant polynomial of degree 5 for different actual value of displacement Z_{in}. In the lower part of Figure 8.7, the absolute value of the error between Z_{in} and the measurement Z_{meas} is compared to the absolute value of the error between Z_{in} and the interpolant polynomial. The maximum error on z-position given by the interpolant polynomial is approximately 0.005 m.

In Figure 8.8, the positions from the ultrasound sensors are shown for points of a cube, for the test SP*. The x, y and z coordinates provided by the motion capture system are corrected by using the polynomials computed for the tests performed individually along the x, y and z axis. The average absolute errors between the actual points and the points computed by the polynomial for the x, y and z coordinates are 0.0054 m, 0.0047 m and 0.0033 m, respectively.

In conclusion, for static position measurements, the ultrasound sensors provide an accuracy of 0.005 m along the x,y and z direction, which is considerably worse that the accuracy of 0.001 m stated by the Hexamite company. It is important to highlight that, the EKF does not show any significant improvement of the position accuracy with respect to the ultrasound sensors, since the acceleration measurements provided by the IMU are affected by a considerable bias and, therefore, the position measurement computed by the inertial navigation equations quickly diverges over time.

In order to statically calibrate the accelerometer of the IMU along the x, y and z direction, the tests SRX and SRZ are used. In fact, as the IMU rotates around the x-axis and z-axis, the components of the gravity vector along the x-axis, y-axis and z-axis of the accelerometer change accordingly. Given a set of different rotations, a calibration procedure for the accelerometers based on the minimization of the squared errors between the applied gravity forces and a model for the accelerometer is proposed in [144]. The model takes into account the scaling factors and biases of the accelerometer sensitivity axis. Furthermore, given that the accelerometer axes are not perfectly orthogonal due to the imprecise manufacturing process, the model also considers the misalignment angles of the accelerometer sensitivity axes with respect to a set of orthogonal axes.

The cost function to be minimized is as follows:

$$\min_{\boldsymbol{\theta}} \quad \sum_{k=1}^{N} (\|\hat{\mathbf{u}}_k\|^2 - \|\mathbf{h}(\hat{\mathbf{y}}_k, \boldsymbol{\theta}\|^2)^2 \tag{8.58}$$

where N is the number of rotation performed, $\hat{\mathbf{u}}_k$ is the applied gravity force vector and $\hat{\mathbf{y}}_k$ is the output of the accelerometer. The vector of the model parameters $\boldsymbol{\theta}$ is as follows:

$$\boldsymbol{\theta} = \left[k_x \; k_y \; k_z \; \alpha_{yz} \; \alpha_{zy} \; \alpha_{zx} \; \beta_x \; \beta_y \; \beta_z\right]^T \tag{8.59}$$

where k_i,α_i, with $i = x, y, z$, are the unknown scaling and bias parameters of the accelerometer along the i direction. The misalignment angles $\alpha_{i,j}$, with $i = y, z$ and $j = x, y, z$, represents the rotation of the i-th accelerometer sensitivity axis around the j-th axis of the orthogonal frame. The model of the accelerometer $\mathbf{h}(\hat{\mathbf{y}}_k, \boldsymbol{\theta})$ is given as follows:

$$\hat{\mathbf{u}}_k = \mathbf{h}(\hat{\mathbf{y}}_k, \boldsymbol{\theta}) \tag{8.60}$$

where:

$$\mathbf{h}(\hat{\mathbf{y}}_k, \boldsymbol{\theta}) = \mathbf{T}\mathbf{K}^{-1}(\hat{\mathbf{y}}_k - \mathbf{b}) \tag{8.61}$$

and:

$$\mathbf{T} = \begin{bmatrix} 1 & -\alpha_{yz} & \alpha_{zy} \\ 0 & 1 & -\alpha_{zx} \\ 0 & 0 & 1 \end{bmatrix} \tag{8.62}$$

$$\mathbf{K} = diag(k_x, k_y, k_z) \tag{8.63}$$

$$\mathbf{b} = [\beta_x \; \beta_y \; \beta_z]^T \tag{8.64}$$

In Table 8.2, the scale factors and biases of the accelerometer sensitivity axes are shown while, in Table 8.3, the misalignment angles of the accelerometer sensitivity axes are shown. Regarding the calibration of the gyroscope, the same calibration procedure applied to the accelerometer can be used. The gyroscope sensitivity axes x, y and z are calibrated by using tests SWX, SWY and SWZ, respectively. The cost function to be minimized is shown in equation (8.58), where N is the number of the constant angular velocities performed. In Table 8.4, the scale factors and biases of the gyroscope sensitivity axis are shown while, in Table 8.5, the misalignment angles of the

Acc-axis	Scale factor	Bias
X	16.55	-4.28
Y	16.65	1.35
Z	16.47	-8.06

Table 8.2: Scale factor and bias for accelerometer sensitivity axis

Acc-angle	Value
α_{yz}	0.0039
α_{zy}	-0.024
α_{zx}	0.0128

Table 8.3: Misalignment angle of accelerometer sensitivity axis

Gyro-axis	Scale factor	Bias
X	0.1039	7.4×10^{-3}
Y	0.1068	2.74×10^{-4}
Z	0.1152	-3.94×10^{-4}

Table 8.4: Scale factors and biases for gyroscope sensitivity axis

Gyro-angle	Value
α_{yz}	-0.0344
α_{zy}	-0.0192
α_{zx}	-0.0204

Table 8.5: Misalignment angle of gyroscope sensitivity axis

gyroscope sensitivity axes are shown.

For the measurement of the static rotations of the IMU around the x-axis, y-axis and z-axis, two different approaches are considered: integration of the angular velocities provided by the gyroscope and measurement of the applied gravity vector given by the calibrated accelerometer. The integration of the angular velocity diverges over time, since the gyroscope is affected by drift. The calibrated accelerometer can be used to measure the rotation of the IMU around the x-axis and z-axis, as the components of the gravity vector along the x-axis, y-axis and z-axis change with the performed rotation angle. However, for measurement of the static rotations of the IMU around the y-axis, the accelerometer cannot be used, since the gravity vector acts along the y-axis and, therefore, no change in the components of the gravity vector is detected along the x-axis and z-axis of the accelerometers.

In the upper part of Figure 8.9, rotation measurements around the x-axis, from the accelerometer and gyroscope ϕ_{meas} for the test SRx, are shown for different actual rotations ϕ_{in}. In the lower part of Figure 8.9, the absolute value of the errors between ϕ_{in} and the measurements ϕ_{meas} from

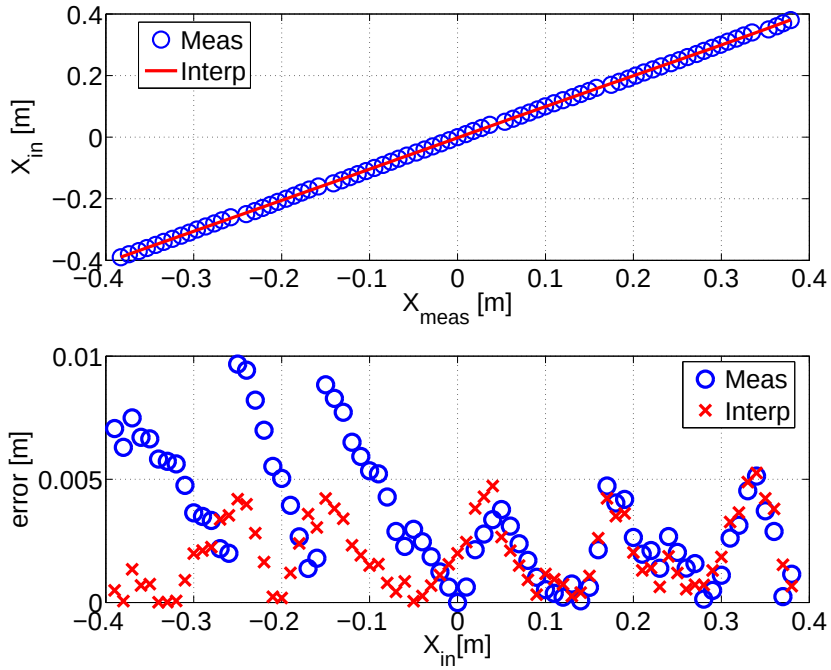

Figure 8.5: Measurement of the x positions of the ultrasound transmitter or the test SPx

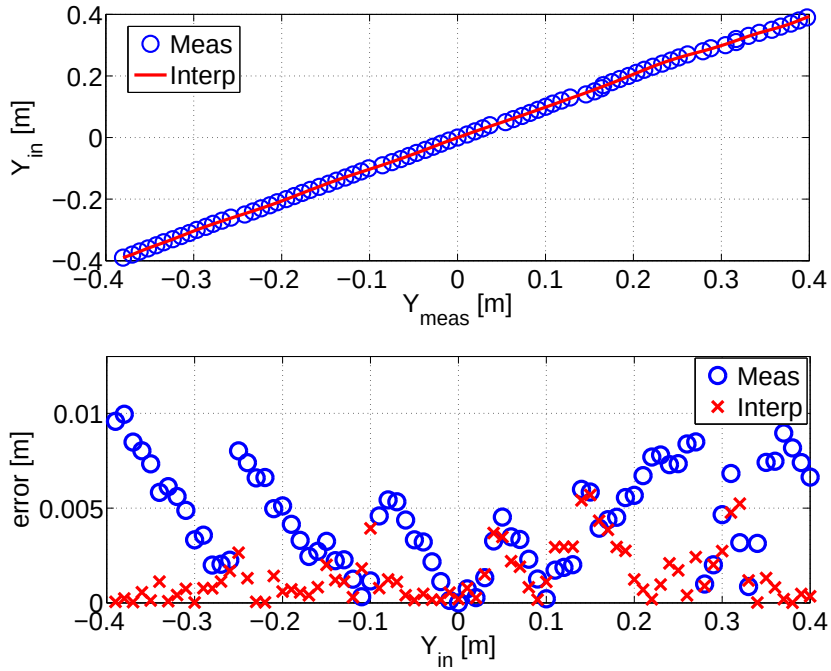

Figure 8.6: Measurement of the y positions of the ultrasound transmitter for the test SPy

the accelerometer and gyroscope are shown. The maximum error on the rotation around the x-axis is 2° and 0.9° for the gyroscope and accelerometer, respectively.

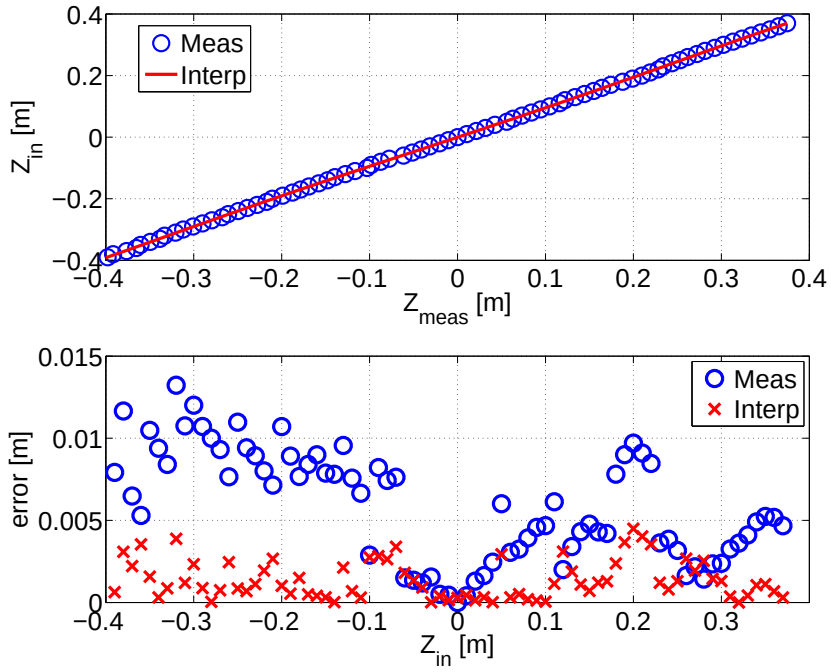

Figure 8.7: Measurement of the z positions of the ultrasound transmitter for the test SPz

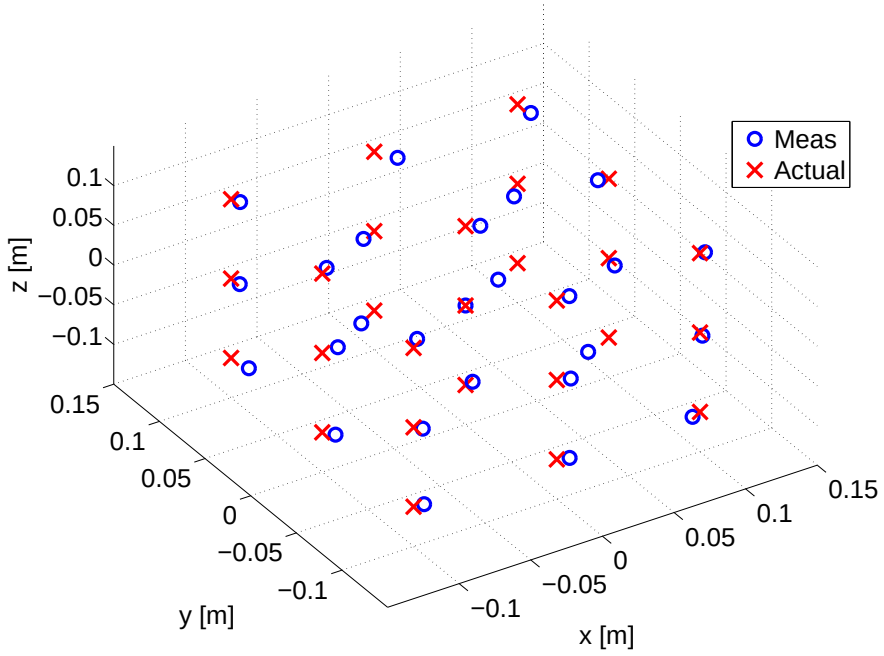

Figure 8.8: Measurement of the x, y and z positions of the ultrasound transmitter for the test SP*

In the upper part of Figure 8.10, rotation measurements around the y-axis, from the gyroscope θ_{meas} for the test SRy, are shown for different actual rotations θ_{in}. In the lower part of Figure 8.10,

the absolute errors between θ_{in} and the measurements θ_{meas} from the gyroscope are shown. The maximum error on the rotation around the y-axis is 4°. Despite the poor accuracy of the measurement of the rotation angle around the y-axis, for a wave tank that only generates plane waves, the rotation of the device around the axis where the gravity vector is acting upon is negligible.

In the upper part of Figure 8.11, the rotations around the z-axis from the accelerometer and gyroscope ψ_{meas}, for the test SRz, are shown for different actual rotations ψ_{in}. In the lower part of Figure 8.11, the absolute value of the errors between ψ_{in} and the measurements ψ_{meas} from the accelerometer and gyroscope are shown. The maximum error on the rotation around the z-axis is 4° and 1° for the gyroscope and accelerometer, respectively.

In conclusion, for static rotation around the x and z axes, the accelerometer provides a bounded error of 1°, while the gyroscope is affected by a considerable bias, which provides an error of 4°. It is important to highlight that, the EKF does not show any significant improvement of the rotation accuracy given by accelerometer, since the gyroscope is affected by a considerable bias and, therefore, the rotation measurement computed by the inertial navigation equations quickly diverges over time.

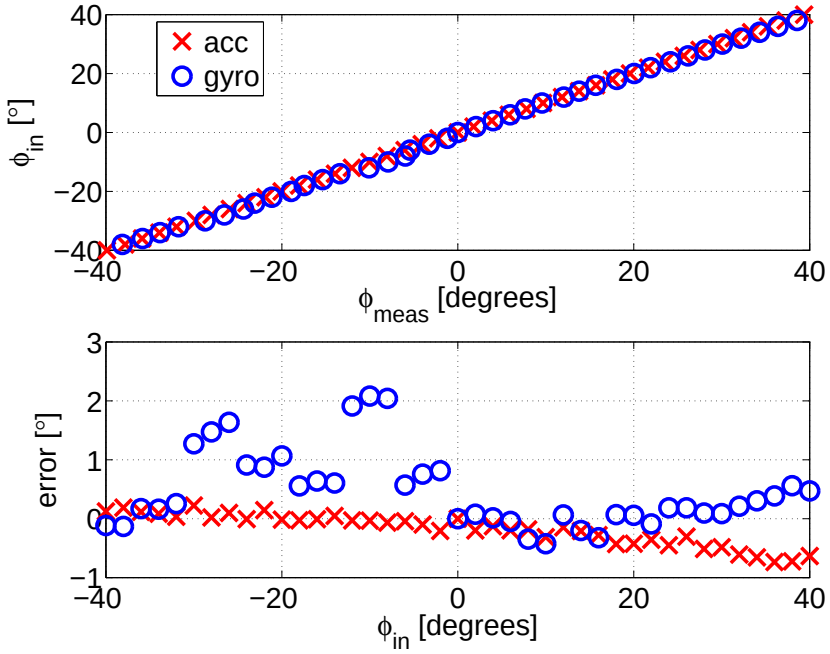

Figure 8.9: Measurement of the angle ϕ around the x-axis of the IMU for the test SRx

8.5.2.2 Dynamic tests

In the upper part of Figure 8.12, the peak-to-peak amplitudes of the x-position from the ultrasound sensors X_{amp}, for the test DPx are shown for different periods of sinusoidal trajectories with a

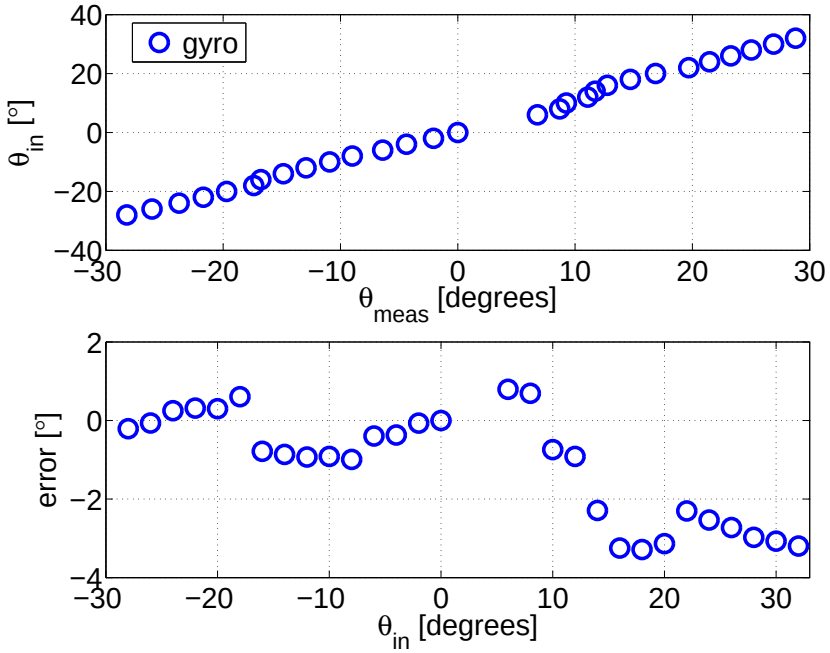

Figure 8.10: Measurement of the angle θ around the *y*-axis of the IMU for the test SRy

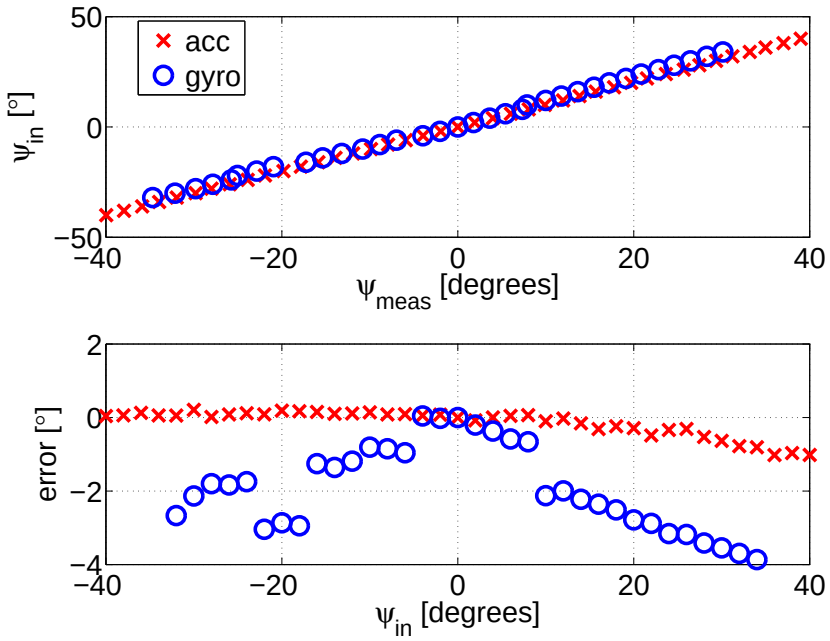

Figure 8.11: Measurement of the angle ψ around the *z*-axis of the IMU for the test SRz

reference peak-to-peak amplitude of 0.2 *m*. In the lower part of Figure 8.12, the absolute value of the errors between X_{amp} and the reference position is shown. Note that, for a period of 1 *s*, the position of the robot was not a perfect sinusoid, due to the high speed required to the robot. Altogether, the accuracy on the *x*-position is of 0.002 *m*.

In the upper part of Figure 8.13, the peak to peak amplitudes of y-position from the ultrasound sensors Y_{amp}, for the test DPy, are shown, for different periods of sinusoidal trajectories, with a reference peak-to-peak amplitude of 0.2 m. In the lower part of Figure 8.13, the absolute value of the errors between Y_{amp} and the reference position is shown. The maximum error on the y-position is of 0.005 m.

In the upper part of Figure 8.14, the peak to peak amplitudes of z-position from the ultrasound sensors Z_{amp}, for the test DPz, are shown for different periods of sinusoidal trajectories with a reference peak-to-peak amplitude of 0.2 m. In the lower part of Figure 8.14, the absolute value of the errors between Z_{amp} and the reference position is shown. The maximum error on the z-position is of 0.005 m.

In conclusion, for dynamic position measurements, the ultrasound sensors provide an accuracy of 0.005 m along the x,y and z direction which is the same as the accuracy provided by the static position tests. The EKF does not show any significant improvement of the position accuracy given by the ultrasound sensors.

In Figure 8.15, the comparison between the angle ϕ computed with the EKF, accelerometers and gyroscope is shown for a sinusoidal angular motion of amplitude A=20° and period T=3.0 s. In Figure 8.16, the comparison between the angle ψ computed with the EKF, accelerometers and gyroscope is shown for a sinusoidal angular motion of amplitude A=20° and period T=3.0 s. As Figure 8.15 and 8.16 show, for the measurement of the dynamic rotations of the IMU around the x-axis and z-axis, the EKF provides a more accurate estimation of the angles than the angles obtained from the accelerometer or from the integration of the gyroscope angular velocities.

In the upper part of Figure 8.17, the rotations around the x-axis from the EKF ϕ_{meas}, for the test DRx, are shown for for different periods of sinusoidal trajectories with a reference peak-to-peak amplitude of 40°. In the lower part of Figure 8.17, the absolute value of the errors between ϕ_{meas} and the reference angle is shown.

In the upper part of Figure 8.18, the rotations around the z-axis from the EKF ψ_{meas}, for the test DRz, are shown for for different periods of sinusoidal trajectories with a reference peak-to-peak amplitude of 40°. In the lower part of Figure 8.18, the absolute value of the errors between ψ_{meas} and the reference angle is shown.

In conclusion, for dynamic rotation measurements, the EKF provides a bounded error of 2°. The gyroscope is affected by a considerable bias and, therefore, the error grows with time. On the other hand, the rotation measurement provided by the accelerometer is not affected by bias but it is noisy.

In Figure 8.19, the trajectory of the position given by the ultrasound sensors along the helix defined for the test DHelix is shown. The error on the diameter is 0.004 m, while the error on the height is 0.002 m. The accuracy along the x, y and z axes are consistent with the accuracy obtained

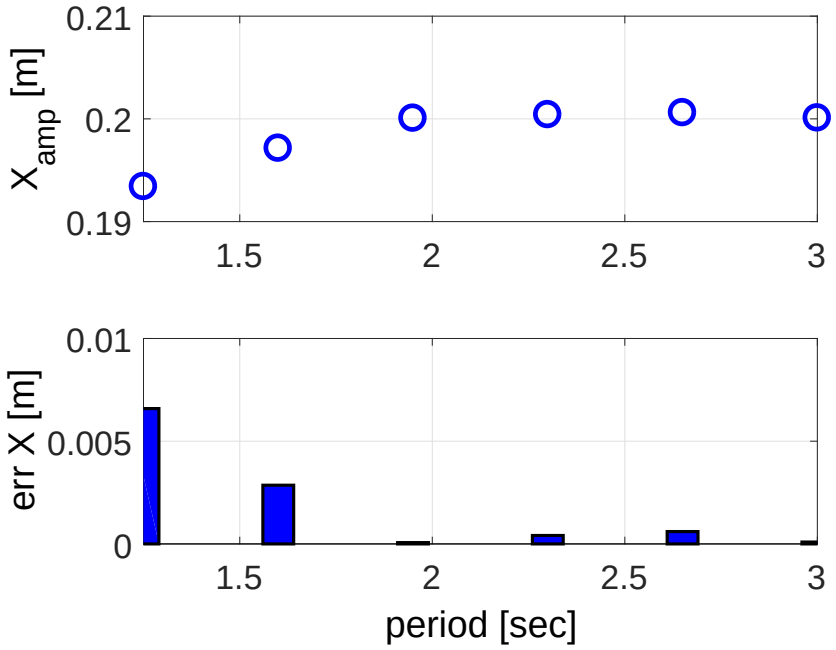

Figure 8.12: Measurement of the *x* positions of the ultrasound transmitter for the test DPx

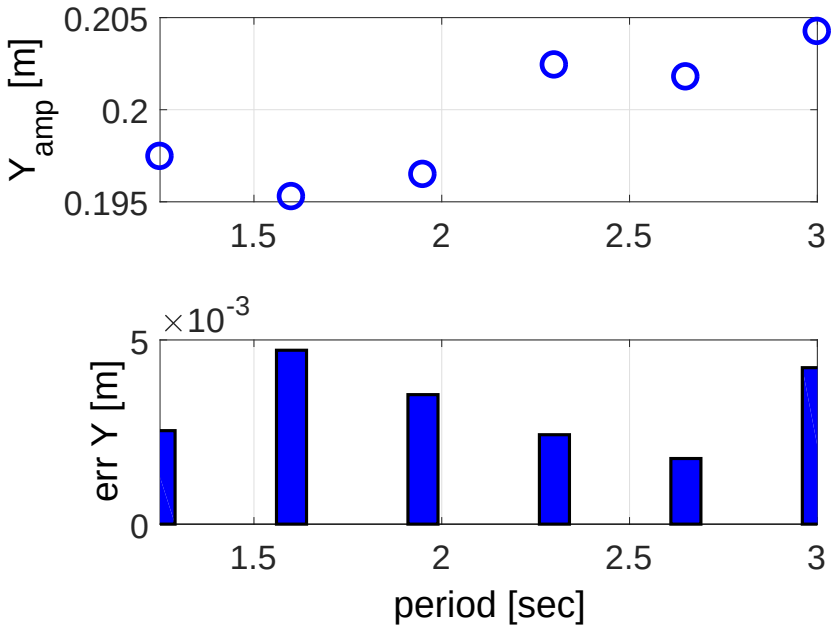

Figure 8.13: Measurement of the *y* positions of the ultrasound transmitter for the test DPy

for the static and dynamic position measurements.

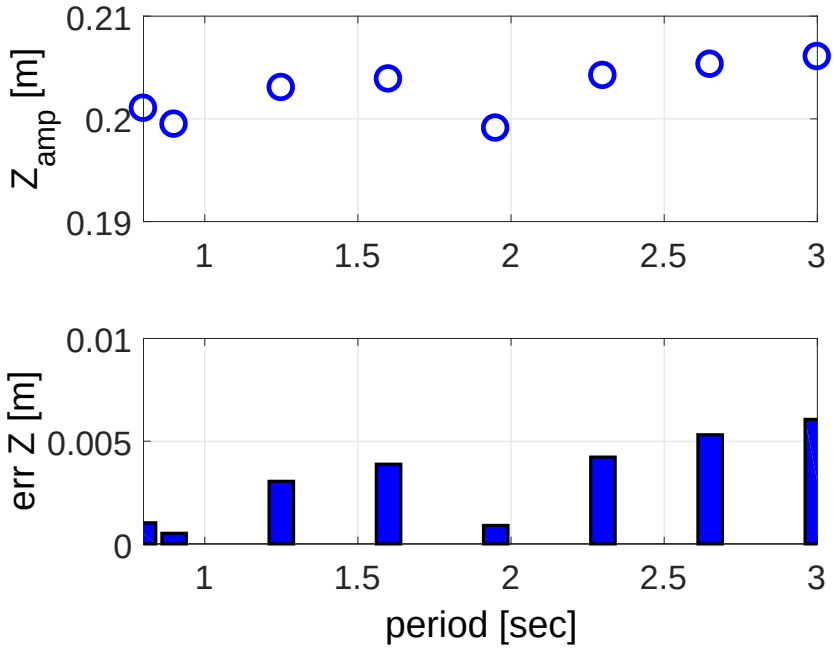

Figure 8.14: Measurement of the z positions of the ultrasound transmitter for the test DPz

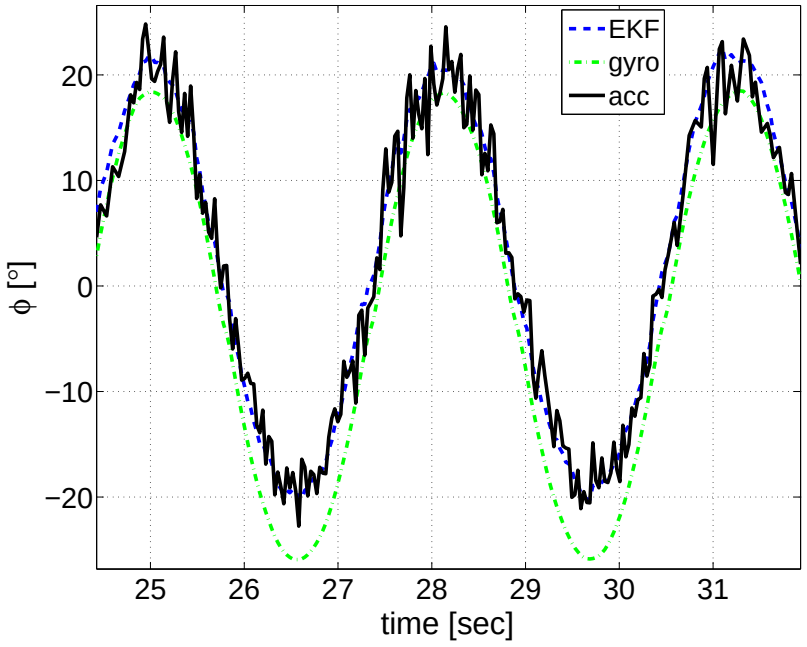

Figure 8.15: Comparison between the angle ϕ around the x-axis of the IMU between computed with the EKF, accelerometer and gyroscope for a period $T = 3.0$ and amplitude $A = 20°$

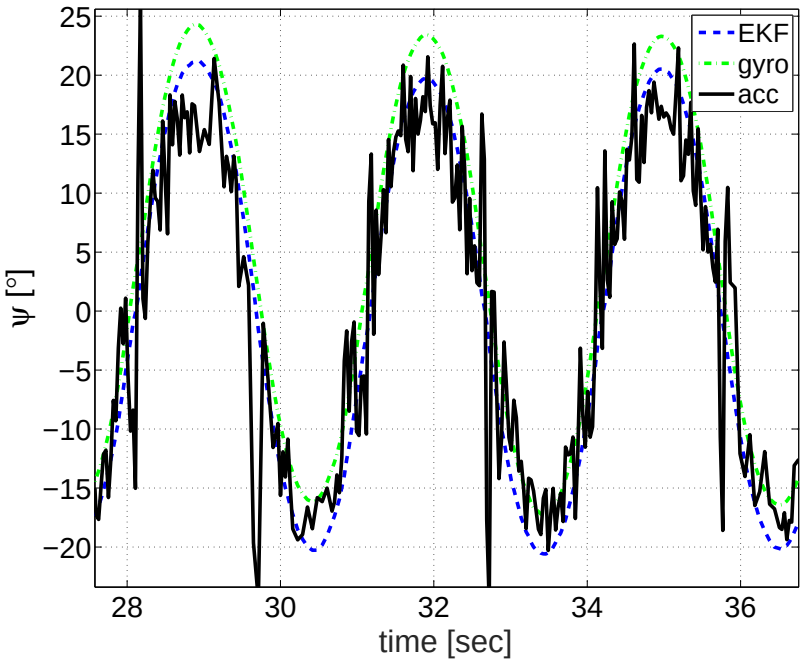

Figure 8.16: Comparison between the angle ψ around the z-axis of the IMU between computed with the EKF, accelerometer and gyroscope for a period $T = 3.0$ and amplitude $A = 20°$

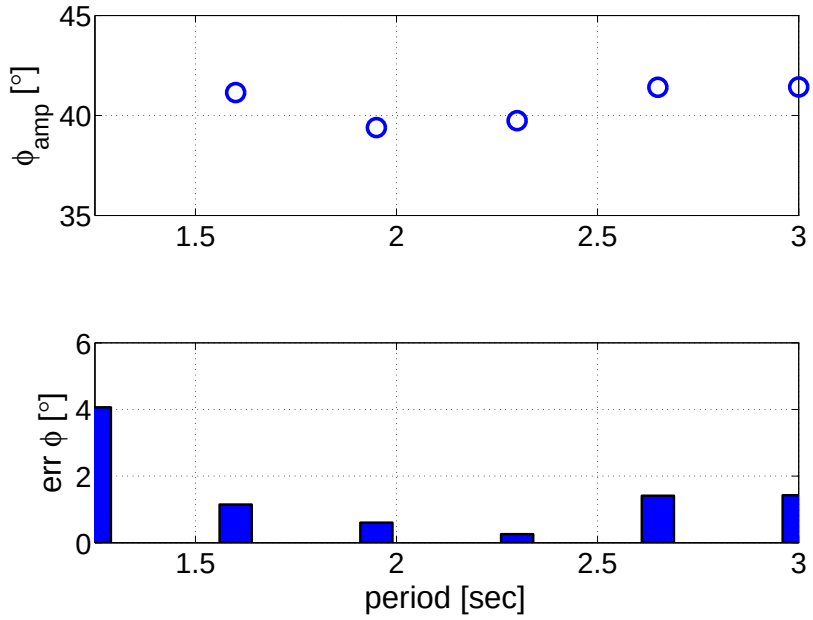

Figure 8.17: Measurement of the angle ϕ around the x-axis of the IMU for the test DRx

8.6 Conclusions

This chapter describes the development, and calibration of, a low-cost motion capture system for wave-tank tests. The motion capture system is based on two different sensors: ultrasound sensors,

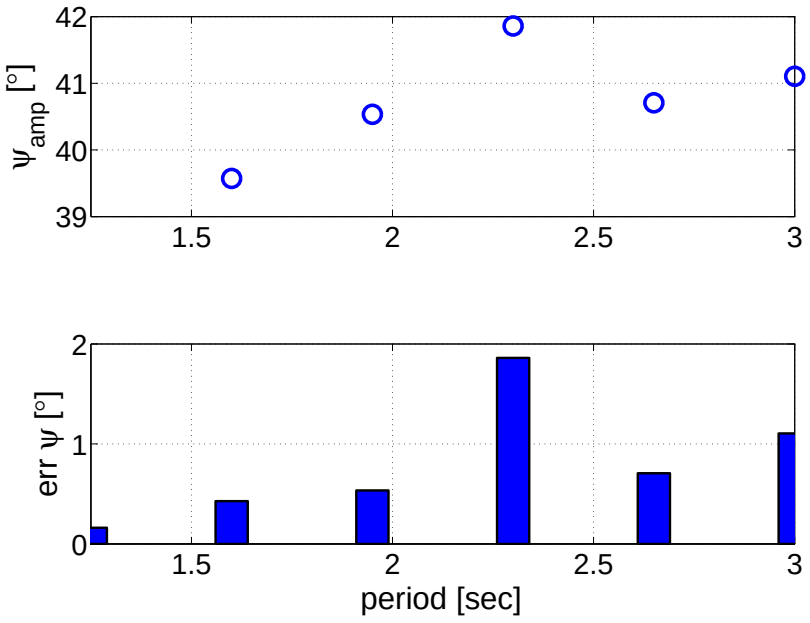

Figure 8.18: Measurement of the angle ψ around the z-axis of the IMU for the test DRz

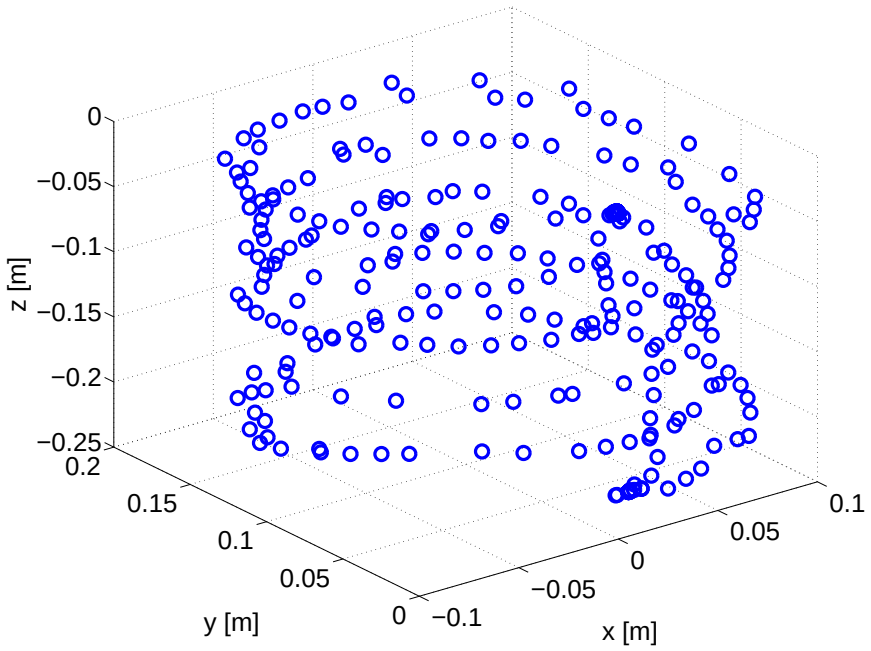

Figure 8.19: Trajectory of the position along a helix for the test DHelix

which provide position measurements with a low sampling rate but bounded errors, and an IMU, which provides accelerations and angular velocities with a high sampling rate, but characterized by biases which induces drifts in the integration process used to obtain positions and orientations.

Given the complementary strength of the two sensor modalities, a natural choice for the fusion of the information from the two sensors is represented by EKF which estimates positions, velocities and orientation more accurately than the two sensors alone.

The tests performed in this chapter show that the ultrasound sensors have a position accuracy of 5 mm along the x, y and z axes, depending on the range of the position. The position accuracy of the ultrasound sensors is considerably worse than the accuracy stated by the Hexamite company of 1 *mm*. The EFK does not show any significant improvement of the position accuracy with respect to the ultrasound sensors. An alternative to the ultrasound sensors is an optical capture system, which gives more precise measurements but at a more expensive cost. In fact, while the ultrasound measurement system used for the study in this chapter costs around € 1.5k, the cost for a optical capture system can range from € 4k to € 10k.

On the other hand, for rotation measurements, the overall accuracy provided by the EKF is good, with bounded errors of 1° around the x and z axis, depending on the range of the rotation. The rotation computed by the integration of the angular velocity provided by the gyroscope is characterized by an error that grows over time. The accelerometer provides an accurate and stable measure of the static rotation, but the dynamic accuracy is affected by the level of noise in the measurements. The EKF optimally combines the strengths of the gyroscope and accelerometer to compute an accurate and stable rotation both in the static and dynamic scenario.

In Chapter 9, the wave-tank tests of a 1/20th scale three-body hinge-barge device, with the motion of the central barge measured by the motion capture system developed and validated in this chapter, are presented, while, the relative pitch motion of the fore and aft barge, with respect to the central barge, is measured by using rotational incremental encoders presented in Chapter 7.

Chapter 9

Wave-tank tests on a 1/20th scale model device

9.1 Introduction

In this chapter, the wave-tank tests performed on a 1/20th scale three-body hinge-barge device, which is shown in Figure 7.1a, are presented. As shown in Figure 7.1a, while the relative pitch motion of fore and aft barge, with respect to the central barge, is measured by using the rotational encoders presented in Chapter 7, the motion of the central barge is measured by using the motion capture system based on the ultrasound sensors and IMU. In particular, the motion of the central barge is computed with an EKF which optimally combines the measurements provided by the ultrasound sensors and IMU. Full details on the ultrasound sensors, IMU and EKF are presented in Chapter 8. The forces applied by the hydraulic dampers shown in Figure 7.1a are measured using the loads cells presented in Chapter 7. As shown in Figure 7.1b, the incident wave is measured using a wave gauge placed 1.2 m up-wave of the device.

The motion of the scale model WEC is restricted to the plane defined by the X_g-Z_g axis, as shown in Figure 8.1, since the wave-tank used for the system set-up presented in Chapter 7, is equipped with a paddle wave maker that can only generate planar regular and irregular waves. Therefore, the motions of interest of the WEC are the heave displacement and pitch rotation of the central barge, and the relative pitch rotation of the fore and aft barge, with respect to the central barge.

In summary, the following measurements were recorded during the wave-tank tests:

- Heave displacement of the central barge, measured by the motion capture system.
- Pitch rotation of the central barge, measured by the motion capture system.
- Relative pitch rotation of the fore and aft barge, with respect to the central barge, measured by rotational encoders.
- Incident wave 1.2 m up-wave of the device, measured by a wave gauge.

- Axial force along the hydraulic dampers, measured by load cells.

A series of tanks tests with regular and irregular waves were performed, with the direction of the waves along the longitudinal direction of the device. For the tests with regular waves, a series of tests with a range of regular wave frequencies from 3.14 rad/sec to 8.4 rad/secs and amplitude of 0.02 m, was performed. For irregular waves, two different tank tests were performed:

- "Irr 1": incident wave made using a Bretschneider spectrum, with a significant wave height $H_s = 15$ cm and peak period $T_p = 1.25$ seconds
- "Irr 2": incident wave made using a Bretschneider spectrum, with a significant wave height $H_s = 15$ cm and peak period $T_p = 1.5$ seconds

Note that the measurement of the heave displacement of the central barge, provided by the ultrasound sensors, is highly affected by the reflection of the ultrasonic waves generated by the ultrasound transmitter placed on the central barge, which is shown in Figure 8.1. The ultrasonic waves generated by the ultrasonic transmitter can be reflected by the water or by the box walls containing the transmitter. Thus, the reflected ultrasonic waves affect the ultrasonic waves transmitted from the ultrasound transmitter to the ultrasound receivers, resulting into a corruption of the measurement of the distance of the ultrasound transmitter from the each receiver. For regular waves with a period between 1.7 seconds to 2 seconds, the effect of the reflect ultrasonic waves is relatively small compared to the heave motion of the central barge. In fact, for regular waves with a period between 1.7 seconds to 2 seconds, the device essentially behaves like a wave follower, with small relative pitch rotations of the fore and aft barge with respect to the central barge, and maximum heave motion of the central barge. However, for regular waves with a period between 0.75 seconds to 1.7 seconds, the heave motion of the central barge is small and, therefore, the effect of the reflected ultrasonic waves, on the measurement of the heave motion of the central barge, is high.

By way of example, in Figure 9.1, the heave displacement of the central barge, measured with the ultrasound sensors only, is shown for a regular wave of period $T = 1.75$ seconds and amplitude A=0.025 m. Note that the EKF does not improve the measurement of the heave motion with respect to the measurement provided by the ultrasound sensors, as presented in Chapter 8. As shown in Figure 9.1, the measurement of the heave motion of the central barge is not purely sinusoidal with one main frequency component, as the ultrasonic measurement is affected by the reflected ultrasonic waves. Therefore, in the remainder of this chapter, the heave displacement of the central barge is not further considered because of the effect of reflected ultrasonic waves on the ultrasonic measurement.

Furthermore, it is noted that, for regular waves with a period between 1.7 seconds to 2 seconds, the damping plate attached to the central barge, as shown in Figure 7.1a, does not reduce the heave motion of the central barge and, therefore, the relative pitch motion between the fore and aft barge,

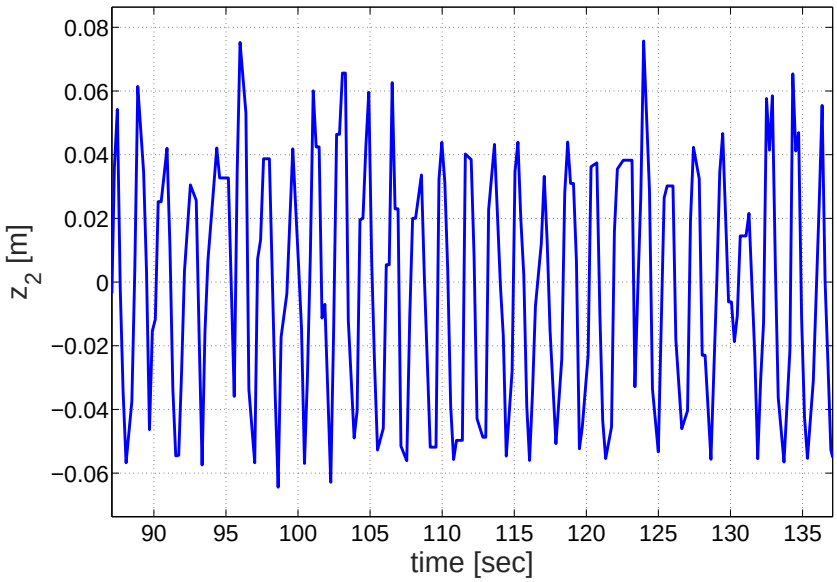

Figure 9.1: Heave displacement of the central barge measured in tank with ultrasound sensors for regular waves of period $T = 1.75$ seconds amplitude 0.02 m.

with respect to the central barge, is not maximized. Thus, the damping plate does not extend the frequency bandwidth over which the maximum power absorption is realized.

The objective of this chapter is to present the wave-tank tests performed on a 1/20th scale hinge-barge device, and derive a linear dynamic model for the device, for model based optimal control. In particular, the dynamic model is described in terms of the pitch rotation of the central barge, and the relative pitch rotation of fore and aft barge, with respect to the central barge. The dynamic model of the three-body hinge-barge device, derived in Section 3.5, is tuned by using the experimental transfer functions between the wave elevation and the pitch rotations of the barges, as presented in Section 3.5.3.2. In particular, given that the device has a resonant frequency around 1.5 seconds, the set of tank tests with irregular waves “Irr 2 ”, is used to tune the dynamic model. Then, the tuned dynamic model is validated against tank tests with irregular waves “Irr 1” and regular waves. The tuned dynamic model is used to derive a control strategy based on optimal linear damping coefficients, as presented in Section 4.5.1.1.

The remainder of the chapter is organized as follows: in Section 9.2, the experimental transfer functions between the wave elevation and the pitch rotations of the barges, and the experimental transfer functions between the wave elevation and the forces exerted by the fore and aft hydraulic damper, are presented. In Section 9.3, a linear dynamic model for a 1/20th scale hinge-barge device is tuned with the tank tests with irregular waves “Irr 2 ” while, in Section 9.4, the tuned dynamic model is validated against the tank tests with irregular waves “Irr 1” and regular waves. In Section 9.5, a control strategy based on optimal linear damping coefficients for the hydraulic dampers is presented. Finally, overall conclusions are drawn in Section 9.6.

9.2 Experimental transfer functions with regular and irregular waves

In this section, the experimental transfer functions between the wave elevation and the pitch rotations of the barges, and the experimental transfer functions between the wave elevation and the forces exerted by the fore and aft hydraulic damper, are calculated using the tank tests with regular waves, and irregular waves "Irr 1" and "Irr 2". The spectral densities of the incoming wave for the tests with irregular waves "Irr 1" and "Irr 2" are shown in Figure 7.14 and 7.16, respectively. For the tank-tests presented in this section, the opening of the flow control valve of the fore and aft hydraulic damper is set to 50%.

In order to facilitate the intepretation of the results, while the fore, central and aft barge are denoted as body 1, 2 and 3, respectively, the fore and aft hydraulic dampers are denoted as damper 1 and 2, respectively. For regular waves, the modulus of the transfer functions between the wave elevation and the pitch rotations of the bodies, and the module of the transfer functions between the wave elevation and the forces exerted by the dampers, are determined by dividing the positive peak value of the pitch rotations and damper forces by the amplitude of the incoming wave, respectively.

For irregular waves, the transfer functions between the wave elevation and the pitch rotations of the bodies, and the transfer functions between the wave elevation and the forces exerted by the dampers, are experimentally computed via equation (3.105).

9.2.1 Experimental transfer functions for pitch rotations

The experimental transfer functions for the pith rotation of body 2 is given as follows:

$$H_{\theta_2}(\omega) = \sqrt{\frac{S_{\theta_2\theta_2}}{S_{\eta\eta}}} e^{j\angle S_{\theta_2\eta}} \tag{9.1}$$

where $S_{\theta_2\theta_i}$, $S_{\eta\eta}$ and $S_{\theta_2\eta}$ are the power spectral density of the pitch rotation of body 2, power spectral density of the wave elevation, and the cross power spectral density between the pitch rotation of body 2 and the wave elevation, respectively. Similarly, for the relative pitch rotation of body 1 and 3 with respect to body 2, the experimental transfer functions are given as follows:

$$H_{\theta_{i,rel}}(\omega) = \sqrt{\frac{S_{\theta_{i,rel}\theta_{i,rel}}}{S_{\eta\eta}}} e^{j\angle S_{\theta_{i,rel}\eta}} \tag{9.2}$$

where $i = 1,3$ and $S_{\theta_{i,rel}\theta_{i,rel}}$ and $S_{\theta_{i,rel}\eta}$ are the power spectral density of the relative pitch rotation of body i, and the cross power spectral density between the relative pitch rotation of body i and the wave elevation, respectively.

In Figure 9.2, the modulus of the experimental transfer functions, between the wave elevation and the pitch rotation of body 1, 2 and 3, are shown for the wave-tank tests with regular waves, irregular waves "Irr 1" and "Irr 2". In Figure 9.3, the phase of the experimental transfer functions between the wave elevation and the pitch rotations of body 1, 2 and 3, are shown for the wave-tank tests with irregular waves "Irr 1" and "Irr 2".

As shown in Figure 9.2, the modulus of the experimental transfer functions between the wave elevation and the pitch rotations of the body 1, 2 and 3, computed with the wave-tank tests with irregular waves "Irr 1", show a good agreement with the module of the transfer functions computed with the wave-tank tests with regular waves and irregular waves "Irr 2". Furthermore, as shown in Figure 9.3, the phase of the experimental transfer functions between the wave elevation and the pitch rotations of the body 1, 2 and 3, computed with the wave-tank tests with irregular waves "Irr 1", show a good agreement with the phase of the transfer functions computed with the wave-tank tests with irregular waves "Irr 2". Therefore, for the wave conditions chosen for the tank tests with regular and irregular waves, the dynamic responses of the pitch rotations of body 1, 2 and 3 are linear with respect to the incoming wave elevation.

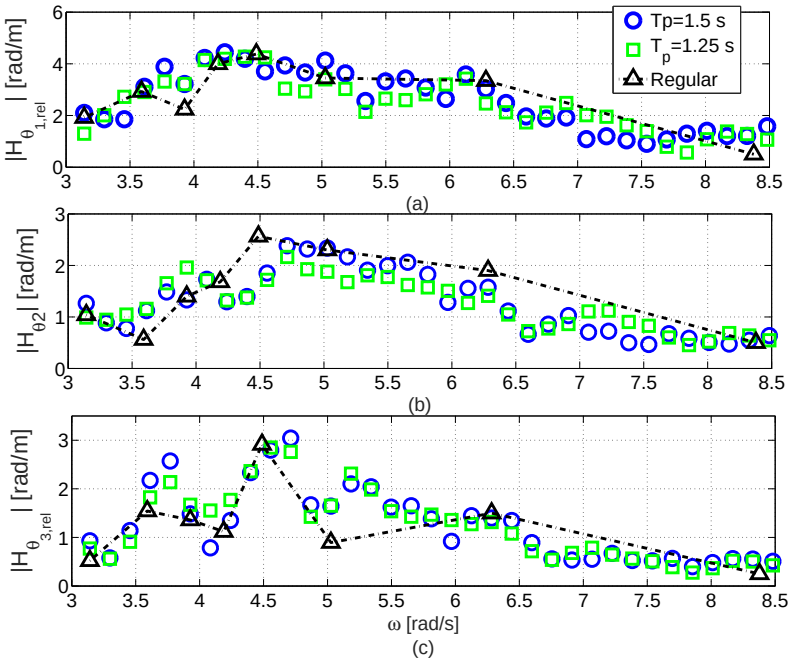

Figure 9.2: Magnitude experimental transfer function between the wave elevation and the pitch rotation of body 2 (b), and magnitude experimental transfer functions between the wave elevation and the relative pitch rotation of bodies 1 (a) and 3 (c), with respect to body 2, of a 1/20th scale three-body hinge-barge device, computed with regular waves, irregular waves "Irr 1" and "Irr 2".

9.2.2 Experimental transfer functions for damper forces

The experimental transfer functions for the forces of dampers 1 and 2 are given as follows:

$$H_{F_{s,i}}(\omega) = \sqrt{\frac{S_{F_{s,i}F_{s,i}}}{S_{\eta\eta}}} e^{j\angle S_{F_{s,i}\eta}} \tag{9.3}$$

where $i = 1, 2$, and $S_{F_{s,i}F_{s,i}}$ and $S_{F_{s,i}\eta}$ are the power spectral density of the force of damper i, and the cross power spectral density between the force of damper i and the wave elevation, respectively.

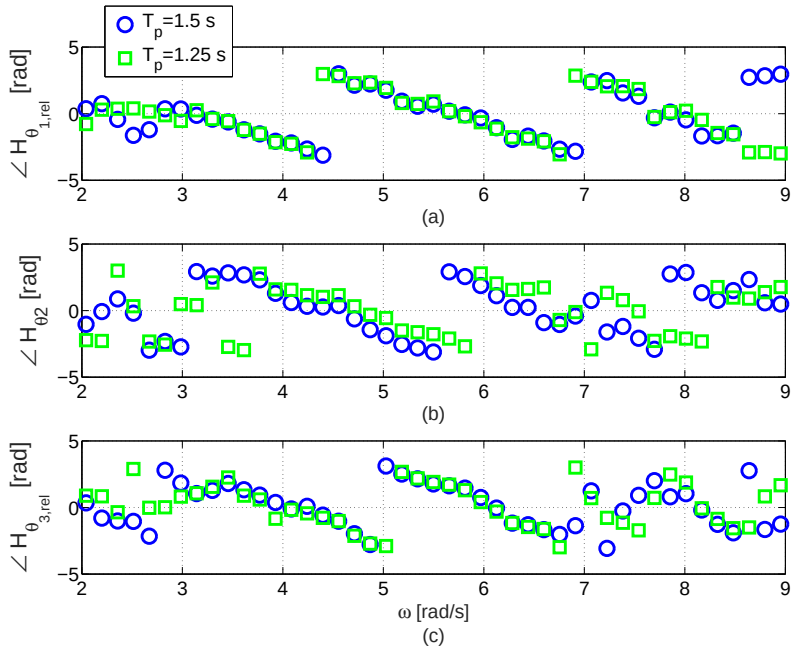

Figure 9.3: Phase experimental transfer function between the wave elevation and the pitch rotation of body 2 (b), and phase experimental transfer functions between the wave elevation and the relative pitch rotation of bodies 1 (a) and 3 (c), with respect to body 2, of a 1/20th scale three-body hinge-barge device, computed with irregular waves “Irr 1” and “Irr 2”.

In Figure 9.4, the modulus of the experimental transfer functions between the wave elevation and the force of damper 1 and 2, with 50% opening of the flow control valves, are shown for the wave-tank tests with regular waves, irregular waves “Irr 1” and “Irr 2”. In Figure 9.5, the phase of the experimental transfer functions between the wave elevation and the force of damper 1 and 2, with 50% opening of the flow control valves, are shown for the wave-tank tests with irregular waves “Irr 1” and “Irr 2”.

As shown in Figure 9.4, the magnitude of the experimental transfer functions between the wave elevation and the force of damper 1 and 2, computed with the tank tests with irregular waves “Irr 1”, show a good agreement with the magnitude of the experimental transfer functions computed with the tank tests with regular waves and irregular waves “Irr 2”. As shown in Figure 9.5, the phase of the experimental transfer function between the wave elevation and the force of damper 1 and 2, computed with the tank tests with irregular waves “Irr 1”, show a good agreement with the phase of the experimental transfer functions computed with irregular waves “Irr 2”. Therefore, for the wave conditions chosen for the tank tests with regular and irregular waves, the dynamic response of the force of damper 1 and 2 is linear with respect to the incoming wave elevation.

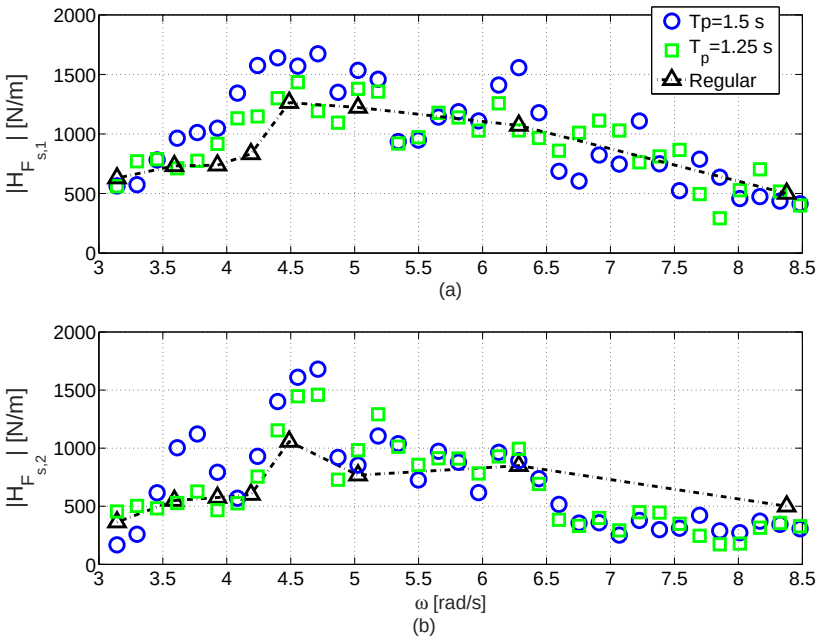

Figure 9.4: Magnitude experimental transfer functions between the wave elevation and the force of dampers 1 (a) and 2 (b), with 50% opening of the flow control valves, of a 1/20th scale three-body hinge-barge device, computed with regular waves, irregular waves “Irr 1” and “Irr 2”.

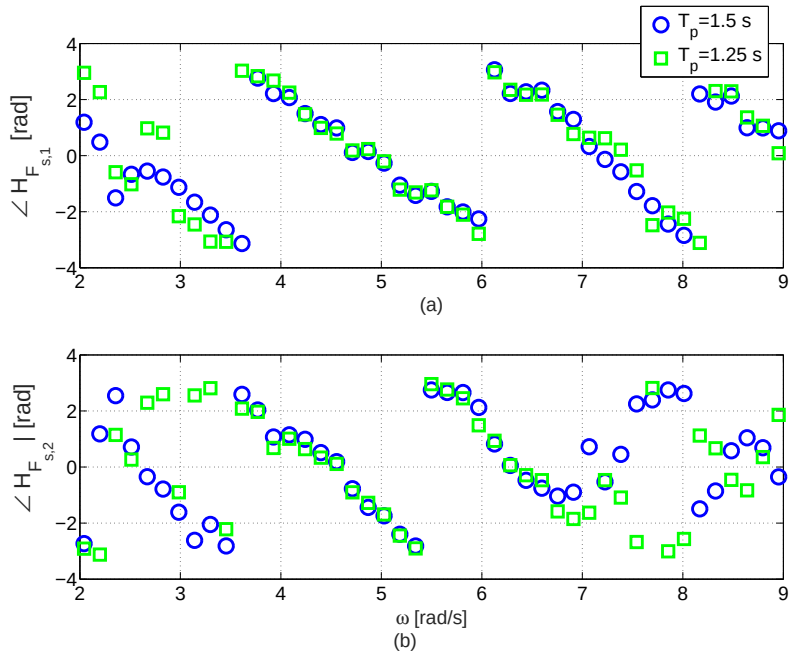

Figure 9.5: Phase experimental transfer functions between the wave elevation and the force of dampers 1 (a) and 2 (b), with 50% opening of the flow control valves, of a 1/20th scale three-body hinge-barge device, computed with irregular waves “Irr 1” and “Irr 2”.

9.3 Model tuning

In this section, the linear dynamic model of a three-body hinge-barge device, derived in Section 3.5, is tuned using the wave-tank tests with irregular waves "Irr 2", given that the device has a resonant period around 1.5 seconds, as shown in Figure 9.2. The dynamic model of the device is tuned in the frequency domain, with the method outlined in Section 3.5.3.2, where the viscous damping matrix is computed so that the theoretical transfer functions of the pitch rotations of the bodies, computed with the model, fit the experimental transfer functions of the pitch rotations of the bodies, computed with tank data.

The theoretical transfer function vector between the wave elevation and the position of the DoF of a three-body hinge-barge device, is given as:

$$\hat{\mathbf{H}}(\omega) = \frac{\mathbf{H}_{wave,s}(\omega)}{-\omega^2(\mathbf{M}_s + \mathbf{M}_{a,s}(\omega)) + j\omega(\mathbf{B}_{visc,s} + \mathbf{B}_{rad,s}(\omega)) + \mathbf{G}_s} \tag{9.4}$$

where $\mathbf{M}_s$ is the inertia matrix, $\mathbf{B}_{visc,s}$ is the linearized viscous damping matrix, $\mathbf{G}_s$ is the hydrostatic stiffness, $\mathbf{M}_{a,s}$ is the added mass, $\mathbf{B}_{rad,s}$ is the radiation damping and $\mathbf{H}_{wave,s}$ is the transfer function betweeen the excitation forces vector and the incident wave. The theoretical transfer function vector $\hat{\mathbf{H}}(\omega)$ is given as follows:

$$\hat{\mathbf{H}}(\omega) = \begin{bmatrix} \hat{H}_{z2}(\omega) \\ \hat{H}_{\theta_2}(\omega) \\ \hat{H}_{\theta_{1,rel}}(\omega) \\ \hat{H}_{\theta_{3,rel}}(\omega) \end{bmatrix} \tag{9.5}$$

where $\hat{H}_{z2}$, $\hat{H}_{\theta_2}$, $\hat{H}_{\theta_{1,rel}}$ and $\hat{H}_{\theta_{3,rel}}$ are the theoretical transfer functions of the heave of body 2, the pitch rotation of body 2, the relative pitch rotation of body 1 and 3, with respect to body 2, respectively. The problem of identification of the viscous damping matrix $\mathbf{B}_{visc,s}$, in equation (9.4), is formulated as an optimization problem as follows:

$$\min_{\mathbf{B}_{visc,s}} \quad J_{LS} \tag{9.6}$$

where the cost function J_{LS} to be minimized is the total sum of squared errors between the theoretical and experimental transfer functions across the range of frequencies of the spectrum of the incident wave:

$$J_{LS} = \sum_{i=1}^{n_f} (\, |H_{\theta_2}(\omega_i) - \hat{H}_{\theta_j}(\omega_i)|^2 + |H_{\theta_{1,rel}}(\omega_i) - \hat{H}_{\theta_{1,rel}}(\omega_i)|^2 + |H_{\theta_{3,rel}}(\omega_i) - \hat{H}_{\theta_{3,rel}}(\omega_i)|^2) \tag{9.7}$$

where n_f is the number of measured frequencies of the spectrum of the incident wave. The elements of the viscous damping matrix $\mathbf{B}_{visc,s}$ are used as decision variables for the computation of the minimum of the cost function defined in equation (9.7).

9.3.1 Experimental and theoretical transfer functions for pitch rotations

In Figure 9.6, the magnitude of the experimental transfer functions between the wave elevation and the pitch rotations of bodies 1, 2 and 3, computed with the wave-tank tests with irregular waves "Irr 2", is compared to the magnitude of the theoretical transfer functions computed with the tuned and original dynamic model.

While the original dynamic model is based only on the hydrodynamic parameters given by the Wamit software [25], the tuned dynamic model is based on the hydrodynamic parameters given by the Wamit software and the damping matrix $\mathbf{B}_{visc,s}$. As shown in Figure 9.6, the natural frequencies for the pitch rotation of bodies 1, 2 and 3, given by the original dynamic model, are lower than the natural frequencies experimentally measured with the tank tests.

In Figure 9.7, the phase of the experimental transfer functions between the wave elevation and the pitch rotations of bodies 1, 2 and 3, computed with the wave-tank tests with irregular waves "Irr 2", is compared to the phase of the theoretical transfer functions computed with the tuned and original dynamic model. As shown in Figure 9.6 and 9.7, the accuracy of the tuned dynamic model, with respect to the experimental transfer functions, is quite good.

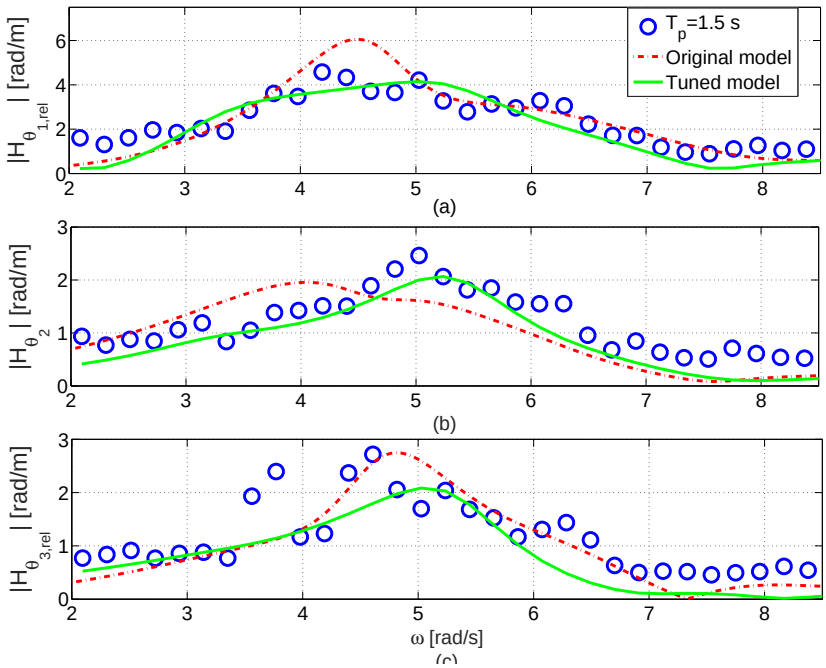

Figure 9.6: Magnitude transfer function between the wave elevation and the pitch rotation of body 2 (b), and magnitude transfer functions between the wave elevation and the relative pitch rotation of bodies 1 (a) and 3 (c), with respect to body 2, computed with irregular waves "Irr 2", original and tuned dynamic model.

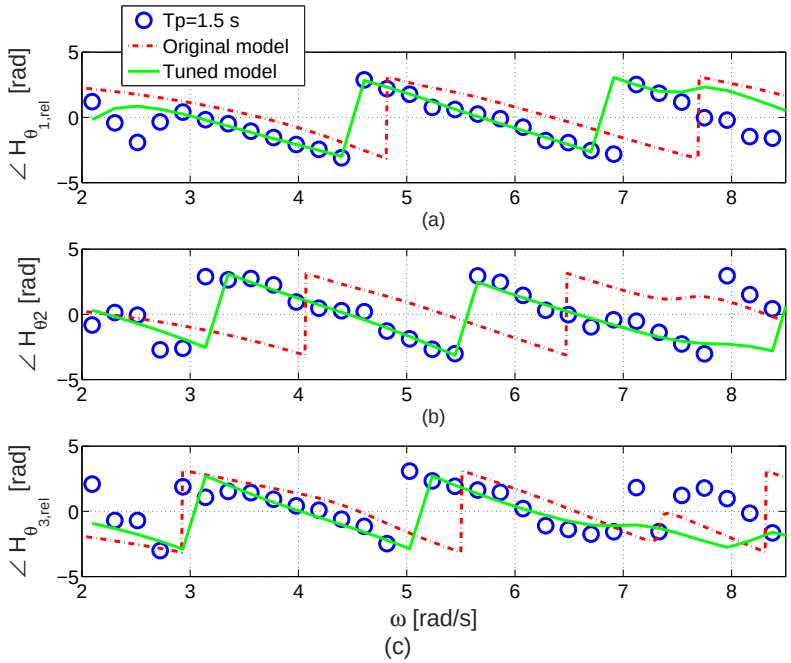

Figure 9.7: Phase transfer function between the wave elevation and the pitch rotation of body 2 (b), and phase transfer functions between the wave elevation and the relative pitch rotation of bodies 1 (a) and 3 (c), with respect to body 2, computed with irregular waves “Irr 2”, original and tuned dynamic model.

9.3.2 Experimental and theoretical transfer functions for damper forces

In Figure 9.8, the magnitude of the experimental transfer functions between the wave elevation and the force of dampers 1 and 2, computed with the wave-tank tests with irregular waves “Irr 2”, are compared to the module of the theoretical transfer functions computed with the original and tuned dynamic model. In Figure 9.9, the phase of the experimental transfer functions between the wave elevation and the force of damper 1 and 2, computed with the wave-tank tests with irregular waves “Irr 2”, are compared to the phase of the theoretical transfer functions computed with the original and tuned dynamic model.

As shown in Figures 9.8 and 9.9, while the original and tuned dynamic model provide a similar magnitude of the transfer functions, the accuracy of tuned dynamic model, with respect to the phase of the experimental transfer functions, is higher than the accuracy of the original model.

9.4 Model validation

In this section, the dynamic model obtained in Section 9.3, tuned with the tank tests with irregular waves “Irr 2”, is validated against the tank tests with regular waves and irregular waves “Irr 1”. The accuracy of the pitch rotation of body 2, computed by the tuned dynamic model, with respect to the tank tests, is measured by using the Normalized Mean Absolute Percentage Error (NMPAE),

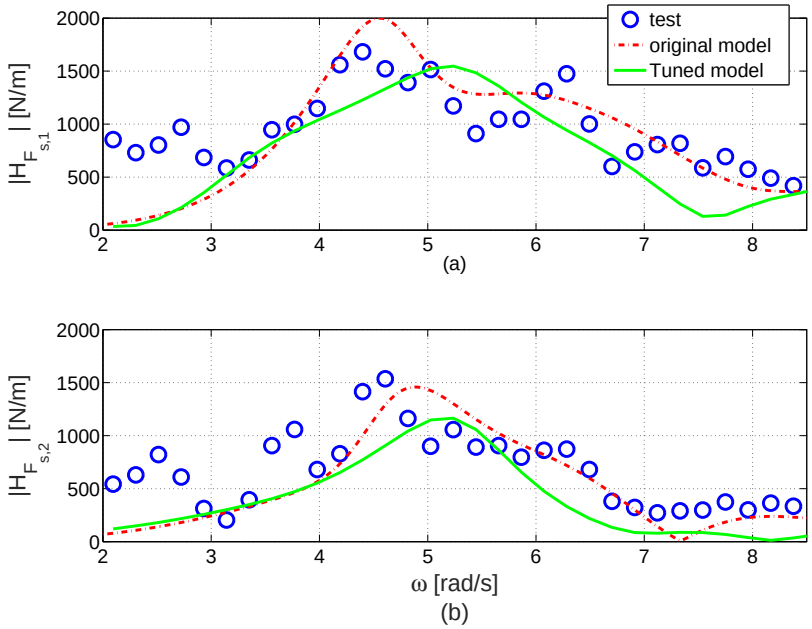

Figure 9.8: Comparison between magnitude experimental transfer functions between the wave elevation and the force of dampers 1 (a) and 2 (b), with 50% opening of the flow control valves, computed with irregular waves "Irr 2", and magnitude theoretical transfer functions computed with original and tuned dynamic model.

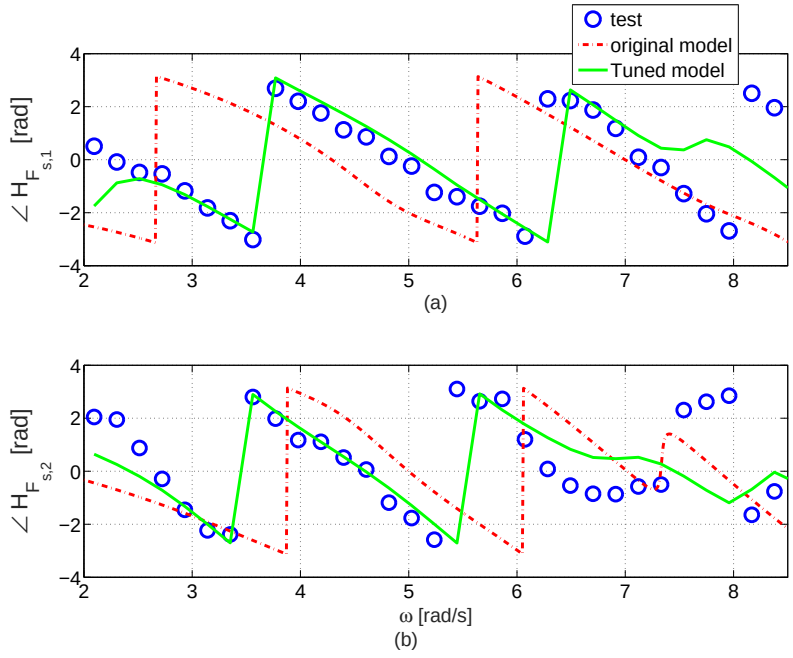

Figure 9.9: Comparison between phase experimental transfer functions between the wave elevation and the force of dampers 1 (a) and 2 (b), with 50% opening of the flow control valves, computed with irregular waves "Irr 2", and phase theoretical transfer functions computed with original and tuned dynamic model.

which is given as follows:

$$NMAPE_{\theta_2} = \frac{100}{N(\overline{\theta}_{2,meas_{max}} - \overline{\theta}_{2,meas_{min}})} \sum_{k=1}^{N} |\theta_{2,meas}(k) - \theta_{2,model}(k)| \tag{9.8}$$

where N is a set of validation data. Similarly, the accuracy for the relative pitch rotation of bodies 1 and 3, with respect to body 2, computed by the tuned dynamic model, with respect to the tank tests, is measured by using the following NMPAE:

$$NMAPE_{\theta_{i,rel}} = \frac{100}{N(\overline{\theta}_{i,rel,meas_{max}} - \overline{\theta}_{i,meas_{min}})} \sum_{k=1}^{N} |\theta_{i,rel,meas}(k) - \theta_{i,rel,model}(k)| \tag{9.9}$$

where $i = 1,3$. The accuracy of the force of dampers 1 and 2, computed by the tuned dynamic model, with respect to the tank tests, is measured by using the following NMAPE:

$$NMAPE_{F_{s,i}} = \frac{100}{N(\overline{F}_{s,i,meas_{max}} - \overline{F}_{s,i,meas_{min}})} \sum_{k=1}^{N} |F_{s,i,meas}(k) - F_{s,i,model}(k)| \tag{9.10}$$

where $i = 1,2$. The accuracy of the mean absorbed power, computed by the tuned dynamic model, with respect to the tank tests, is measured by the Percentage Mean Power Error (PMPE) defined as follows:

$$PMPE = 100\frac{|\overline{P}_{meas} - \overline{P}_{model}|}{\overline{P}_{meas}} \tag{9.11}$$

9.4.1 Model validation with regular waves

In Figure 9.10, the frequency response of the pitch rotation of bodies 1, 2 and 3, obtained from the tank experiments, is compared to the response obtained from the tuned dynamic model. The uncertainty on the measurement of the frequency response of the pitch rotation of bodies 1, 2 and 3, obtained from the tank experiments, is represented by using error bars with interval $\pm\sigma_\theta$, where σ_θ is the standard deviation. For each frequency of the regular wave, the standard deviation σ_θ is computed as follows:

$$\sigma_\theta = \sqrt{\frac{\sum_k^{n_{data}} (\Theta_i(k) - \overline{\Theta}_i)^2}{n_{data}}} \tag{9.12}$$

where n_{data} is the number of peaks of the pitch rotation of body i, $\Theta_i(k)$ is the amplitude of the peak k-th and $\overline{\Theta}_i$ is the average peak amplitude. In Figure 9.11, the frequency response of the force of dampers 1 and 2, obtained from the tank experiments, is compared to the response obtained from the tuned dynamic model. Similarly to the frequency response of the pitch rotation of the bodies 1, 2 and 3, the uncertainty on the measurement of the frequency response of the force of the dampers 1 and 2, obtained from the tank experiments, is represented by using error bars with interval $\pm\sigma_{F_s}$. For each frequency of the regular wave, the standard deviation σ_{F_s} is computed as

follows:

$$\sigma_{F_s} = \sqrt{\frac{\sum_k^{n_{data}} (F_{s,i}(k) - \overline{F}_{s,i})^2}{n_{data}}} \tag{9.13}$$

where n_{data} is the number of peaks of the force of damper i, $F_{s,i}(k)$ is the amplitude of the peak k-th and $\overline{F}_{s,i}$) is the average peak amplitude.

By way of example, the time response of the pitch rotation of bodies 1, 2 and 3, computed by the tuned dynamic model compared to the tank tests, is shown for regular waves of amplitude 0.025 m and period $T = 1.75$ in Figure 9.12, $T = 1.4$ seconds in Figure 9.14, and $T = 1.25$ seconds in Figure 9.16.

Also, by way of example, the time response of the force of dampers 1 and 2, with openings of the flow control valves of 50%, computed by the tuned dynamic model compared to the tank tests, are shown for regular waves of amplitude 0.025 m and period $T = 1.75$ in Figure 9.13, $T = 1.4$ seconds in Figure 9.15, and $T = 1.25$ seconds in Figure 9.17.

In Table 9.1, the NMAPE for the pitch rotation of body 2, relative pitch rotation of bodies 1 and 3, with respect to body 2, damper forces 1 and 2, and PMPE, given by the tuned dynamic model, is computed for regular waves with a range of periods from $T = 0.75$ seconds to $T = 2$ seconds. As shown, in Table 9.1, for regular waves of small period from $T = 0.75$ seconds to $T = 1.25$ seconds, the accuracy of the motion of the device and forces applied by the dampers, computed by the dynamic model, is, on average, poorer than for regular waves of long period from $T = 1.4$ seconds to $T = 2$ seconds.

In particular, for regular waves of small period from $T = 0.75$ seconds to $T = 1.25$ seconds, the NMAPE for the forces applied by dampers 1 and 2 is, on average, 26% and 28%, respectively. The poor accuracy of the motion of the device and force applied by the dampers, computed by the tuned dynamic model, for regular waves of small period from $T = 0.75$ seconds to $T = 1.25$ seconds, is probably due to the relative large sampling period which is 0.2 seconds. Therefore, the high-frequency components of the measured variables are not adequately represented in the computation of the experimental transfer functions in Section 9.2.

In Figure 9.18, a comparison between the average absorbed power measured in tank, and the average power absorbed with the tuned dynamic model, is shown for regular waves with a frequency range from 3.14 rad/s to 8.5 rad/s, and amplitude 0.025 m. The uncertainty on the measurement of the average absorbed power σ_{pow} can be obtained from the uncertainty on the measurement of the relative pitch velocities of bodies 1 and 3. Given that the average absorbed power is computed as follows:

$$\overline{P} \pm \sigma_{pow} = \frac{1}{2}(\, c_{pto,1} |\overline{\dot{\theta}}_{rel,1} \pm \sigma_{\dot{\theta}_{rel,1}}|^2 + c_{pto,2} |\overline{\dot{\theta}}_{rel,3} \pm \sigma_{\dot{\theta}_{rel,3}}|^2) \tag{9.14}$$

where $\sigma_{\dot{\theta}_{rel,1}}$ and $\sigma_{\dot{\theta}_{rel,3}}$ are the uncertainty on the measurement of the relative pitch velocity of

body 1 and 3, respectively. Therefore, an upper bound on the uncertainty σ_{pow} is given as follows:

$$\sigma_{pow} = \frac{1}{2}(c_{pto,1}|\sigma_{\dot{\theta}_{rel,1}}|^2 + c_{pto,2}|\sigma_{\dot{\theta}_{rel,3}}|^2) \tag{9.15}$$

In Figure 9.19, a comparison between the total average absorbed power, average power absorbed by the fore and aft damper, given by the tank tests, is shown for regular waves with a frequency range from 3.14 rad/s to 8.5 rad/s and amplitude 0.025 m. As shown in Table 9.1 and Figure 9.18, the error on the mean absorbed power is quite high, as the instantaneous absorbed power depends on both the force applied by the dampers 1 and 2, and the relative angular velocities of bodies 1 and 3, with respect to body 2. Therefore, small errors on the force applied by the dampers 1 and 2, and the relative pitch velocities of bodies 1 and 3, with respect to body 2, computed by the tuned dynamic model, are summed up in the calculation of the instantaneous absorbed power, resulting into large errors in the mean absorbed power.

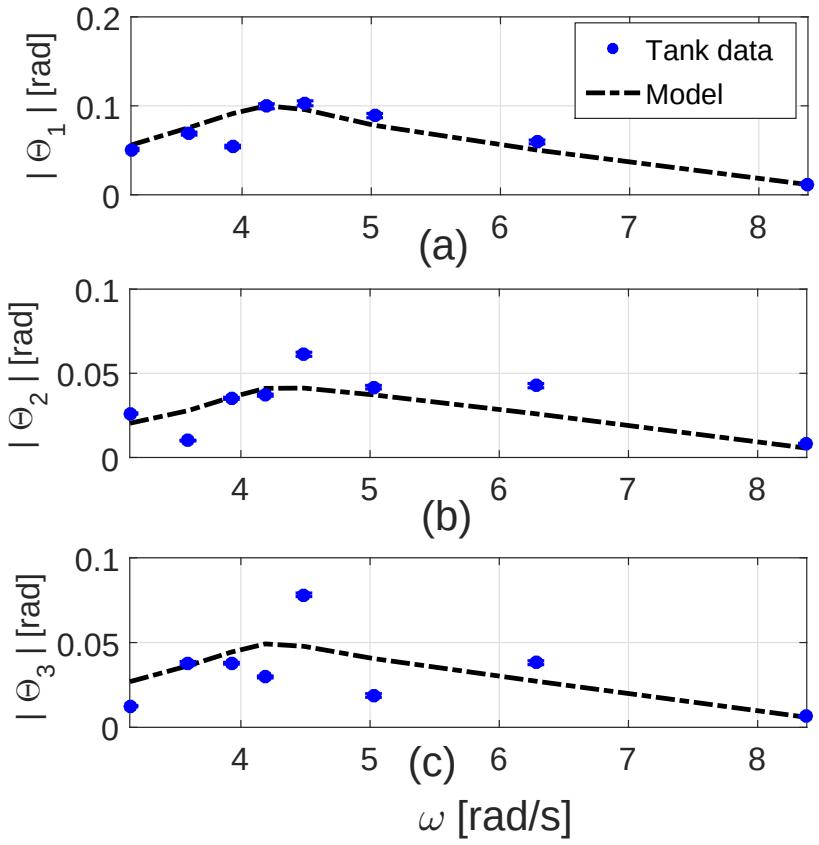

Figure 9.10: Frequency response of the pitch rotation of body 2 (b), and frequency response of the relative pitch rotation of bodies 1 (a) and 3 (c), with respect to body 2, obtained with the tank experiments with error bars for the uncertainty and tuned dynamic model with regular waves.

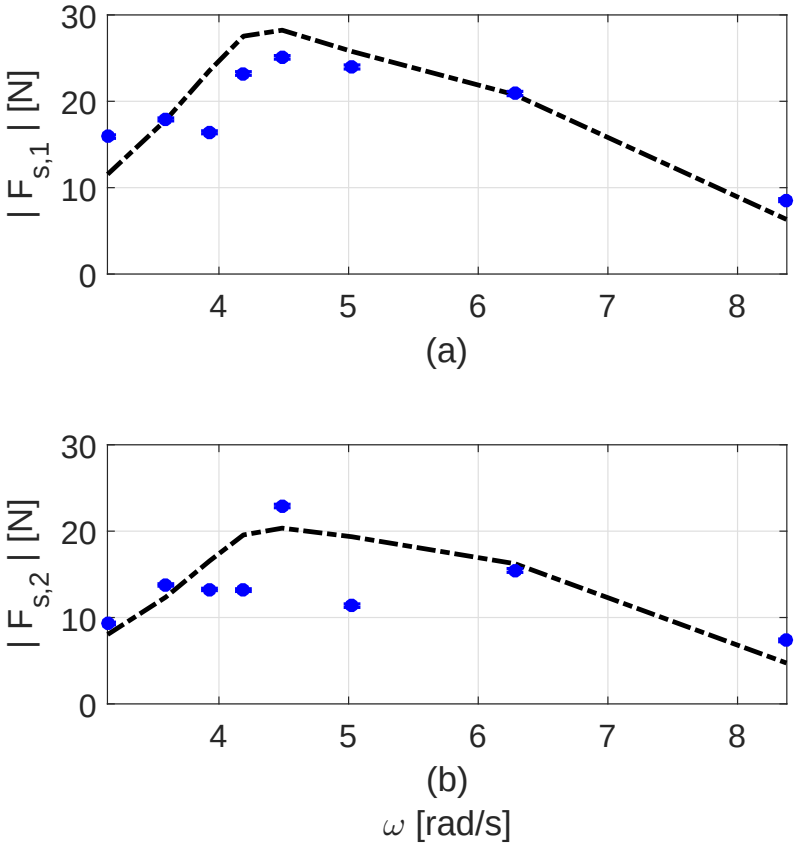

Figure 9.11: Frequency response of the force of dampers 1 (a) and 2 (b) obtained with the tank experiments with error bars for the uncertainty and tuned dynamic model with regular waves.

9.4.2 Model validation with irregular waves

In Figures 9.20, the frequency responses of the pitch angles, obtained from the tank experiments with irregular waves “Irr 1”, are compared to the responses obtained from the tuned dynamic model. In Figures 9.21, the frequency responses of the forces of the dampers, obtained from the tank experiments with irregular waves “Irr 1”, are compared to the responses obtained from the tuned dynamic model. In Figures 9.22, the frequency responses of the pitch angles, obtained from the tank experiments with irregular waves “Irr 2”, are compared to the responses obtained from the tuned dynamic model. In Figures 9.23, the frequency responses of the forces of the dampers, obtained from the tank experiments with irregular waves “Irr 2”, are compared to the responses obtained from the tuned dynamic model. The uncertainty on the measurement of the frequency response of the pitch angles and forces of the dampers, with the irregular wave test “Irr 1” and “Irr 2”, is chosen equal to the maximum uncertainty of the tests with regular waves of comparable scale.

By way of example, the time responses of the pitch rotations of bodies 1, 2 and 3, computed by the tuned dynamic model compared to the tank tests, are shown for the tank tests with irregular

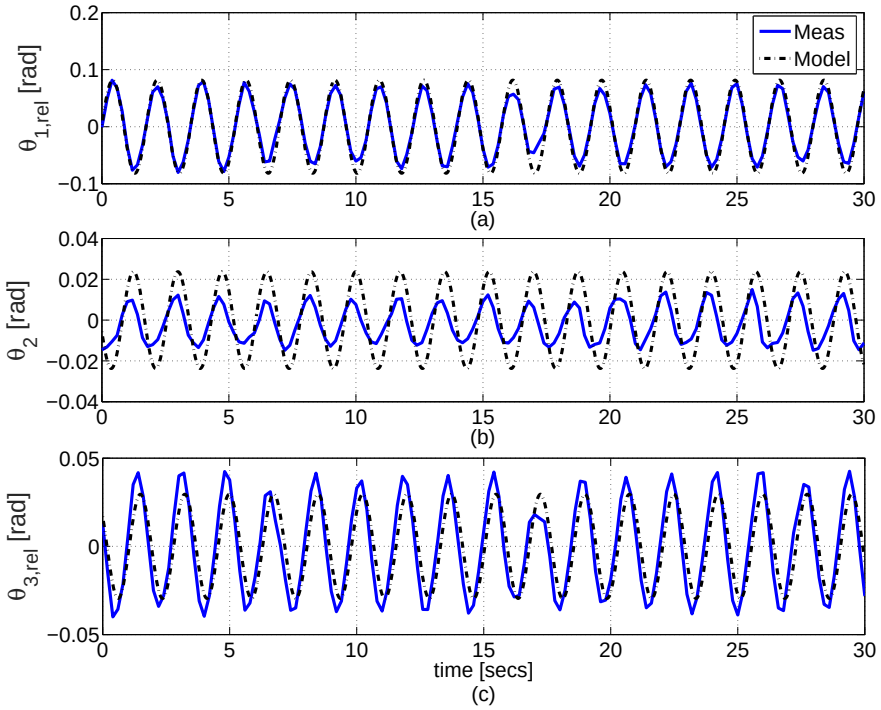

Figure 9.12: Comparison in the time domain between pitch rotation of body 2 (b), and relative pitch rotation of bodies 1 (a) and 3 (c) with respect to body 2, measured in tank and computed with the tuned dynamic model, for regular waves of period $T = 1.75$ seconds and amplitude 0.025 m.

waves "Irr 1" in Figure 9.24 and "Irr 2" in Figure 9.26, respectively.

Also, by way of example, the time response of the force of dampers 1 and 2, with 50% opening of the flow control valves, computed by the tuned dynamic model compared to the tank tests, are shown for the tank tests with irregular waves "Irr 1" in Figure 9.25 and "Irr 2" in Figure 9.27, respectively.

In Table 9.2, the NMAPE for pitch rotation of body 2, relative pitch rotation of body 1 and 3 with respect to body 2, force damper 1 and 2, and PMPE, given by the tuned dynamic model, with respect to the tank tests, is presented for irregular waves. As shown in Table 9.2 and Table 9.1, the accuracy of the motion of the device and force applied by the dampers, computed by the dynamic model, for irregular waves, is similar to the accuracy for regular waves with a range of periods from 1.4 seconds to 2 seconds. Note that the error on the mean absorbed power for the tank tests with irregular waves "Irr 2", is smaller than the error for the tank tests with with irregular waves

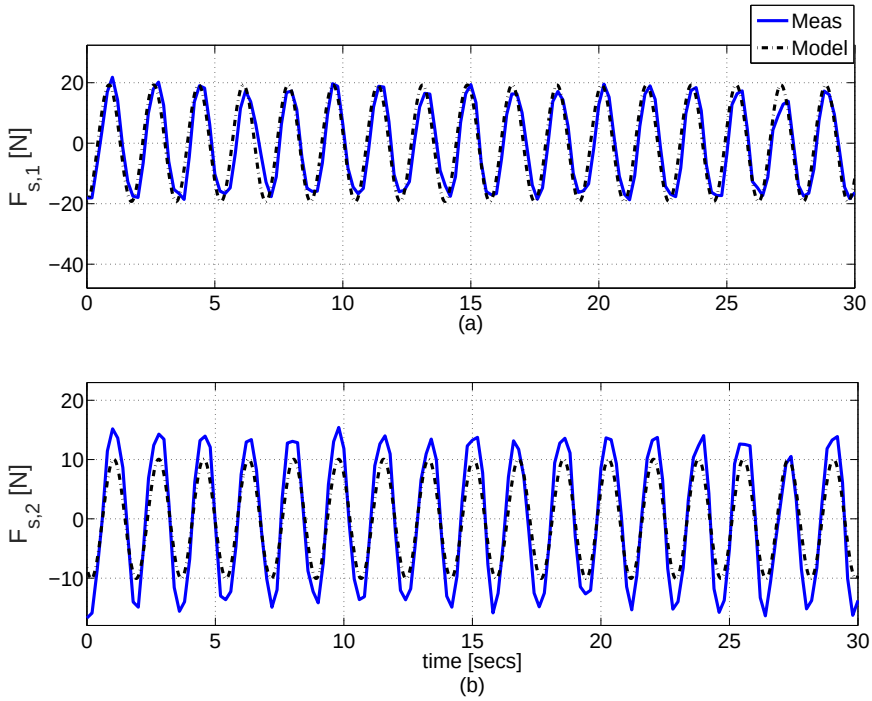

Figure 9.13: Comparison in the time domain between the force of dampers 1 (a) and 2 (b), with 50% opening of the flow control valves, measured in tank and computed with the tuned dynamic model, for regular waves of period $T = 1.75$ seconds and amplitude 0.025 m.

"Irr 1", as the dynamic model is tuned with irregular waves "Irr 2".

9.5 Optimal linear passive dampers

In this section, the optimal linear damping coefficients for dampers 1 and 2, which maximize the energy absorption of the WEC, are computed for each regular wave frequency. The method for the computation of the optimal linear damping coefficients is outlined in Section 4.5.1.1. In particular, the linear damping coefficient of each damper is optimized within an interval of values delimited by the minimum and maximum damping allowed by the damper. In particular, as shown in Figure 7.28, the minimum and maximum damping coefficients of damper 1 are 650 Ns/m and 950 Ns/m, respectively. For the damper 2, as shown in Figure 7.29, the minimum and maximum damping coefficients of damper are 1200 Ns/m and 2000 Ns/m, respectively. The maximum and minimum damping coefficients of the dampers are different, due to the air bubbles trapped inside the hydraulic circuit of each damper, which add compressibility to the hydraulic fluid.

In Figure 9.28, a comparison between the average absorbed power given by the tank tests, tuned dynamic model, and dynamic model with optimal linear dampers, is shown for regular waves with a frequency range from 3.14 rad/s to 8.5 rad/s and amplitude 0.025 m. As shown in Figure 9.28, the dynamic model with optimal linear dampers shows a small increase of the average absorbed power, with respect to the tuned dynamic model, around the resonant frequency of the

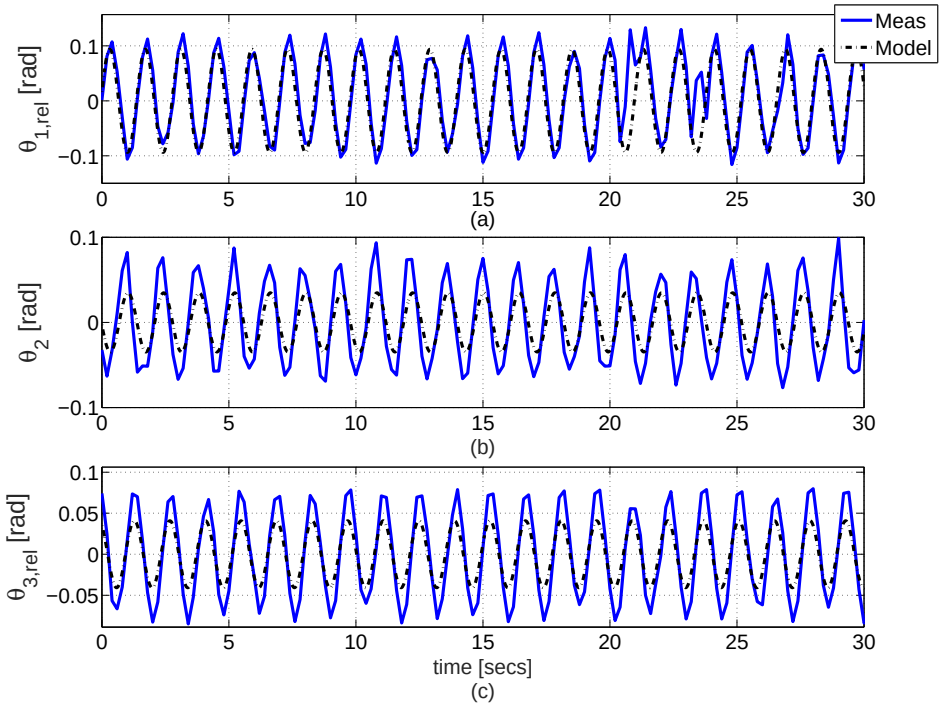

Figure 9.14: Comparison in the time domain between pitch rotation of body 2 (b), and relative pitch rotation of body 1 (a) and 3 (c) with respect to body 2, measured in tank and computed with the tuned dynamic model, for regular waves of period $T = 1.4$ seconds and amplitude 0.025 m.

device.

In Figure 9.29, the average absorbed power, given by the tank tests, is shown for different opening of the flow control valve of the fore and aft damper, for regular waves with period T=1.5 seconds and amplitude 0.025 m. The opening of the flow control valve of the fore and aft hydraulic damper is varied from 0% to 100%, with an increase of the opening of the flow control valve of 10% between each test. As shown in Figure 9.29, the variation of the opening of the flow control valves does not show any significant change of the average absorbed power.

9.6 Conclusions

This chapter presents the wave-tank tests carried out on a 1/20th scale three-body hinge-barge device. In particular, while the relative pitch motion of fore and aft barge, with respect to the central barge, is measured by using the rotational encoders, the motion of the central barge is measured by using the motion capture system based on the ultrasound sensors and IMU. A linear dynamic model is tuned using the wave-tank tests, with irregular waves, with a peak period around the resonant period of the device. The tuned dynamic model is used to formulate a control strategy based on optimal linear damping coefficients for the hydraulic dampers.

During the wave-tank tests, in contrast to the validation tests of the motion capture system with

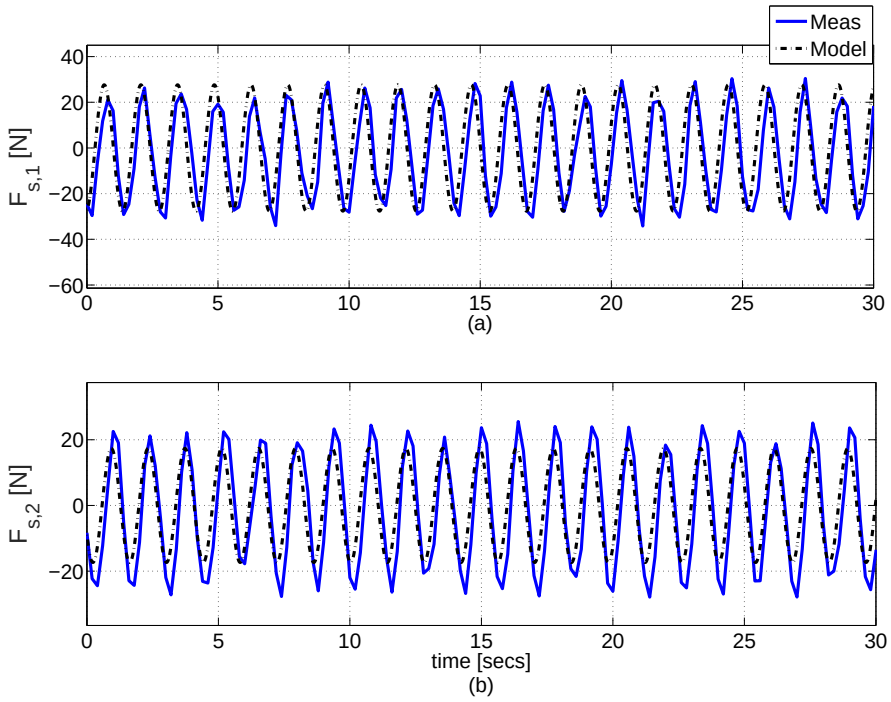

Figure 9.15: Comparison in the time domain between the force of dampers 1 (a) and 2 (b), with 50% opening of the flow control valves, measured in tank and computed with the tuned dynamic model, for regular waves of period $T = 1.4$ seconds and amplitude 0.025 m.

a six-axis robot arm presented in Chapter 8, the measurements provided by the ultrasound sensors are highly affected by the reflection of the ultrasonic waves generated by the ultrasound transmitter placed on the central barge. The ultrasonic waves generated by the ultrasonic transmitter can be reflected by the water or by the walls of the box containing the transmitter. Therefore, the heave displacement of the central barge cannot be considered in the analysis of the motion of the device, because of the adverse effect of reflected ultrasonic waves on the ultrasonic measurement.

Furthermore, it is noted that, for regular waves with a period between 1.7 seconds to 2 seconds, the damping plate attached to the central barge does not reduce the heave of the central barge and, therefore, the relative pitch motion between the fore and aft barge, with respect to the central barge, is not maximized. Thus, the inclusion of a damping plate in the design of a three-body hinge-barge device does not seem necessary, as the damping plate does not extend the frequency bandwidth over which the maximum power absorption is realized.

The tuned dynamic model shows good accuracy in the computation of the motion of the WEC and forces exerted by the dampers, with respect to the tank tests, with both regular and irregular waves. Therefore, for the wave conditions chosen for the tank tests, with regular and irregular waves, the dynamic response of the pitch rotations of the barges and the force exerted by the dampers, are linear with respect to the incoming wave elevation. However, the accuracy of the mean absorbed power computed by the tuned dynamic model is quite low, as the instantaneous absorbed power depends on both the forces applied by dampers 1 and 2, and the relative angular

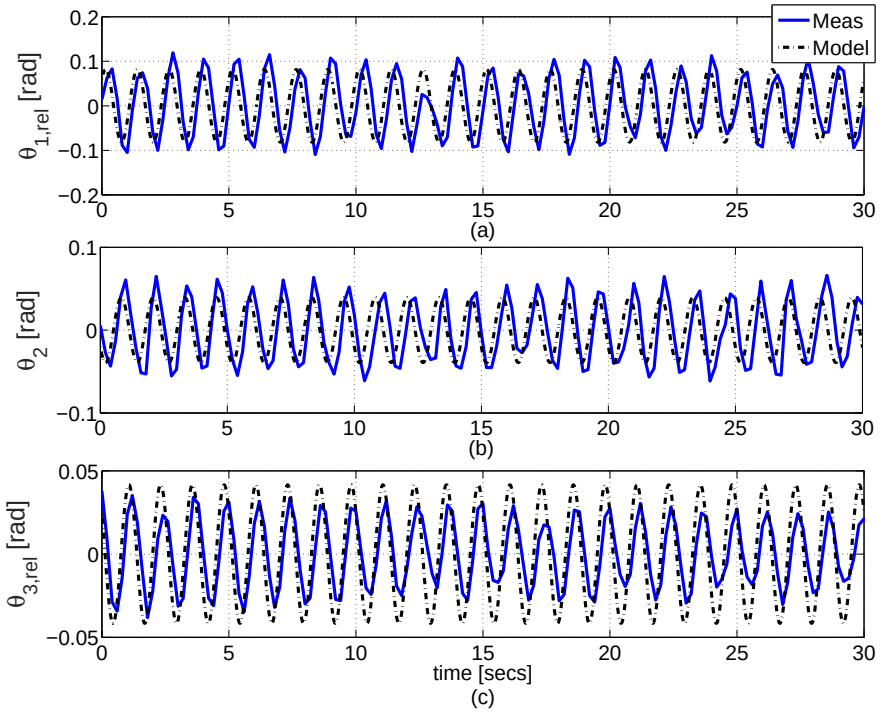

Figure 9.16: Comparison in the time domain between pitch rotation of body 2 (b), and relative pitch rotation of body 1 (a) and 3 (c) with respect to body 2, measured in tank and computed with the tuned dynamic model, for regular waves of period $T = 1.25$ seconds and amplitude 0.02 m.

velocities of bodies 1 and 3, with respect to body 2. Therefore, small errors on the forces applied by the dampers 1 and 2, and the relative pitch velocities of bodies 1 and 3, with respect to body 2, computed by the tuned dynamic model, are summed up in the calculation of the instantaneous absorbed power, resulting in large errors in the mean absorbed power.

As expected, the wave-tank tests show that the motion of the fore barge is larger than the motion of the central and aft barges, with most of the energy extracted by the fore damper. Thus, the WEC behaves more like a two-body hinge-barge device, rather than a three-body hinge-barge device. The wave-tank tests, shown in this chapter, offer useful insight into the motivation that led to the design of most of the hinge-barge WECs presented in Chapter 2 as, for example, the Sea Power, Mocean and M4 WECs, which are composed of two-bodies, rather than three.

For the particular dampers used in this study, a control strategy, based on optimal linear damping coefficients, does not provide any significant increase of the average power absorbed by the device. Furthermore, for regular waves of period T=1.5 seconds, the wave-tank tests show that variation in the opening of the flow control valves has little effect on the average absorbed power. The power absorption performance of a control strategy, based on optimal linear damping coefficients, can be improved by using hydraulic dampers that allows a greater range of damping than the damping range of the dampers used in this work.

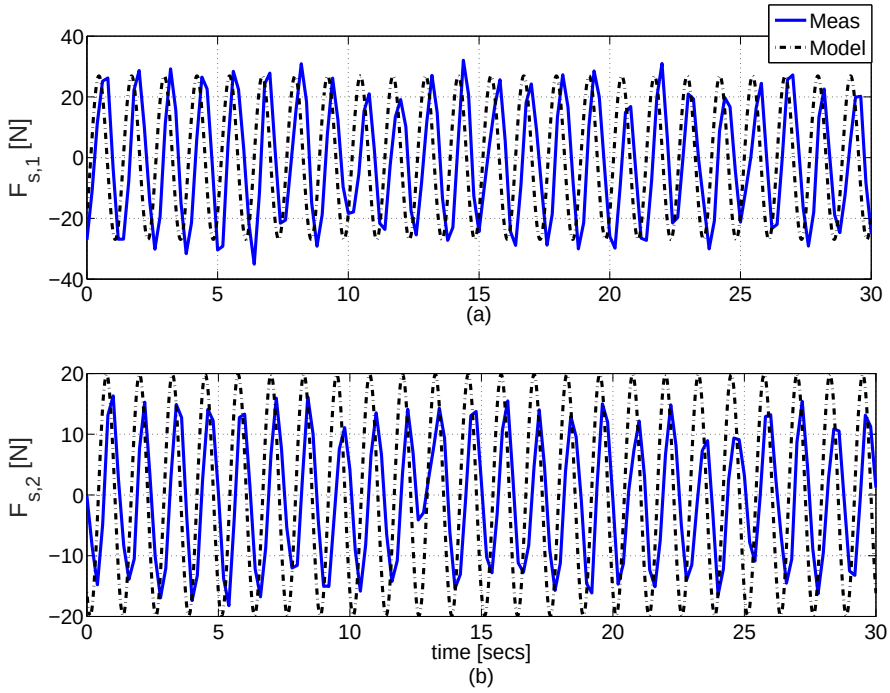

Figure 9.17: Comparison in the time domain between the force of dampers 1 (a) and 2 (b), with 50% opening of the flow control valves, measured in tank and computed with the tuned dynamic model, for regular waves of period $T = 1.25$ seconds and amplitude 0.02 m.

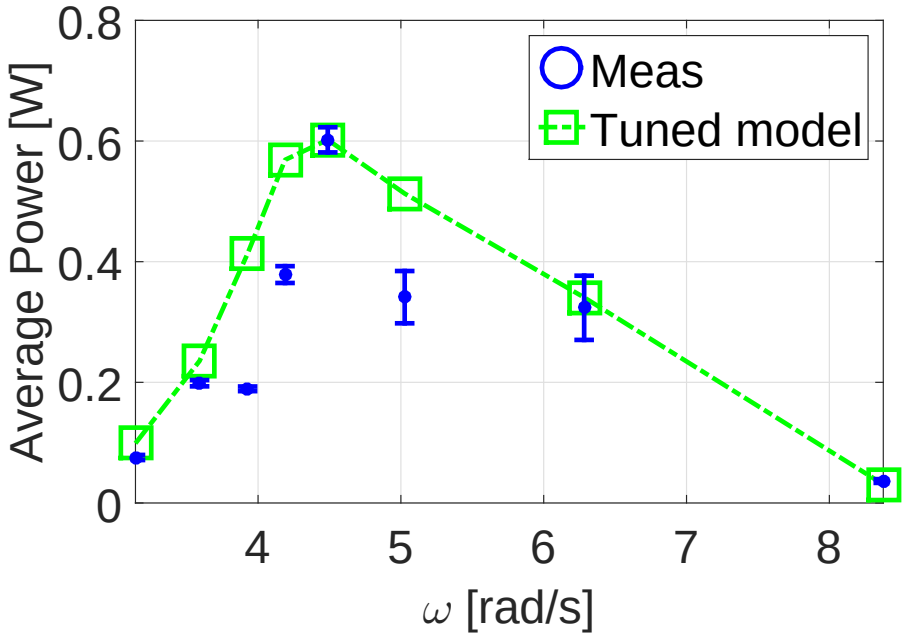

Figure 9.18: Comparison between the average absorbed power measured in tank with error bars for the uncertainty and the average power absorbed with the tuned dynamic model, for regular waves with a frequency range from 3.14 rad/s to 8.5 rad/s and amplitude 0.025 m.

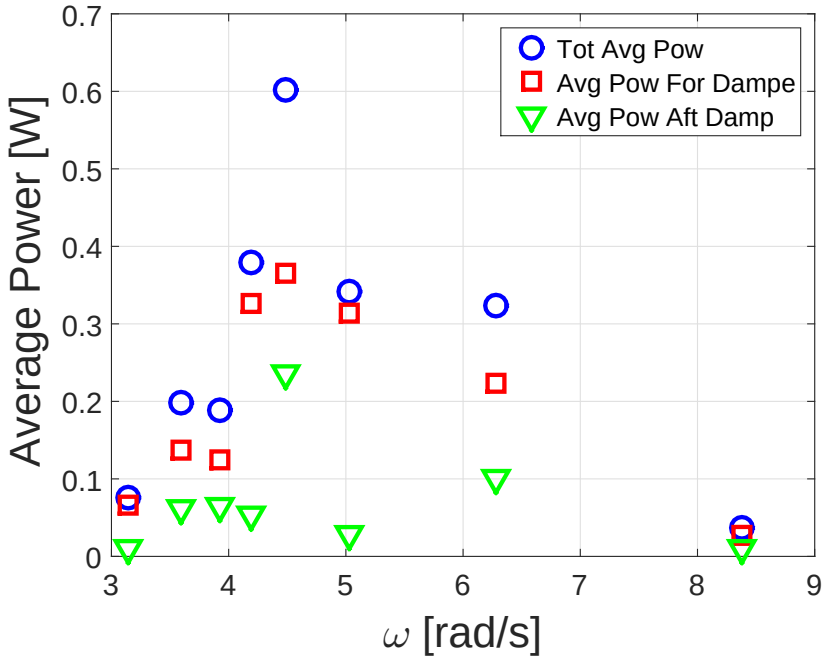

Figure 9.19: Comparison between the total average absorbed power, average power absorbed by the fore and aft damper given by the tank tests for regular waves with a frequency range from 3.14 rad/s to 8.5 rad/s and amplitude 0.025 m.

T [s]	$NMAPE_{\theta_{1,rel}}$ [%]	$NMAPE_{\theta_2}$ [%]	$NMAPE_{\theta_{3,rel}}$ [%]	$NMAPE_{F_{s,1}}$ [%]	$NMAPE_{F_{s,2}}$ [%]	PMPE [%]
0.75	23.5261	23.8350	19.0442	33.0876	22.1819	19.74
1	15.5000	19.0908	24.0543	27.5684	28.7332	0.09
1.25	16.3494	19.3872	23.6441	24.4103	28.1491	44.055
1.4	7.3792	14.9882	13.5461	14.6435	12.8080	1.82
1.5	7.2933	8.8853	8.9734	15.0864	15.1374	46.09
1.6	12.9824	11.2459	12.7194	16.5269	21.0611	113.49
1.75	6.3788	33.5234	14.9231	8.1070	12.3749	16.33
2.0	7.6201	12.0243	37.8092	11.5355	32.5675	25.2519

Table 9.1: Normalized Mean Absolute Percentage Error (NMAPE) for pitch rotation of body 2, relative pitch rotation of body 1 and 3 with respect to body 2, force damper 1 and 2, and Percentage Mean Power Error (PMPE) given by the tuned dynamic model with respect to the tank tests with regular waves.

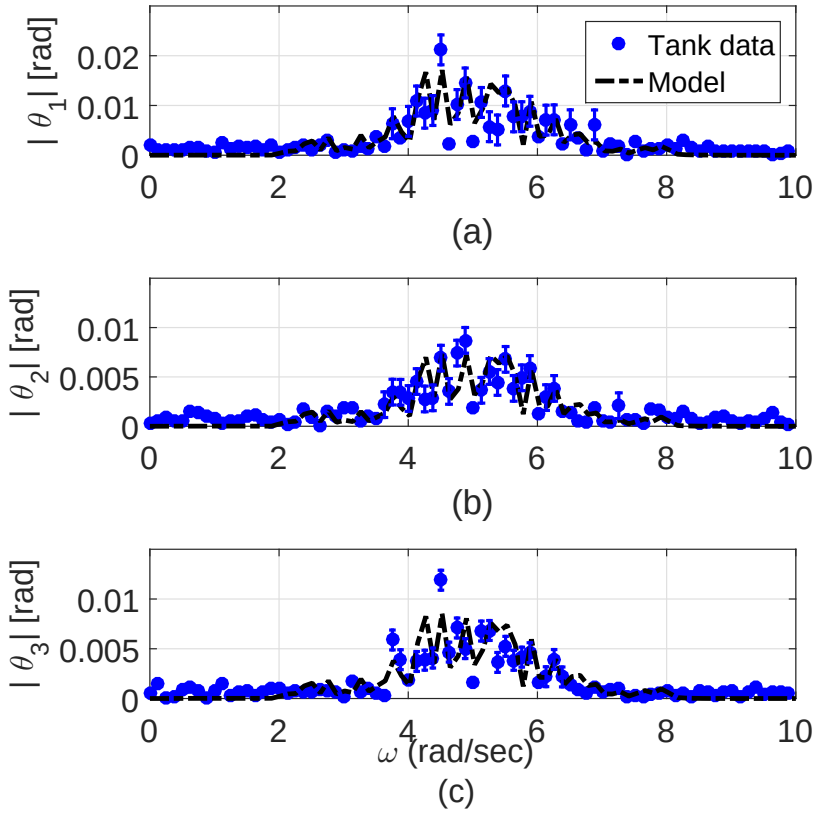

Figure 9.20: Frequency response of the pitch rotation of body 2 (b), and frequency response of the relative pitch rotation of bodies 1 (a) and 3 (c), with respect to body 2, obtained with the tank experiments with error bars for the uncertainty and tuned dynamic model with irregular wave "Irr 1".

T_p [s]	$NMAPE_{\theta_{1,rel}}$ [%]	$NMAPE_{\theta_2}$ [%]	$NMAPE_{\theta_{3,rel}}$ [%]	$NMAPE_{F_{s,1}}$ [%]	$NMAPE_{F_{s,2}}$ [%]	PMPE [%]
1.25	16.9317	17.5822	20.4850	19.3411	22.3854	15.32
1.5	15.5828	13.0110	12.9585	17.0422	16.6618	3.4

Table 9.2: Normalized Mean Absolute Percentage Error (NMAPE) for pitch rotation of body 2, relative pitch rotation of body 1 and 3 with respect to body 2, force damper 1 and 2, and Percentage Mean Power Error (PMPE) given by the tuned dynamic model, with respect to the tank tests with irregular waves.

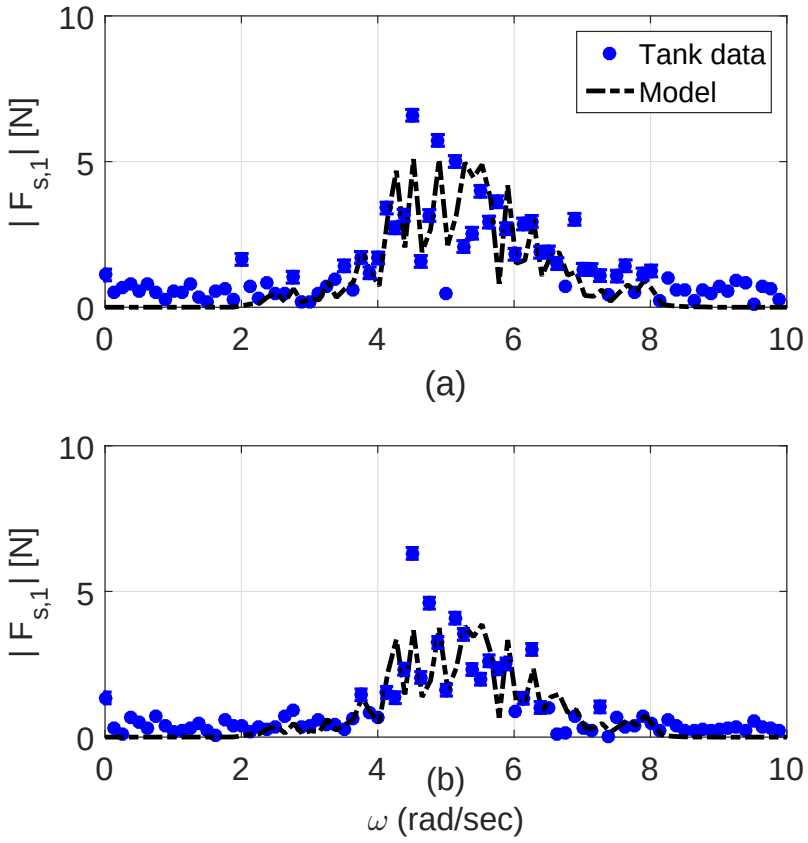

Figure 9.21: Frequency response the force of damper 1 (a) and 2 (b), with 50% opening of the flow control valves, obtained with the tank experiments with error bars for the uncertainty and tuned dynamic model with irregular wave “Irr 1”.

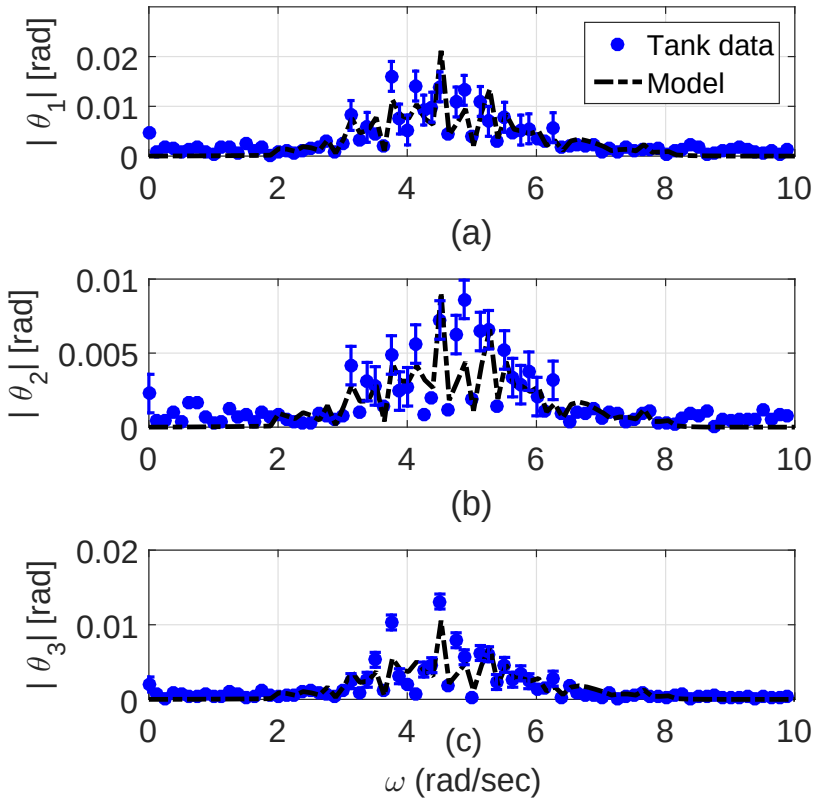

Figure 9.22: Frequency response of the pitch rotation of body 2 (b), and frequency response of the relative pitch rotation of bodies 1 (a) and 3 (c), with respect to body 2, obtained with the tank experiments with error bars for the uncertainty and tuned dynamic model with irregular wave "Irr 2".

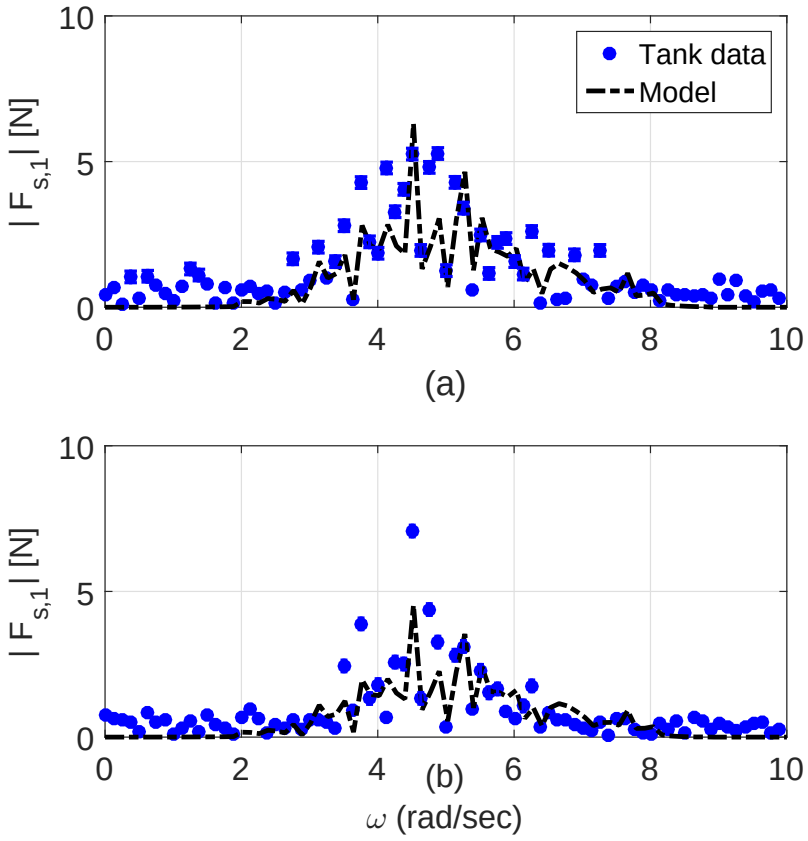

Figure 9.23: Frequency response the force of damper 1 (a) and 2 (b), with 50% opening of the flow control valves, obtained with the tank experiments with error bars for the uncertainty and tuned dynamic model with irregular wave “Irr 2”.

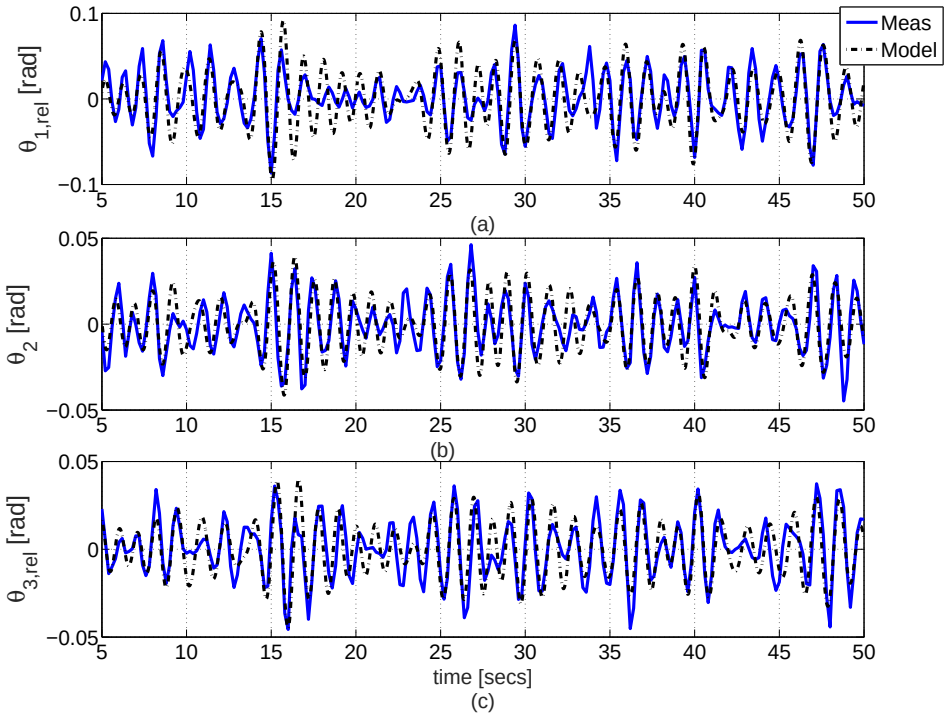

Figure 9.24: Comparison in the time domain between pitch rotation of body 2 (b), and relative pitch rotation of body 1 (a) and 3 (c) with respect to body 2, measured in tank with irregular waves "Irr 1" and computed with the tuned dynamic model.

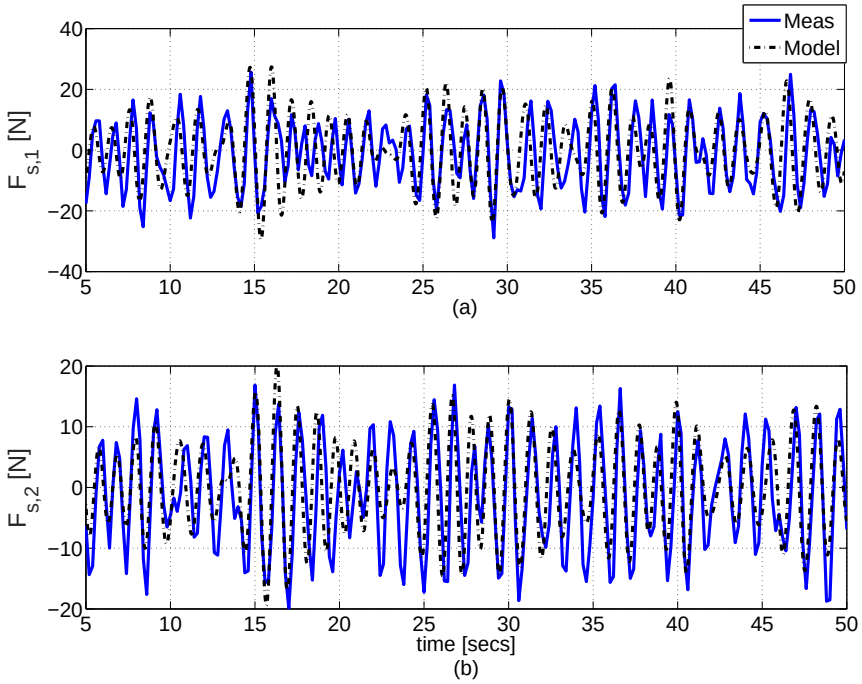

Figure 9.25: Comparison in the time domain between the force of damper 1 (a) and 2 (b), with 50% opening of the flow control valves, measured in tank with irregular waves "Irr 1" and computed with the tuned dynamic model.

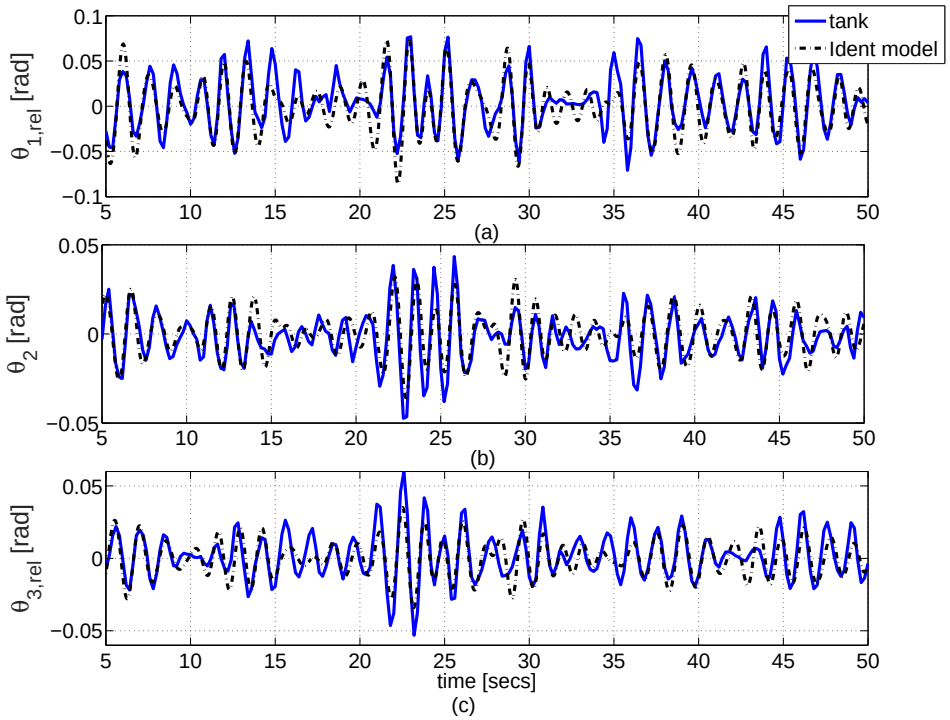

Figure 9.26: Comparison in the time domain between pitch rotation of body 2 (b), and relative pitch rotation of body 1 (a) and 3 (c) with respect to body 2, measured in tank with irregular waves "Irr 2" and computed with the tuned dynamic model.

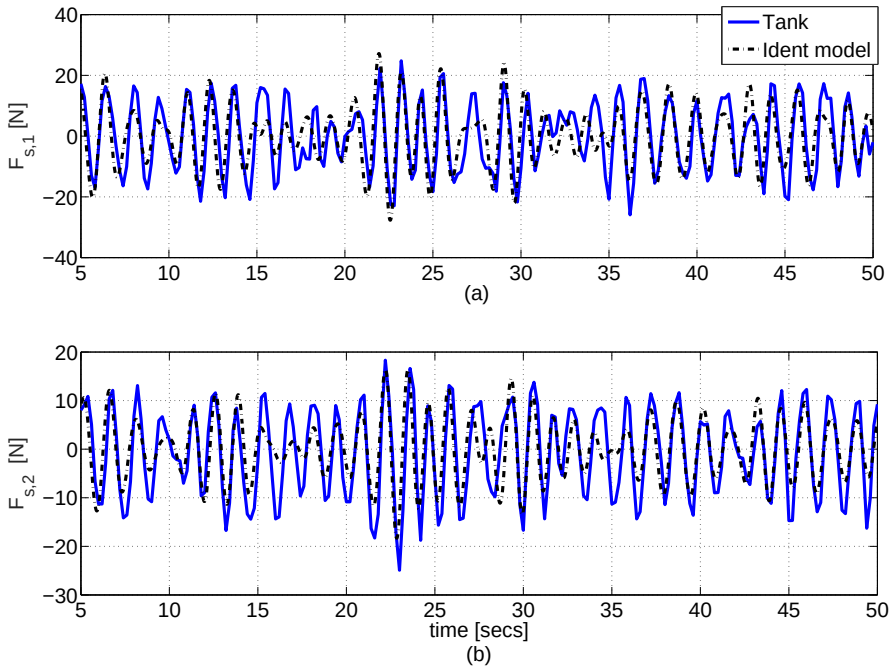

Figure 9.27: Comparison in the time domain between the force of damper 1 (a) and 2 (b), with 50% opening of the flow control valves, measured in tank with irregular waves "Irr 2" and computed with the tuned dynamic model.

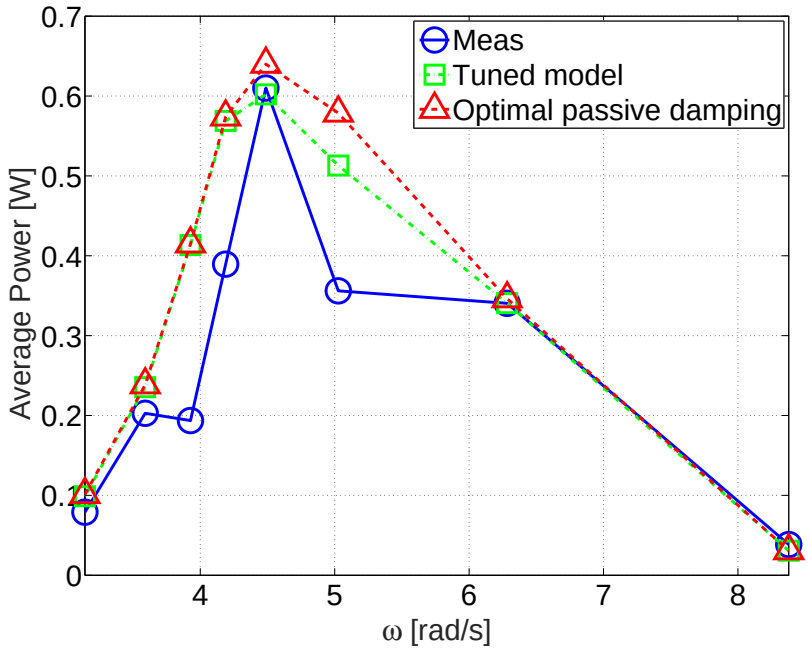

Figure 9.28: Comparison between the average absorbed power given by the tank tests, tuned dynamic model and optimal linear damping for regular waves with a frequency range from 3.14 rad/s to 8.5 rad/s and amplitude 0.025 m.

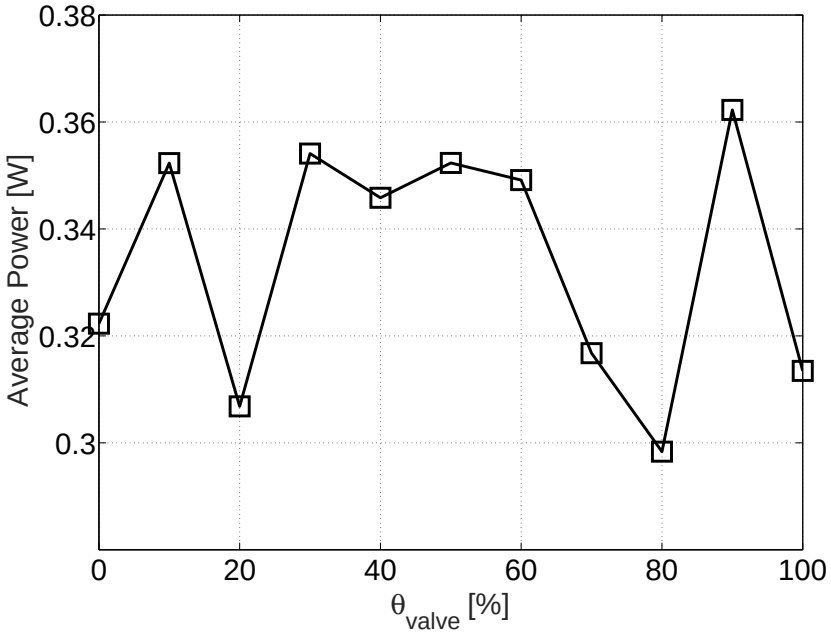

Figure 9.29: Average absorbed power given by the tank tests for different opening of the flow control valve of the fore and aft damper, for regular waves with period T=1.5 seconds and amplitude 0.025 m.

Chapter 10

Conclusions and future work

In this chapter, overall conclusions, that are derived from the research work presented in this thesis, are drawn in Section 10.1. Possible future work is also presented, in Section 10.2.

10.1 Overall conclusions

The objective of this thesis is to increase the energy that can be extracted by a three-body hinge-barge WEC using an optimal control strategy, which computes the optimal loads applied by the PTOs driven by the relative motion between the bodies. The optimal control strategy is based on a dynamic model of the WEC and, therefore, a significant part of this thesis is dedicated to the development of two dynamic modelling methodologies for multibody hinge-barge WECs. The modeling methodologies developed in this thesis are generic enough, so that they can be applied to other types of multibody WEC.

Moreover, as the power absorption performance of the optimal control strategy heavily depends on the quality of the dynamic model of the WEC, the two modeling methodologies developed in this thesis, are validated against wave-tank tests carried out on small scale multibody hinge-barge WECs. A system set-up for the wave-tank testing of a small scale three-body hinge-barge WEC is presented, which features a low-cost motion capture system. The low-cost motion capture system is designed so that it can be adopted for the wave-tank testing of other types of WECs.

Altogether, the topics treated in this thesis are characterized by a high level of variety, due to the different natures of the challenges that the optimal control of a multibody hinge-barge WEC involves. In this perspective, this thesis can be mainly divided into 4 parts:

- Dynamic modeling of a multibody hinge-barge WEC.
- Formulation of an optimal control strategy for a three-body hinge-barge WEC.
- Estimation and prediction of excitation forces acting on a three-body hinge-barge WEC.
- Wave-tank testing of a small scale three-body hinge-barge WEC.

For the dynamic modeling of a multibody hinge-barge WEC, in Chapter 3, two different modeling methodologies are developed: the DAE and ODE formulations. In order to validate the dynamic models obtained with the DAE and ODE formulations, wave-tank tests are carried out on small scale multibody hinge-barge devices. While in Chapter 3, wave-tank tests are carried out on a 1/7th scale two-body hinge-barge device and 1/25th scale three-body hinge-barge device, in Chapter 9, wave-tank tests are carried out on a 1/20th scale three-body hinge-barge device. In particular, the dynamic models of the small scale hinge-barge devices, obtained with the DAE and ODE formulations, are linearized around the equilibrium position of the WECs, and the resulting linearized dynamic models are solved with PS methods, based on Fourier basis functions. For the 1/25th and 1/20th scale three-body hinge-barge devices, an additional linearized viscous damping matrix is added into the linear dynamic models of the devices, which is tuned using a set of wave-tank tests with irregular waves.

In Chapter 3, results show that, PS methods with Fourier basis functions, applied for the solution of the linearized dynamic models of a 1/7th scale two-body hinge-barge device and 1/25th scale three-body hinge-barge, show a good agreement with the experimental tests in terms of devices motions. Also, in Chapter 9, PS methods with Fourier basis functions, applied for the solution of the linearized dynamic model of a 1/20th scale three-body hinge-barge, show good agreement with the experimental tests in terms of device motion. Therefore, it can be concluded that, for the wave conditions chosen for the wave-tank tests, a linear dynamic model represents a sufficiently accurate representation of the dynamics of a multibody-hinge barge WEC.

Moreover, results show that the linearized dynamic models of the small-scale hinge-barge WECs, obtained with ODE formulation, are equivalent representations of the linearized dynamic models of the WECs obtained with the DAE formulation. However, when nonlinearities are introduced in the dynamic models of the WECs, the DAE and ODE formulations can provide different representations of the dynamics of the WECs.

In terms of computational efficiency of PS methods based on Fourier basis functions, in Chapter 3, it is shown that, for a two-body and three-body hinge-barge device, the PS ODE formulation is superior to the PS DAE formulation in terms of computational time required to obtain the motion of the device, as the PS ODE formulation involves a smaller number of variables than the PS DAE formulation. With respect to reference methods based on the integration of the equations of motion, e.g. the Runge-Kutta (R-K) method, PS methods based on Fourier basis functions are computationally more efficient for short time steps. In fact, the computational time required by PS methods does not change for different sizes of the time step since the PS DAE and PS ODE formulations are solved with a fixed number of collocation points, and then, the solution is interpolated along the simulation time for different time steps. Therefore, the computational time required by the PS DAE and PS ODE formulations is independent of the size of the time step. Also, while the size of the time step in the R-K method must be bounded in order to guarantee stability, PS methods are naturally stable, since motion variables are composed of the sum of bounded functions.

As for the calculation of the solution to the dynamics of a three-body hinge-barge WEC, in

Chapter 4, it is shown that the optimal control problem of a three-body hinge-barge device, for a finite time horizon, can be solved using PS methods based on Fourier basis functions. In order to implement a RH real-time optimal control of a three-body hinge-barge device, that maximizes the energy extracted by the WEC over a moving control horizon, in Chapter 5, PS control based on HRCF basis functions is proposed. In contrast to Fourier basis functions, HRCF basis functions are well suited for the approximation of non-periodic signals, allowing the representation of both the transient and steady-state response of the WEC. In Chapter 5, results show that there are no computational disadvantages in using HRCF basis functions, rather than Fourier basis functions, for the formulation of the optimal control problem.

The complexity of PS optimal control based on Fourier and HRCF basis functions is greatly reduced using the reduced equivalent dynamic model presented in Chapter 4, instead of the DAE and ODE formulations, for the description of the dynamics of the device. The reduced equivalent model is described in terms of the relative pitch rotations only, which are the modes that are used to extract energy from the device. However, with the equivalent reduced dynamic model, no information on the heave and pitch rotation of the central barge is provided. Thus, with the reduced equivalent model, no constraints on the heave and absolute pitch rotation of the central barge can be enforced, as the reduced equivalent model is described in terms of the relative pitch rotations only. Therefore, the equivalent reduced dynamic model represents a less comprehensive description of the motion of the device than the ODE and DAE formulations, but considerably reduces the computational effort required for the calculation of PS optimal control with Fourier and HRCF basis functions.

Chapters 4 and 5 show that PS optimal control, based on Fourier and HRCF basis functions, can be formulated for a three-body hinge-barge WEC with either active or passive PTOs. In terms of convexity of PS active optimal control, based on Fourier and HRCF basis functions, the use of the ODE formulation for the description of the dynamics of the WEC, leads to an optimization problem with a quadratic, but non-convex, cost function. Therefore, with a non-convex quadratic cost function, a global optimal solution cannot be guaranteed. However, for PS active optimal control, based on Fourier and HRCF basis functions, the use of the reduced equivalent model yields to an optimization problem with a convex quadratic cost function, which has an unique and globally optimal solution. However, for PS passive optimal control, based on Fourier and HRCF basis functions, the use of the reduced equivalent model yields an optimization problem with a convex quadratic cost function, and quadratic, but non-convex, inequality constraints, introduced by the passivity condition of the PTOs.

In terms of power absorption performance of a 1/25th scale three-body hinge-barge device for regular waves, Chapters 4 and 5 show that PS active and passive optimal control, based on Fourier and HRCF basis functions, with the reduced equivalent model formulation, outperform a standard control strategy based on optimal linear damping coefficients for the PTOs. For regular waves, PS active optimal control, based on Fourier and HRCF basis functions, with the reduced equivalent model formulation, guarantees an average absorbed power which is the same as the theoretical maximum power that can be absorbed by the complex-conjugate control. Furthermore, for regular

waves, the optimal torques and relative pitch velocities computed by PS active optimal control, based on HRCF basis functions, converge to the optimal torques and relative pitch velocities computed by PS active optimal control, based on Fourier basis functions. In fact, if the dynamic model of the device is linear, and the incoming wave is monochromatic, the solution to the active control problem is unique.

In contrast to the case with regular waves, for irregular waves, although the average absorbed power computed by PS active optimal control, based on HRCF and Fourier basis functions, is the same as the theoretical maximum power that can be absorbed by the complex-conjugate control, the optimal trajectories of the relative velocities and torques computed by PS active optimal control based on HRCF basis functions, are different from the optimal trajectories of the relative velocities and torques computed by PS active optimal control based on Fourier basis functions.

For both regular and irregular waves, the average absorbed by PS passive optimal control, based on Fourier basis functions, is greater than the average absorbed by PS passive optimal control, based on HRCF basis functions. The discrepancy between the average absorbed power for PS passive optimal control based on Fourier basis functions, and the absorbed power for PS passive optimal control based on HRCF basis functions, is due to the nonconvexity of the passive control problem, which does not guarantee an unique solution to the optimization problem. Furthermore, for both regular and irregular waves, the optimal torques and relative pitch velocities computed by PS passive optimal control, based on HRCF basis functions, do not converge to the optimal torques and relative pitch velocities computed by PS passive optimal control, based on Fourier basis functions. However, for regular waves, the optimal trajectories of positions, velocities and control torques computed by PS passive optimal control, based on HRCF and Fourier basis functions, show a similar phase delay, with a difference between their peak values.

In terms of real-time control of passive PTOs, in Chapters 5, it is shown that the computational time required by PS optimal passive control, based HRCF basis functions, is around 1-2 seconds, using interpreted (not compiled) Matlab code. A computational time of 1-2 seconds is acceptable for the control of a full scale three-body hinge-barge device. However, for the control of a small scale three-body hinge-barge device, a computational time of 1-2 seconds is well beyond the maximum computational time available to the real-time controller of the device, which is around 50-100 *ms*.

Regarding the estimation of the excitation forces acting on a three-body hinge-barge device, in Chapter 6, two different types of estimator, are presented: feedback and feedforward. While the feedback estimator only requires information on the motion of the device, the feedforward estimator requires the information of both the motion of the device and wave elevation up-wave of the device. Therefore, the feedback estimator is simpler to implement than the feedforward estimator, as only motion sensors deployed on the device are required, without the need to deploy a wave gauge for the measurement of the wave elevation up-wave of the device. Also, the complicating effects of multi wave directionality have to be taken into account in the implementation of the feedfoward estimator. Furthermore, for the feedforward estimator, a long observation time of the motion of the device and wave elevation up-wave of the device is needed in order to achieve a fine

frequency resolution of the transfer function of the excitation forces, which guarantees accurate estimation of the excitation forces. Results of the feedback and feedforward estimator, applied to a 1/25th scale three-body hinge-barge device, for the estimation of the excitation forces, show that the feedforward estimator performs slightly better than the feedback estimator, with an accuracy of the estimation that is 20% higher than the accuracy of the estimation given by the feedback estimator. However, both estimators are based on perfect knowledge of the dynamic model of the device. It is expected that, in a more realistic scenario, where the knowledge of the parameters of the dynamic model is affected by a certain degree of uncertainty, the feedback estimator is likely to perform better than the feedforward estimator. In fact, the feedback estimator is naturally robust to uncertainty in the parameters of the dynamic model, as the feedback on the position and velocity of the device corrects the estimates of the excitation forces computed based on the dynamic model of the device only. In contrast, the feedforward estimates the excitation forces purely on the basis of the dynamic model of the device. Therefore, a small variation of the parameters of the dynamic model of the device could potentially lead to a large decrease of the performance of the feedforward estimator.

In Chapter 7, a system set-up for wave-tank testing of a 1/20th scale three-body hinge-barge WEC, is presented for the experimental validation of a control strategy based on optimal damping coefficients of the hydraulic dampers. The flow of the hydraulic fluid, in each hydraulic damper, is regulated using a flow control valve, whose opening is controlled with a stepper motor. The force exerted by each hydraulic damper on the device is measured using a load cell, and the damping force can be changed by varying the opening of the flow control valve. The wave-tank tests presented in Chapter 9, show that, for the particular dampers used in the system set-up presented in Chapter 7, a control strategy based on optimal linear damping coefficients, does not provide any significant increase of the average power absorbed by the device due to the small variation of the damping force of the fore and aft damper, for different values of the opening of the control valves. PS methods with HRCF basis functions, for real-time control of the damping forces of the hydraulic dampers, could not be implemented due to the high computational time required to solve the optimal control problem, and the slow dynamic response of the stepper motors for the control valves, which only allows a maximum variation of the opening of the valve of 10%, in real-time. Obviously, a maximum variation of the opening of the valve of 10% greatly reduces the power absorption that can be achieved by real-time control, with respect to the control strategy based on optimal constant damping for the dampers.

In summary, from the research work presented in this thesis, the following conclusions and recommendations can be drawn:

- A three-body hinge-barge WEC, with no control applied, extracts energy from the waves over a frequency range which is broader than the frequency range of a point absorber. Therefore, for a sea-state characterized by a broad spectral distribution, a three-body hinge-barge WEC is likely to perform better than a point absorber.

- The wave-tank tests carried out on a small scale three-body hinge-barge device show that

the motion of the fore barge is larger than the motion of the central and aft barges, with most of the energy extracted by the fore damper. Thus, the WEC behaves more like a two-body hinge-barge device, rather than a three-body hinge-barge device. Furthermore, the wave-tank tests show that the inclusion of a damping plate in the design of a three-body hinge-barge device does not seem necessary, as the damping plate does not extend the frequency bandwidth over which the maximum power absorption is realized. However, further numerical and experimental studies are required to better assess the value of the damping plate for a three-body hinge-barge device.

- For a three-body hinge-barge WEC with passive PTOs, a control strategy, based on optimal linear damping coefficients of the PTOs, does not show any significant increase of the absorbed power, with respect to a strategy based on non-optimal damping coefficients. On the other hand, the application of PS optimal control, which adjusts the damping forces of the PTOs, in real-time, shows great benefits in terms of absorbed power, with a power absorption performance that is comparable to reactive control. Therefore, the need to resort to expensive active PTOs, can be obviated with the use passive PTOs whose damping forces are changed, in real-time, with PS optimal control.

- The computational time required by PS optimal control to change both the damping forces exerted by passive PTOs of a three-body hinge-barge WEC, is far beyond the maximum computational time allowed for real-time control. Given that the WEC behaves more like a two-body hinge-barge WEC, rather than a three-body hinge-barge WEC, PS optimal control can be implemented, in real-time, if only the damping force of the fore damper is controlled, and the damping of the aft damper is constant and set to its optimal value.

- The development of a good dynamic model for a hinge-barge WEC represents a challenging task, due to the complex hydrodynamic and kinematic interactions between the bodies. A linear dynamic model represents a suitable choice for a hinge-barge WEC, as it allows to tune a linearized viscous damping matrix to fit the response of the dynamic model to the wave-tank tests, using the frequency response between the incoming wave elevation and the device motion. Also, the use of a linear dynamic model greatly reduces the computation effort required by PS optimal control. It is expected that PS optimal control would be sensitive to modelling errors on the excitation, radiation and viscous damping forces, since that the condition for maximum power absorption, under reactive control, involves the excitation, radiation and viscous damping forces.

10.2 Future work

The research presented in this thesis highlights possible future work, that can be addressed in order to advance the development of a real-time optimal controller of a multibody hinge-barge device. Given the variety of the topics treated in this thesis, possible work on both the theoretical and

experimental aspect of this thesis, can be undertaken in the future. In particular, possible future theoretical work can be:

- Development of nonlinear hydrodynamic models for multibody hinge-barge WECs that accurately represent the dynamic behavior of the WEC under large wave amplitudes.
- Reduction of the computational effort required by PS passive optimal control using a computationally more efficient formulation of the control problem.
- Design of a Multi-Input Multi-Output (MIMO) low-level control, for a multi-body hinge-barge device, that tracks the optimal reference velocity computed by PS optimal control, considering all the interactions between the control forces and the motion coordinates of the device.
- Study of the effects of the prediction errors of the excitation forces acting on a multi-body hinge-barge WECs, on the optimal control strategy.

Possible future experimental work includes:

- Deployment of an optical motion capture system, instead of ultrasound sensors and IMU, for the wave-tank testing of small scale WECs.
- Deployment of stepper motors with a faster rotational speed than the stepper motors presented in this thesis, for real-time control of the damping forces of the hydraulic dampers of a 1/20th scale three-body hinge-barge device.
- Deployment of hydraulic dampers, for a 1/20th scale three-body hinge-barge device, that allow a greater range of damping force than the range of the damping force of the hydraulic dampers used in this thesis.
- Design of an active PTO, for a 1/20th scale three-body hinge-barge device, allowing an increase in the power absorption of the device, with respect to simple hydraulic dampers with adjustable damping force. Such active PTO would likely be electromechanical, with a facility for bi-directional power flow.
- Reduction of the computational time required by PS passive optimal control by implementation of the PS passive control problem in a computationally faster language than Matlab such as, for example, the C-language.

Bibliography

[1] ExxonMobil, "The outlook for energy: a view to 2040," tech. rep., Exxonmobi, 2012.

[2] Lopez, I., Andreu, J., Ceballos, S., Martnez de Alegra, I., and Kortabarria, I., "Review of wave energy technologies and the necessary power-equipment," *Elsevier, Renewable and Sustainable Energy Reviews*, vol. 27, pp. 413–434, 2013.

[3] Drew, B., Plummer, A., and Sahinkaya, M., "A review of wave energy converter technology," *Proceedings of the Institution of Mechanical Engineers, Part A: Journal of Power and Energy*, vol. 223, no. 8, pp. 887–902, 2009.

[4] Astariz, S. and Iglesias, G., "The economics of wave energy: A review," *Elsvier, Renewable and Sustainable Energy Reviews*, vol. 45, pp. 397–408, 2015.

[5] Falcão, A., "Wave energy utilization: A review of the technologies," *Renewable and Sustainable Energy Reviews*, vol. 14, no. 3, pp. 899–918, 2010.

[6] Gieske, P., "Model predictive control of a wave energy converter: Archimedes wave swing," Master's thesis, Delft University of Technology, Netherlands, 2007.

[7] Yemm, R., Pizer, D., Retzler, C., and Henderson, R., "Pelamis: experience from concept to connection," *Philosophical Transactions of the Royal Society A*, vol. 370, pp. 365–380, 2012.

[8] Titah-Benbouzid, H. and Benbouzid, M., "Ocean wave energy extraction: Up-to-date technologies review and evaluation," in *Proc. of 2014 International Power Electronics and Application Conference and Exposition, Shanghai*, pp. 338–342, 2014.

[9] Ringwood, J.V., Bacelli, G., and Fusco, F., "Energy maximising control of wave energy converters," *IEEE Control Systems Magazine*, vol. 34, no. 5, pp. 30–55, 2014.

[10] J. Falnes, *Ocean Waves and Oscillating Systems*. Cambridge, U.K.: Cambridge University Press, 2002.

[11] Fusco, F. and Ringwood, J.V., "A simple and effective real-time controller for wave energy converters," *IEEE Transactions on Sustainable Energy*, vol. 4, no. 1, pp. 21–30, 2013.

[12] F. Fusco and J. V. Ringwood, "A study on the prediction requirements in real-time control of wave energy converters," *IEEE Transactions on Sustainable Energy*, vol. 3, no. 1, pp. 176–184, 2012.

[13] Polinder, H., Mueller, M.A., Scuotto, M., and Goden de Sousa Prado M., "Linear generator systems for wave energy conversion," in *Proc. of 7th European Wave and Tidal Energy Conference, Porto, Portugal*, 2007.

[14] Costello, R., Weber, J., and Ringwood, J.V., "Comparison of two alternative hydraulic PTO concepts for wave energy generation," in *Proc. 9th European Wave and Tidal Energy Conference (EWTEC), Southampton, UK.*, 2011.

[15] Retes, M. P., Giorgi, G., and Ringwood, J. V., "A review of non-linear approaches for wave energy converter modelling," in *Proc. 11th European Wave and Tidal Energy Conference, Nantes, France*, 2015.

[16] Penalba, M., Sell, N., Hillis, A., and Ringwood, J. V., "Validating a wave-to-wire model for a wave energy converter - part i: The hydraulic transmission system," *Submitted to Energies*, 2017.

[17] Kraemer, D., *The motion of hinged-barge systems in regular seas*. PhD thesis, Johns Hopkins University, Baltimore, Maryland, USA, 2001.

[18] Henderson, R., "Design, simulation, and testing of a novel hydraulic power take-off system for the Pelamis wave energy converter," *Renewable Energy*, vol. 31, no. 2, pp. 271–283, 2006.

[19] Moore, R., Murtagh, C., and Elsaesser, B., "Design optimisation of an attenuator wave energy converter," in *Proc. of the 11th European Wave and Tidal Energy Conference, Nantes, France*, 2015.

[20] Sea Power Ltd (2008), "Sea Power Ltd Official Website." [online] Available at: http://www.seapower.ie. [Accessed 20 March 2017].

[21] Mocean Energy (2015), "Mocean Energy Official Website." [online] Available at: http://www.moceanenergy.com/. [Accessed 20 March 2017].

[22] Taylor, R. E. , Taylor, P.H., and Stansby, P.K., "A coupled hydrodynamicstructural model of the M4 wave energy converter," *Elsevier, Journal of Fluids and Structures*, vol. 63, pp. 77–96, 2016.

[23] Stansby, P., Carpintero Moreno, E., Stallard, T., and Maggi, A., "Three-float broad-band resonant line absorber with surge for wave energy conversion," *Elsevier, Renewable Energy*, vol. 78, pp. 132 – 140, 2015.

[24] Costello, R., Boris, T., and Ringwood, J.V., "Techno-economic optimisation for wave energy converters," in *Proc. of the 4th International Conference on Ocean Energy, Dublin, Ireland*, 2012.

[25] Massachusetts Institute of Technology, USA, *WAMIT User Manual Version 7.0*.

[26] Padeletti, D., Costello, R., and Ringwood, J.V., "A multi-body modelling approach for wave energy converters employing nonlinear joint representation," in *Proc. of the ASME 2014 33rd International Conference on Ocean, Offshore and Arctic Engineering, San Francisco, California, USA*, 2014.

[27] Faltinsen, O. M., *Sea loads on ships and offshore structures*. Cambridge University Press, 1990.

[28] Ó'Catháin, M., Leira, B. J., Ringwood, J. V. , and Gilloteaux, J.-C. , "A modelling methodology for multi-body systems with application to wave-energy devices," *Ocean Engineering*, vol. 35, no. 13, pp. 1381–1387, 2008.

[29] Ó'Catháin, M., "Modelling of multibody marine systems," Master's thesis, Deparment of Electronic Engineering, NUI Maynooth, 2007.

[30] Mackay, E., Cruz, J., Retzler, C., Arnold, P., Bannon, E., and Pascal, R., "Validation of a new wave energy converter design tool with large scale single machine experiments," in *Proc. of 1st Asian Wave and Tidal Conference Serie, Jeju, Korea*, 2012.

[31] Rongère, F. and Clément, A., "Systematic dynamic modeling and simulation of multibody offshore structures: Application to wave energy converters," in *Proc. of the ASME 2013 32nd International Conference on Ocean, Offshore and Arctic Engineering, Nantes, France*, 2013.

[32] Taylor, E. R. and Zietsman, J., "A comparison of localised finite element formulations for two dimensional wave diffraction and radiation problems," *International Journal of Numerical Methods in Engineering*, vol. 17, no. 9, pp. 1355–1384, 1981.

[33] Øyvind Ygre Rogne, *Numerical and Experimental investigation of a hinged 5-body wave energy converter*. PhD thesis, Norwegian University of Science and Technology, Faculty of Engineering Science and Technology, Department of Marine Technology, 2014.

[34] Brodtkorb, P.A., Johannesson, P., Lindgren, G., Rychlik, I., Rydn, J., and Sj, E., "WAFO - a Matlab toolbox for analysis of random waves and loads," in *Proc. 10th Int. Offshore and Polar Eng. Conf., Seattle, USA.*, vol. 3, pp. 343 – 350, 2000.

[35] Gear, C. W., Leimkuhler, B., and Gupta G. K., "Automatic integration of Euler-Lagrange equations with constraints," *J. Comput. Appl. Math.*, vol. 12&13, pp. 77–90, 1985.

[36] Maggi, G. A., *Principii della Teoria Matematica del Movimento Dei Corpi: Corso di Meccanica Razionale*. Ulrico Hoepli, 1896.

[37] Laulusa, A. and Bauchau, O. A., "Review of classical approaches for constraint enforcement in multibody systems," *Journal of Computational and Nonlinear Dynamics*, vol. 3, p. 011004 (8 pages), January 2008.

[38] Neimark, J. I. and Fufaev, N. A., *Dynamics of Nonholonomic Systems*. American Mathematical Society, Providence, RI, 1972.

[39] Hemami, H. and Weimer, F. C., "Modeling of nonholonomic dynamic systems with applications," *ASME J. Appl. Mech.*, vol. 48, pp. 177–182, 1981.

[40] Udwadia, F. E., Kalaba, R. E., and Eun, H. C., "Equations of motion for constrained mechanical systems and the Extended D'Alembert's Principle," *Q. Appl. Math.*, vol. 55, no. 2, pp. 321–331, 1997.

[41] García de Jalón, J., Unda, J., Avello, A., and Jiménez, J. M., "Dynamic analysis of three-dimensional mechanisms in "Natural" coordinates," *ASME J. Mech., Transm., Autom. Des.*, vol. 109, pp. 460–465, 1987.

[42] Unda, J., García de Jalón, J., J., Losantos, F., and Enparantza, R., "A comparative study on some different formulations of the dynamic equations of constrained mechanical systems," *ASME J. Mech., Transm., Autom.Des.*, vol. 109, pp. 466–474, 1987.

[43] Orlandea, N., Chace, M. A., and Calahan, D. A., "A sparsity-oriented approach to the dynamic analysis and design of mechanical systems. Part slowromancapi@," *ASME J. Eng. Ind.*, vol. 99, no. 3, pp. 773–779, 1977.

[44] Orlandea, N., Calahan, D. A., and Chace, M. A., "A sparsity-oriented approach to the dynamic analysis and design of mechanical systems. Part slowromancapii@," *ASME J. Eng. Ind.*, vol. 99, no. 3, pp. 780–784, 1977.

[45] Canuto, C., Hussaini, Y., Quarteroni, A., and Zang, T., *Spectral Methods: Fundamentals in Single Domains*. Springer, 2006.

[46] Fornberg, B., *A Practical Guide to Pseudospectral Methods*. Cambridge University Press, 1996.

[47] Bacelli, G. and Ringwood, J.V., "Numerical optimal control of wave energy converters," *IEEE Transactions on Sustainable Energy*, vol. 6, no. 2, pp. 294–302, 2015.

[48] Fossen, T. I., *Handbook of marine craft hydrodynamics and motion control*. Wiley, 2011.

[49] Ó'Catháin, M., Fossen, T. I., and Leira, B. , "Control-oriented modeling of a 2-body interconnected marine structure," in *Proc. of the IFAC MCMC'06, Lisbon, Portugal*, 2006.

[50] Shabana, A. A., *Dynamics of multibody systems*. Cambridge University Press, 2005.

[51] Ogilvie, T., "Recent progress toward the understanding and prediction of ship motions," in *Proc. of 5th Symposium on Naval Hydrodynamics, Bergen, Norway.*, 1964.

[52] Elnagar, G., Kazemi, M. A., and Razzaghi, M., "The Pseudospectral Legendre method for discretizing optimal control problems," *IEEE Transactions on Automatic Control*, vol. 40, no. 10, 1995.

[53] Ross, I. M. and Karpenko, M., "A review of pseudospectral optimal control: From theory to flight," *Annual Reviews in Control*, vol. 36, no. 2, pp. 182–197, 2012.

[54] Perez, T. and Fossen, T. I., "A Matlab Toolbox for Parametric Identification of Radiation-Force Models of Ships and Offshore Structures," *Modeling, Identification and Control*, vol. 30, no. 1, pp. 1–15, 2009.

[55] Paulmeno, A., "An Experimental Analysis of the Optimal Design Conditions for a Model Scale McCabe Wave Pump," independent research in ocean engineering honors final report, Department of Naval Architecture and Ocean Engineering, United States Naval Academy Annapolis, Maryland 21402, May 2013.

[56] Genest, R., *Développement et validation expérimentale de stratégies de contrôle des récupérateurs de l'énergie des vagues*. PhD thesis, École centrale de Nantes, 2015.

[57] F. Fusco and J. V. Ringwood, "A study on the prediction requirements in real-time control of wave energy converters," *IEEE Transactions on Sustainable Energy*, vol. 3, no. 1, pp. 176–184, 2012.

[58] Genest, R. and Ringwood, J.V., "A critical comparison of model-predictive and pseudospectral control for wave energy devices," *Journal of Ocean Engineering and Marine Energy*, vol. 2, no. 4, pp. 1–15, 2016.

[59] Herber, D.R. and Allison, J.T. , "Wave energy extraction maximization in irregular ocean waves using pseudospectral methods," in *Proceedings of the ASME 2013 International Design Engineering Technical Conferences and Computers and Information in Engineering Conference IDETC/CIE, Portland, Oregon, USA*, 2013.

[60] S. Salter, "Power conversion systems for ducks," in *Proc. of International Conference on Future Energy Concepts*, pp. 100–108, 1979.

[61] P. Nebel, "Maximizing the efficiency of wave-energy plant using complex-conjugate control," in *Proc. of the Institution of Mechanical Engineers, Part I: Journal of Systems and Control Engineering*, vol. 206, pp. 225–236, 1992.

[62] Hals, J., Bjarte-Larsson, T., and Falnes, J., "Optimum reactive control and control by latching of a wave-absorbing semisubmerged heaving sphere.," in *ASME. International Conference on Offshore Mechanics and Arctic Engineering, 21st International Conference on Offshore Mechanics and Arctic Engineering.*, vol. 4, pp. 415–423, 2002.

[63] Clement, A. and Maisondieu, C., "Comparison of time domain control law for a piston wave absorber," in *Proc. of European Wave Energy Symposium, UK.*, pp. 117–122, 1993.

[64] Fusco, F. and Ringwood, J.V., "Suboptimal causal reactive control of wave energy converters using a second order system model," in *Proc. of 21st International Offshore (Ocean) and Polar Engineering Conference (ISOPE)*, 2011.

[65] Lattanzio, S. and Scruggs, J., "Maximum power generation of a wave energy converter in a stochastic environment," in *Proc. of Control Applications (CCA), 2011 IEEE International Conference*, pp. 1125 –1130, 2011.

[66] Scruggs, J., Lattanzio, S., Taflanidis, A. A., and Cassidy, I.L. , "Optimal causal control of a wave energy converter in random sea," *Applied Ocean Research*, vol. 42, pp. 1–15, 2013.

[67] Nielsen, S.R.K, Zhou, Q., Kramer, M.M., Basu, B., and Zhang, Z., "Optimal control of nonlinear wave energy point converters," *Ocean Engineering*, vol. 72, pp. 176–187, 2013.

[68] Budal, K. and Falnes, J., "Apparatus for utilising or absorbing wave energy," Britih Patent No 1587344, 1978.

[69] Guenther, D.A., Jones, D., and Brown, D.G., "An investigative study of a wave-energy device," *Energy*, vol. 4, pp. 299–306, 1979.

[70] French, M.J. , "A generalized view of resonant energy transfer," *Journal Mechanical Engineering Science*, vol. 21, pp. 299–300, 1979.

[71] Babarit, A., Guglielmi, M., and Clement, A., "Declutching control of a wave energy converter," *Ocean Engineering*, vol. 36, no. 12, pp. 1015–1024, 2009.

[72] Garcia-Rosa, P. B. and Ringwood, J. V., "On the sensitivity of optimal wave energy device geometry to the energy maximizing control system," *IEEE Trans. on Sustainable Energy*, vol. 7, no. 1, pp. 419–426, 2016.

[73] Clement, A.H. and Babarit, A., "Discrete control of resonant wave energy devices," *Philosophical Transactions of the Royal Society A: Mathematical,Physical and Engineering Sciences*, vol. 370, no. 1959, pp. 288–314, 2012.

[74] Evans, D. V., "Maximum wave-power absorption under motion constraints," *Applied Ocean Research*, vol. 3, no. 4, 1981.

[75] Backer, G. D., Vantorre, M., Banasiak, R., Rouck, J. D., Beels, C., and Verhaeghe, H., "Performance of a point absorber heaving with respect to a floating platform," in *Proceedings of the 7th European Wave and Tidal Energy Conference, Porto, Portugal*, 2007.

[76] Hals, J., Falnes, J., and Moan, T., "Constrained optimal control of a heaving buoy wave-energy converter," *J. Offshore Mech. Arct. Eng.*, vol. 133, pp. 0114011–01140115, 2011.

[77] Cretel, J. A. M. , Lightbody, G., Thomas, G.P., and Lewis, A.W., "Maximisation of energy capture by a wave-energy point absorber using model predictive control," in *Proc. of IFAC World Congress*, 2011.

[78] Tom, N. and Yeung, R.W., "Non-linear model predictive control applied to a generic ocean-wave energy extractor," in *Proc. of 32nd International Conference on Ocean, Off-shore and Arctic Engineering (OMAE2013)*, 2013.

[79] Richter, M., Magana, M., Sawodny, O., and Brekken, T., "Nonlinear model predictive control of a point absorber wave energy converter," *IEEE Trans. on Sustainable Energy*, vol. 4, no. 1, pp. 118–126, 2013.

[80] Genest, R. and Ringwood, J.V., "Receeding horizon pseudospectral control for energy maximisation with application to wave energy devices," *IEEE Transactions on Control System Technology*, vol. 25, no. 1, pp. 29 – 38, 2016.

[81] G. Li., "Nonlinear model predictie control of a wave energy converter based on difdifferent flatness parametrization," *Internation Journal of Control*, pp. 1–10, 2015.

[82] Babarit, A., *Optimisation hydrodynamique et controle optimal dun recuperateur de lenergie des vagues*. PhD thesis, École centrale de Nantes, 2005.

[83] Olaya, S., Bourgeot, J. M., and Benbouzid, M., "Optimal control for a self-reacting point absorber: A one-body equivalent model approach," in *Proc. of Power Electronics and Application Conference and Exposition (PEAC)*, 2014.

[84] Gill, P. E., Murray, W., and Wright, M.H., *Practical Optimization*. Academic Press, 1981.

[85] Boyd, S. and Vandenberghe, L., *Convex Optimization*. Cambridge University Press, 2004.

[86] Byrd, R. H., Gilbert, J. C., and Nocedal, J., "A trust region method based on interior point techniques for nonlinear programming,," *Mathematical Programming*, vol. 89, no. 1, pp. 149–185, 2000.

[87] Tedeschi, E., Carraro, M., Molinas, M., and Mattavelli, P., "Effect of control strategies and power take-off efficiency on the power capture from sea waves," *IEEE TRANSACTIONS ON ENERGY CONVERSION*, vol. 26, no. 4, pp. 1088–1098, 2011.

[88] Genest, R., Bonnefoy, F., Clément, A. H., and Babarit, A., "Effect of non-ideal power take-off on the energy absorption of a reactively controlled one degree of freedom wave energy converter," *Applied Ocean Research*, vol. 48, pp. 236–243, 2014.

[89] Cretel, J., Lewis, A.W., Lightbody, G., and Thomas, G.P., "An application of model predictive control to a wave energy point absorber," in *Proc. of IFAC conference on Control Methodologies and Technology for Energy Efficiency*, vol. 43, pp. 267–272, 2010.

[90] D. Huybrechs, "On the fourier extension of nonperiodic functions," *SIAM J. Numer. Anal.,*, vol. 47, no. 6, pp. 4326–4355, 2010.

[91] Orel, B. and Perne, A., "Computations with half-range chebyshev polynomials," *J. Comput. Appl. Math.*, vol. 236, no. 7, pp. 1753–1765, 2012.

[92] Morari, M. and Evanghelos, Z., *Robust Process Control*. Englewood Cliffs, NJ: Prentice-Hall, 1989.

[93] Sa de costa, J., Beirao, P., and Valerio, D., "Internal model control applied to the archimedes wave swing," in *Proc. 16th Int. Conf. Control Systems and Computer Science (CSCS), Bucharest, Romania*, 2007.

[94] Kokotovi, P. V., "The joy of feedback: Nonlinear and adaptive," *IEEE Control Syst.*, vol. 12, no. 3, pp. 7–17, 1992.

[95] Falnes, J., "A review of wave-energy extraction," *Marine Structures*, vol. 20, no. 4, pp. 185–201, 2007.

[96] Fusco, F. and Ringwood, J.V., "A Model for the Sensitivity of Non-Causal Control of Wave Energy Converters to Wave Excitation Force Prediction Errors," in *Proc. 9th European Wave and Tidal Energy Conference (EWTEC)*, 2011.

[97] Bacelli, G., Balitsky, P., and Ringwood, J.V., "Coordinated control of arrays of wave energy devices benefits over independent control," *IEEE Transactions on Sustainable Energy*, vol. 4, no. 4, pp. 1–9, 2013.

[98] Falcão, A., "Phase control through load control of oscillating-body wave energy converters with hydraulic PTO system," *Ocean Engineering*, vol. 35, no. 3, pp. 358–366, 2008.

[99] Newman, J. N., *Marine Hydrodynamics*. 1977.

[100] Abdelkhalik ,O., Zou, S., Bacelli, G., Robinett, R.D., Wilson, D.G., and Coe, R.G., "Estimation of excitation force on wave energy converters using pressure measurements for feedback control," in *OCEANS 2016 MTS/IEEE Monterey*, 2016.

[101] Abdelrahman, M., Patton, R., Guo, B., and Lan, J., "Estimation of wave excitation force for wave energy converters," in *2016 3rd Conference on Control and Fault-Tolerant Systems (SysTol)*, pp. 654–659, 2016.

[102] Jiang, B., Staroswiecki, M., and Cocquempot, V., "Fault accommodation for nonlinear dynamic systems," *IEEE Transactions on Automatic Control*, vol. 51, no. 9, pp. 1578 – 1583, 2006.

[103] Ling, B.A. and Batten, B.A. , "Real time estimation and prediction of wave excitation forces on a heaving body," in *ASME 2015 34th International Conference on Ocean, Offshore and Arctic Engineering*, vol. 9: Ocean Renewable Energy, 2015.

[104] Brask, A. K., "Control and estimation of wave energy converters," Master's thesis, Norwegian University of Science and Technology, Department of Marine Technology, 2015.

[105] F. Fusco and J. V. Ringwood, "Short-term wave forecasting for real-time control of wave energy converters," *IEEE Transactions on Sustainable Energy*, vol. 1, pp. 99–106, July 2010.

[106] B. Fischer, P. Kracht, and S. Perez-Becker, "Online-algorithm using adaptive filters for short-term wave prediction and its implementation," in *Proc. International Conference on Ocean Energy*, 2012.

[107] M. P. Schoen, J. Hals, and T. Moan, "Wave prediction and robust control of heaving wave energy devices for irregular waves," *IEEE Transactions on Energy Conversion*, vol. 26, no. 2, pp. 627–638, 2011.

[108] A. Price and A. Wallace, "Non-linear methods for next wave estimation," in *Proc. 7th European Wave and Tidal Energy Conference*, 2007.

[109] Lewis, F.L., Xie, L., and Popa, D., *Optimal and Robust Estimation*. CRC Press, 2nd ed., 2008.

[110] D. S. Shook, C. Mohtadi, and S. Shah, "Identification for long-range predictive control," in *Proc. Inst. Elect. Eng., D Control Theory and Applications*, vol. 138, pp. 75–84, 1991.

[111] K. Monk, D. Conley, M. Lopes, and Q. Zou, "Pneumatic power regulation by wave forecasting and real-time relief valve control for an OWC," in *Proc. of the European Wave and Tidal Energy Conference Series, Aalborg, Denmark.*, 2013.

[112] Paparella, F. , Monk, K., Winands, V., Lopes, M.F.P., Conley, D., and Ringwood, J.V., "Upwave and autoregressive methods for short-term wave forecasting for an oscillating water column," *IEEE Transactions on Sustainable Energy*, vol. 6, no. 1, pp. 171 – 178, 2015.

[113] WECCA (2013), "WECCA Official Website." [online] Available at: https://weccamerica.com/. [Accessed 20 March 2017].

[114] OMEY labs (2013), "OMEY labs Official Website." Available at: http://www.omeylabs.com/. [Accessed 20 March 2017].

[115] Roessling, A., "Testing of OMEY Labs low-end wave tank," tech. rep., Maynooth University, 2014.

[116] Marinet, "Tank test related instrumentation and best practice," tech. rep., Marinet, 2014.

[117] Mc Kiernan, K, "Wave tank sensor suite report," tech. rep., Centre for Ocean Energy Research (COER), Maynooth University, 2016.

[118] RBR (2015), "RBR Official Website." [online] Available at: https://rbr-global.com/. [Accessed 20 March 2017].

[119] FUTEK (1998), "FUTEK Official Website." [online] Available at: http://www.futek.com/. [Accessed 20 March 2017].

[120] AUTOMATION DIRECT (1998), "AUTOMATION DIRECT Official Website." [online] Available at: https://www.automationdirect.com/. [Accessed 20 March 2017].

[121] Neuroscience and Robotics Lab (NxR) (2006), "Neuroscience and Robotics Lab (NxR) Official Website." [online] Avaiable at: http://hades.mech.northwestern.edu/. [Accessed 20 March 2017].

[122] McMASTER-CARR (2000), "McMASTER-CARR Official Website." [online] Available at: https://www.mcmaster.com/. [Accessed 20 March 2017].

[123] Rhinefrank, K., Schacher, A., Prudell, J., Stillinger, C., Naviaux, D., Brekken, T., Jouanne, A.V., Newborn, D., Yim, S., and Cox, D., "High resolution wave tank testing of scaled wave energy devices," in *Proc. 29th International Conference on Offshore Mechanics and Arctic Engineering (OMAE)*, 2010.

[124] Bosma, B., Sheng, W., and Thiebaut, F., "Performance assessment of a floating power system for the galway bay wave energy test site," in *Proc. International Conference on Ocean Energy (ICOE)*, 2014.

[125] Qualisys (2002), "Qualisys Official Website." [online] Available at: http://www.qualisys.com/. [Accessed 20 March 2017].

[126] Holmes, B., "Tank testing of wave energy conversion systems: Marine renewable energy guides," 2009.

[127] Welch, G. and Foxlin, E., "Motion tracking: No silver bullet, but a respectable arsenal," *IEEE Computer Graphics and Applications*, vol. 22, no. 6, pp. 24–38, 2002.

[128] Cooper, S. and Durrant-Whyte, H., "A Kalman filter model for GPS navigation of land vehicles," in *Proc. IEEE/RSJ/GI International Conference on Intelligent Robots and Systems '94 . 'Advanced Robotic Systems and the Real World', IROS '94*, 1994.

[129] Skog, I., "A low-cost GPS Aided inertial navigation system for vehicular applications," Master's thesis, Royal Institute of Technology, Stockholm, Sweden, 2005.

[130] Foxlin, E., Harrington, M., and Pfeifer, G., "Constellation^{TM} : A wide-range wireless motion-tracking system for augmented reality and virtual set applications," in *Proc. SIGGRAPH 98 Computer Graphics*, 1998.

[131] Titterton, D.H. and Weston, J.L., *Strapdown Inertial Navigation Technology -2nd Edition*. The Institution of Electrical Engineers and The American Institute of Aeronautics and Astronautics, 2004.

[132] Hieu, L. N. and Nguyen, V.H., "Loosely coupled GPS/INS integration with Kalman filtering for land vehicle applications," in *Proc. 2012 International Conference on Control, Automation and Information Sciences (ICCAIS)*, 1998.

[133] Hexamite (1999), "Hexamite Official Website." [online] Available at: http://www.hexamite.com/. [Accessed 20 March 2017].

[134] Heller, V., "Model-prototype similarity," tech. rep., Imperial College London, 2012.

[135] Babarit, A., Hals, J., Kurniawan, A., Muliawan, M, Moan, T., and Krokstad, J., "Numerical estimation of energy delivery from a selection of wave energy converters," tech. rep., Ecole Centrale de Nantes, 2011.

[136] Tarrant, K. and Meskell, C., "Investigation on parametrically excited motions of point absorbers in regular waves," *Ocean Engineering*, vol. 111, pp. 67–81, 2015.

[137] Retes, M. P., Merigaud, A., Gilloteaux, J.C., and Ringwood, J.V, "Nonlinear Froude-Krylov force modelling for two heaving wave energy point absorbers," in *Proc. 11th European Wave and Tidal Energy Conference, Nantes, France*, (Nantes, France), 2015.

[138] Wavestar (2000), "Wavestar Official Website." [online] Available at http://wavestarenergy.com/. [Accessed 20 March 2017].

[139] Paparella, F. and Ringwood, J.V., "Optimal control of a three-body hinge-barge wave energy device using pseudo-spectral methods," *IEEE Transactions on Sustainable Energy*, vol. 8, no. 1, pp. 200–208, 2017.

[140] Zhao, H. and Wang, Z., "Motion measurement using inertial sensors, ultrasonic sensors, and magnetometers with Extended Kalman Filter for data fusion," *IEEE Sensors Journal*, vol. 12, no. 5, 2012.

[141] Farrell, J. and Barth, M., *The Global Positioning System and Inertial Navigation*. McGraw-Hill, 1999.

[142] Slabaugh, G. G., "Computing euler angles from a rotation matrix," tech. rep., City Univ. London, London, 1999.

[143] *Stäubli Arm - TX series 60 family, Instruction Manual*.

[144] Skog, I. and Händel, P., "Calibration of a MEMS inertial measurement unit," in *Proc. XVII IMEKOWORLD CONGRESS Metrology for a Sustainable Development*, 2006.